MODELING OF PEM FUEL CELL SYSTEMS INCLUDING CONTROLS AND REFORMING EFFECTS FOR HYBRID AUTOMOTIVE APPLICATIONS

DISSERTATION

Presented in Partial Fulfillment of the Requirements for

The Degree Doctor of Philosophy in the Graduate

School of The Ohio State University
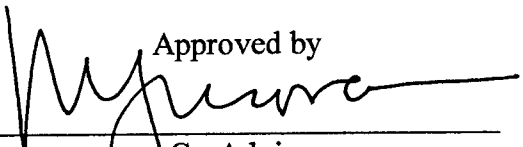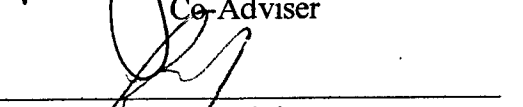
By

Daisie D. Boettner, M.S.E.

* * * * *

The Ohio State University
2001

Dissertation Committee:

Professor Michael J. Moran, Co-Adviser

Professor Yann Guezennec, Co-Adviser

Professor Giorgio Rizzoni

Approved by

_____
Co-Adviser

_____
Co-Adviser
Mechanical Engineering Graduate Program

ABSTRACT

Due to the nature of fuel cell reactions, fuel cells have the potential of being more fuel efficient while generating fewer harmful emissions than conventional automotive power systems. Additionally, by hybridizing a fuel cell system with a battery, opportunities may exist for significantly improving overall performance.

This study develops models for a stand-alone Proton Exchange Membrane (PEM) fuel cell stack, a direct-hydrogen fuel cell system including auxiliaries, and a methanol reforming fuel cell system for integration into a vehicle performance simulator. Exergetic efficiencies associated with the three models are examined and sources of inefficiency are identified. Fuel cell stack efficiency is highest when operating at low current density. Air compressor power consumption and losses associated with reformer operation significantly lower the overall system efficiency and highlight the importance of low-level control of components within the system.

By incorporating the models developed in this study into the vehicle performance simulator, alternative fuel cell vehicle configurations can be explored using various driving cycles, component sizing, and control strategies to determine effects on overall vehicle performance and fuel economy. For a typical sport utility vehicle operating over the *Federal Urban Driving Schedule* and *Federal Highway Driving Schedule* driving

cycles, the simulator is used to examine fuel economy in four cases: direct-hydrogen fuel cell vehicle, methanol reforming fuel cell vehicle, direct-hydrogen hybrid (fuel cell system/battery) vehicle, and methanol reforming hybrid vehicle. Results indicate the direct-hydrogen hybrid vehicle shows the strongest potential for high fuel economy.

Additionally, for the direct-hydrogen hybrid vehicle, simple supervisory control strategies for the fuel cell system and battery are used to examine component sizing and operational limits. Dominance filtering is employed to identify component sizing and operational limits that provide the potential for highest fuel economy. Results of this analysis can be used as a point of departure to develop more advanced supervisory and component-level control strategies. Using appropriate supervisory and component-level control strategies to improve total system performance is key to realizing the benefits of fuel cell system integration for automotive applications.

Dedicated to my father and mother

ACKNOWLEDGMENTS

VITA

January 16, 1959	Born – Saint Louis, Missouri
1981	B.S., United States Military Academy, West Point, New York
1991	M.S.E. Mechanical Engineering, University of Michigan, Ann Arbor, Michigan
1981 – Present	Officer, United States Army
1991-1993	Instructor/Assistant Professor, Thermodynamics, United States Military Academy, West Point, New York

PUBLICATIONS

Research Publication

1.   Potter, R. A., King, D. J., Weitzel, D. P., and Boettner, D. D., 1995, "ASHRAE Research Project 766: Study of Operational Experience with Thermal Storage Systems," ASHRAE Transactions, Volume 101, Part 2, pp. 549-557.

2.   Boettner, D. D. and Ward, A. C., 1992, "Design Compilers and the Labeled Interval Calculus," *Artificial Intelligence in Engineering Design Volume 1*, C. Tong and D. Sriram, ed., Academic Press, Inc., Boston, pp. 135-192.

3.   Bains, N. S., Boettner, D. D., and Ward, A. C., 1991, "End Point Non-uniqueness in Labeled Interval Calculus Operations," ASME, Design Engineering Division (Publication) DE, Volume 31, pp. 265-270.

4.   Boettner, D. D., 1991, "An In Depth Look at the Labeled Interval Calculus and the Mechanical Design Compiler." Master's Thesis, University of Michigan, Ann Arbor, Michigan.

FIELDS OF STUDY

Major Field: Mechanical Engineering, Engineering Thermodynamics

TABLE OF CONTENTS

LIST OF TABLES

LIST OF FIGURES

xiv

CHAPTER 1

INTRODUCTION

1.1. Exergy Conversion Systems

An important subspecialty in mechanical engineering practice is the devising of systems that produce mechanical and/or electrical power from fossil fuel inputs. These systems are conventionally referred to as *energy* conversion systems, but more precisely are *exergy* conversion systems.

Figure 1.1 shows an exergy conversion system represented as a control volume at steady state. Components within the control volume that allow the desired exergy conversion to be achieved might include internal combustion engines, batteries, fuel cells, turbines, compressors, pumps, heat exchangers, and so on. A single fuel input is shown for simplicity, but applications involving multiple fuels are not excluded from present consideration.

For the control volume of Fig. 1.1, the rate of exergy transfer into the control volume, $\dot{E}_F$, exceeds the rate of exergy transfer from the control volume. The difference is the rate of *exergy destruction* due to *internal irreversibilities*. Exergy is transferred from the control volume as mechanical and/or electrical power, $\dot{E}_P$, and via heat transfer and mass flows. Not all exergy transfers from the control volume are valuable; some

Transfers of Exergy to Surroundings
(via heat transfer, mass flows)

$\dot{E}_F$ __fuel__

oxidizer

Destructions
of Exergy,

$\dot{E}_D$

$\dot{E}_P$
(Electricity,
Mechanical Power)

Components within box
achieve exergy conversion
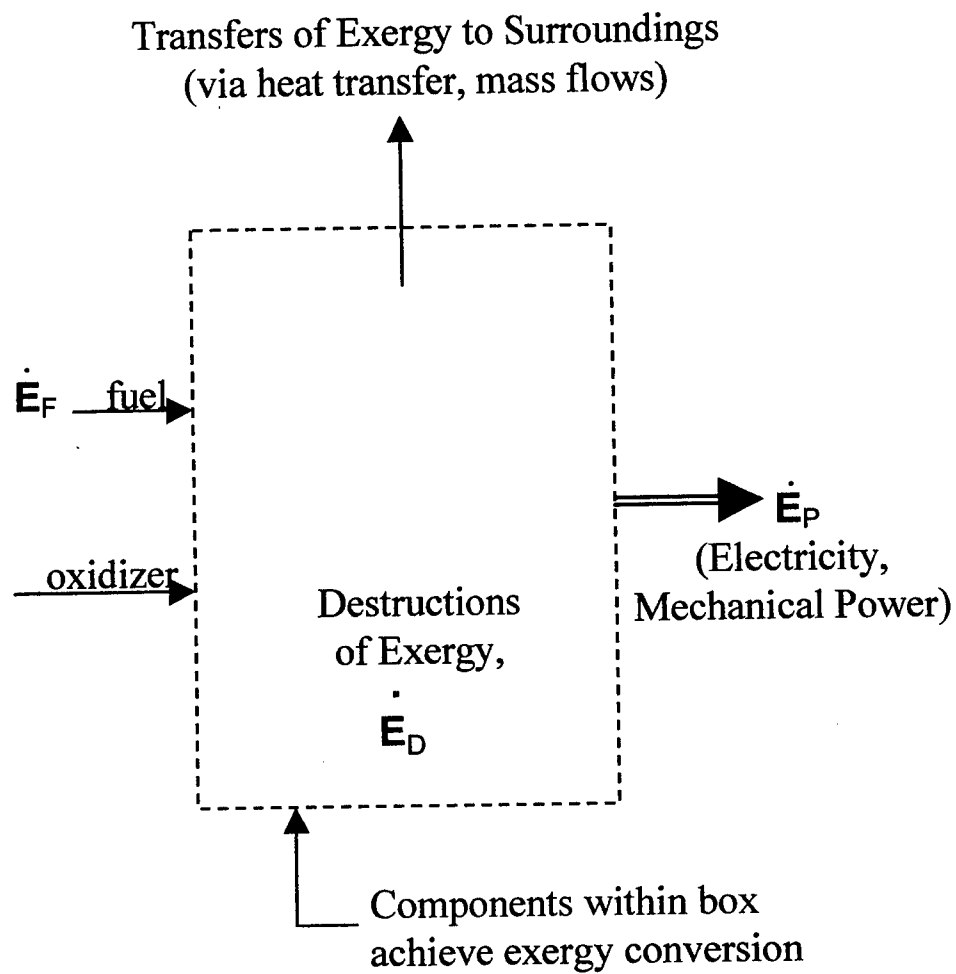
Figure 1.1: System Exergy Balance

may be regarded as losses, for example exergy in effluents. Each component has associated exergy destructions and also may contribute to exergy loss. Irreversibilities destroy exergy while exergy losses further reduce the magnitude of the desired exergy product. From a *second law of thermodynamics* perspective, the goal is to achieve an integration of all necessary components that maximizes the exergy product while minimizing exergy destruction and loss. To be viable, however, the system integration must take into consideration constraints such as total cost, weight, volume, and environmental impact. According to Bejan et al. (1996) cost-optimal integrations are typically distinct from thermodynamic-optimal integrations.

1.2. Exergetic Efficiency

The *exergetic efficiency* (ε) measures the extent of the conversion of the exergy input to the desired exergy product. For the case of Fig. 1.1, when the exergy transfers via heat transfer and mass flows are regarded as losses, the exergy product is $\dot{E}_P$, and the exergetic efficiency is simply

$$\varepsilon = \frac{\dot{E}_P}{\dot{E}_F} \tag{1.1}$$

The exergy entering with the oxidizer, normally air, is considered negligible. Following Bejan et al. (1996), the exergy entering with the fuel is predominantly *chemical* exergy. The chemical exergy can be approximated satisfactorily by the fuel *heating value*, the magnitude of the enthalpy of combustion of fuel. Then

$$\varepsilon = \frac{\dot{E}_P}{\dot{m}_F \times HV} \tag{1.2}$$

where:

$\dot{m}_F$ = the mass flow rate of fuel into the control volume

HV = the fuel heating value.

The *lower heating value* (*LHV*) is typically used for automotive exergetic efficiency calculations since water in the vapor phase is one of the combustion products. If the only exergy conversion component in the control volume in Fig. 1.1 is a fuel cell, then Eq. 1.2 determines the fuel cell exergetic efficiency.

Significant exergy destructions and losses are associated with the chemical processing required to produce fuels from feedstock. In writing Eq. 1.1 consideration is given only to conversion from refined fuel to useful product, which for automotive applications may be called the *fuel tank-to-wheels* conversion. When using the exergetic efficiency, it is important to understand whether refined fuel or feedstock is considered as the exergy input. An exergetic efficiency based on the chemical processing feedstock, which for automotive applications may be called the *well-to-wheels* conversion, is typically much less than would be determined using Eq. 1.1. Wang (1999 and 1999a) provides several conversion efficiencies associated with converting feedstock into refined fuel as summarized in Table 1.1. According to Wang (2000), the fuel conversion efficiency is computed by dividing the product of the mass of the refined fuel and its lower heating value by the product of the mass of the feedstock and its lower heating value, and thus is an exergetic efficiency.

1.3. Automotive Power Systems

The present study concerns automotive power systems involving fuel cells. Of particular interest are *hybrid systems* that include fuel cells, batteries, and combinations

Refined Fuel	Conversion Efficiency	Feedstock
Conventional Gasoline	85%	Petroleum
Conventional Diesel	89%	Petroleum
Compressed Natural Gas	97%	Natural Gas
Methanol	65%	Natural Gas
Gaseous Hydrogen	71%	Natural Gas (Central Plant Production) (excluding compression)

Table 1.1: Conversion Efficiencies for Refined Fuels from Feedstock

of the two with or without an internal combustion engine. Contemporary interest in such hybrid systems is spurred by the objective of achieving increased power system exergetic efficiency and/or decreased environmental impacts.

Figure 1.2 illustrates potential hybrid configurations. The battery and the fuel cell produce electric power. An electric motor converts electric power to mechanical power. The internal combustion engine produces mechanical power. The total mechanical power produced is the output from the system. From this internal combustion engine/battery/ fuel cell hybrid automotive energy conversion model, several subset configurations are possible: internal combustion engine only, internal combustion engine/battery hybrid, internal combustion engine/fuel cell hybrid, battery only, battery/fuel cell hybrid, and fuel cell only.

When exergy conversion devices for automotive use are arranged in a hybrid configuration, a *driving strategy* is required: a plan specifying under what conditions each device is operated. A goal of the driving strategy is to produce sufficient power to meet the load demand of the vehicle while achieving high exergetic efficiency. Exergy conversion device hybridization with a battery/electric motor also offers the advantage that some of the exergy normally destroyed during vehicle braking can be recouped via regenerative braking and used to charge the battery. The electric motor can operate in reverse converting input torque into voltage to recharge the battery. Additionally, power produced by the internal combustion engine and/or fuel cell in excess of the power required by the wheels can be used to recharge the battery.
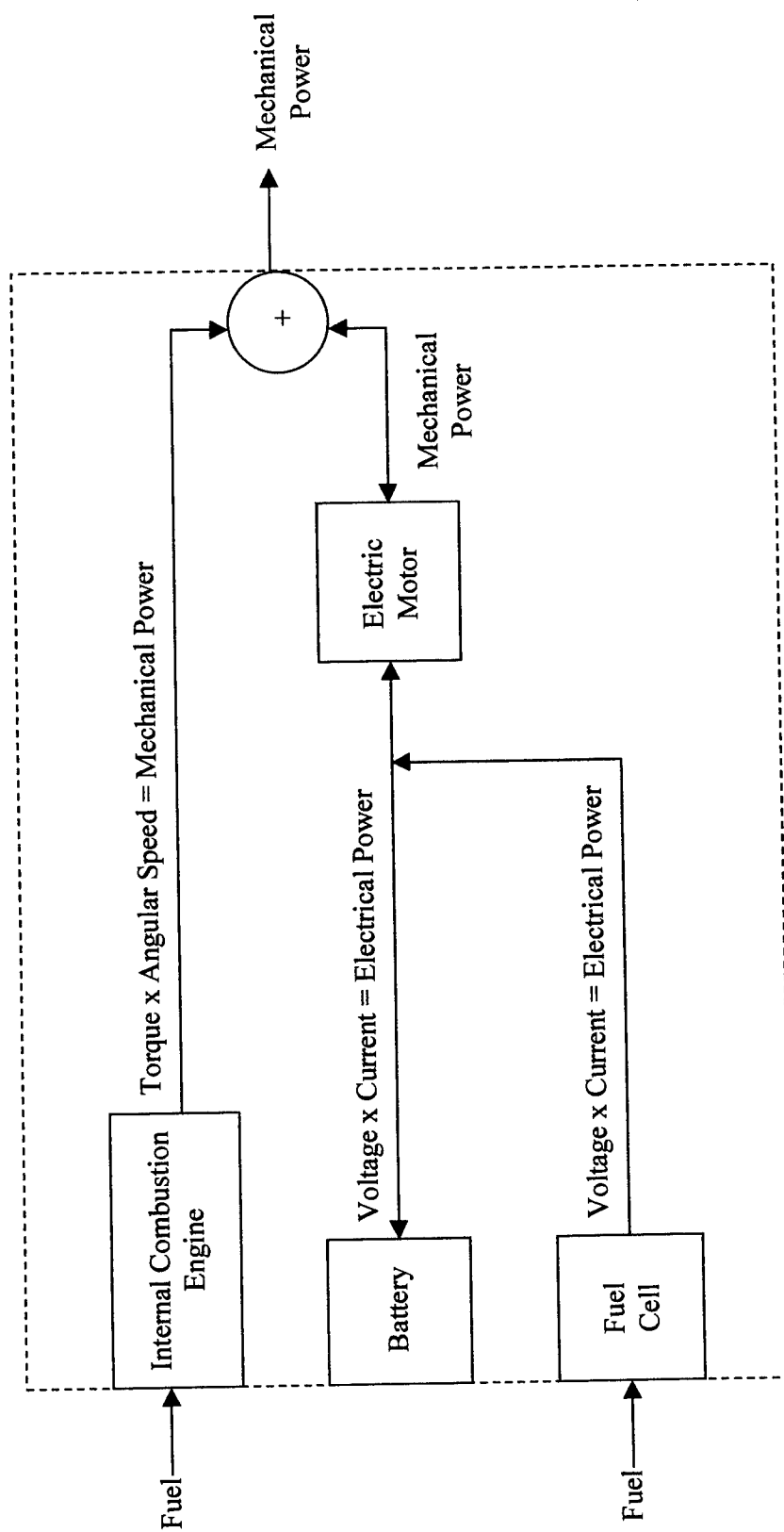
Figure 1.2: Automotive Power System Schematic

1.4. Scope of Research

This study focuses on exergy conversion using fuel cells in automotive applications. Scope of work includes issues associated with fuel cells, modeling of fuel cells, and simulation of fuel cell systems in automotive applications.

1.4.1. Previous Studies

Several researchers have examined performance of fuel cell power systems for automotive applications. Johansson and Alvfors (2000) examine performance of a fuel cell system at steady state. Using a typical automotive nominal load of 50 kW, analyses at 100% load and 50% load are conducted to determine recommended operating conditions.

Ogden et al. (1999) analyze a fuel cell/battery hybrid automotive system operating on three different fuels: hydrogen, methanol, and gasoline. The system is subjected to two driving cycles, the Federal Urban Driving Schedule (FUDS) that simulates city driving and the Federal Highway Driving Schedule (FHDS) that simulates highway driving. Driving cycles specify various vehicle velocities for a specified time period to simulate acceleration, cruising, deceleration and braking of the vehicle. From the results of the simulations, Ogden et al. (1999) recommend hydrogen as the preferred fuel.

Friedman (1999) compares performance of a fuel cell only power system with a fuel cell/battery hybrid power system. Simulations are performed for two driving cycles: FUDS and a high speed/high cycle load driving cycle designated US06. Results from the simulations indicate that hybridization may not be beneficial for driving conditions with high power requirements.

Burke and Miller (2000) examine relative fuel economies of transit buses. Using the Central Business District and the New York City Bus driving cycles simulations are conducted for four engine configurations: (1) diesel electric hybrid, (2) compressed natural gas engine-generator series hybrid, (3) direct-hydrogen fuel cell, and (4) methanol reforming fuel cell/battery hybrid with regenerative braking. Results are compared with fuel economy data for three conventional engines presently used in transit buses: conventional diesel, conventional compressed natural gas, and diesel electric hybrid. Simulation results for the four engine configurations show fuel economies higher than those associated with the three conventional engines. Direct-hydrogen fuel cell engine fuel economy was the highest.

Eggert et al. (2001) simulate performance of a methanol reforming fuel cell vehicle based on a model described by Hauer et al. (2000). Steady-state fuel cell system efficiency, reformer efficiency, and overall system efficiency are compared to corresponding *dynamic* efficiencies over the FUDS driving cycle. Results indicate that fuel cell system dynamic efficiency is very close to fuel cell system steady-state efficiency. Reformer dynamic efficiency is significantly lower than reformer steady-state efficiency causing lower overall system dynamic efficiency compared to the steady-state case. The authors identify burner control within the fuel processor and fuel processor dynamic response as the primary opportunities for improved dynamic efficiency.

Hauer et al. (2001) develop an indirect methanol fuel cell system/battery hybrid model for automotive applications. The system is subjected to the US06 driving cycle to examine regenerative braking potential. Increasing the degree of regenerative braking

results in lower fuel cell power demand with accompanying lower fuel consumption but induces higher stress on the battery due to increased charge and discharge activity.

Rodatz et al. (2000) examine a fuel cell/supercapacitor hybrid power system. Since the supercapacitor provides only short-term energy storage, this study centers on driving strategy control options to meet vehicle demands. No analysis involving a driving cycle is performed.

Georgetown University and Booz-Allen & Hamilton, Inc. (1999) conduct a study for the U.S. Army to determine the feasibility of incorporating fuel cell systems into three current military vehicles: Family of Medium Tactical Vehicle (FMTV) 2.5 ton cargo truck, M915A2 tractor, and M113A3 armored personnel carrier. Fuel cell only and fuel cell/battery hybrid configurations are considered. Both configurations are subjected to two driving cycles. The first cycle is a bus profile for suburban duty. The cycle includes acceleration from 0 to 40 mph, a brief period at 40 mph, deceleration, and complete stop. The second cycle includes acceleration from 0 to 55 mph for 2 minutes followed by 5 minutes at 55 mph. Results of the analysis indicate that the power requirements exceed power production capabilities of currently developed fuel cells. Concerns are expressed whether fuel cell/battery hybrid can deliver full requirements over sufficient time due to decreased battery state of charge. An additional conclusion is that a fuel cell power system cannot fit into existing space available for the power train due to additional equipment necessary for cooling.

1.4.2. Research Objectives

The focus of the current study is to analyze exergy conversion by a fuel cell/ battery hybrid system in automotive applications. One objective of the study is to

10

establish a baseline performance level using simple control strategies. Results of this study are expected to provide a benchmark for more advanced control strategies. A second objective is to determine effects of on-board reforming on overall fuel economy compared to use of direct-hydrogen. Specific primary tasks include:

(1) Create a PEM fuel cell stack model that is computationally efficient and accurate. Validate results from the model to verify model accuracy. The model is described in Sec. 3.2.2.

(2) Extend the fuel cell stack model to a fuel cell system model by incorporating auxiliary components required for air flow, fuel flow, cooling, and humidification. The fuel cell system model is described in Sec. 3.2.3.

(3) Embed the system model into a vehicle simulator. An overview of the vehicle simulator with fuel cell system model is described in Section 4.1.

(4) Perform direct-hydrogen fuel cell vehicle simulations. Assess fuel cell system performance in vehicles operating under specified driving cycles. Simulation results are described in Sec. 4.3.

(5) Develop a methanol reformer model and integrate the reformer model with the fuel cell system model in the vehicle simulator. The reformer model is described in Section 5.3. Perform fuel cell vehicle simulations. Determine the effects of fuel reforming on fuel cell system performance and overall vehicle fuel economy. Simulation results are described in Section 5.5.

(6) Employ a direct-hydrogen fuel cell system/battery hybrid using simple control strategies to assess system performance in vehicles operating under specified driving cycles. Determine sizing trade-offs for fuel cell stack and battery to meet

11

required load while minimizing overall fuel consumption. Determine fuel cell system and battery operational parameters to achieve these objectives. Simulation results are described in Secs. 6.6 and 6.7.

(7) Conduct simulations to determine fuel economy for a fuel cell vehicle and a fuel cell system/battery hybrid vehicle using direct-hydrogen and methanol reforming. Results are described in Sec. 7.2.

Conclusions and recommendations for further study are discussed in Chapter 8.

CHAPTER 2

FUEL CELL OVERVIEW

2.1. Introduction

Commonly used exergy conversion devices such as internal combustion engines and

gas turbines involve combustion of fuel to produce hot gases that are used to generate

electrical or mechanical power. A fuel cell does not require an intermediate combustion

process to accomplish exergy conversion. The fuel cell produces electricity via *cell*

reactions from chemical exergy stored in fuel. Elimination of the combustion process

reduces inherent combustion exergy destruction and may lower/eliminate undesirable

emissions. Consequently, fuel cells have the potential to provide more work from a given

quantity of fuel and be less polluting than internal combustion engines and gas turbine

engines. The object of this chapter is to provide an overview of fuel cell technology

currently under consideration for various power generation applications.

2.1.1. Mode of Operation

Hirschenhofer et al. (1998) and Thomas and Zalbowitz (1999) provide detailed

descriptions of the basic operation of a fuel cell. As shown in Fig. 2.1, a fuel cell consists

of two electrodes, an anode and a cathode, with an electrolyte membrane sandwiched

between the two. The anode/electrolyte membrane/cathode unit is the basis of a fuel cell
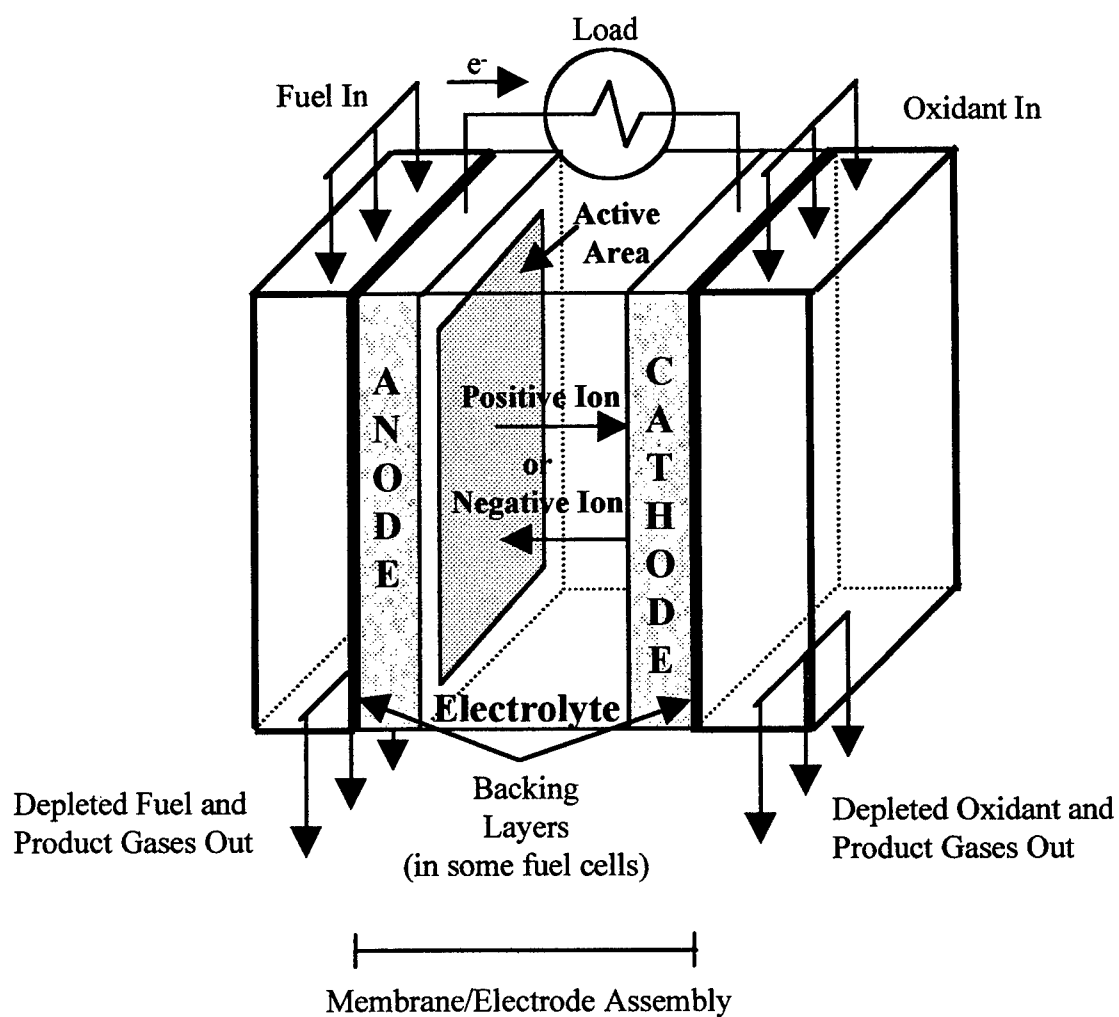
Figure 2.1: Schematic of an Individual Fuel Cell

and is called the membrane/electrode assembly. The electrodes support chemical reactions. The electrolyte membrane provides a conductive path for ions while keeping the anode and cathode reactants separated.

Separate gas flow channels exist for continuous fuel flow to the anode and continuous oxidant flow to the cathode. In some cells the anode and the cathode each have a porous, electrically conductive backing layer that allows diffusion of the reacting gases from the flow channel to the electrode. Intermediate chemical reactions occur at each electrode. Each electrode uses an appropriate catalyst at the reaction sites to increase the rate of reaction. The cross-sectional area of the electrode containing chemical reaction-supporting catalyst is called the *active area* of the fuel cell. This is suggested on Fig. 2.1 by the shaded area. The fuel is oxidized at the anode and the oxidant is reduced at the cathode. Ions produced at one electrode flow through the electrolyte membrane to the other electrode. An external circuit provides a route for flow of electrons produced at the anode to complete the circuit to the cathode. Choice of electrolyte influences the *fuel cell operating temperature*, temperature at which the anode and cathode gas flows exit the fuel cell (see Sec. 2.2), and consequent requirements to maintain the target temperature.

As an example, the following cell reactions correspond to a fuel cell involving hydrogen as the fuel and oxygen as the oxidant:

Anode: $\qquad$ $H_2 \rightarrow 2H^+ + 2e^-$ $\hspace{4cm}$ (2.1)

Cathode: $\qquad$ $\frac{1}{2}O_2 + 2H^+ + 2e^- \rightarrow H_2O$ $\hspace{3cm}$ (2.2)

Overall Reaction: $\qquad$ $H_2 + \frac{1}{2}O_2 \rightarrow H_2O$ $\hspace{3.5cm}$ (2.3)

15
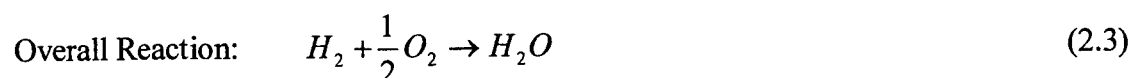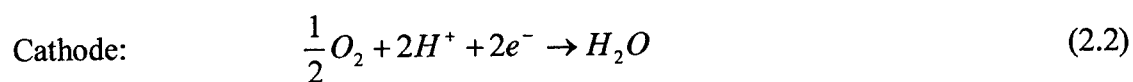
In this example hydrogen dissociates into two hydrogen protons and two electrons at the anode, Eq. 2.1. The hydrogen protons flow through the electrolyte membrane to the cathode while the two electrons flow through an external circuit to the cathode. At the cathode oxygen reacts with the hydrogen protons and electrons to form water, Eq. 2.2. The sum of the anode reaction and the cathode reaction is the overall reaction in the fuel cell, Eq. 2.3. All fuel cell overall reactions can be divided into two partial reactions: one at the anode and the other at the cathode. These partial reactions are called *half-cell reactions*. Addition of the two half-cell reactions gives the overall reaction.

The flow of electrons from the anode through the external circuit to the cathode is electric current. The driving force behind electric current is the cell potential (voltage). In the same way that the fuel cell overall reaction may be considered as the sum of two half-cell reactions, the fuel cell potential may be considered as the sum of two half-cell potentials. Associated with the half-cell reactions at the anode and cathode are corresponding standard half-cell potentials determined under reversible conditions at specified standard temperature and pressure. Addition of the two half-cell potentials gives the maximum voltage that the fuel cell can develop. When the fuel cell operates, the voltage is less than the maximum voltage due to the effect of irreversibilities (see Sec. 2.3.1.1). The product of the current and the actual cell voltage is the electrical power produced by the fuel cell.

2.1.2. Fuel Cell Stacks

A single fuel cell does not produce sufficient voltage for many practical applications. To increase the voltage output, fuel cells are connected in series to form a fuel cell stack as shown in Fig. 2.2. A bipolar plate, which provides separate channels for

16
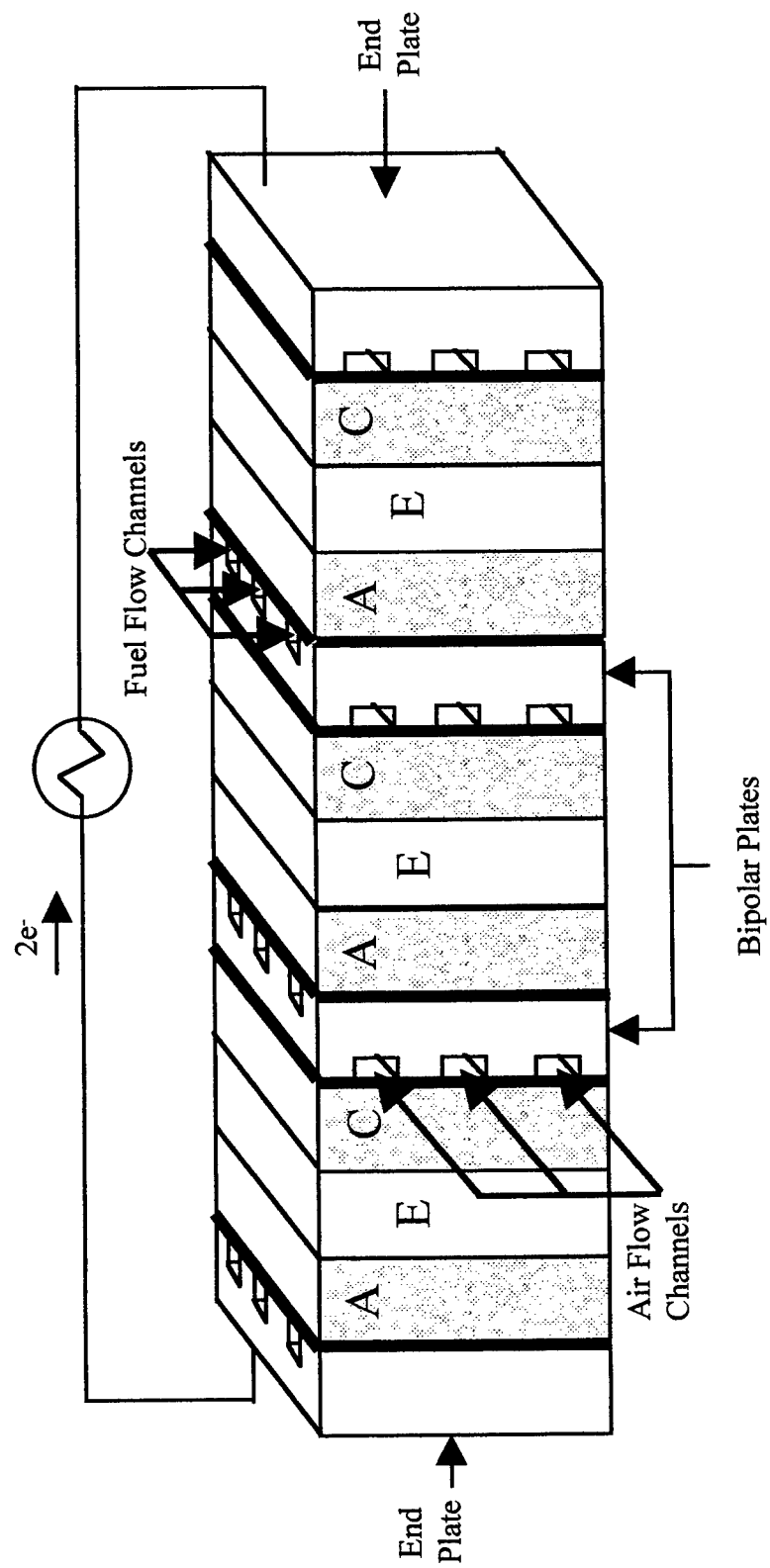
Figure 2.2: Fuel Cell Stack

fuel and oxidant flow and is an electrical conductor, is layered between each fuel cell. The bipolar plate material does not allow mixing of the fuel and oxidant. The oxidant has access to the cathode on one side of the bipolar plate while the fuel has access to the anode on the other side of the plate. Electrons produced at the anode side of each bipolar plate flow through the plate to the cathode on the other side of the plate. These electrons participate in the cathode half-cell reaction and also provide an electrical connection between the individual fuel cells. End plates are used at each end of the fuel cell stack. The external circuit is connected from one end plate to the other end plate to complete the circuit. Total voltage produced in the fuel cell stack is the sum of the individual fuel cell voltages.

Since temperature control is essential for proper fuel cell operation, cooling passages may also be integrated into a fuel cell stack. Coolant flows through these passages to effectively transfer energy by heat away from the fuel cells to maintain a desired fuel cell stack operating temperature.

Because the fuel cell stack is composed of repetitive sections, the fuel cell stack can be tailored to meet a given requirement. Applications ranging from very small power requirements (less than 500 Watts) to very large requirements (Megawatts) are possible. Fuel cell stacks can be connected in series or in parallel providing flexibility in power source configurations.

2.1.3 Fuel Considerations

Direct fuels are those fuels fed directly from a storage tank to the fuel cell anode where they are oxidized. Other fuels require an intermediate process to produce species

that can be oxidized, typically hydrogen, in the fuel cell anode. This is known as *fuel reforming*. Direct fuels and fuels requiring reforming each have inherent advantages and disadvantages.

2.1.3.1. Direct Fuels

Use of direct fuels eliminates any requirement for auxiliary fuel processing equipment between the fuel tank and the fuel cell stack. Two direct fuels, hydrogen and methanol, currently are considered to be feasible for use in fuel cell stacks.

Hydrogen is a direct fuel that has excellent *electrochemical reactivity*: the ability to produce electrons during chemical reaction. It also produces no harmful emissions. Drawbacks to hydrogen as a direct fuel include on-board storage challenges for automotive applications, lack of current infrastructure for refueling, and safety issues.

Hydrogen Storage Issues. Casten et al. (2000) describe three commercially available on-board hydrogen storage technologies: compressed hydrogen, liquefied hydrogen, and metal hydrides. The chemical exergy stored per unit of volume, the *exergy density*, of compressed hydrogen can reach 4 MJ/liter at 5,000 psi. Storage pressures of 5,000 psi and above are required to minimize storage tank volume. The power required to compress hydrogen to these high pressures is significant. Due to the small molecular diameter of hydrogen coupled with high pressure, leakage also is a concern. According to Casten et al. (2000) Ballard fuel cell buses operating in Chicago and the Ford P2000 prototype have successfully demonstrated compressed hydrogen storage. The exergy density of liquefied hydrogen can reach 8.5 MJ/liter. Power required to liquefy hydrogen is also significant. Evaporation of liquefied hydrogen and subsequent escape from the storage tank in a closed environment can pose an explosion

19

hazard. DaimlerChrysler's NECAR 4 demonstration fuel cell vehicle exhibited in Washington, D.C., in 1999 uses liquefied hydrogen storage. Metal hydride storage in which hydrogen is stored in a hydrogen-metal complex can achieve an exergy density of 9-12 MJ/liter. Honda's experimental fuel cell vehicle, FCX V1, uses hydrogen metal hydride storage. Typically the amount of hydrogen stored per kilogram of metal complex is relatively low, resulting in a high overall fuel storage weight. Additionally, several of the metals used for the metal hydride are expensive. With current technology metal hydride storage systems require complex fluid and gas flow packaging, heat transfer subsystems, and thermal expansion and contraction allowance. Current metal hydride storage limitations make the development of this storage system challenging for transportation applications. Other experimental hydrogen storage systems include carbon micro-fiber storage and high-pressure storage in small glass microspheres (Stephens, 1999).

Hydrogen Infrastructure and Safety Issues. Ogden et al. (1999) note that hydrogen production, storage, and transportation technology is mature and routine for chemical industry applications. The infrastructure to support mass-market hydrogen demand does not currently exist, however, and the costs associated with infrastructure development are open to speculation. Kalhammer et al. (1998) conclude that such costs will be prohibitive until hydrogen becomes competitive with current fuels and the demand for hydrogen as a primary fuel is realized.

Hydrogen is a highly flammable gas. Hydrogen gas and cryogenic liquid hydrogen storage and handling procedures are markedly differently from current gasoline

20

and diesel fuels handling procedures. Accordingly, consumer perceptions about well-known safety issues associated with hydrogen are likely to influence its acceptability.

Another direct fuel is methanol. Methanol is the only practical carbonaceous fuel with significant electrochemical reactivity for use in the lower temperature fuel cells best suited for automotive applications (discussed further in Sec. 2.2.1). The reactions involving methanol as the fuel and oxygen as the oxidant are:

Anode: $$CH_3OH + H_2O \rightarrow CO_2 + 6H^+ + 6e^-$$ (2.4)

Cathode: $$\frac{3}{2}O_2 + 6H^+ + 6e^- \rightarrow 3H_2O$$ (2.5)

Overall Reaction: $$CH_3OH + \frac{3}{2}O_2 \rightarrow CO_2 + 2H_2O$$ (2.6)
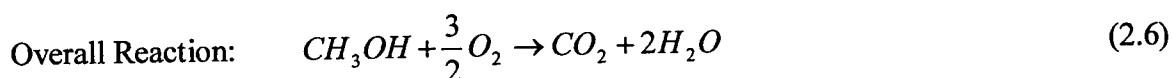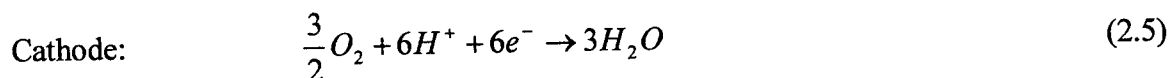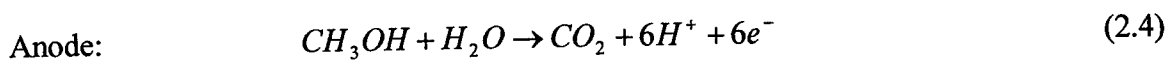
Water and carbon dioxide are the only products from the overall fuel cell reaction using direct methanol and oxygen. Because methanol is stored as a liquid at ambient temperature and pressure, on-board storage is similar to current liquid fuel storage systems. A limited liquid methanol infrastructure currently exists in California. Mok and Martin (1999) indicate that methanol can be distributed from conventional gas stations; however, tanks and dispensing units would need modification due to the corrosiveness of methanol with some materials.

Kalhammer et al. (1998) identify significant fuel cell operational problems associated with direct methanol. Direct methanol produces a much smaller *current density*: current per fuel cell active area than needed for automotive applications. Lower current density results in lower *power density*: power produced per fuel cell active area. The power density of a direct methanol fuel cell currently is no greater than 20% of the

power density of a direct hydrogen-air fuel cell. The amount of costly platinum catalyst required for oxidation of methanol is also much larger than that required for hydrogen. Furthermore, methanol has a tendency to rapidly diffuse from the anode through the electrolyte membrane to the cathode where it is oxidized. This is known as a *crossover reaction*. Such reactions waste fuel and decrease oxygen reduction at the cathode. Research to develop new electrolyte membranes that inhibit methanol diffusion is necessary to overcome the crossover problem. The American Methanol Institute introduced a direct methanol fuel cell concept vehicle in 1997. While promising from a fuel storage and distribution standpoint, fuel cells using direct methanol require significant research and development to overcome inherent operational problems and become viable for commercialization.

2.1.3.2. Reforming Issues

An alternative to direct fuels is reforming. During reforming, fuel reacts in the presence of a catalyst with other species to produce oxidizable species, typically hydrogen, and accompanying by-products. Reforming allows commonly available fuels to be used in fuel cells, thus eliminating/reducing costs associated with fuel infrastructure development. Reforming methods include *steam reforming, partial oxidation, autothermal reforming*, and *thermal decomposition*. Berlowitz and Darnell (2000) and Miller (2000) provide an overview of the various reforming methods. Although many of the reforming methods can be used for fuels containing hydrogen, the chemical nature of the fuel may favor one method over another method.

During the steam reforming process a fuel reacts with water to produce carbon monoxide and hydrogen. This process is highly endothermic and requires a significant

22

thermal input. Steam reforming normally occurs between 760 and 980°C. Steam reforming is typically used on natural gas, light hydrocarbons (butane and propane), methanol, and naphtha (with a special catalyst). The general form of the steam reforming reaction is:

$$C_nH_m + nH_2O \rightarrow nCO + \left(n + \frac{m}{2}\right)H_2 \qquad (2.7)$$
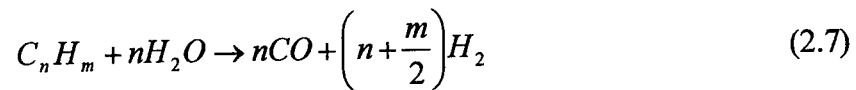
Partial oxidation is a process in which a fuel reacts with oxygen to form hydrogen and carbon monoxide. The process is exothermic. Typical fuels undergoing partial oxidation are distillate, naphtha, diesel oil, and heavy fuel oil. Kalhammer et al. (1998) report that Hydrogen Burner Technology in Long Beach, California, has developed a partial oxidation process to generate hydrogen from diesel fuels and JP-8, the primary fuel used by the military. The general form of the partial oxidation reaction is:

$$C_nH_m + \left(\frac{n}{2}\right)O_2 \rightarrow nCO + \left(\frac{m}{2}\right)H_2 \qquad (2.8)$$
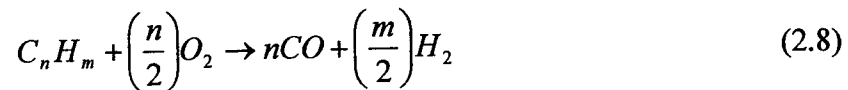
Autothermal reforming is a combination of partial oxidation and steam reforming. Energy transfer by heat from partial oxidation is available to support the endothermic steam reforming process. According to Bonville et al. (1996) International Fuel Cells Corporation in South Windsor, Connecticut, achieved autothermal reforming of diesel and JP-8 in a 100 kW power plant test. Kumar, et al. (1996) describe a methanol reformer that operates using autothermal reforming principles. This reformer is examined in greater detail in Sec. 5.3.1. The pertinent reactions during autothermal reforming are Eqs. 2.7 and 2.8.

Thermal decomposition uses an energy transfer by heat to decompose a hydrocarbon into carbon and hydrogen. It is an endothermic process. The general form of the thermal decomposition reaction is:

$$C_nH_m \rightarrow nC + \left(\frac{m}{2}\right)H_2 \qquad (2.9)$$

Reforming occurring outside the fuel cell proper is classified as *external reforming*. External reforming requires auxiliary fuel processing equipment between the fuel tank and the fuel cell as well as thermal and water management. Reforming within the fuel cell is classified as *internal reforming*. Maggio et al. (1998) describe two internal reforming methods: direct internal reforming and indirect internal reforming, the primary difference being the location of the reforming catalyst in the fuel cell. Direct internal reforming catalysts are located in the anode chamber while indirect internal reforming catalysts are physically separated from the anode compartment. Internal reforming increases the complexity of the fuel cell stack.

Fuel cells that operate at temperatures above 760°C (see Table 2.1) have the potential to reform fuel internally. Steam reforming of natural gas in the presence of a catalyst to produce hydrogen can occur at temperatures starting at ~760°C. Energy transfer by heat from the exothermic fuel cell reaction supports the endothermic steam reforming process.

2.1.3.3. Contaminant Effects

Fuel impurities and reforming by-products can have detrimental effects on catalysts used in reformers and fuel cell electrodes. Principal contaminants causing concern include sulfur, carbon monoxide, and carbon.

Sulfur reacts with catalyst materials currently used in fuel cells significantly reducing catalyst activity and life. Natural gas, gasoline, diesel, and JP-8 are fuels that contain sulfur. Braun et al. (1996) describe a hydrodesulphurizer unit used in a fuel cell demonstration power plant. As natural gas mixed with a small amount of hydrogen passes over a catalyst, hydrogen sulfide forms and is absorbed by zinc oxide pellets. King et al. (2000) describe automotive application efforts to reduce sulfur from fuel prior to reforming through selective adsorbents in replaceable canisters. Ongoing federal standard initiatives to reduce sulfur levels in transportation fuels as a means to lower internal combustion engine emissions would benefit fuel cells using such fuels.

As indicated by the chemical reaction equations for steam reforming, partial oxidation, and autothermal reforming, raw reformate gas contains significant amounts of carbon monoxide. In some fuel cells and under certain conditions carbon monoxide can be oxidized in the anode to produce electrons. In other fuel cells using platinum catalysts, carbon monoxide adheres to the catalyst in the anode reducing the number of sites for fuel oxidation. Removal of carbon monoxide from reformate is achieved through the *water gas shift reaction* that converts carbon monoxide in the presence of water to carbon dioxide and hydrogen:

$$CO + H_2O \rightarrow CO_2 + H_2 \qquad (2.10)$$
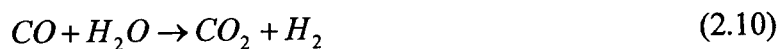
Additional carbon monoxide removal can be achieved by passing reformate through a selective catalytic oxidizer after the water shift reaction. In the selective oxidizer, two competing reactions occur:

$$CO + \frac{1}{2}O_2 \rightarrow CO_2 \qquad\qquad (2.11)$$

and

$$H_2 + \frac{1}{2}O_2 \rightarrow H_2O \qquad\qquad (2.12)$$
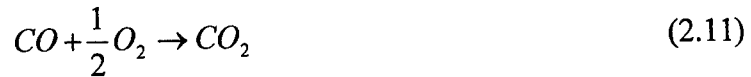
A fine balance between the two reactions is required to remove carbon monoxide while minimizing the consumption of hydrogen.

According to Call (1996) a practical problem associated with using methane for high temperature fuel cells is *coking*: the formation of solid carbon during decomposition of CH_4. Coking is detrimental to fuel cell operation because it clogs gas passages in the anode. Proper humidification is required to avoid coking.

Moore et al. (2000) analyze the effects on fuel cell operation of both common air pollutants and potential battlefield chemical warfare agents. Presence of common air pollutants including carbon monoxide, nitrogen dioxide, sulfur dioxide, benzene, and propane in the oxidant flow is reported to have little or no impact on fuel cell power output. However, the chemical agents sarin, sulfur mustard, cyanogen chloride, and hydrogen cyanide cause power output to drop at least 70% from power levels achieved with contaminant-free air. Mitigation of chemical warfare agent effects is necessary for military fuel cell applications operating on atmospheric air.

2.2. Fuel Cell Types

Categorized by the type of electrolyte used, the four most common types of fuel cells are: Proton Exchange Membrane (PEM) fuel cell, Phosphoric Acid Fuel Cell

(PAFC), Solid Oxide Fuel Cell (SOFC), and Molten Carbonate Fuel Cell (MCFC). Appleby and Foulkes (1993), Kordesch and Simaden (1996), and Hirschenhofer et al. (1998) review the various types of fuel cells. Lloyd (1999), Hirschenhofer et al. (1998), and Thomas and Zalbowitz (1999) provide comparisons of the most common fuel cell types, as summarized in Table 2.1.

2.2.1. Proton Exchange Membrane (PEM) Fuel Cell

The PEM fuel cell anode and cathode are made of carbon. The electrolyte is usually a fluorinated sulfonic acid polymer membrane or similar polymer membrane. This type of membrane is a hydrogen ion conductor while acting as an electronic insulator. The sulfonic acid molecules are fixed to the membrane by chemical bonding while protons can move freely through the membrane. High membrane water content is required for acceptable ion conductivity. The water requirement restricts PEM fuel cell operational temperature below the water boiling point. Typical operating temperature range is 60 to 100°C. Due to low temperature operation, costly platinum catalyst is required in both the anode and cathode to promote electrode reaction rates. The PEM fuel cell has a backing layer, which is porous carbon with waterproof coating. This type of backing layer allows reactant gases to diffuse to the catalyst layer, provides simultaneous liquid and vapor water supply and removal, and is electronically conductive in a wet environment.

A schematic of a PEM fuel cell is shown in Fig. 2.3. In the PEM fuel cell, hydrogen reacts with oxygen to form water. Separate reactions occur at the anode and cathode resulting in the overall reaction. These reactions are given in Sec. 2.1.1 and are repeated for ease of reference.

	(a) PEM	(b) PAFC	(c) SOFC	(d) MCFC
Transportation Application	Automotive power	Large vehicle power	Vehicle auxiliary power Heavy vehicle propulsion	
Other Applications	Portable power Small-scale stationary power	On-site cogeneration Electrical power generation	On-site cogeneration, Electrical power generation	On-site cogeneration, Electrical power generation
Electrolyte	Ion Exchange Membrane	Liquid Phosphoric Acid	Solid Oxide Ceramic	Liquid Molten Carbonate
Operating Temperature Range	60-100°C	150-220°C	800-1000°C	600-700°C
Charge Carrier through Electrolyte	H^+	H^+	$O^=$	$CO_3^=$
Prime Cell Components	Carbon-based	Graphite-based	Ceramic	Stainless Steel
Catalyst	Platinum	Platinum	Perovskites	Nickel
Product Water Management	Evaporative	Evaporative	Gaseous Product	Gaseous Product
Product Heat Management	Process Gas + Independent Cooling Medium	Process Gas + Independent Cooling Medium	Internal Reforming + Process Gas	Internal Reforming + Process Gas
Start-up Time	Second-minutes	Hours	Hours	Hours
Power Density [kW/m^2 of Active Cell Area]	3.8 – 6.5	0.8 – 1.9	1.5 – 2.6	0.1 - 1.5
Reformer	External	External	Internal or External	Internal or External
Status of Development	Demonstration systems up to 50 kW 250 kW units expected in next few years	Commercial systems operating, most at 200 kW An 11-MW model has been tested	Demonstration systems up to 100 kW	Demonstration systems up to 2 MW
Technical Challenges	Lower Costs Catalyst Electrolyte Improve Performance High temperature CO tolerance High current density	Lower Costs Catalyst Bi-polar plate Improve Performance High power density Corrosion resistant materials	Lower Costs Bi-polar plate Production High cost elements	Improve Performance Electrolyte leakage Structural stability and composition Sulfur tolerance Bi-polar plate corrosion

Table 2.1: Summary of Major Differences of the Fuel Cell Types

28
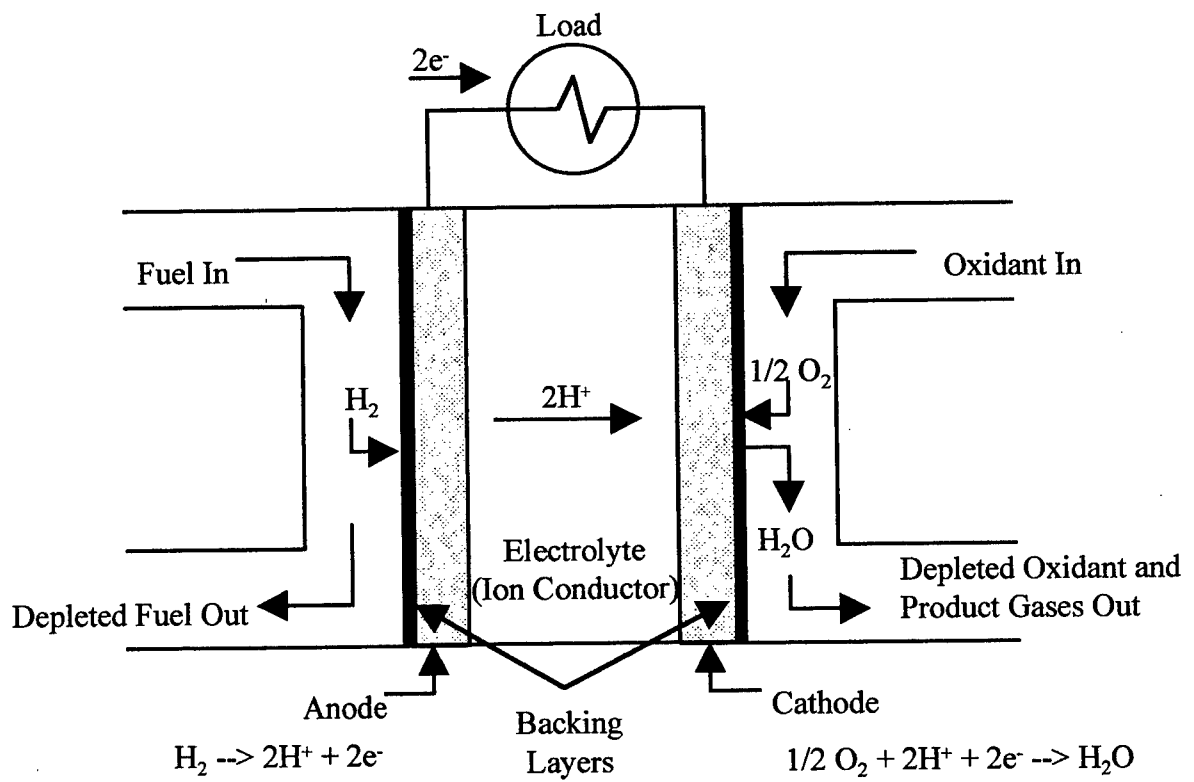
Figure 2.3: Schematic of PEM or PAFC Fuel Cell

Anode:
$$H_2 \rightarrow 2H^+ + 2e^-$$
(2.1)

Cathode:
$$\frac{1}{2}O_2 + 2H^+ + 2e^- \rightarrow H_2O$$
(2.2)

Overall Reaction:
$$H_2 + \frac{1}{2}O_2 \rightarrow H_2O$$
(2.3)
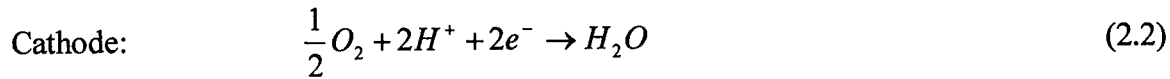
At the anode catalyst sites hydrogen dissociates into hydrogen protons and electrons. Hydrogen protons flow through the anode and the hydrated electrolyte membrane to the cathode side while electrons flow through the anode and an external circuit to the cathode side. At the cathode catalyst sites oxygen reacts with hydrogen protons and electrons to form water. Water exits the fuel cell with depleted oxidant. The overall reaction is exothermic. Exergy exits the fuel cell with product gas flows and via energy transfer by heat.

Hydrogen can be provided either as direct hydrogen or from external reforming. If external reforming is used, measures to remove carbon monoxide from reformate are required. Platinum catalyst is especially susceptible to carbon monoxide contaminant effects at temperatures less than 150°C. At PEM fuel cell operating temperatures, carbon monoxide will preferentially absorb on the platinum catalyst surface, reducing the number of sites available for the hydrogen to dissociate into hydrogen protons and electrons. Consequently, fuel used in a PEM fuel cell must contain no more than ten parts per million (ppm) of carbon monoxide.

External reforming involves a significant thermal input. Since the PEM fuel cell operates at low temperatures, thermal integration of the reformer with the fuel cell stack

is challenging. Fuel may be burned in a separate chamber to provide necessary thermal input for endothermic reforming processes. Exothermic reforming processes produce significant thermal energy that must be removed by heat transfer.

Water management is critical to ensure the membrane is properly hydrated to support ionic conduction. Surplus water dilutes reactant gases with water vapor and/or floods electrodes with liquid water inhibiting gas diffusion to the electrodes. Water deficit causes membrane dehydration reducing ionic conductivity. Humidification of the reactants is one method to ensure sufficient water is available in the membrane.

According to Kordesch and Simader (1996) advantages associated with PEM fuel cells include relatively quick start-up, relatively fast response to changes in demand, minimal corrosion problems, cell fabrication simplicity, demonstrated long life, and ability to sustain operation at high current densities. As soon as fuel and oxidant flow to the anode and cathode and a load is applied, the PEM fuel cell produces power. Time necessary to reach the desired operating condition ranges from several seconds to several minutes due to the low PEM fuel cell operating temperature range. PEM fuel cells respond almost instantaneously to changes in current demand as long as sufficient hydrogen and oxidant flows are available. Since sulfonic acid molecules are fixed to the electrolyte membrane, corrosion is minimal and electrolyte sealing is simplified. PEM fuel cells have demonstrated long life. PEM fuel cells can operate at high current densities for long periods. They also have a high power density. As a result, PEM fuel cells have the potential for low weight, cost, and volume.

Potential applications for PEM fuel cells include automotive applications, portable power, and small-scale stationary power. The major automakers have

31

announced development of several PEM fuel cell powered vehicles. Honda has two experimental fuel cell vehicles, the FCX V1 using direct hydrogen stored in metal hydrides and the FCX V2 using reformed methanol. DaimlerChrysler's New Electric Car (NECAR) 3 runs on reformed methanol while its NECAR 4 is powered by liquid hydrogen. Other vehicles using reformed methanol include Ford's FC5 fuel cell concept vehicle, General Motors' fuel cell EV1, and Nissan's Fuel Cell Vehicle (FCV). Vehicles using hydrogen from metal hydride storage include Toyota's Fuel Cell Electric Vehicle (FCEV) and Mazda's Demio FCEV experimental prototype. Dyer (1999) provides an overview of opportunities for replacing batteries by fuel cells in portable devices such as cellular phones, laptop computers, and camcorders. Stephens (1999) and Jones et al. (1999) discuss efforts to develop fuel cells for military portable power applications. According to Hirschenhofer et al. (1998) Ballard Generation Systems is the only company that has produced a PEM fuel cell stationary on-site plant. This plant has a 250 kW power capacity and operates on natural gas.

Hirschenhofer et al. (1998) state that technical challenges facing PEM fuel cells involve lowering costs and improving cell performance. Reducing catalyst requirements and lowering membrane cost will reduce fuel cell costs. Methods to improve performance include increased operational temperature range for the membrane, carbon monoxide mitigation from the fuel stream or increased carbon monoxide tolerance by the anode catalyst, and improved cathode performance at high current densities while operating on air.

Direct methanol is a potential alternative fuel for PEM fuel cells. Direct Methanol fuel cell (DMFC) reactions repeated from Sec. 2.1.3 for ease of reference are:

Anode:
$$CH_3OH + H_2O \rightarrow CO_2 + 6H^+ + 6e^-$$
(2.4)

Cathode:
$$\frac{3}{2}O_2 + 6H^+ + 6e^- \rightarrow 3H_2O$$
(2.5)

Overall Reaction:
$$CH_3OH + \frac{3}{2}O_2 \rightarrow CO_2 + 2H_2O$$
(2.6)
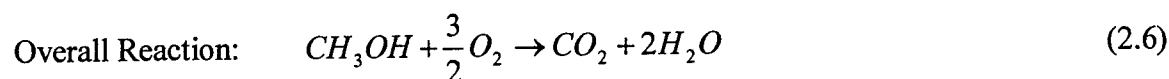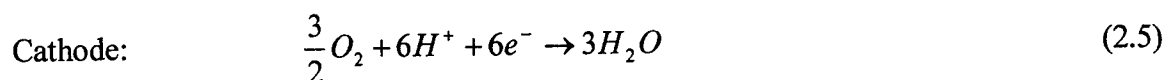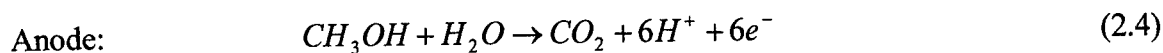
As discussed in Sec. 2.1.3.1, direct methanol fuel cells require technological improvements, including advanced electrolyte membrane materials to prevent crossover reactions and more active anode catalysts to promote methanol oxidation. Should these technological challenges be met, direct methanol would become an attractive option for PEM fuel cell automotive applications as no external reforming is required and methanol fuel infrastructure has potential for development.

2.2.2. Phosphoric Acid Fuel Cell (PAFC)

The phosphoric acid fuel cell consists of an anode and a cathode made of carbon paper containing carbon black supporting platinum catalyst particles. The electrolyte support matrix is polytetrafluoroethylene (PTFE)-bonded silicon carbide. The electrolyte is phosphoric acid (H_3PO_4). At the PAFC operating temperature range of 150 to 220°C, phosphoric acid has good ionic conductivity and relatively high stability. At temperatures below 150°C phosphoric acid is a poor ionic conductor while at temperatures above 220°C phosphoric acid becomes unstable. Platinum catalysts in the anode and cathode are required to promote sufficient chemical reaction at the operating temperature of the PAFC. The PAFC electrodes have a backing layer, wet-proofed carbon paper.

A schematic of a PAFC fuel cell is shown in Fig. 2.3. Reactions occurring in the PAFC are the same as those in the PEM fuel cell: Eqs. 2.1 through 2.3.

Direct hydrogen or hydrogen produced by external reforming can be used in PAFCs. If external reforming is used, carbon monoxide removal is an issue. Since the PAFC operates above 150°C, the platinum catalyst can tolerate up to 1% carbon monoxide in the fuel. Removal of sulfur from fuel is required. Sulfur in the form of hydrogen sulfide (H_2S) and carbonyl sulfide (COS) adsorbs on platinum, blocking active sites for hydrogen oxidation. Hirschenhofer et al. (1998) cite limits of 50 ppm H_2S and COS combined or 20 ppm H_2S for anode fuel. Anode exhaust gas is typically burned to provide thermal input required for external reforming.

Higher operating temperatures influence PAFC operation and opportunities. Longer start-up time is required to achieve desired operating temperature. Thermal management to maintain desired fuel cell stack temperature is accomplished by either liquid or air coolant flow through cooling channels in the stack. Hirschenhofer et al. (1998) cite the advantage of higher temperature operation for cogeneration of hot water and/or air.

Corrosion is an issue for the PAFC. Kalhammer et al. (1998) indicate that the PAFC must operate below 0.8 volts per cell to prevent corrosion of carbon and platinum components in the fuel cell. Expensive, corrosion-resistant, graphite bipolar plates are used in PAFC stacks. These bipolar plates also store additional phosphoric acid to replenish supply lost by evaporation.

According to Appleby and Foulkes (1993) water management is not critical since phosphoric acid electrolyte has adequate ionic conductivity at typical PAFC operating

conditions. Kordesch and Simader (1996) state that PAFC has the advantage of relatively simple electrolyte construction. Methods to process carbon, PTFE, and silicon carbide have been used for several years.

Potential applications for PAFC are large vehicle power systems, on-site cogeneration power plants, and dispersed power plants. Bonville et al. (1996) describe a program at Georgetown University to develop a 100 kW PAFC propulsion system for transit buses. The bus was introduced in May 1998 at the American Public Transit Association's Bus Operations Conference held in Phoenix, Arizona. According to Bonville et al. (1996) and Hirschenhofer et al. (1998) the PC-25 PAFC system developed by International Fuel Cells Corporation and manufactured by ONSI Corporation is the only commercially available fuel cell system. The PC-25 provides 200 kW of on-site power together with cogenerated hot water and/or air. It can operate on a variety of fuels including natural gas, propane, butane, landfill gas, and hydrogen. Take et al. (1996) describe efforts to develop a 200 kW PAFC power plant, which operates on either pipeline gas or liquid propane gas.

Hirschenhofer et al. (1998) state that technical challenges involve reducing costs and increasing power density for PAFC systems to achieve economic competitiveness with other power production methods. Reducing catalyst requirements and lowering bipolar plate costs are necessary. Development of corrosive-resistant materials that can withstand higher voltage is important to improve power density.

2.2.3. Solid Oxide Fuel Cell (SOFC)

The SOFC anode is metallic nickel on yittria-stabilized zirconia. The cathode is doped lanthanum manganite. Both electrodes are porous to allow diffusion of reactant

35

and product gases. The electrolyte is zirconia doped with yttria. Oxygen ions provide ionic conductivity by moving through electrolyte vacant lattice sites. SOFCs usually operate at 1000°C. Electrolyte temperature greater than 800°C is required to attain the activation energy of oxygen ion transport and achieve sufficient conductivity.

A schematic of a SOFC fuel cell is shown in Fig. 2.4. SOFC reactions are:

Anode: $\qquad$ $H_2 + O^= \rightarrow H_2O + 2e^-$ $\qquad$ (2.13)

Cathode: $\qquad$ $\frac{1}{2}O_2 + 2e^- \rightarrow O^=$ $\qquad$ (2.14)

Overall Reaction: $\qquad$ $H_2 + \frac{1}{2}O_2 \rightarrow H_2O$ $\qquad$ (2.15)
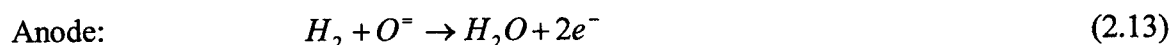
Hydrogen oxidation by oxygen ions at the anode produces water and electrons. Electrons flow through the anode and an external circuit to the cathode. At the cathode oxygen reacts with electrons to produce oxygen ions. Oxygen ions conduct negative charges from the cathode through the solid oxide electrolyte to the anode completing the circuit. The overall reaction is exothermic. Exergy exits the fuel cell with product gas flows and via exergy transfer by heat.

According to Srinivasan et al. (1993) carbon monoxide can also be oxidized in the anode. Carbon monoxide reacts with oxygen ions in the anode to produce carbon dioxide and electrons. Alternate SOFC reactions are:

Anode: $\qquad$ $CO + O^= \rightarrow CO_2 + 2e^-$ $\qquad$ (2.16)

Cathode: $\qquad$ $\frac{1}{2}O_2 + 2e^- \rightarrow O^=$ $\qquad$ (2.17)

Overall Reaction: $\qquad$ $CO + \frac{1}{2}O_2 \rightarrow CO_2$ $\qquad$ (2.18)
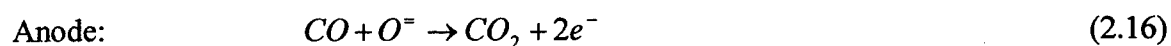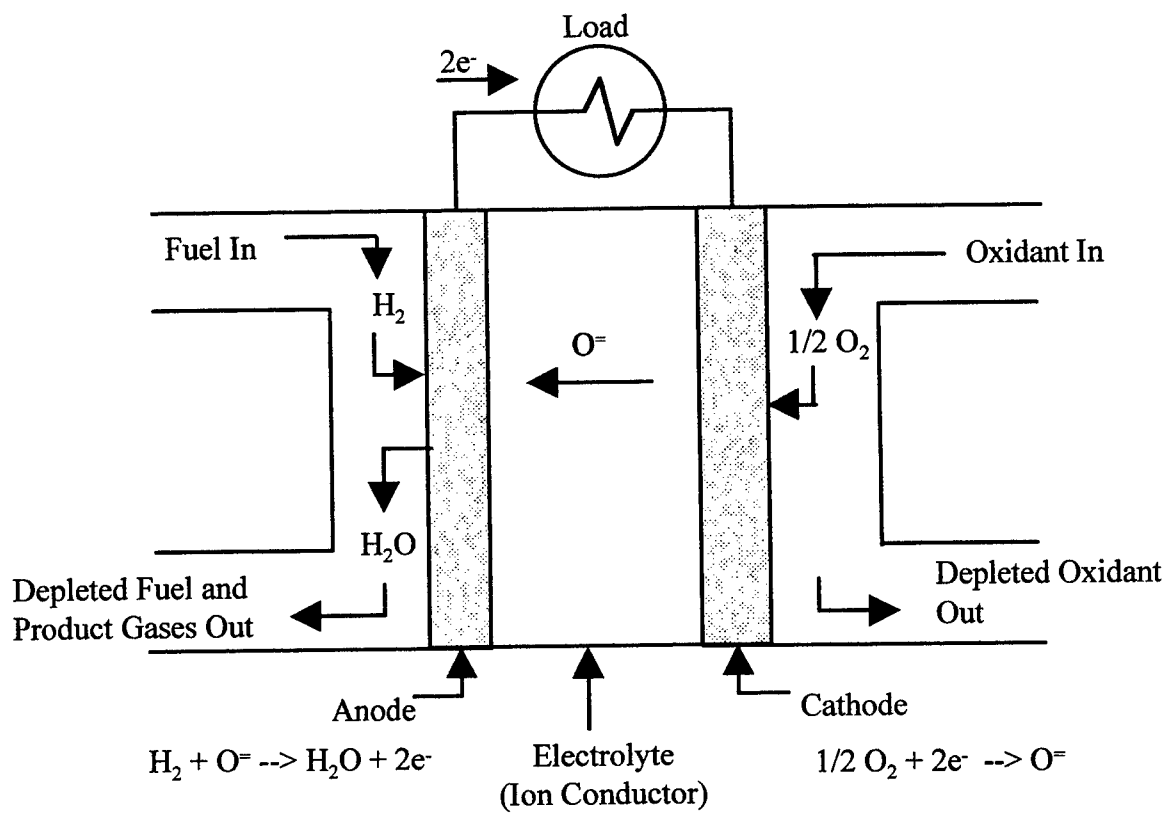
Figure 2.4: Schematic of SOFC Fuel Cell

If hydrogen and carbon monoxide enter the fuel cell together, product water from hydrogen oxidation will react with carbon monoxide in the water gas shift reaction (Eq. 2.10) instead of Eqs. 2.16 through 2.18 occurring.

Operationally, the SOFC can run on a wide assortment of fuels. No platinum catalyst is necessary to promote electrode reactions. According to Appleby and Foulkes (1993) fuel compositions will spontaneously internally reform and then oxidize rapidly to chemical completion without specialized catalysts. Excess steam is required to prevent coking. SOFCs can tolerate up to 1.0 ppm of sulfur in fuel.

The relatively high SOFC operating temperature (1000°C) provides advantages and disadvantages. Owing to high temperature operation SOFCs can provide the thermal input required for cogeneration or a bottoming cycle. Since all components of the SOFC are solid, SOFC configuration is flexible. Two most common designs are the Siemens Westinghouse Power Corporation developed tubular design and the flat plate design. Disadvantages due to high temperature operation are long start-up time, thermal enclosure requirements to protect other system components, thermal expansion mismatches among various materials used in the fuel cell, higher electrical resistivity in the electrolyte, and difficult fabrication.

Applications of SOFC in auxiliary power generation for heavy and light duty vehicles and heavy-duty vehicle propulsion are being explored. McConnell (2000) proposes potential SOFC auxiliary power unit markets include luxury vehicles, recreational vehicles, heavy-duty trucks, short haul trucks, and passenger vehicles. Dobbs (2000) promotes SOFC as an excellent candidate for future military heavy vehicles. Gavalas et al. (1994) conclude that when technology reaches maturity, SOFC is

38

a candidate for locomotive applications. However, the primary focus of SOFC development thus far has been for use in utility and industrial applications. According to Joon (1998) and Hirschenhofer et al. (1998) Siemens Westinghouse Power Corporation has two demonstration SOFC plants operating, a 25 kW test plant in Irvine, California, and a 100 kW plant operating in Westvoort, The Netherlands.

Bagger et al. (1996) and Hirschenhofer et al. (1998) cite technical challenges facing the SOFC. Challenges are primarily in lowering costs. Options include redesign of high cost elements and/or use of less expensive materials where acceptable, developing a lower cost fuel cell bipolar plate, and improvement in production procedures.

2.2.4. Molten Carbonate Fuel Cell (MCFC)

The components of the molten carbonate fuel cell consist of a nickel alloy anode, a nickel oxide cathode, and a $LiAlO_2$ ceramic electrolyte support matrix. The electrolyte is a combination of alkali carbonates of lithium, sodium, and/or potassium. At the MCFC operating temperature range of 600 to 700°C, the alkali carbonates form a highly conductive molten salt. Nickel contained in the anode and cathode promotes sufficient chemical reaction due to the high operating temperature of the MCFC. Carbonate ions provide ionic conduction.

A schematic of a MCFC fuel cell is shown in Fig. 2.5. MCFC reactions are:

Anode: $\qquad H_2 + CO_3^= \rightarrow H_2O + CO_2 + 2e^-$ $\qquad\qquad$ (2.19)

Cathode: $\qquad \frac{1}{2}O_2 + CO_2 + 2e^- \rightarrow CO_3^=$ $\qquad\qquad$ (2.20)

Overall Reaction: $\quad H_2 + \frac{1}{2}O_2 + CO_2(cathode) \rightarrow H_2O + CO_2(anode)$ $\qquad$ (2.21)
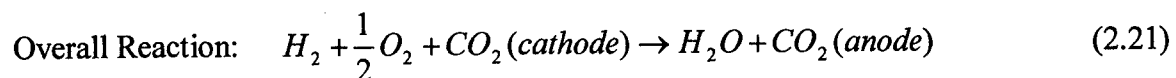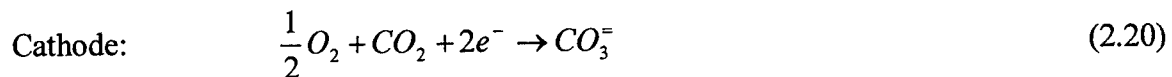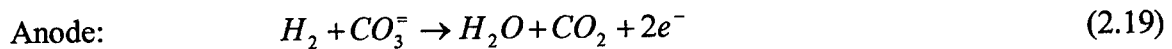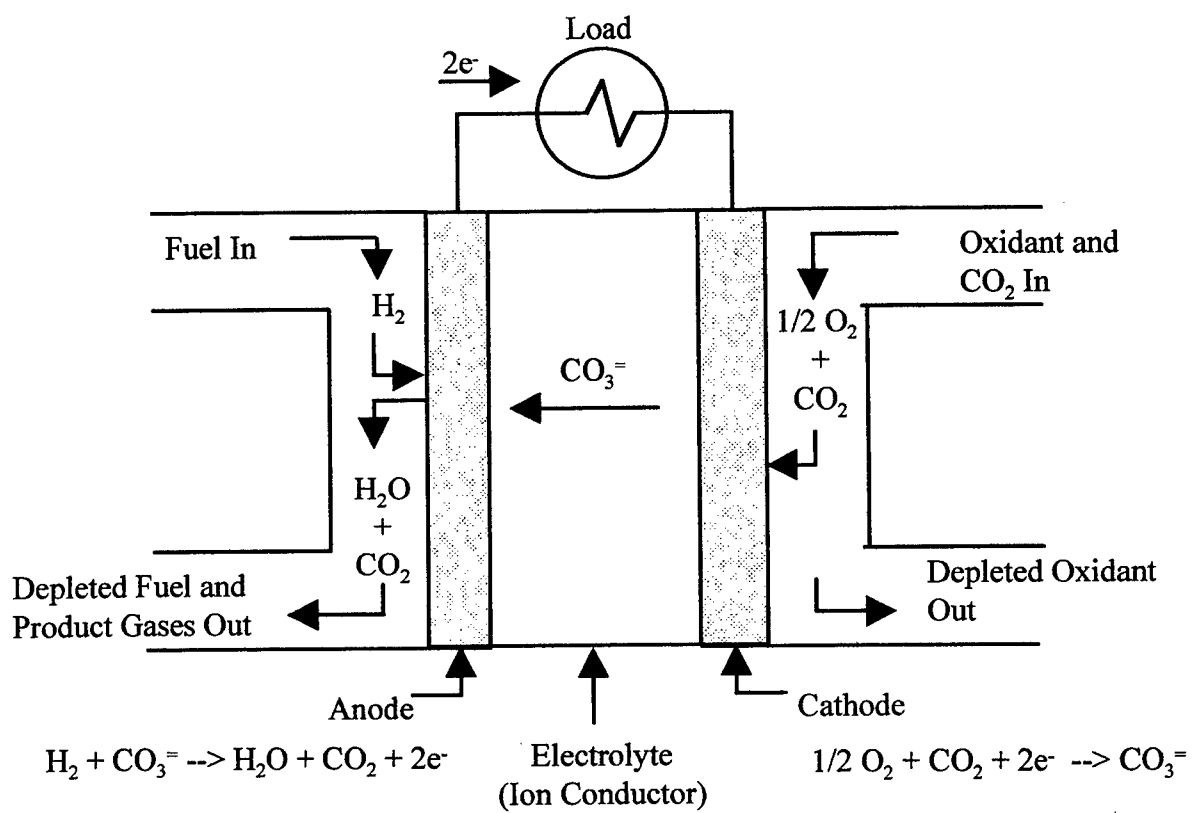
Figure 2.5: Schematic of MCFC Fuel Cell

Oxidation by carbonate anions of hydrogen at the anode produces water, carbon dioxide, and electrons. Electrons flow through the anode and an external circuit to the cathode. At the cathode oxygen and carbon dioxide react with electrons to produce carbonate anions. Carbonate anions conduct negative charges from the cathode through the molten electrolyte to the anode completing the circuit. Anode exhaust is typically burned to form carbon dioxide and water. Carbon dioxide is routed to the cathode for use during oxygen reduction. The overall reaction is exothermic. Exergy exits the fuel cell with product gas flows and by exergy transfer via heat.

Operationally, the MCFC can run on a wide assortment of fuels. Since the MCFC operates at a relatively high temperature (650°C) and does not use platinum as a catalyst, carbon monoxide by-product from external reforming can be processed by the fuel cell. In the anode hydrogen oxidation occurs more rapidly than carbon monoxide oxidation, producing water product. Water product reacts with carbon monoxide in the anode via the water-gas shift reaction (Eq. 2.10) producing additional hydrogen for the fuel cell reaction. Anode exhaust gas combustion provides the thermal input to support external reforming. Higher operating temperature also supports internal steam reforming of fuel. Typical fuels that can be internally reformed in MCFCs include methane, methanol, propane, and naphtha. The fuel cell reaction provides the thermal input needed to support internal reforming. Internal reforming reduces the cooling requirement to maintain operating temperature.

Fuel sulfur levels greater than 0.5 ppm are detrimental to MCFC operation. Sulfur compounds react with nickel to block potential anode reaction sites. Additionally, any sulfur present in anode exhaust becomes sulfur dioxide during combustion. The

41

sulfur dioxide is recycled with carbon dioxide to the cathode, where sulfur dioxide will react with carbonate ions in the electrolyte. To prevent carbon formation and deposit on the anode manifold and flow channels, water in the anode exhaust gas is recycled to provide humidification.

Disadvantages of the MCFC are the highly corrosive nature of the molten carbonate electrolyte, the need for carbon dioxide for the cathode half-cell reaction, low tolerance to sulfur, electrolyte leakage, and material requirements for operation in a high temperature environment. Advantages of the MCFC are ability to internally reform fuel, less costly nickel catalysts, utilization of carbon monoxide as a fuel, and the potential for cogeneration.

MCFCs typically operate between 0.1 and 0.2 amps per square centimeter at 0.75 to 0.9 volts per cell. The primary application of MCFCs is production of power for electric utility and industrial cogeneration. MCFC systems are still in the development, testing, and demonstration phase. According to Hirschenhofer et al. (1998) a consortium headed by M-C Power Corporation successfully tested a 250 kW nominal capacity natural gas fired MCFC power plant at Miramar Naval Air Station, California. Fuel Cell Energy (formerly Energy Research Corporation) successfully demonstrated a 2 MW power plant in Santa Clara, California.

Hirschenhofer et al. (1998) indicate that technical challenges for MCFC development include reduction of electrolyte leakage, development of fabrication techniques to improve composition and reduce thickness of the electrolyte, improvement of nickel-based electrode structural stability, reduction in bi-polar plate corrosion and gas leaks, and increased sulfur tolerance.

42

2.3. Fuel Cell Modeling and Analysis

According to Hirschenhofer et al. (1998) modeling can be used to characterize actual fuel cell operation and to conduct system analysis studies. Modeling used to characterize actual fuel cell operation is normally very complex, based on cell component designs such as physical dimensions and material properties and physical considerations such as transport phenomena and electrochemistry. This complex modeling typically is used for design and development of fuel cells. Modeling of fuel cells for systems analysis is a simpler approach based on equations that describe cell performance as operating conditions change. This type of modeling is used in the present study (Sec. 3.2.2) to analyze fuel cell performance when integrated into a total automotive system.

Due to its strong potential for automotive applications, the PEM fuel cell is chosen for the present study. The following sections address second law issues associated with fuel cells, modeling of PEM fuel cells, and incorporation of second law considerations in fuel cell modeling.

2.3.1. Second Law Issues

Following Sec. 1.1, irreversibilities in a fuel cell destroy exergy while exergy losses from a fuel cell further reduce the desired product, power output. Furthermore, when a fuel cell is combined with other components to form a power plant for a transportation application, say, each such component has associated exergy destructions and losses that affect power output. From a second law perspective, the goal is to achieve an integration of all necessary components that maximizes power output while minimizing exergy destruction and loss, subject to constraints such as total cost, weight, volume, and environmental impact.

2.3.1.1. Fuel Cell Irreversibilities and Losses

Irreversibilities that destroy exergy during fuel cell operation include internal heat transfer, chemical reaction, electric current and ion flow through resistance, and friction from fluid flow. During actual fuel cell operation temperature gradients within the fuel cell induce localized heat transfer within the fuel cell. Crossover reactions and varying reaction kinetics contribute to temperature gradients. Viscous effects between flows and channel walls/electrode passages create pressure drops in the electrodes during actual fuel cell operation.

When current flows, the effect of irreversibilities within the cell is to reduce the voltage from the ideal *open-circuit* value. According to Hirschenhofer et al. (1998) these voltage reductions (or polarizations) are activation polarization, ohmic polarization, and concentration polarization respectively. Figure 2.6 shows a typical plot of cell voltage as a function of current density and illustrates the effect of these irreversibilities. Hirschenhofer et al. (1998) provide general equations to describe the magnitude of voltage reduction due to each type of polarization. Fuel cell operating temperature, *cathode pressure* (pressure of gas flow through cathode), *anode pressure* (pressure of gas flow through anode), and *level of humidification* of gas flows can influence the actual voltage-current density relationship discussed further in Sec. 3.1.2.

According to Appleby and Foulkes (1993) activation polarization results from slow reaction rates causing limited charge transfer at the electrode-electrolyte interface. Lee et al. (1998) describe activation polarization irreversibility in a PEM fuel cell. Reactions at the anode catalyst surface involve breakage of hydrogen bonds, formation of new bonds between hydrogen atoms and the catalyst surface, electron transfer, and

44

Ideal Voltage-Current Curve

Region of Activation Polarization
(Reaction Rate Irreversibility)

Actual Voltage-Current Curve

Cell Voltage [V]

Region of Ohmic Polarization
(Resistance Irreversibility)

Region of Concentration Polarization
(Gas Transport Irreversibility)

Current Density [A/cm²]
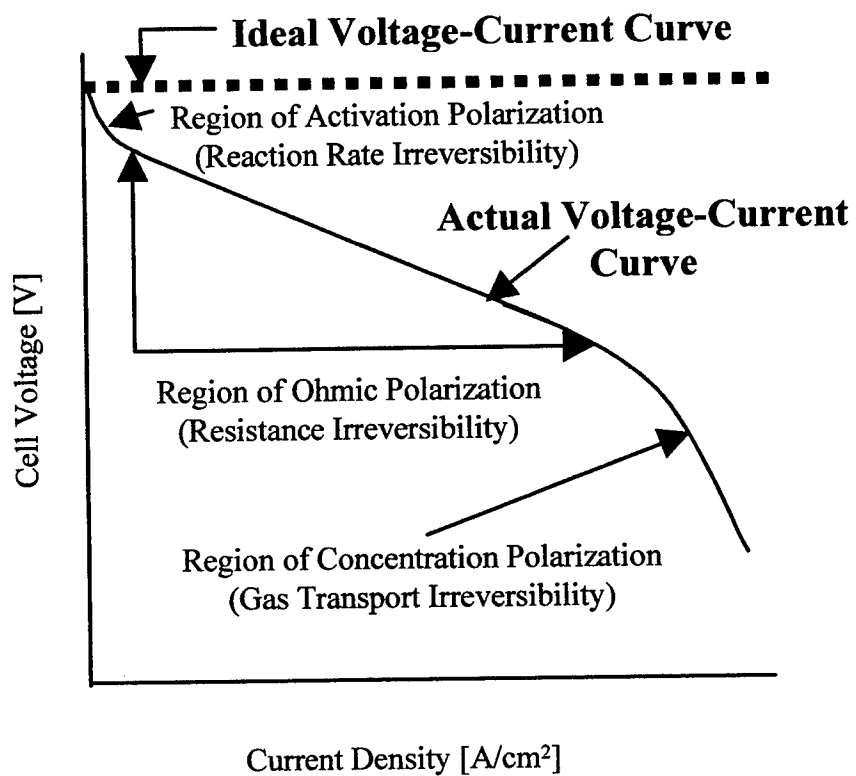
Figure 2.6: Ideal and Actual Fuel Cell Voltage/Current Characteristic

desorption of protons. Cathode catalyst surface reactions involve breakage of oxygen bonds, adsorption of oxygen atoms on the catalyst surface, reaction of oxygen atoms with protons and electrons, and formation of water molecules. Exergy from the fuel provided to the fuel cell is used to break and reform these bonds. As the reaction rate increases, process gas flow increases with corresponding increase in kinetic energy at the microscopic level. Increased kinetic energy supports breakage of bonds, reducing fuel exergy consumption.

A decrease in cell voltage results from voltage being used to drive the electron transfer rate to the rate required by the current demand. Factors that affect activation polarization are electrode materials, ion-ion interactions, and electrode-electrolyte interface. Activation polarization can be reduced by increasing operating temperature, increasing electrode activity with catalysts, and increasing electrode active surface area.

Ohmic polarization occurs as a result of resistance to ion and electron flow by the fuel cell components. It is directly proportional to the current density. Electronic resistance occurs in materials used for the electrodes and in bipolar plates used in fuel cell stacks. Ionic resistance occurs in the electrodes and the electrolyte membrane through which ions travel. Both electronic resistance and ionic resistance depend on material properties. Ionic resistance also depends on electrode separation distance. Ohmic polarization can be reduced by minimizing electrolyte membrane thickness, by using materials with high ionic and electronic conductivity, and by operating at low current densities.

According to Appleby and Foulkes (1993) concentration polarization is caused by mass transport limitations of reacting species near the electrode-electrolyte interface. A

constant supply of reactants is required for electrode reactions to sustain electric current. Slow transport of reactants to reaction sites and/or slow transport of products from reaction sites cause a concentration gradient at the reaction sites. Concentration polarization can be reduced by improving porous gas diffusion electrode design to enhance diffusion of reactants and products and by operating at low current density.

To maintain the fuel cell at desired operating temperature, heat transfer from the fuel cell to a coolant is necessary. Depleted oxidant and fuel streams exiting the fuel cell also carry exergy with them. If not exploited outside the cell, exergy transfers accompanying heat transfer and mass flows are losses.

2.3.1.2. System Integration

For practical applications fuel cell stacks are integrated with other components to form overall systems. Components providing air flow, fuel storage, fuel reforming, humidification, heat exchange, and/or coolant flow are necessary to support operation of the fuel cell. These components have associated sources of irreversibility and loss. Fuel reformers involve chemical reactions that may be significant sources of exergy destruction. Additionally, burners used to provide the thermal input required by reformers involve combustion, which invariably is a major source of exergy destruction. Air compressors used to achieve the desired cathode pressure and pumps used for coolant and water flows necessarily operate with friction. Flows in connections between components also experience pressure drops due to viscous effects.

Exergy analysis provides information on the locations and magnitudes of exergy destructions and losses within a system. Braun et al. (1995) use exergy analysis to examine a PAFC cogeneration system and identify improvements in heat recovery via

47

integration of the fuel cell with hot water and steam boiler systems. Cui et al. (1995) analyze the same PAFC cogeneration system using exergy analysis with *pinch* analysis, a heat exchange network optimization technique, and propose improvements via system reconfiguration. Moody et al. (1995) analyze a SOFC cogeneration system conceptual design using exergy analysis. They propose alternative reconfigurations that reduce high temperature heat exchange and thus improve overall system performance. Braun et al. (1995a) use exergy analysis to examine a proposed MCFC power plant design, and propose a redesign that captures exergy losses from the system through incorporation of a gas turbine into the system. Their analysis does not consider economic factors. Results of exergy analysis allow the designer to target areas that will provide the greatest potential for system improvement.

The overall objective of systems integration of a fuel cell is to produce a specified range of power within certain limits such as system cost, weight, volume, and exergetic efficiency depending on the system application. For automotive applications, system weight and volume are important while for on-site power generation these issues are not as important. Cost is important for all applications.

2.3.2. PEM Modeling

Modeling of fuel cells allows assessment of fuel cell performance under varying conditions. Models can be developed for the fuel cell itself and for fuel cell systems containing several auxiliary components.

2.3.2.1. Fuel Cell Operation

Several researchers have developed models to characterize actual PEM fuel cell operation. Springer et al. (1991) develop an isothermal, one-dimensional, steady state

model for a PEM fuel cell constructed with a 117 Nafion membrane, neglecting anode overpotential due to the high rate of anode catalytic activity. This model provides insight into cell water transport mechanisms and the resulting effects on cell performance. The model corresponded well to experimental results when excess liquid water was not present at the cathode.

Srinivasan et al. (1991) conduct studies of four PEM fuel cells: 125 μm thick Dow membrane with high platinum loading (10 mg/cm^2) electrodes and with low platinum loading (0.4 mg/cm^2) electrodes, a 100 μm thick Nafion membrane with low platinum loading, and a 175 μm thick Nafion membrane with low platinum loading. Equation 2.22 is used to describe fuel cell voltage as a function of current density:

$$E = E_o - b\log(i) - Ri \tag{2.22}$$

where:

E = fuel cell potential or voltage

E_o = ideal fuel cell potential

b = Tafel slope for oxygen reduction reaction

R = cell resistance (primarily ohmic and charge transfer resistance)

i = current density.

The second term on the right hand side of Eq. 2.22 represents activation polarization effects while the third term represents ohmic resistance effects. Based on experimental results, non-linear least-squares fit technique is used to determine E_o, b, and R for each fuel cell analyzed.

Amphlett et al. (1995 and 1995a) develop a steady-state model for a Ballard PEM fuel cell using a combined mechanistic and empirical approach. Using mass transport analysis, oxygen and hydrogen partial pressures and concentrations at the catalyst surfaces are determined. An expression for the actual voltage is developed based on ideal voltage at standard temperature and pressure, activation polarization as a function of temperature, current density, and oxygen concentration, and ohmic polarization as a function of temperature and current density. Using experimental data from a single Ballard Mark IV PEM fuel cell, parametric coefficients for the activation polarization and ohmic polarization functions are determined. For the range of values used for temperature, oxygen partial pressure, and current density, the experimental data for actual voltage agree well with the model results.

Mann et al. (2000) extend the steady-state Ballard PEM fuel cell model of Amphlett et al. (1995 and 1995a) to apply to fuel cells with different physical characteristics and dimensions. The resulting model accounts for fuel cell active area, electrolyte membrane thickness, and membrane aging. Comparison of model results with published data for various fuel cells is mostly favorable. Cases where the model does not agree with experimental results may be due to differences in electrocatalyst.

Lee et al. (1998) develop a model for a PEM membrane/electrode assembly that can be integrated into a numerical model of a complete fuel cell stack. Empirical equations are used to model physical processes, polarizations, and electrical characteristics. These equations are incorporated into a larger dynamic model to determine electrical performance of a fuel cell stack. The dynamic model accounts for

differences in local temperature, pressure, humidity, and oxygen concentration within the stack. Results from the model are reasonable in comparison to established performance experimental results.

Gurau et al. (1998) develop a two-dimensional, non-isothermal mathematical model for a PEM fuel cell. To simulate transport phenomena and performance of PEM fuel cells, equations are developed to calculate actual concentration distributions along the interface between the gas diffuser and catalyst layer. Nondimensional transport equations are applied to three domains: the cathode gas channel-gas diffuser-catalyst layer for the air mixture, the cathode gas diffuser-cathode catalyst layer-membrane-anode catalyst layer-anode gas diffuser for liquid water, and the anode gas channel-gas diffuser-catalyst layer for hydrogen. The transport equations are solved numerically. Results from the mathematical model are compared with previously published results based on one-dimensional numerical models. The authors suggest that the results should be considered mostly qualitatively. Unlike other models, this model is able to predict phenomena in the region where concentration polarization is predominant.

2.3.2.2. Systems Analysis

Many researchers have developed systems models incorporating fuel cells in automotive applications. Ogden et al. (1999) use current-voltage curves for existing PEM fuel cells to model fuel cell performance. Assuming auxiliary power is proportional to fuel flow rate, fuel cell voltage is reduced to account for compressor power consumption, expander power generation, and type of fuel used. Fuel reformer

performance is modeled using ASPEN-plus software. The model is used in a vehicle simulator to compare performance, fuel economy, and alternative fuel cell vehicle designs operating on hydrogen, methanol, and gasoline.

Rodatz et al. (2000) develop a model of a fuel cell/supercapacitor hybrid electric vehicle to examine potential operating conditions. The fuel cell system operating on direct hydrogen consists of the fuel cell, air compressor, hydrogen recirculation pump, and cooling water pump. Fuel cell performance is based on a simplified expression for voltage based on open circuit voltage reduced by ohmic resistance. Power consumptions by the auxiliary components are modeled by equations developed from an energy balance and device isentropic efficiencies. The model is used in a vehicle simulation to identify control issues for a defined driving strategy.

Johansson and Alvfors (2000) develop a direct hydrogen PEM fuel cell system model for transportation applications to examine the effects of operating temperature, pressure, and water content on system performance. The fuel cell model is based on the cell voltage model developed by Springer et al. (1991). The fuel cell system model is for steady-state conditions. Studies at full load (50kW nominal power) and 50% load were conducted. Results from the parametric study indicate that PEM fuel cells should operate at pressures less than 2 bar.

Barbir et al. (1999) develop a steady-state mathematical model for an automotive application PEM fuel cell system. The fuel cell model is based on polarization curves determined experimentally from operation of a prototype PEM fuel cell. The system includes gasoline reformer, air compressor, cooling system, and air humidification system. System components are described by equations based on conservation of mass

52

and energy, accounting for chemical reactions and phase changes in each component. The model is used to conduct trade-off analysis for various system configurations and operating pressure and temperature.

Friedman (1999) examines the effects of hybridization of batteries with a PEM fuel cell automotive system. The fuel cell stack model is based on the Springer et al. (1991) PEM fuel cell model. Modeling of other fuel cell system components is based on manufacturer's data and experimental results. The fuel cell automotive system both with and without battery hybridization is analyzed under various driving cycles. For the cases considered hybridization may improve efficiency for driving cycles with lower power requirements while it does not provide an advantage for driving cycles with high power requirements.

A system analysis program, GCtool, developed by Geyer and Ahluwalia (1998) contains a PEM fuel cell model. The PEM model determines fuel cell voltage based on fuel cell operating temperature, current density, cathode pressure, and oxygen partial pressure at the cathode inlet. The GCtool model is based on the model developed by Srinivasan et al. (1991) with adjustments made to account for temperature and concentration polarization. GCtool is described in greater detail in Sec. 3.1 and is applied in the present study.

2.3.3. Second Law Modeling

Dunbar and Gaggioli (1988) model the performance of a solid oxide fuel cell stack operating on hydrogen and air using a mathematical model based on physical characteristics of the fuel cells and appropriate governing equations for the stack operation. Their model employs energy and chemical species balances in the fuel stream,

53

oxidant stream, and electrolyte; rate equations for mass transports and chemical kinetics; thermochemical property relations; and boundary conditions for a twenty-cell stack. Equations are iteratively applied over incremental lengths of each individual fuel cell in the stack. Application of the model quantifies the influence of irreversible processes within the fuel cell and determines the consequent voltage loss. From the results of the modeling, the authors develop voltage-current curves. The curves agree well with published data on the 20-cell stack.

Dunbar and Gaggioli (1990) conduct parametric studies using the Dunbar and Gaggioli (1988) SOFC model to analyze effects of feed stream temperature, amount of excess air, electrolyte thickness, and heat transfer from the reaction zone through the electrolyte to the air stream. When feed stream temperature increases, fuel and oxygen depletion causes a drop in cell voltage. At lower temperatures the fuel and oxygen depletion effect is less significant, but overall performance drops due to decreased ionic conductivity of the electrolyte. Thinner electrolyte membranes result in better performance. Excess air has little effect on performance at high fuel flow rates, in which the fuel utilization is low. At lower fuel flow rates in which the fuel utilization is high, excess air improves performance. Reducing heat transfer, if possible, improves overall performance. The authors are able to quantify the effect of various parameters on the performance of the stack. Such information is useful for improving the design of fuel cells and fuel cell stacks.

Ratkje and Moller-Holst (1992) use the Dunbar and Gaggioli (1988) model to examine irreversibilities in a SOFC with external reforming. Analysis focuses on irreversibilities associated with reformer combustion, incomplete cell reactions, and heat

54

transfer resulting from anode and cathode activation polarizations and electrolyte ohmic polarization. Irreversibilities contributing most to exergy destruction and consequent reduced power output are identified as reformer combustion and incomplete cell reactions. This type of analysis identifies areas in which improvements will have the greatest potential to reduce exergy destruction.

2.4. Closure

In the chapters to follow, models are developed for a stand-alone PEM fuel cell stack, a direct-hydrogen fuel cell system, and a methanol reforming fuel cell system. The exergetic efficiency associated with each model is examined and sources of inefficiency are identified. The models developed in this study are embedded in a vehicle simulator. Using the FUDS and FHDS driving cycles, fuel economy is determined in four cases: direct-hydrogen fuel cell vehicle, methanol reforming fuel cell vehicle, direct-hydrogen hybrid (fuel cell system/battery) vehicle, and methanol reforming hybrid vehicle.

CHAPTER 3

DIRECT-HYDROGEN PEM FUEL CELL AUTOMOTIVE MODEL

3.1. GCtool

In this chapter a fuel cell system analysis program developed at Argonne National Laboratory, GCtool version 2.21 for Windows 95 PC, is discussed and applied. GCtool is a C-language interpreter to which the developers precompiled component model, thermodynamic property code, and mathematical utilities functions. The program user develops system configurations of component models interconnected by various flows. The program performs steady-state and dynamic-system simulations of these lumped component systems. GCtool version 2.21 also runs on Windows 98 and Windows NT.

Within GCtool fluid flow is represented by the *Gastype flow class*. The user defines the type of fluid flow from the following Gastype flow class choices: "GAS" (mixture of gases in chemical equilibrium), "STM" (water/steam), "LIQ-species" (pure liquid species), "THR-species" (liquid, gas, or two-phase flow of indicated species), and "HC-label species_list" (liquid, gas, or two-phase multi-component flow of species within species_list). Individual components are represented by component data structures called *model classes*. Model class components can be used as stand-alone systems or can be connected to create integrated systems. Model classes that could be used to create fuel cell systems include PEM fuel cell, PAFC, MCFC, SOFC,

compressor, gas turbine, fluid flow heat exchanger, pump, fluid flow mixer, fluid flow splitter, combustor, and methane/methanol reformer. Additional model classes are listed in the GCtool user manual, Geyer and Ahluwalia (1998). This manual specifies procedures for the UNIX version of GCtool. For version 2.21 documentation available within the GCtool program itself provides instructions for use of GCtool.

Strengths of GCtool include access to gas phase chemical equilibrium codes, single and multi-component hydrocarbon property codes, liquid phase property codes, and water/steam property codes. The ability to integrate several components into a system for analysis provides user flexibility to analyze several configurations. A weakness of the program is the format required to establish a system and run the program. The program is based on the C-language requiring specific formatting of command lines. Users unfamiliar with the C-language may find using GCtool challenging. Geyer and Ahluwalia (1998) provide several examples with associated command lines. Understanding these examples with their associated command line formats is the easiest way to become familiar with use of GCtool.

3.1.1 Background

For this study *virtual experiments* representing direct-hydrogen PEM fuel cell operating scenarios were conducted. The PEM model was used as a stand-alone system. For the PEM modeling, the model classes, *gas* and *pem*, were used. The *gas* model initiates fluid flow while the *pem* model represents operation of a PEM fuel cell.

Two *gas* models are defined to represent air and hydrogen. Information specified by the user includes user-chosen name for gas model, Gastype flow class (id=" "), mass

57

flow rate (m) [kg/s], temperature (t) [K], pressure (p) [atm], mole fraction of each

species, i, within the gas flow (comp[i]), and relative humidity of gas flow (humid).

Examples of command lines for air and hydrogen are:

gas air={id="GAS"; m=0.1; t=323; p=2; comp[O2]=0.21; comp[N2]=0.79; humid=1.0;};

gas fuel={id="GAS"; m=0.00002; t=323; p=2; comp[H2]=1.0; humid=1.0;};

The *pem* model represents operation of a PEM fuel cell. User specifies fuel cell

operating temperature (celltemp) [K]. Depending on the user-specified design mode:

design (d), off-design (o), or utilization (u), the user specifies two of the following three

parameters: cell active area (area) [m^2], current density (curden) [A/cm^2], and fuel

utilization (fuelutil). Using the two parameters provided, the pem model solves for the

third parameter using Eq. 3.1:

$$i = \frac{2(\mu \times n_{a,in,h2})F}{A} \tag{3.1}$$

where:

i is the current density [A/cm^2]

μ is the fuel utilization (fraction of incoming fuel used in the fuel cell chemical

reaction)

$n_{a,in,h2}$ is the molar flow rate of hydrogen entering the fuel cell anode [kmol/s]

F is Faraday's constant (96,487,000 Coulombs/kmol equivalent e$^-$)

A is the fuel cell active area [cm^2].

In writing Eq. 3.1 note that two kmol of electrons are transferred for each kmol of

hydrogen consumed during the PEM fuel cell reaction (see Eq.2.1). Faraday's constant is

the quantity of electric charge associated with a kmol of electrons. The resulting current from the electrochemical reaction is the product of the amount of electrons transferred, the amount of hydrogen consumed, and Faraday's constant.

User specifies among three options to determine fuel cell voltage denoted respectively t, m, and v. Depending on the voltage option selected the model determines the fuel cell voltage. The table (t) option returns voltage from table lookup based on current density and cathode pressure. According to Geyer (2000) the model (m) option determines voltage from a curve fit based on a PEM model developed by Srinivasan et al. (1991) and Allison Gas Turbine Division of General Motors research and development information. The model option describes the current density-voltage relationship based on current density, fuel cell temperature, cathode inlet pressure, and oxygen partial pressure at cathode inlet. The voltage (v) option requires user specification of voltage.

User specifies between two options to model PEM fuel cell water management, denoted respectively s and *no option*. As mentioned in Sec. 2.2.1, for PEM fuel cells water management is critical to maintain adequate hydration for ion flow through the electrolyte while avoiding electrolyte dehydration and electrode flooding. Geyer and Ahluwalia (1998) describe water transport processes occurring in PEM fuel cells. Hydrated protons transport water from anode to cathode. In some fuel cells cathode gas flow pressure is maintained higher than anode gas flow pressure to reduce this flow of hydrated protons. Both anode and cathode gas flows carry water away from the fuel cell acting as drying flows. GCtool does not model each of these water transport processes individually. Instead the overall water transport effects are modeled by assuming the anode exhaust flow is just saturated. User either specifies the model option *saturated*

59

anode exhaust flow (s) or *no option* in which case the anode exhaust flow has the same water quantity as the anode inlet flow. An example of a command line for pem model is:

pem pem={mode="o", option="ms", area=0.0929; celltemp=323; curden=0.7;};

Once the *gas* and *pem* models are specified, the user calls the model entries in the appropriate order to simulate performance of the fuel cell. The pem model entries are ".ain" (obtains anode input flow and does not generate exit flow), ".c" (obtains cathode input flow and generates cathode exit flow), ".a" (generates anode exit flow), and "cool" (optional entry to process coolant flow through the fuel cell). User must ensure that the appropriate gas model is specified before it is needed in a subsequent model. An example of appropriate entries for the PEM fuel cell simulation is:

fuel.c; pem.ain; air.c; pem.c; pem.a;

GCtool provides several output choices. The command, "mods.print" produces the "Output of Model Parameters" table, which summarizes values for parameters used for each model. The command, "gass.print", produces the "Output of Model Gastype Flows" table, which provides thermodynamic property data for each fluid flow at the exit of each component in the system model. The command, "gass.mprint", produces the "Output of Species Molar Flow Rates and Mole Fractions" table, which provides the species flow rates and mole fractions for each fluid flow at the exit of each component. The command, " pows.print" produces the "Output of Model Powers" table, which provides the power produced and consumed for each device and the heat transfer input and output for each device. A command line example to produce these tables as outputs is:

mods.print; gass.print; gass.mprint; pows.print;

60

The user can define variables within the program using data generated during GCtool simulation. Output data can be printed to a text file and then manipulated for graphing and presentation purposes.

3.1.2. Sample Results

Using GCtool an exhaustive number of virtual experiments was conducted to determine performance trends of PEM fuel cells while several parameters were varied. The voltage model option and saturated anode exit option were used. Results were graphed using Microsoft Excel. Examples of results include the effects of cathode pressure (Sec. 2.3.1.1), fuel cell operating temperature (Sec. 2.1.1), and current density (Sec. 2.1.3.1) on output voltage and power density (Sec. 2.1.3.1). Other GCtool outputs include heat transfer from the fuel cell and fuel cell exergetic efficiency (Sec. 1.2).

For fuel cell operating temperature of 353K, Fig. 3.1 shows the effects on voltage by varying cathode pressure and current density. This plot reflects the same trends illustrated in the generic voltage-current plot in Fig. 2.6. Increasing cathode pressure results in a flatter slope in the ohmic polarization region with corresponding higher voltage for a given current density. Additionally, the onset of concentration polarization occurs at higher current densities as cathode pressure increases.

At a lower fuel cell operating temperature of 323K, Fig. 3.2 shows the effects on voltage by varying cathode pressure and current density. The same trends noted for fuel cell operating temperature of 353K are present at operating temperature of 323K. Although increasing cathode pressure results in a flatter slope in the ohmic polarization region, at 323K the variance in slopes among the five pressures is much less compared with the slope variances at 353K. At 3 atm the slope in the ohmic polarization region is

61
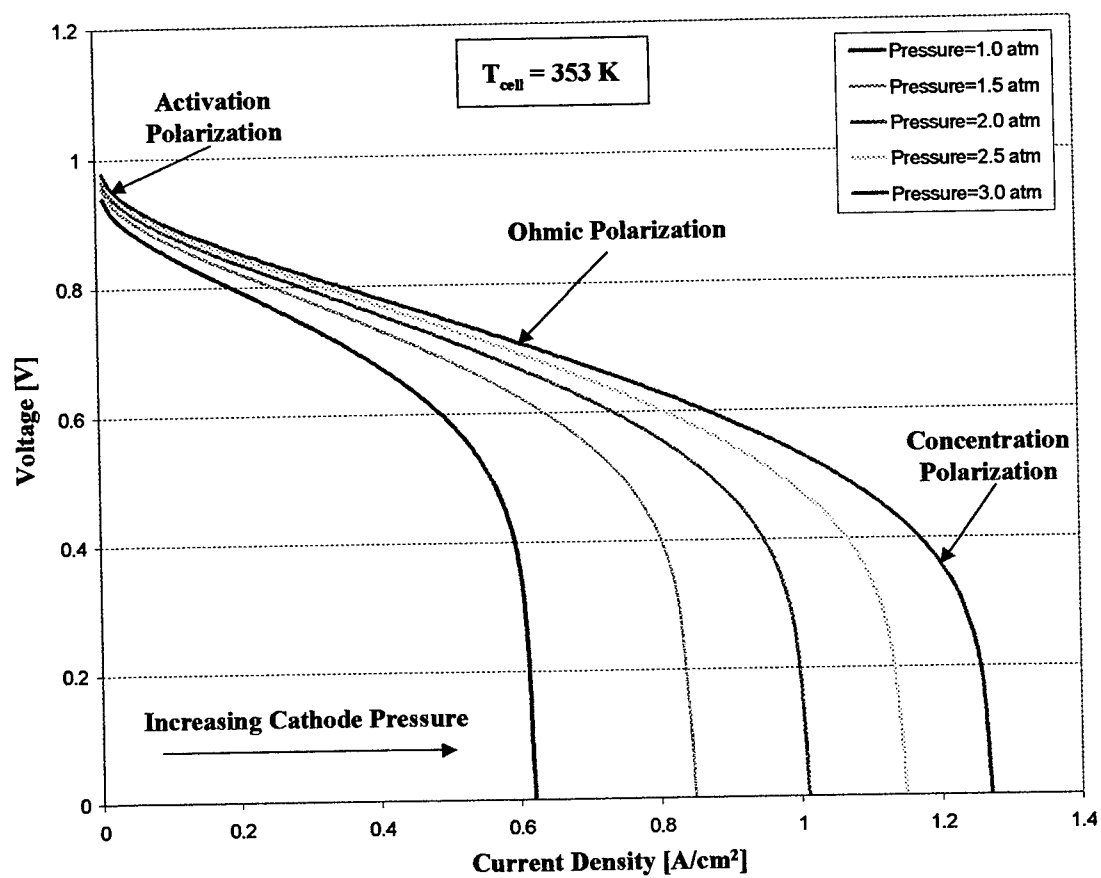
Figure 3.1: Effects of Cathode Pressure and Current Density on Voltage at Fuel
Cell Operating Temperature of 353K

62
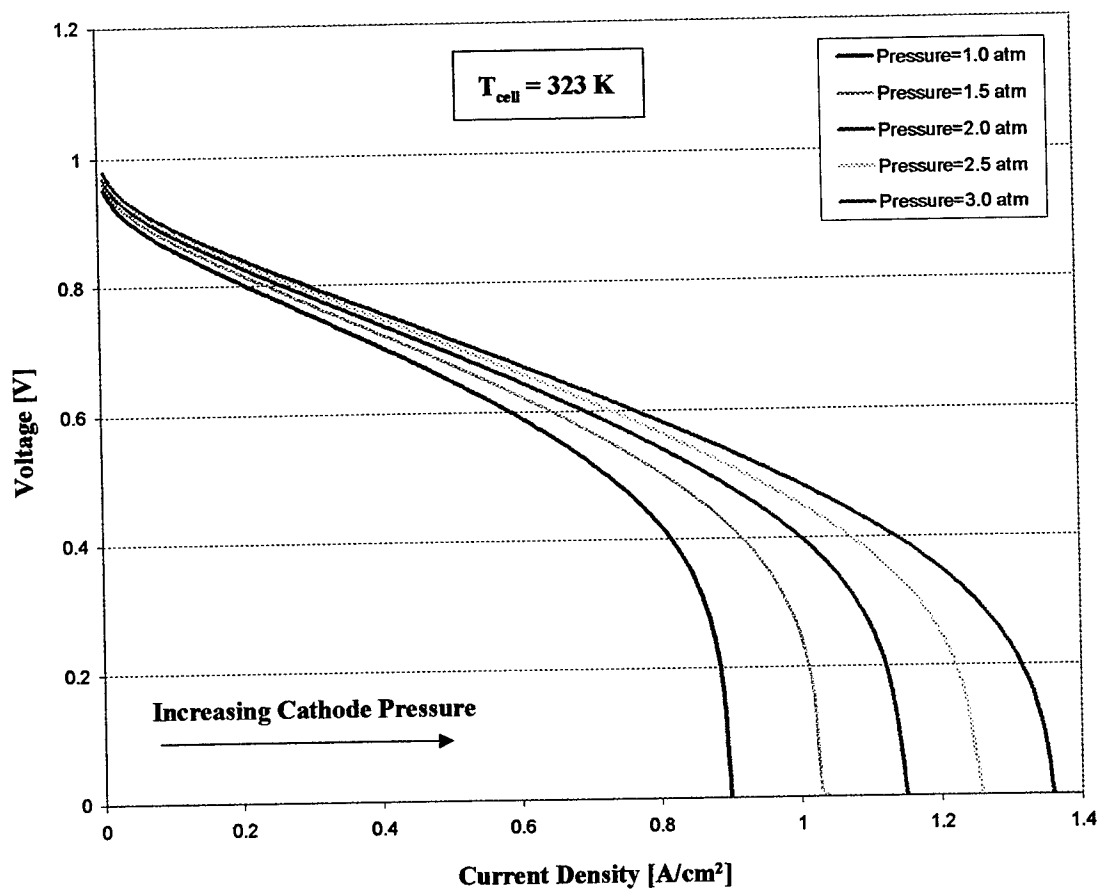
Figure 3.2: Effects of Cathode Pressure and Current Density on Voltage at Fuel Cell Operating Temperature of 323K

steeper at 323K than at 353K while at 1 atm the slope is similar at both 323K and 353K. The onset of a significant voltage drop due to concentration polarization occurs at higher current density at 323K than when the fuel cell operating temperature is 353K.

The effects of further reduction in fuel cell operating temperature to 293K are shown in Fig. 3.3. The same general trends of increased voltage with increased pressure are present. In the ohmic polarization region the variance in slopes among the five pressures is less than that at 323K and 353K while the slopes of the curves are much steeper at 293K. Consequently, at 293K larger voltage drops occur as current density increases. Concentration polarization never becomes dominant. Comparison of Figs. 3.1 through 3.3 indicates that temperature affects both ohmic polarization and concentration polarization: as temperature decreases, ohmic polarization tends to be more significant than concentration polarization, the effect of which nearly vanishes at 293K.

The general relationship shown in Figs. 3.1 through 3.3 of decreasing voltage with increasing current density causes the product of these two terms, power density, to increase to a maximum value and then decline as current density further increases. The relationship between power density and current density is illustrated in Fig. 3.4. Comparison of Fig. 3.4 with Fig. 3.1 indicates maximum power density occurs near the transition of the ohmic polarization region to the concentration polarization region: near a current density where the slope of the voltage-current density curve starts to deviate from the slope of the linear ohmic polarization region. In Fig. 3.4 the sharp decline in power density beyond the maximum power density point is due to the predominance of concentration polarization in this region. At fuel cell operating temperature of 353K,
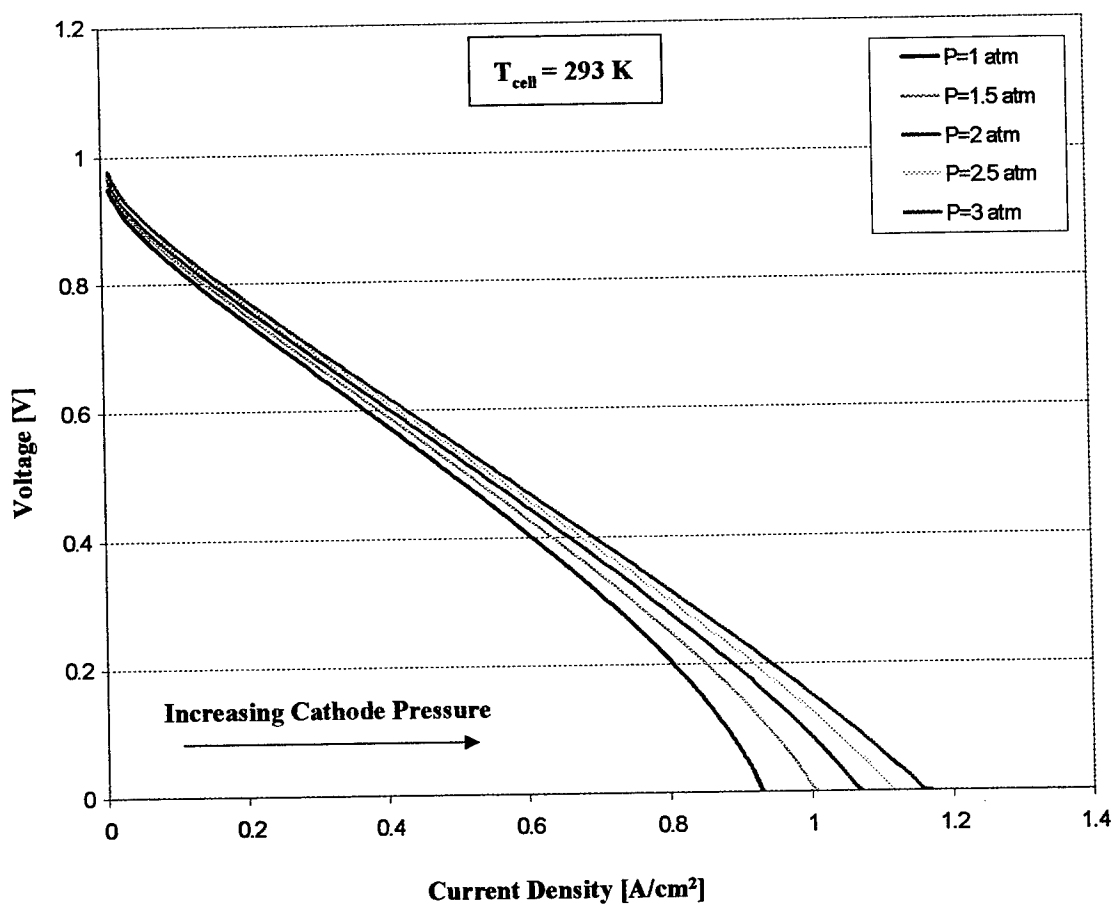
Figure 3.3: Effects of Cathode Pressure and Current Density on Voltage at Fuel Cell Operating Temperature of 293K
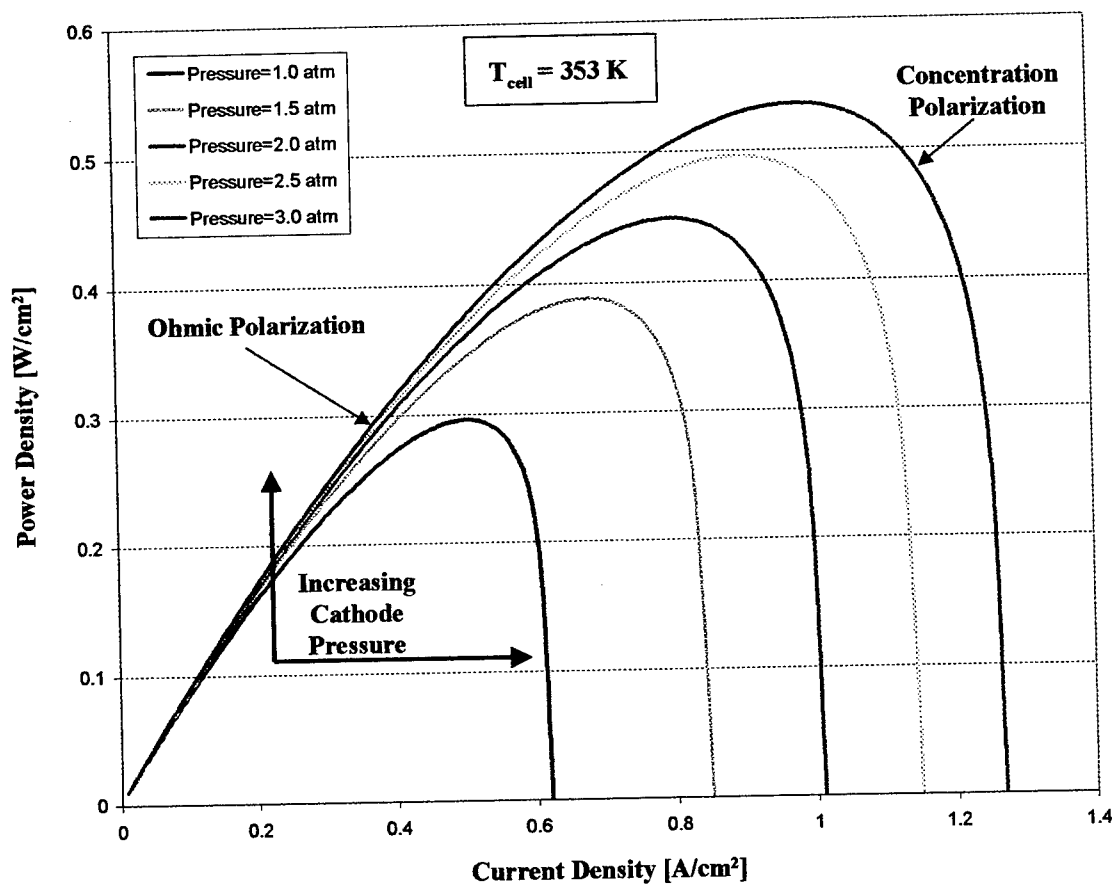
Figure 3.4: Effects of Cathode Pressure and Current Density on Power Density at Fuel Cell Operating Temperature of 353K

66

increased cathode pressure results in greater power density for a given current density. As cathode pressure increases, the current density at which maximum power density occurs shifts to the right.

At a lower fuel cell operating temperature of 323K, the effects on power density by varying cathode pressure and current density are shown in Fig. 3.5. The same general power density trends noted for fuel cell operating temperature of 353K are present at an operating temperature of 323K. Comparison of Fig. 3.5 with Fig. 3.4 indicates that for a cathode pressure of 3 atm the power density curve at 323K falls below that at 353K over most of the current density range. This results from the steeper slope of the voltage-current density curve in the ohmic polarization region at 323K compared with 353K. At a cathode pressure of 1 atm the reverse is observed: the power density curve at 323K falls above that at 353K. This results from onset of concentration polarization at a much higher current density at 323K compared with 353K since the slopes of the voltage-current density curves in the ohmic polarization region are similar.

At a lower fuel cell operating temperature of 293K, Fig. 3.6 shows that power density still increases with increasing cathode pressure for a given current density. However, the increase is much less significant. For a given cathode pressure the maximum power density of Fig. 3.6 is less than the maximum power density at 353 and 323K shown in Figs. 3.4 and 3.5. Since concentration polarization is not significant at 293K, the maximum power density occurs due to cumulative ohmic polarization voltage drop as current density increases. Comparing Fig. 3.6 with Figs. 3.4 and 3.5, the slope of
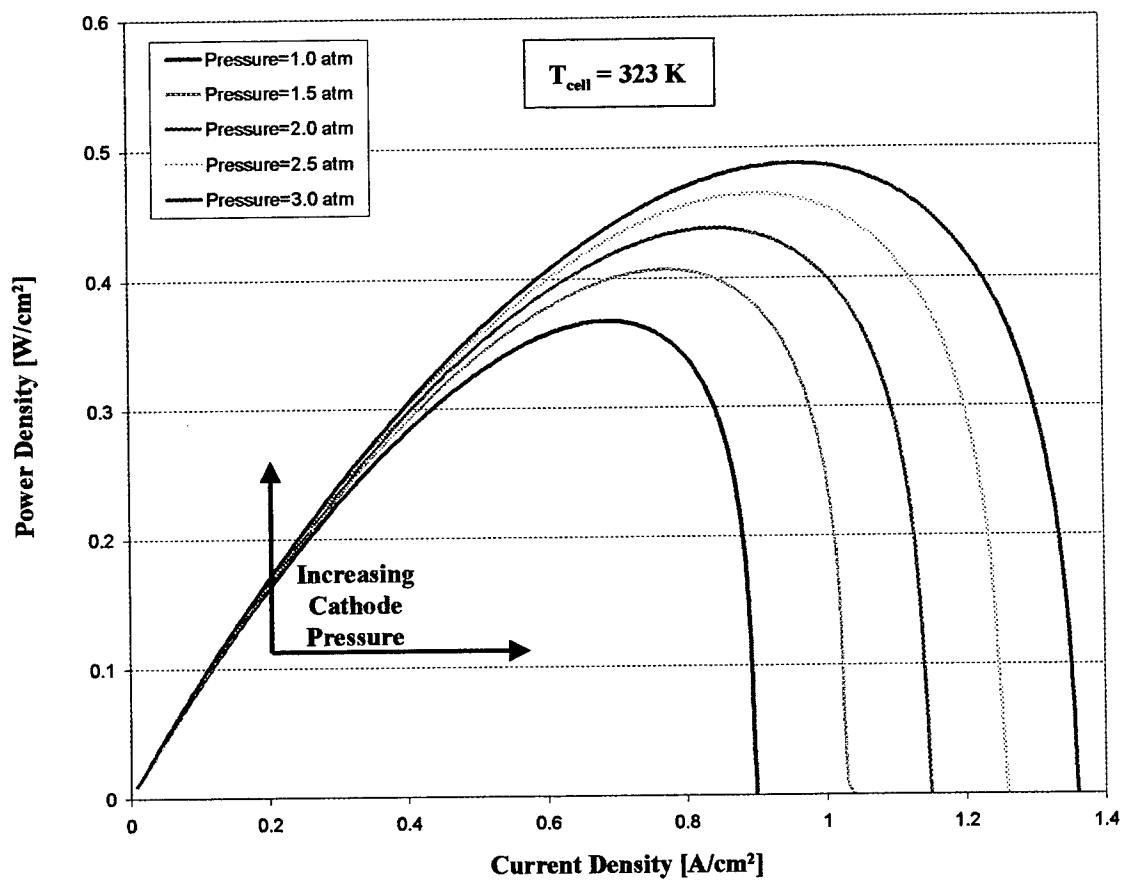
Figure 3.5: Effects of Cathode Pressure and Current Density on Power Density at Fuel Cell Operating Temperature of 323K

68
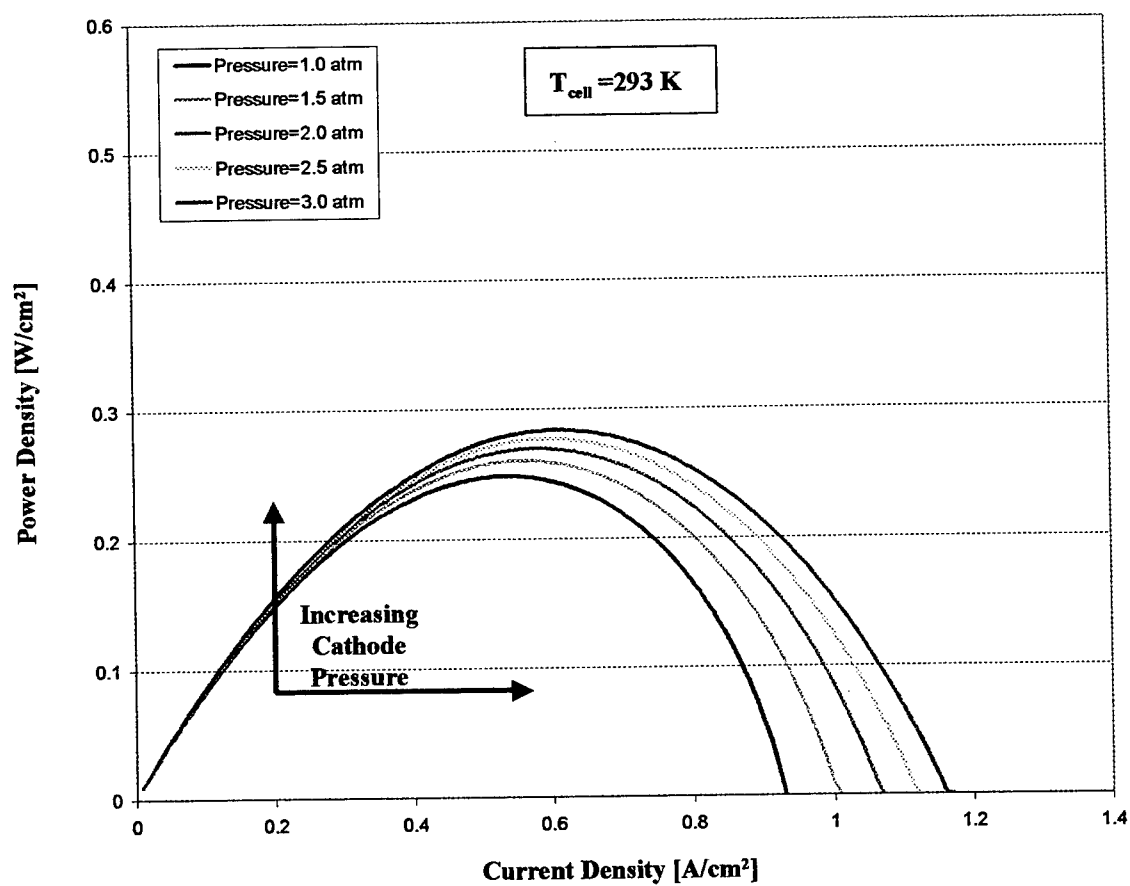
Figure 3.6: Effects of Cathode Pressure and Current Density on Power Density at Fuel Cell Operating Temperature of 293K

69

the power density curve beyond the point of maximum power density is not as steep as the slopes at 353K and 323K due to absence of concentration polarization effects at a temperature of 293K.

As shown by Figs. 3.7 through 3.9 fuel cell exergetic efficiency plotted against current density shows the same trend as the voltage-current density curves in Figs. 3.1 through 3.3. The similarity in shapes of the curves is due to the fact that fuel cell exergetic efficiency is directly proportional to fuel cell power, which is directly proportional to voltage for a given current density.

For fuel cell cathode pressure of 3 atm, the effects on voltage by varying fuel cell operating temperature and current density are shown in Fig. 3.10. Generally as temperature increases, the voltage for a given current density increases. This trend changes at high current density in the region of concentration polarization dominance. The onset of concentration polarization occurs at lower current densities as fuel cell operating temperature increases. This effect is illustrated by the crossing of the curves on the graph. At 293K ohmic polarization effects dominate with no significant concentration polarization.

At a lower cathode pressure of 2 atm, the effects on voltage by varying fuel cell operating temperature and current density are shown in Fig. 3.11. The same trends noted for cathode pressure of 3 atm are present at cathode pressure of 2 atm. However, the onset of significant voltage drop due to concentration polarization occurs at lower current density than at 3 atm. At 293K ohmic polarization effects are still dominant with the slope of the voltage-current density curve steeper at 2 atm compared with 3 atm.

70
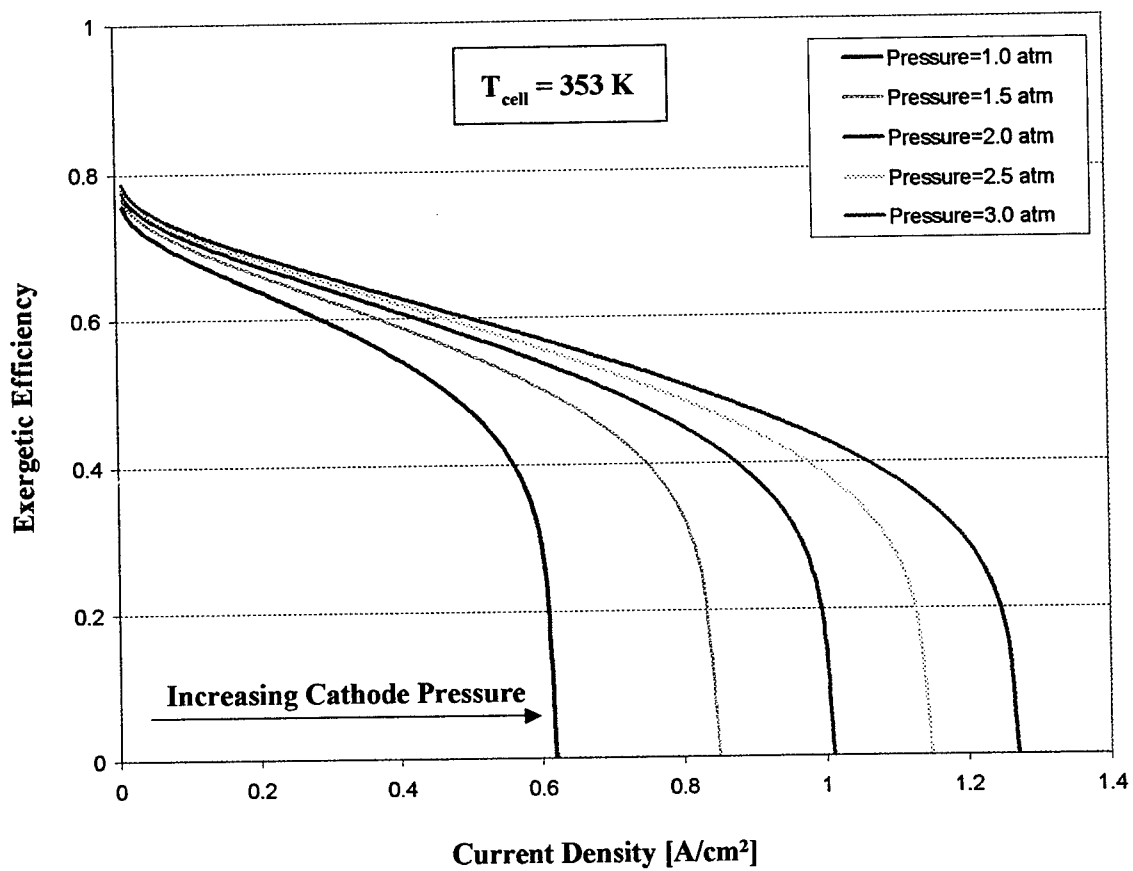
Figure 3.7: Effects of Cathode Pressure and Current Density on Exergetic Efficiency at Fuel Cell Operating Temperature of 353K

71
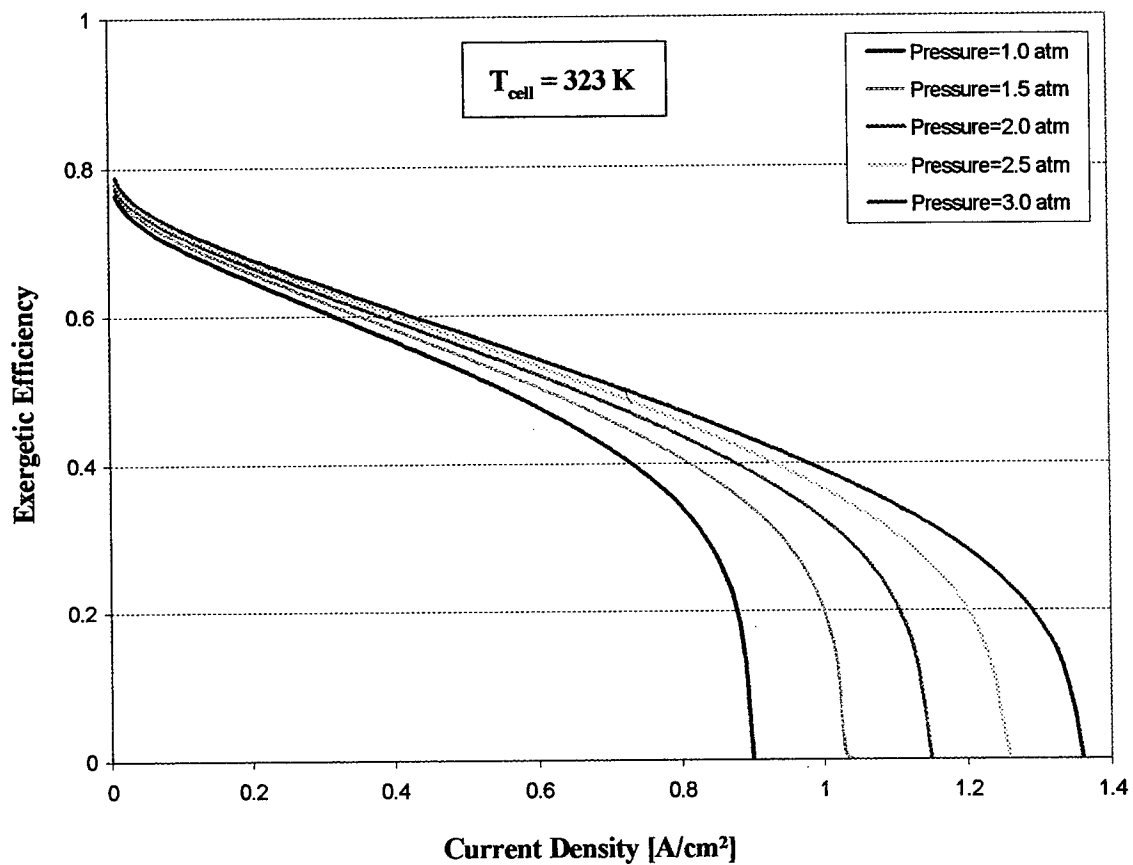
Figure 3.8: Effects of Cathode Pressure and Current Density on Exergetic Efficiency at Fuel Cell Operating Temperature of 323K
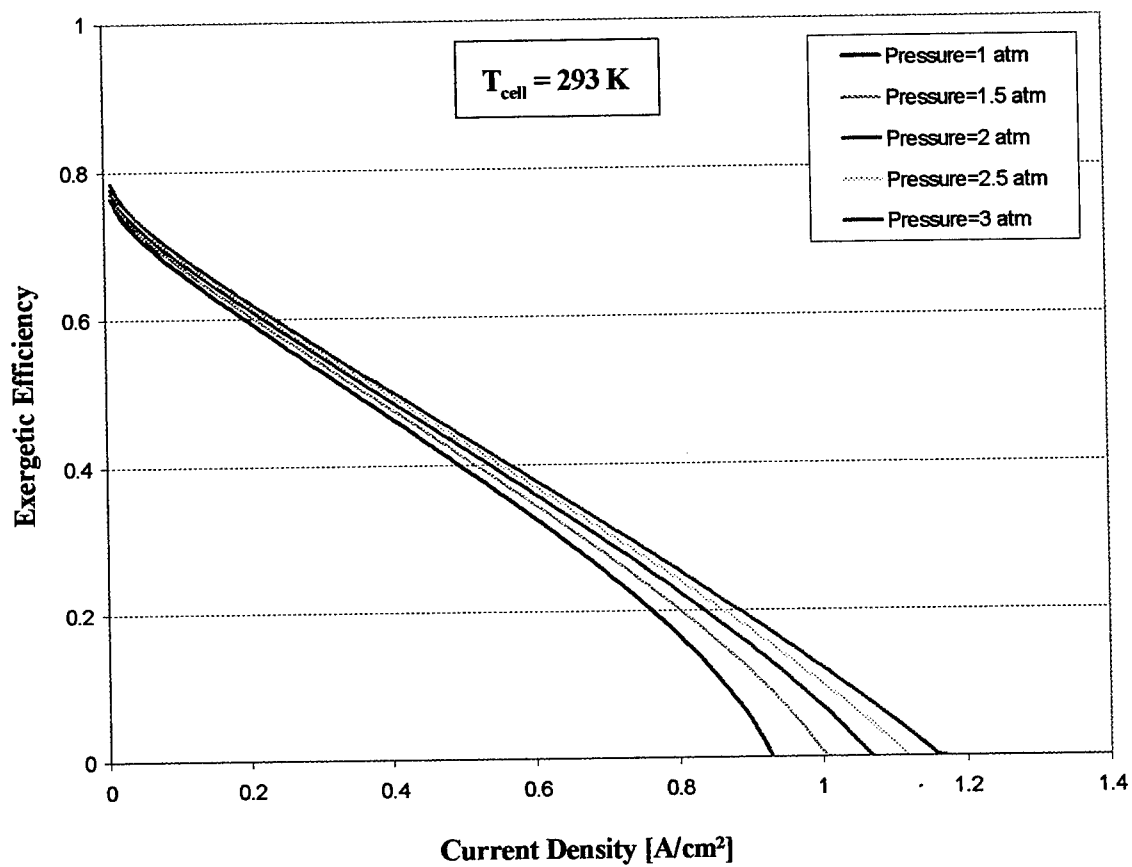
Figure 3.9: Effects of Cathode Pressure and Current Density on Exergetic Efficiency at Fuel Cell Operating Temperature of 293K
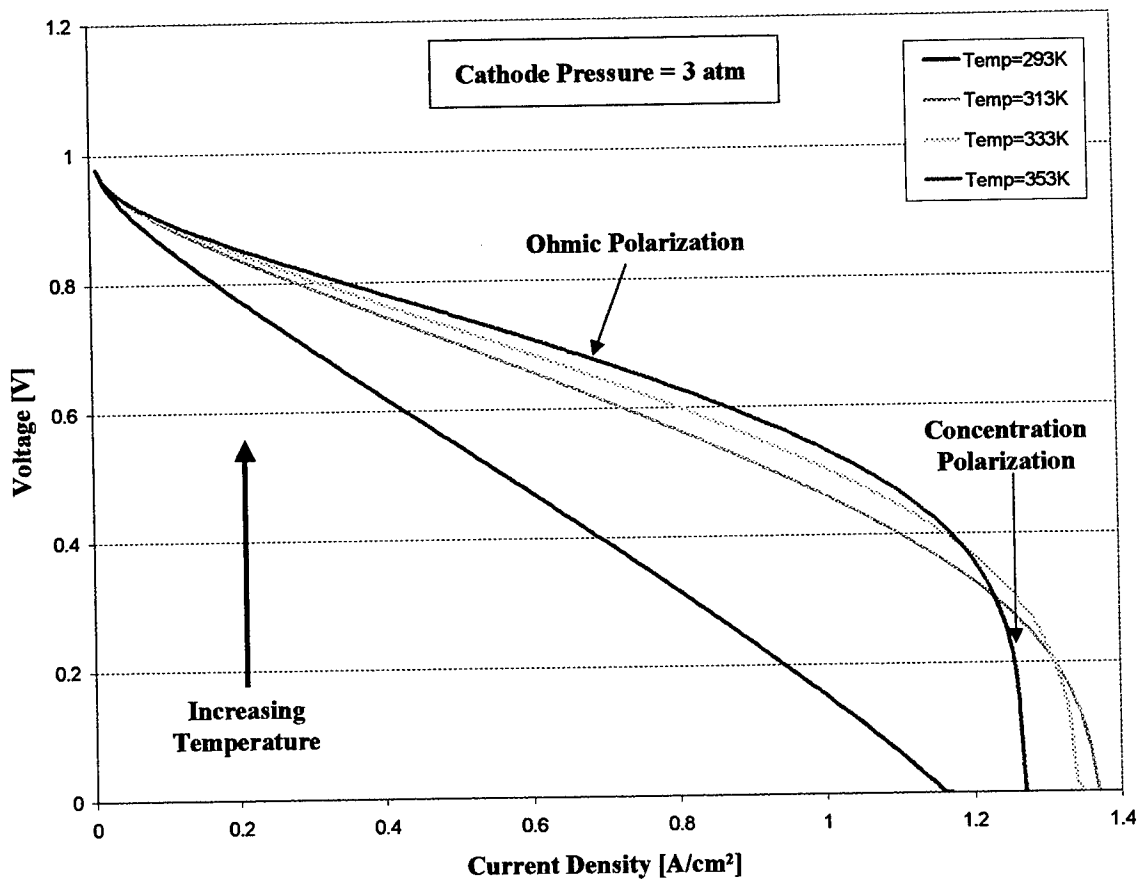
Figure 3.10: Effects of Fuel Cell Operating Temperature and Current Density on Voltage at Cathode Pressure of 3 atm
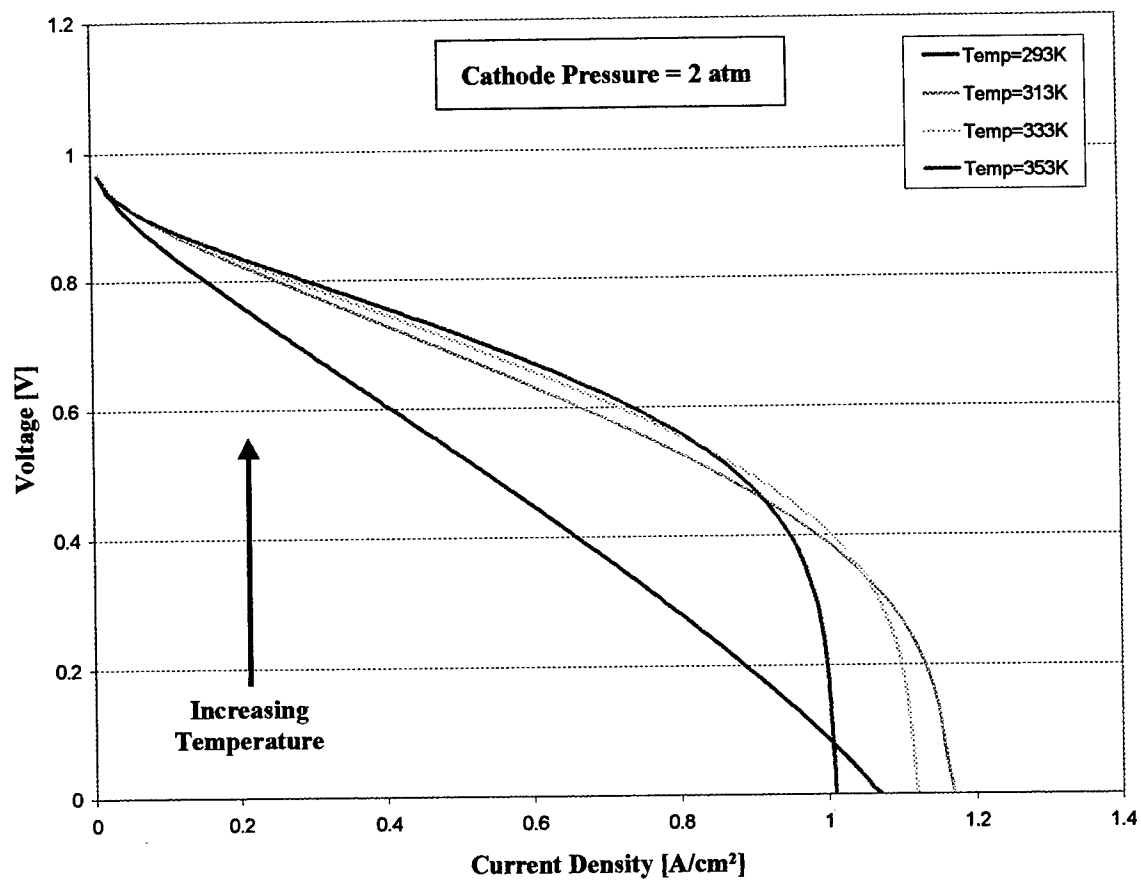
Figure 3.11: Effects of Fuel Cell Operating Temperature and Current Density on Voltage at Cathode Pressure of 2 atm

The effects of further reduction in cathode pressure to 1 atm are shown in Fig. 3.12. Onset of concentration polarization at significantly lower current density results in a much earlier crossing of the curves on the graph. At 293K the slope of the curve is steeper than that at cathode pressures of 2 atm and 3 atm with ohmic polarization effects still dominant.

Power density trends at a cathode pressure of 3 atm are illustrated in Fig. 3.13. As current density increases, power density reaches a maximum value and then sharply declines at fuel cell operating temperatures of 353, 333, and 313K due to predominance of high concentration polarization. At a temperature of 293K power density decline is more gradual beyond the point of maximum power density due to cumulative ohmic polarization effects since concentration polarization is not significant at this temperature. At a cathode pressure of 3 atm, increased fuel cell operating temperature results in increased power density for a given current density. As fuel cell operating temperature increases, the maximum power density occurs at higher current density. The crossing of the curves indicates effects of earlier onset of concentration polarization as temperature increases.

As cathode pressure decreases to 2 atm, maximum power density for each temperature is less than that at 3 atm as shown in Fig. 3.14. Additionally, at 2 atm for temperatures of 353, 333, and 313K the maximum power density and onset of concentration polarization dominance occur at a much lower current density compared with 3 atm. At a temperature of 293K maximum power density and power density decline due to cumulative ohmic polarization effects occur at a slightly lower current density compared with 3 atm.
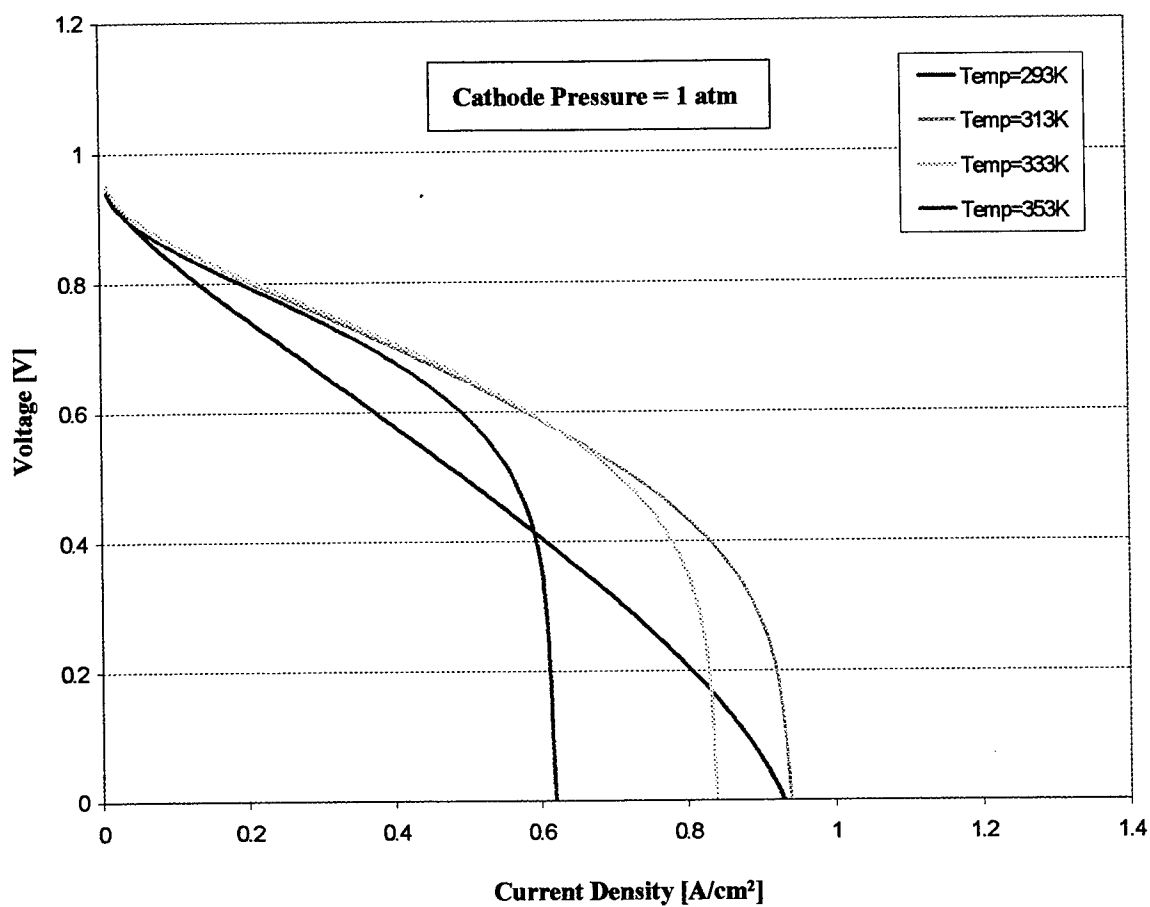
Figure 3.12: Effects of Fuel Cell Operating Temperature and Current Density on Voltage at Cathode Pressure of 1 atm
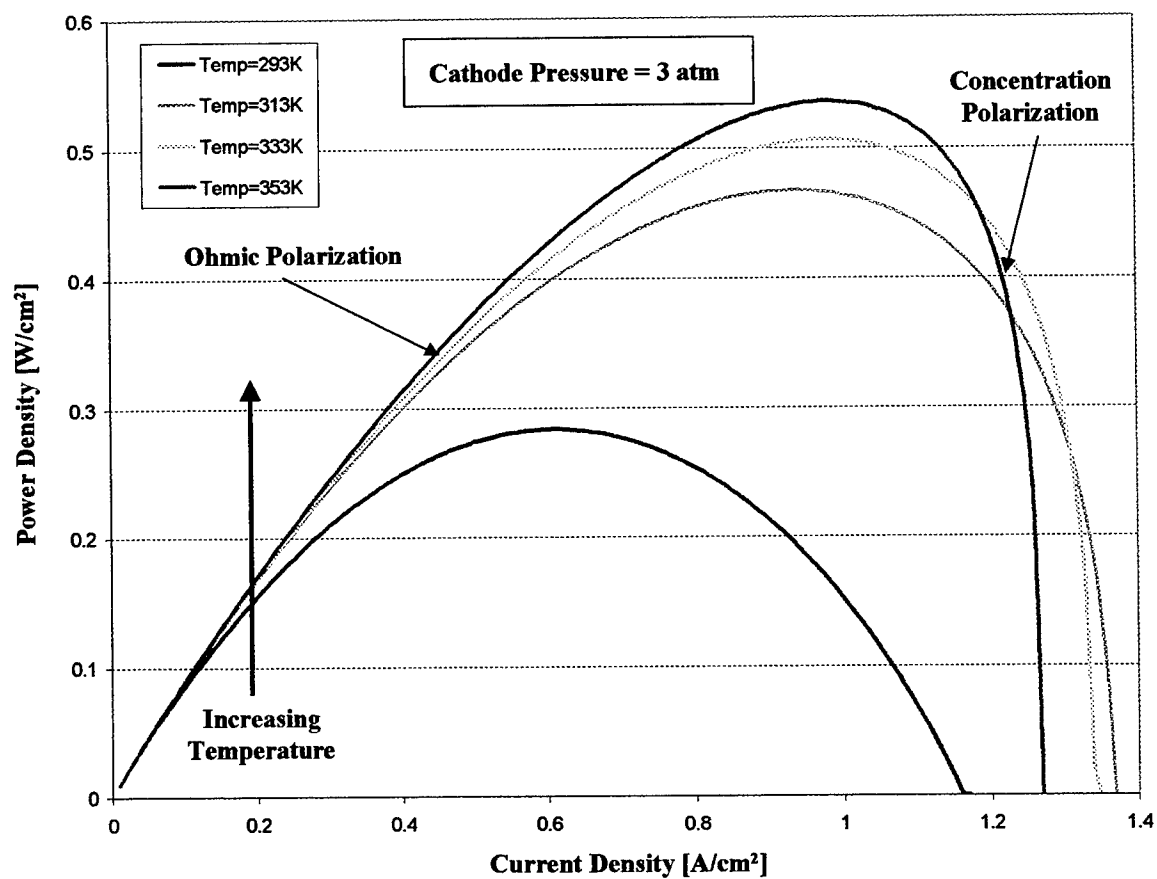
Figure 3.13: Effects of Fuel Cell Operating Temperature and Current Density on Power Density at Cathode Pressure of 3 atm
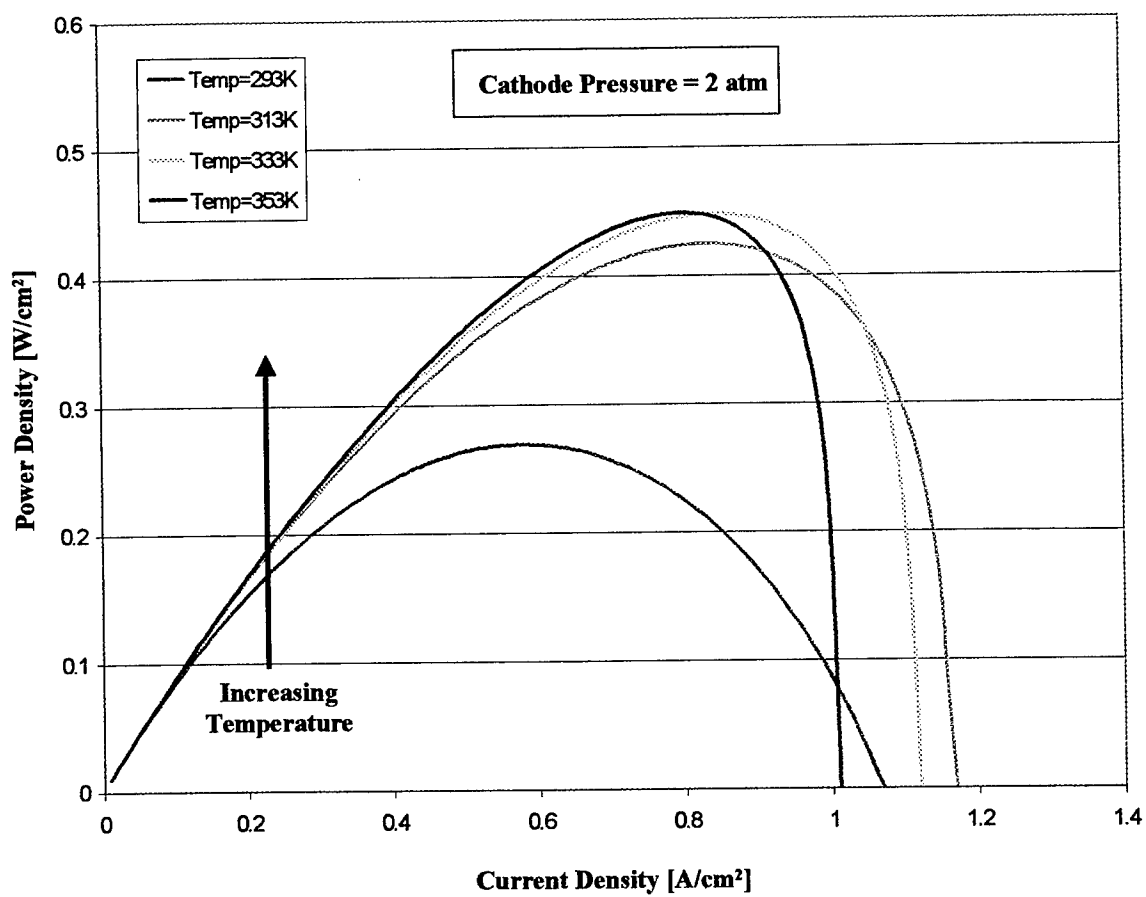
Figure 3.14: Effects of Fuel Cell Operating Temperature and Current Density on Power Density at Cathode Pressure of 2 atm

As cathode pressure is reduced to 1 atm, maximum power density at each temperature is further reduced from that at higher pressures as illustrated in Fig. 3.15. At 1 atm for temperatures of 353, 333, and 313K onset of concentration polarization at significantly lower current density results in decreasing power density with increasing fuel cell operating temperature. At a temperature of 293K maximum power density and power density decline due to cumulative ohmic polarization effects occur at a slightly lower current density compared with 2 atm and 3 atm.

Referring to Figs. 3.1 through 3.9, for a given current density, higher cathode pressure and higher operating temperature result in higher voltage, power density and fuel cell exergetic efficiency. When the fuel cell is integrated into a fuel cell system, however, auxiliary component exergy destruction and/or power consumption offsets some of the exergetic efficiency gains of high-pressure operation (see Sec. 3.2.3). There is also a trade-off between power density and exergetic efficiency. As current density increases, exergetic efficiency decreases while power density increases to its maximum (compare Figs. 3.4 and 3.7). Operation at current densities beyond maximum power density should be avoided due to concentration polarization effects. Operation at low current density gives a high efficiency but a low power output *per fuel cell active area* (compare Figs. 3.4 and 3.7 at a current density of 0.2 A/cm^2, for example). Accordingly, to achieve a high power output at low current density, a greater fuel cell active area would be required: the fuel cell stack would have to be larger. Consequently, steady-state applications such as stationary power production in which fuel cell stack size is not
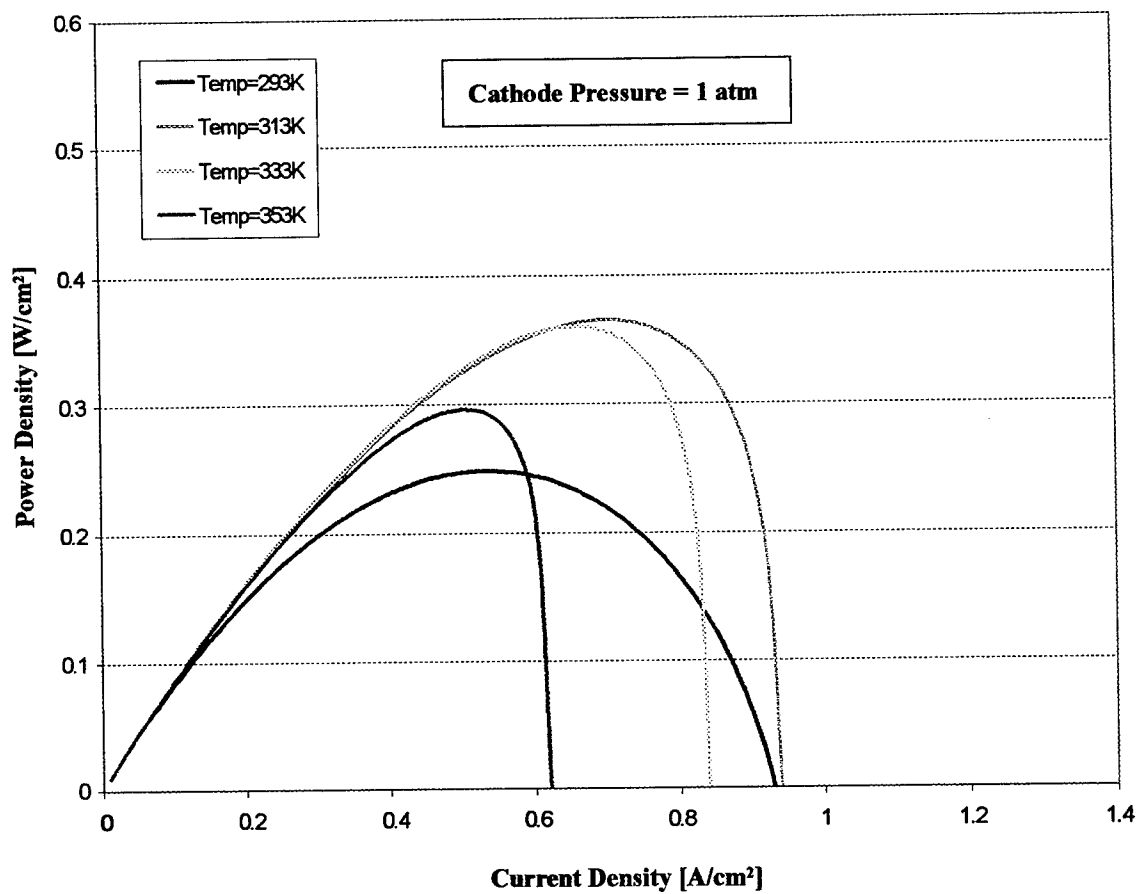
Figure 3.15: Effects of Fuel Cell Operating Temperature and Current Density on Power Density at Cathode Pressure of 1 atm

81

a critical issue would operate at low current density to achieve greater efficiency. For automotive applications in which power requirements continually vary, a fixed operating point is not feasible.

3.2. MATLAB Adaptation

A goal of this study is to analyze PEM fuel cell performance in automotive applications. Using the GCtool virtual experiment results and PEM analysis methodology, the computational process used in GCtool was adapted into a MATLAB program. A MATLAB program is more conducive to integration into a vehicle simulation program.

3.2.1. Power Density Function

For the MATLAB adaptation the possibility of expressing power density and fuel cell exergetic efficiency as a function of current density and fuel cell operating temperature was *explored* as follows: Based on GCtool-generated data for PEM fuel cell operation in the current density range of 0.1 to 1.0 Amps/cm^2, linear regression techniques were used to develop empirical equations to describe power density and fuel cell exergetic efficiency (Sec. 1.2). From power density and current density, the voltage can be computed. For constant hydrogen and air inlet temperature and relative humidity, regression analysis indicated power density is a cubic function of current density as given by Eq. 3.2:

$$Power\, Density = a_0 + a_1 i + a_2 i^2 + a_3 i^3 \qquad (3.2)$$

where:

a_0, a_1, and a_3 are constant coefficients

82

a_2 is a linear function of cell temperature:

$$a_2 = a_{21} + a_{22}T_{cell}$$ (3.3)

a_{21}, and a_{22} are constant coefficients.

For constant hydrogen and air inlet temperature and relative humidity, regression analysis indicated fuel cell exergetic efficiency (ε) is a cubic function of current density as given by Eq. 3.4:

$$\varepsilon = a_0 + a_1 i + a_2 i^2 + a_3 i^3$$ (3.4)

where:

a_0, a_2, and a_3 are constant coefficients

a_1 is a linear function of cell temperature:

$$a_1 = a_{11} + a_{12}T_{cell}$$ (3.5)

a_{11}, and a_{12} are constant coefficients.

For constant operating conditions these empirical equations are within 2% of the GCtool-computed power density and fuel cell exergetic efficiency. Although these empirical equations provide a simple relationship for power density and exergetic efficiency as functions of current density and fuel cell operating temperature, analysis of various operating conditions requires new empirical constants for each set of conditions, which is burdensome. Since vehicle simulation applications involve constantly changing conditions, linear regression-developed empirical equations are not practical to use. As a result the GCtool model equation for computing voltage is used in the MATLAB adaptation. Power density is computed as the product of voltage and current density.

3.2.2. Fuel Cell Module

As shown in Figs. 3.4 through 3.6 and Figs. 3.13 through 3.15, once maximum power density is achieved, further increase in current density results in significant decline in power density owing to concentration polarization effects or cumulative ohmic polarization effects. These results indicate the fuel cell should not be operated beyond its maximum power density point. To ensure that the fuel cell does not operate at current densities where concentration polarization effects are dominant, it is necessary to identify a maximum current density corresponding to each cathode pressure/fuel cell operating temperature combination. This was explored in two ways: (1) Base the maximum current density on a current density at which a significant increase (taken to be 50%) in slope of the voltage-current density curve occurs thus avoiding operation in the region of dominant concentration polarization. (2) Base the maximum current density on the current density at which maximum power density occurs.

A comparison of maximum current densities based on an increase in slope of 50% and maximum power is shown in Figs. 3.16 through 3.18. At fuel cell operating temperatures of 353K and 323K maximum current densities corresponding to an increase in slope of 50% do not fall in the area of significant voltage drop due to concentration polarization. At the fuel cell operating temperature of 293K, the slope of the voltage-current density curve never increases by 50% due to minimal concentration polarization at this temperature. Accordingly, determination of maximum current densities based on change in slope is not possible at this temperature. For all three temperatures considered, maximum current densities corresponding to current densities at maximum power are shown. At a fuel cell operating temperature of 353K maximum current density values are
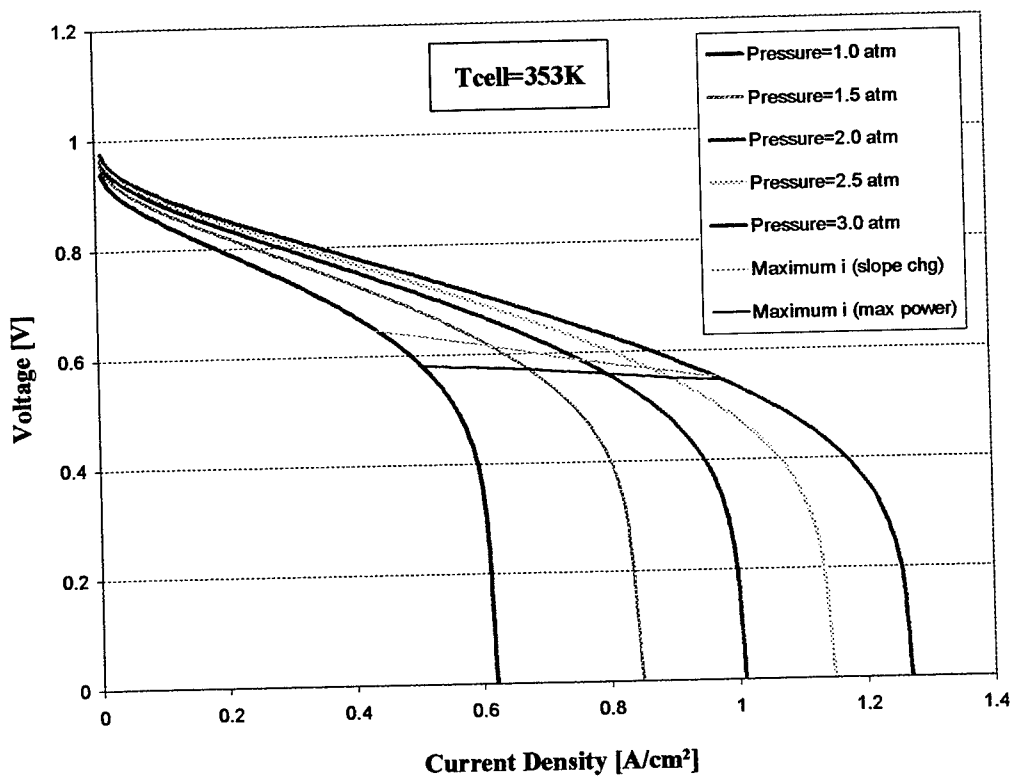
Figure 3.16: Comparison of Maximum Current Density Criteria Results at Fuel Cell Operating Temperature of 353K
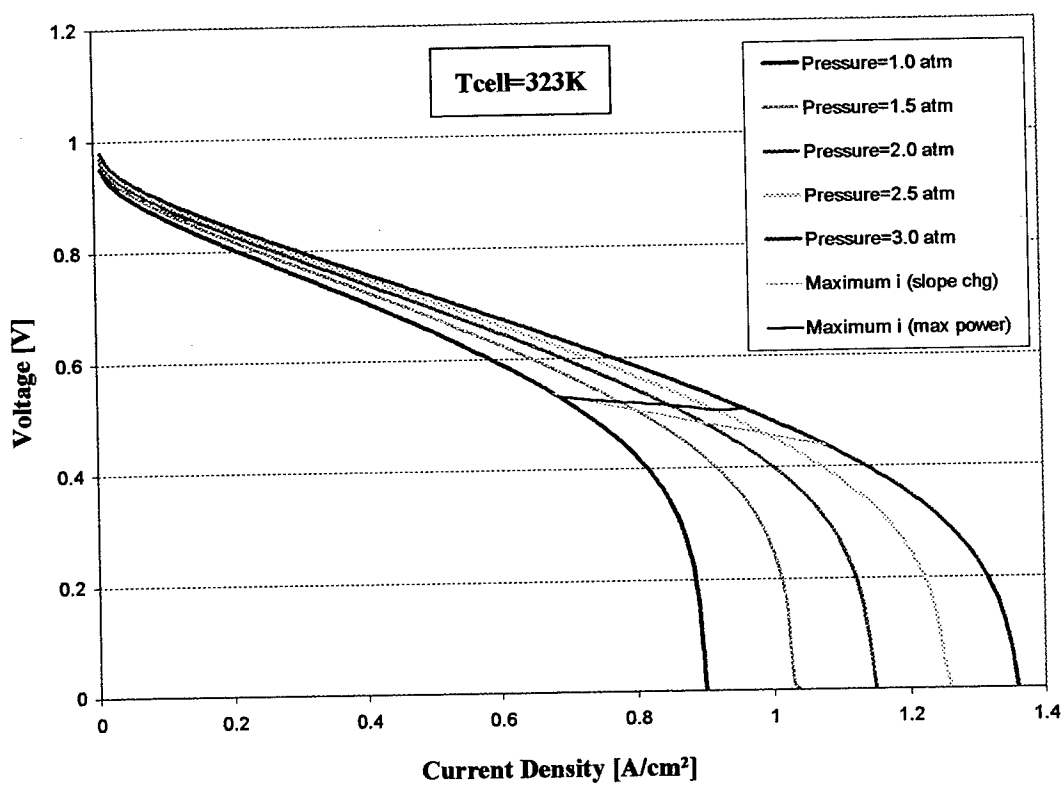
Figure 3.17: Comparison of Maximum Current Density Criteria Results at Fuel Cell Operating Temperature of 323K

86
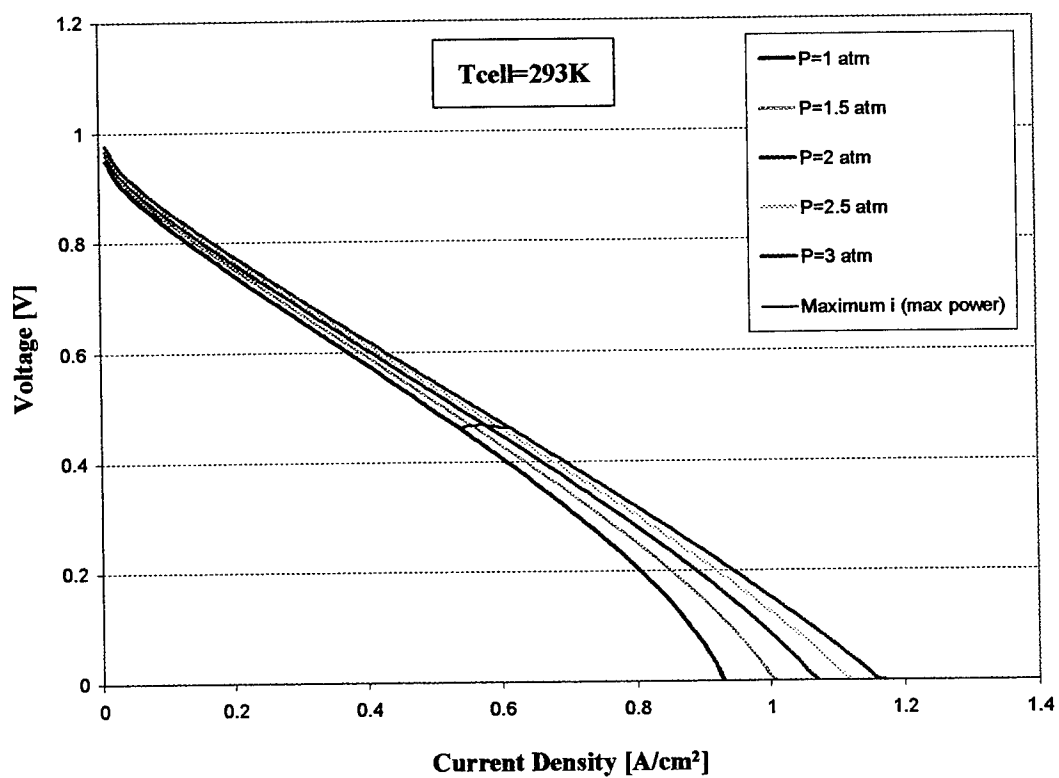
Figure 3.18: Comparison of Maximum Current Density Criteria Results at Fuel Cell Operating Temperature of 293K

somewhat higher than those computed using the slope change criterion. At the fuel cell operating temperature of 323K maximum current density values are mostly less than those computed using the slope change criterion. Since the 50% slope increase criterion is not applicable at lower fuel cell operating temperatures and results in maximum current densities that correspond to current densities beyond maximum power density, the maximum power density criterion is used to determine maximum current density in the MATLAB program.

The MATLAB program uses the same methodology as GCtool to solve for actual voltage, heat transfer associated with the fuel cell, and mass flow composition at electrode exits. A copy of the MATLAB fuel cell system program is provided in Appendix A. Development of equations used in the MATLAB program is in Appendix B. The general procedure used in the MATLAB program is as follows:

Step 1: Specify values for fuel cell operating temperature (T_{cell}), air temperature (T_{air}) and relative humidity ($\phi_{air,in}$) at cathode inlet, hydrogen temperature (T_{h2}) and relative humidity ($\phi_{h2,in}$) at anode inlet, molar air-fuel ratio ($\overline{AF}$), cathode inlet pressure ($P_{cathode,in}$), anode inlet pressure ($P_{anode,in}$), current density (i), and fuel utilization (μ).

Step 2: Determine maximum current density for specified cathode pressure and fuel cell operating temperature. Maximum current density is the current density value at maximum power. Verify specified current density does not exceed maximum current density.

To compute saturation pressure (P_g) an empirical relationship for saturation pressure as a function of temperature derived from steam table data and linear regression (Eq. 3.12) is used.

$$P_g [atm] = exp\left(11.7384 - 3875.52\left(\frac{1}{T[K]}\right) - 159,296\left(\frac{1}{T[K]}\right)^2 - 10,651,805\left(\frac{1}{T[K]}\right)^3 \right)$$ (3.12)

Step 4: Compute power density, the product of voltage and current density.

Step 5: Compute mass flow of hydrogen entering the fuel cell using Eq. 3.1.

Step 6: Compute species inlet and exit flow rates based on balanced chemical reaction for hydrogen with air and conservation of mass.

Step 7: Compute heat transfer associated with the fuel cell using conservation of energy analysis.

Step 8: From Eq. 1.2, compute fuel cell exergetic efficiency based on fuel consumption:

$$\varepsilon = \frac{Fuel\ Cell\ Power\ Density}{Mass\ Flow\ per\ Area_{hydrogen\ consumed} \times Lower\ Heating\ Value_{hydrogen}}$$ (3.13)

All mass flows and exergy transfers are computed on a per fuel cell active area basis. This allows results to be scaled for various sized fuel cell stacks. Scaling is accomplished by multiplying mass flows per area and exergy transfers per area by the fuel cell active area and number of cells in the stack.

3.2.3. Fuel Cell Systems

To develop a fuel cell system, auxiliary components for air flow, hydrogen recirculation, cooling, and humidification are required. Figure 3.19 shows a schematic of the direct-hydrogen fuel cell system analyzed in the MATLAB program.
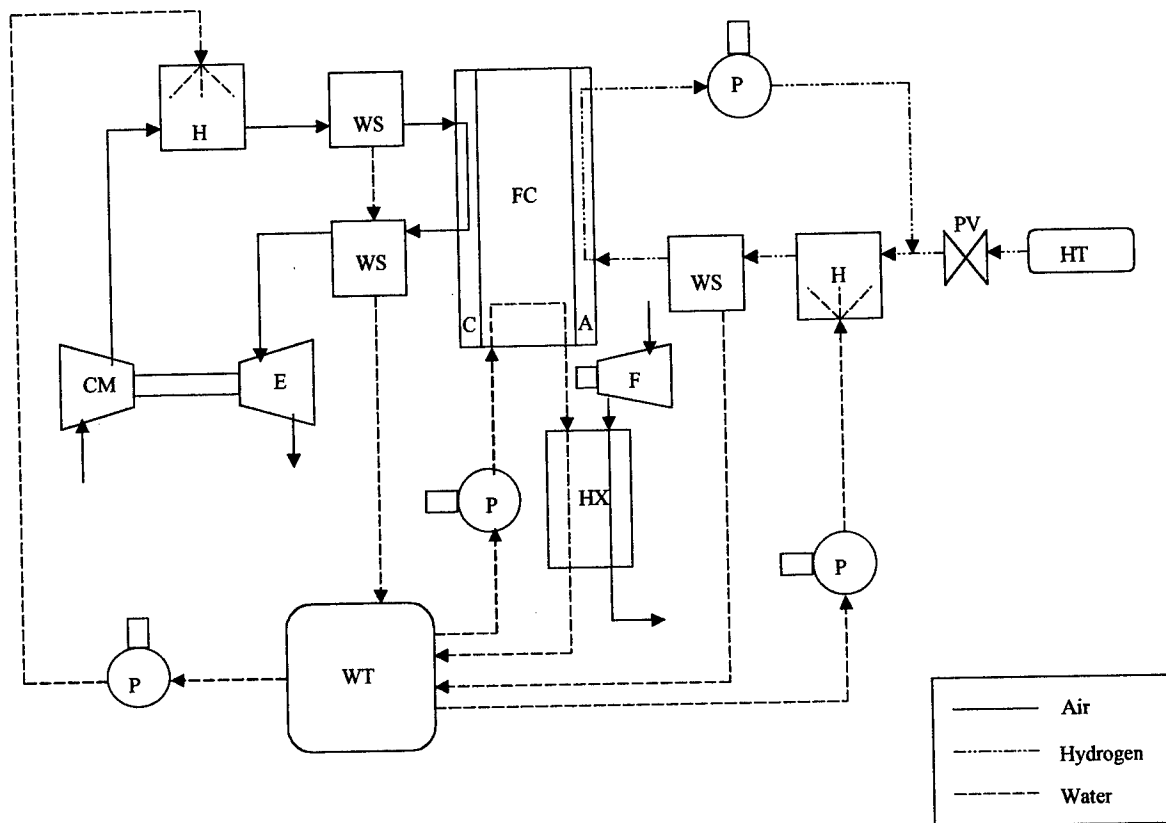
A = Anode
C = Cathode
CM = Compressor
E = Expander
F = Fan
FC = Fuel Cell Stack
H = Humidifier

HT = Hydrogen Tank
HX = Heat Exchanger
P = Pump
PV = Pressure Valve
WS = Water Separator
WT = Water Tank

Figure 3.19: Schematic of Direct-Hydrogen PEM Fuel Cell System

To determine system performance, power requirements associated with auxiliary components must be computed. Expressions for power are derived from an energy balance for each component. Compressor and optional expander isentropic efficiencies can vary with air mass flow or can be assumed constant. Pump and fan isentropic efficiencies are specified constants. Additionally, user specifies cooling loop pressure drop, coolant temperature change through the fuel cell and radiator, and air temperature change through the radiator. The power requirements are computed on a per fuel cell active area basis to be consistent with the fuel cell power and heat transfer computations. An overall fuel cell system exergetic efficiency is calculated based on the system net power density as shown by Eq. 3.14.

$$\varepsilon_{sys} = \frac{Net\ System\ Power\ Density}{Mass\ Flow\ per\ Area_{hydrogen\,consumed} \times Lower\ Heating\ Value_{hydrogen}} \qquad (3.14)$$

Since some auxiliary components in the fuel cell system consume power, all components have associated exergy destruction, and losses occur, the exergetic efficiency of the fuel cell system, ε_{sys}, is characteristically less than for the stand-alone fuel cell, ε, given by Eq. 3.13.

To analyze fuel cell system performance in an automotive application, the MATLAB program requires integration into a vehicle simulation program. Chapter 4 provides an overview of the vehicle simulation program used and simulation results for a direct-hydrogen fuel cell powered vehicle. Chapter 5 examines effects of on-board methanol reforming on fuel cell powered vehicle performance. Performance of a direct-hydrogen fuel cell system/battery hybrid powered vehicle is examined in Chapter 6 using

two control strategies. In Chapter 7 vehicle performance is compared among four cases:

direct-hydrogen and methanol reforming fuel cell vehicle and direct-hydrogen and

methanol reforming hybrid (fuel cell system/battery) vehicle.

CHAPTER 4

DIRECT-HYDROGEN PEM FUEL CELL AUTOMOTIVE SIMULATION

4.1. Background

To conduct a comparative analysis among various engine configurations and

driving profiles, a simulation tool, Vehicle Performance Simulator (VP-SIM) developed

at The Ohio State University, is used. Rizzoni et al. (2000) provide an overview of the

modeling approach used in VP-SIM. Each component within the simulator has a general

structure (unified description) that uses input/output power to provide relationships with

other components. Components within the simulator are scalable, allowing the same

basic model, independent of size, to describe a class of components. Various component

sizes are generated by specifying scaling parameters associated with each component.

Arbitrary system models are easily constructed (composable) from the given set of

component models. VP-SIM predicts the ability of a powertrain to meet a desired vehicle

driving cycle, estimates fuel economy, and implements a supervisory control strategy. It

is written in MATLAB/Simulink computer language. It consists of three main blocks at

the top layer: the driver, the powertrain, and the vehicle dynamics. Based on a given

cycle of vehicle speed, VP-SIM determines the driver's inputs (accelerator pedal and

brake pedal positions) needed to follow the cycle. The control block within the

powertrain block interprets the driver's input and produces appropriate input commands to the exergy conversion system. These commands translate through the powertrain to provide the moving vehicle forces at the wheels.

The current study includes development of a scalable PEM fuel cell module for incorporation into the powertrain model. The fuel cell system schematic shown in Fig. 3.19 is still applicable. Using the MATLAB PEM fuel cell system program (Sec. 3.2.2) as a starting point, a PEM fuel cell module was developed. Operational improvements to the MATLAB model (Sec. 3.2.3) were incorporated into the VP-SIM module: (1) compressor and expander performance data to allow variance in pressure ratio and isentropic efficiency with variance in mass flow through the devices was used instead of constant pressure ratio and constant isentropic efficiency values, (2) a pressure drop proportional to mass flow rate through the cathode was added, and (3) an initial temperature rise from ambient to fuel cell operating temperature simulates cold start of the fuel cell. The auxiliary components in the fuel cell system have associated power consumption and exergy destruction that cause a decrease in fuel cell system power production and exergetic efficiency compared with those of the fuel cell stack.

Within the simulator environment the fuel cell system can be analyzed as a stand-alone system responding to a user-specified current density request or as part of a total powertrain operating in response to a driving cycle of vehicle speed. Section 4.2 assesses stand-alone fuel cell system performance based on current density request while Sec. 4.3 addresses fuel cell system performance and fuel economy during vehicle simulations.

4.2. Stand-Alone Fuel Cell System Assessments

Two assessments were conducted using the stand-alone fuel cell system to determine: (1) relative impact of fuel cell system auxiliary components on power density and (2) opportunity for fuel cell system efficiency improvement via auxiliary component control efforts. Both assessments were conducted by varying the fuel cell stack current density request from 0 to 1.0 A/cm^2. Constant fuel cell operating parameters used during the assessments are representative of automotive fuel cell operation: nominal fuel cell stack operating temperature of 353K, anode pressure of 2 atm, fuel utilization of 0.8, molar air-fuel ratio of 2, hydrogen and air relative humidity of 100%, and reactant temperature of 333 K at fuel cell electrode inlets.

During assessment of the relative impact on power density by auxiliary components, power density production and consumption by each component within the fuel cell system was examined for each current density request. Figure 4.1 illustrates the difference between fuel cell stack power production and fuel cell system power production due to auxiliary component power requirements. The figure also indicates the magnitude of auxiliary power produced and consumed. Figure 4.2 compares power consumption by auxiliary components over the range of current density. The air compressor has the greatest average power consumption (~93.5%) followed by the cooling fan (~5%), the cooling water pump (~1%), and the hydrogen recirculation pump (~0.5%). Power consumed by the air humidification pump and the hydrogen humidification pump is negligible. For the auxiliary components in the fuel cell system, these results indicate reduction in compressor power consumption would contribute most
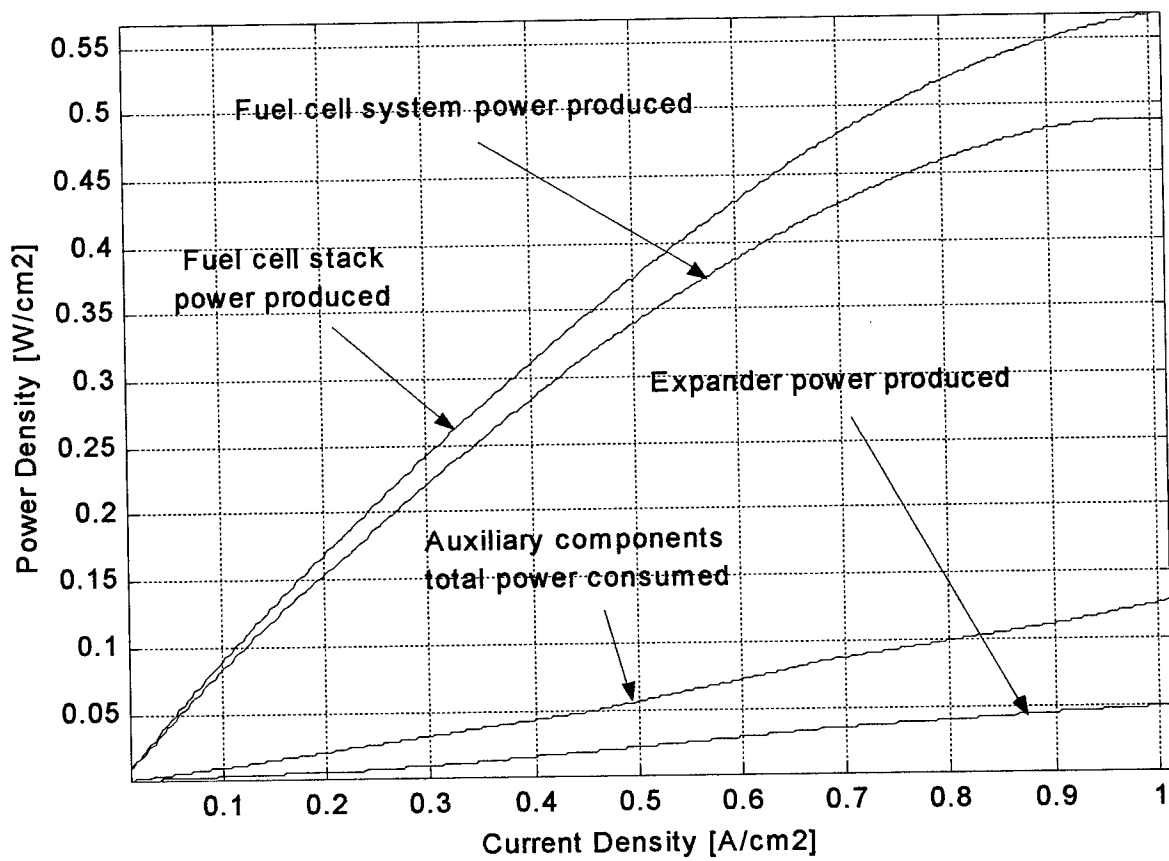
Figure 4.1: Fuel Cell and Fuel Cell System Power Density vs. Current Density
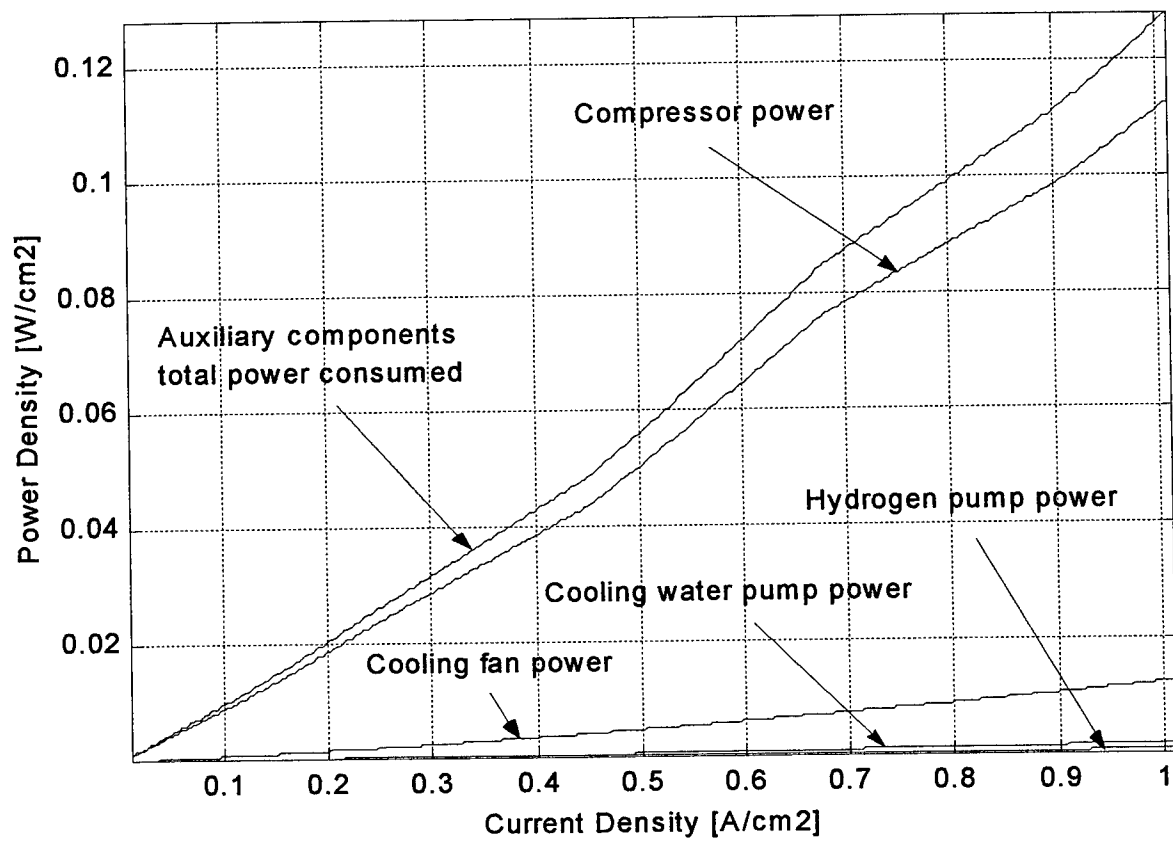
Figure 4.2: Relative Magnitude of Auxiliary Components Power Requirements

to increased fuel cell system net power output. Hence, performance capability and operational control of the air delivery component should be the highest priority to maximize fuel cell system efficiency.

The second assessment considered the impact on efficiency of component controls and established expected efficiency limits for best-case and worst-case control of the compressor. Figure 4.3 compares fuel cell system efficiencies for five cases: (1) stand-alone fuel cell stack, (2) fuel cell system with *ideal control* (the mass flow rates of fuel and air instantaneously match the fuel cell demand to maintain operating parameters) and an expander, (3) fuel cell system with ideal control but without an expander, (4) fuel cell system with *no air control* (constant air flow) and an expander, and (5) fuel cell system with no air control but without an expander. All other operating parameters are the same as described above. The two ideal control efficiency lines define the best possible performance of the respective fuel cell systems: with and without expander. The two no control efficiency lines define the worst possible performance of the respective fuel cell systems: with and without expander. With no air control, at very low current densities (0 to 0.13 A/cm^2 approximately) the power consumed by the auxiliary components equals or exceeds the power generated by the fuel cell stack, and thus no net power is developed and the exergetic efficiency is assigned a zero value.

The region on Fig. 4.3 between the best and worst performance lines represents opportunity for performance improvement via fuel cell system component control efforts. As indicated by results from the first assessment, low-level control efforts targeting the compressor have the greatest potential for improved system performance. Consideration
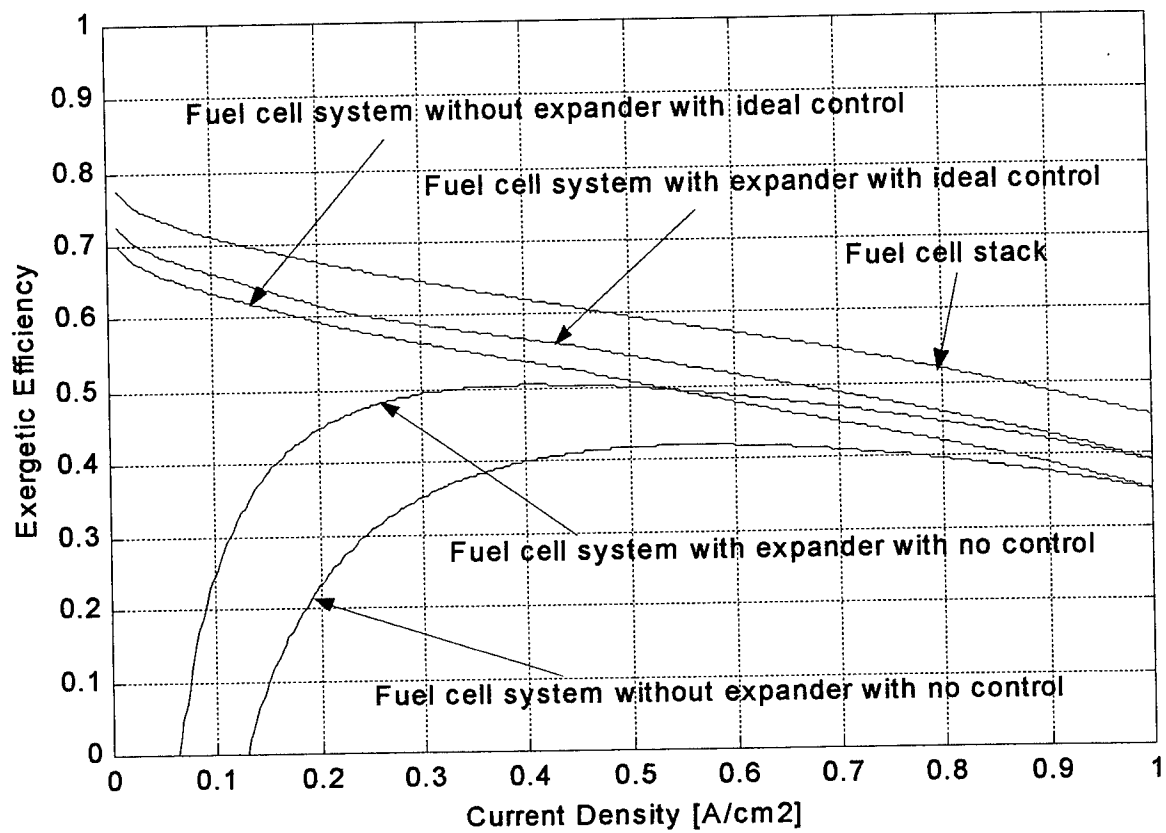
Figure 4.3: Exergetic Efficiency Comparison of Ideal Control against No Air Control

of alternative air flow strategies will indicate which air flow strategy affects system efficiency most favorably while maintaining required system performance level.

A simple air flow strategy is to continuously operate the compressor to provide constant mass flow of air and pressure ratio to meet maximum demand. Another strategy is to continuously operate a compressor that provides variable mass flow of air and variable pressure ratio. Using variable mass flow introduces a new constraint: the *dynamics* (time response) of the air supply system. Another strategy is to operate the compressor in an on/off mode to provide constant mass flow of air and constant pressure ratio while coupling the compressor with an accumulator to store excess air and provide air flow supply when the compressor is turned off. Consideration of these and other low-level control strategies for the compressor may reduce compressor power requirements and thus increase the overall fuel cell system power production and exergetic efficiency.

4.3. Vehicle Simulation Results

The vehicle simulator with the embedded fuel cell system was used to investigate fuel cell system and overall powertrain performance during two driving cycles: FUDS and FHDS. The vehicle modeled during the simulations is a sport utility-type vehicle with vehicle mass of 1452 kg (3200 pounds), vehicle frontal area of 2.7 m^2, coefficient of drag of 0.4, and coefficient of rolling resistance of 0.015. Individual fuel cell active area is taken as 400 cm^2 with 220 cells in the stack. The same representative fuel cell operating parameters for nominal fuel cell stack operating temperature, anode pressure, fuel utilization, molar air-fuel ratio, hydrogen and air relative humidity, and reactant temperature at fuel cell electrode inlets employed in the assessments described in Sec. 4.2 are used during the direct-hydrogen fuel-cell powered vehicle simulations.

The fuel cell system has ideal control (Sec. 4.2) and includes an expander and a compressor that can provide variable mass flow of air and variable pressure ratio between 2.1 and 3.2. Compressor isentropic efficiency ranges between 49% and 71%. Cathode inlet temperature is dependent upon ambient temperature, compressor pressure ratio, compressor isentropic efficiency, and humidification level. Although ambient temperature and relative humidity are constant for the simulations, the compressor pressure ratio and isentropic efficiencies vary with air flow. Still, for simplicity the same average cathode inlet temperature of 333K from Sec. 4.2 is assumed. The assumed average cathode inlet temperature of 333K is within 3% of the temperatures associated with the average pressure ratios during FUDS and FHDS: 2.2 and 2.3, respectively. The maximum fuel cell stack power capacity is 50 kW at nominal temperature while the maximum fuel cell system net power capacity is 42 kW at nominal temperature.

4.3.1. FUDS Simulation Results

Cold-start of the vehicle is simulated during the FUDS cycle by assuming initial fuel cell stack operating temperature is ambient temperature. Figure 4.4 shows the 1380-second FUDS cycle used during simulation. The fuel cell system generally meets the load demand. During the simulation, hydrogen consumption is 0.1460 kg. To determine fuel economy hydrogen usage is converted to equivalent gasoline usage based on the relative lower heating values of hydrogen and gasoline (see Eq. 6.1). Fuel economy during the FUDS simulation is 52.9 mpg.

Figure 4.5 shows the change in fuel cell operating temperature with time during the cycle. The fuel cell is initially at ambient temperature, 293K. As the fuel cell stack operates for longer periods, heat transfer due to the cell reactions causes the fuel cell

102
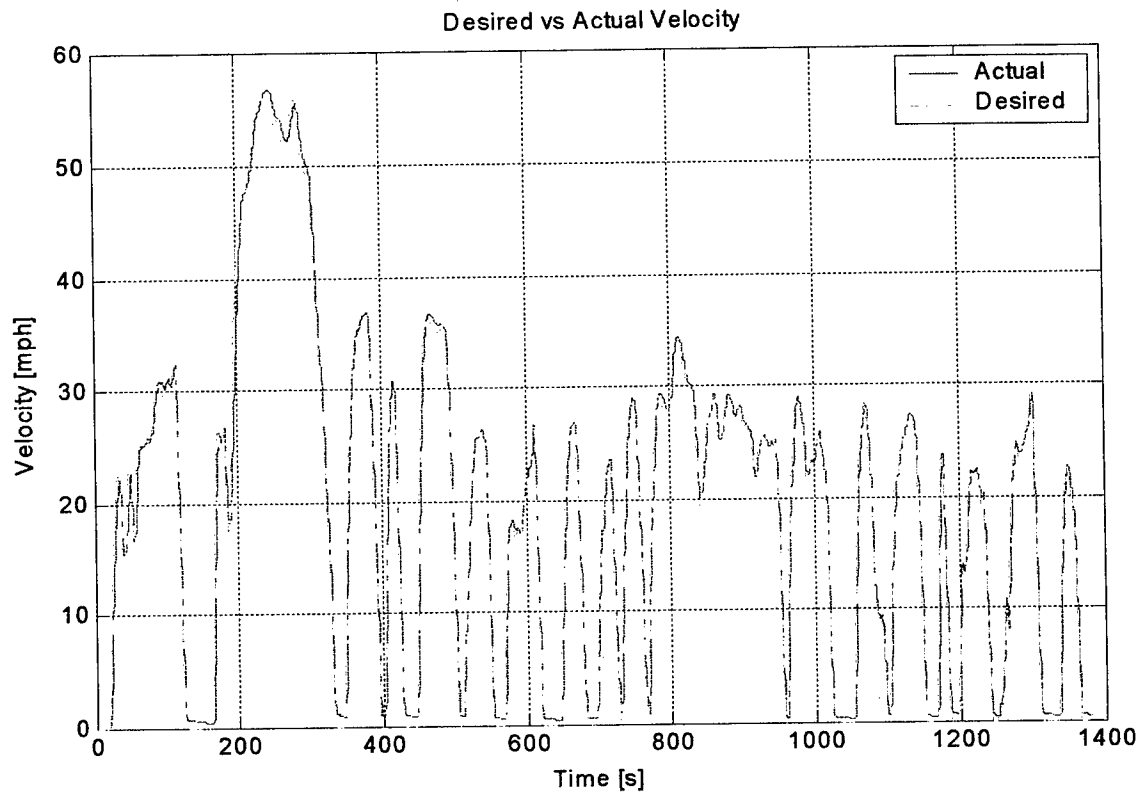
Figure 4.4: Vehicle Speed over FUDS Cycle

103
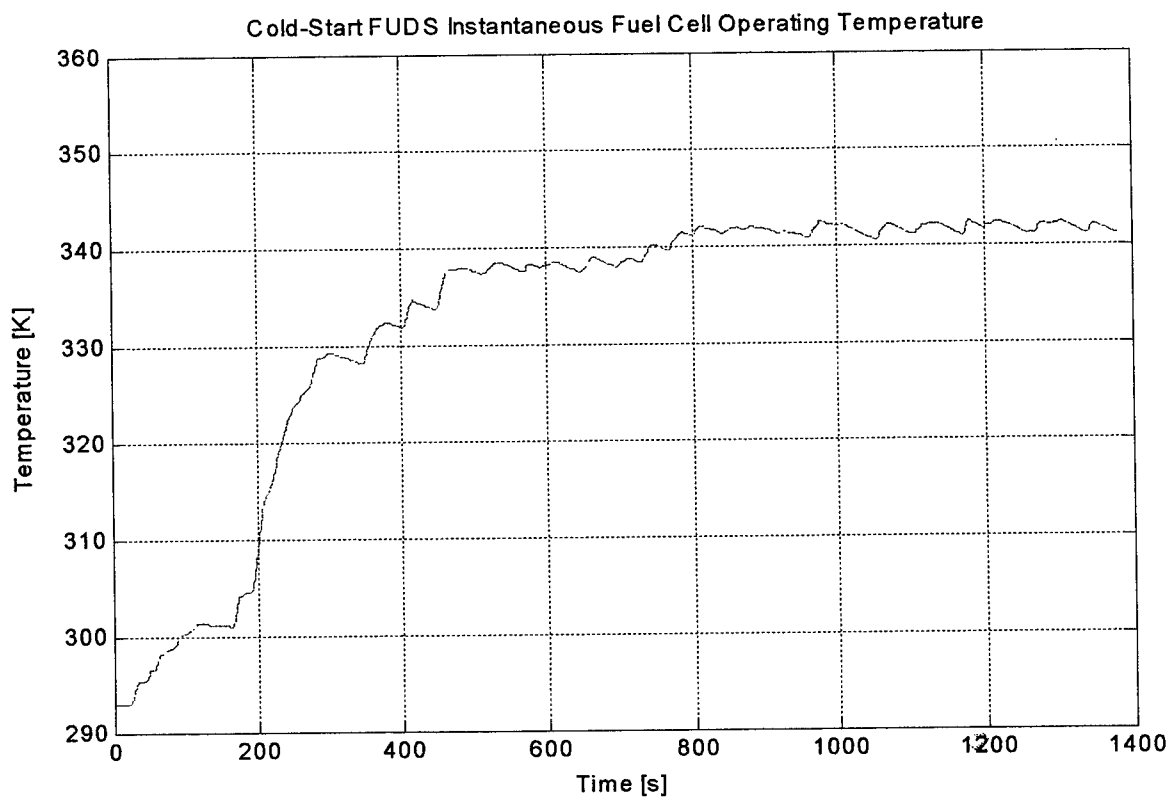
Figure 4.5: Cold-Start FUDS Instantaneous Fuel Cell Stack Temperature

stack temperature to rise. Note that during the 1380-second cycle, the fuel cell stack does not reach its target operating temperature of 353K where better performance can be expected (see Figs. 3.7 through 3.9). Additionally, since the fuel cell stack does not reach nominal fuel cell operating temperature, the cooling system never operates during the cycle.

Figure 4.6 compares the instantaneous fuel cell stack current density with the maximum current density limit. For the assumed fuel cell size operating under the FUDS cycle, actual fuel cell current density is always less than maximum fuel cell current density. If the fuel cell stack size were too small, the stack would typically show periods of operation at maximum current density in an effort to provide the power required. If stack size is too small, the fuel cell stack may not be able to provide the power required by the load at times during the cycle.

Fuel cell stack and fuel cell system instantaneous exergetic efficiencies are shown in Fig. 4.7. The average exergetic efficiency over the cycle for the fuel cell stack is 62.04% while that for the fuel cell system is 56.43%. The effects associated with chemical processing to produce hydrogen from feedstock and compression of hydrogen for storage in on-board tanks are not included in these exergetic efficiency values. Assuming approximate exergetic compressor efficiency of 86% based on values reported by Wang (1999 and 1999a) and using the hydrogen conversion efficiency of 71% from Table 1.1, conversion efficiency to produce compressed hydrogen from feedstock is about 61% (the product of 86% and 71%). Consideration of hydrogen conversion efficiency results in substantially lower total exergetic efficiencies of 37.8% for the fuel cell stack and 34.4% for the fuel cell system.
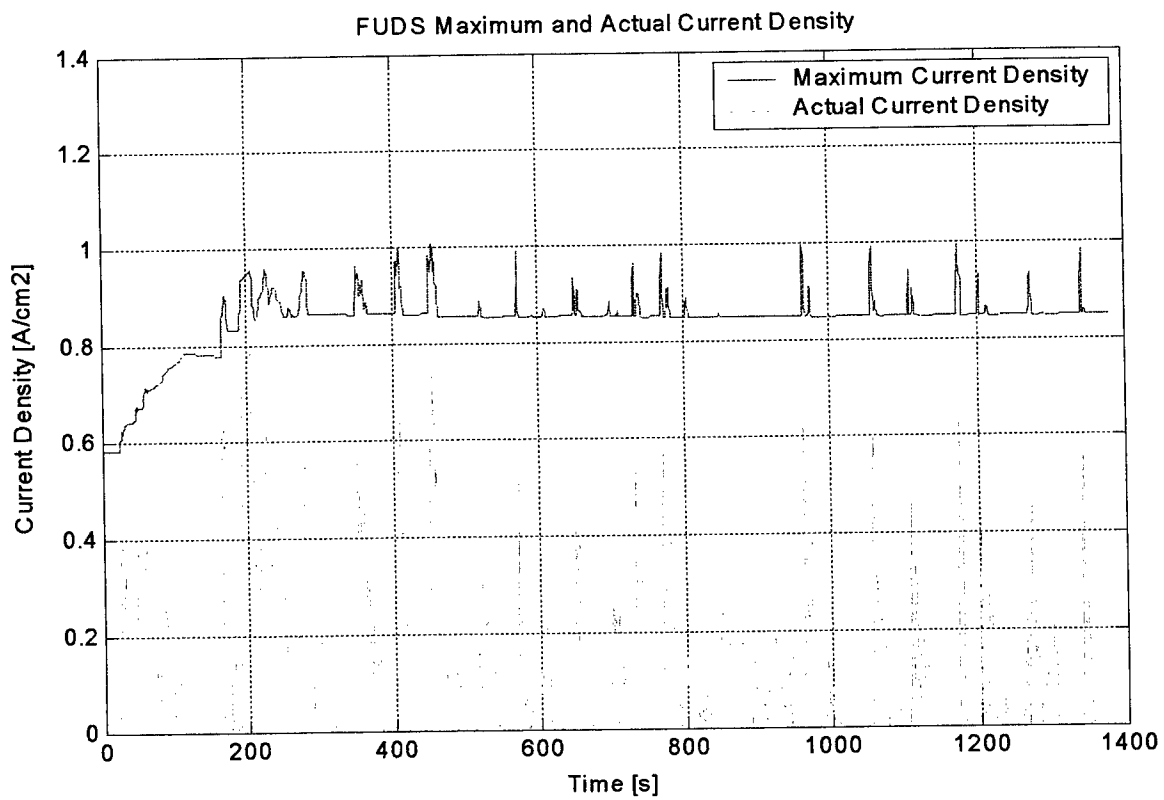
Figure 4.6: FUDS Maximum and Actual Current Density
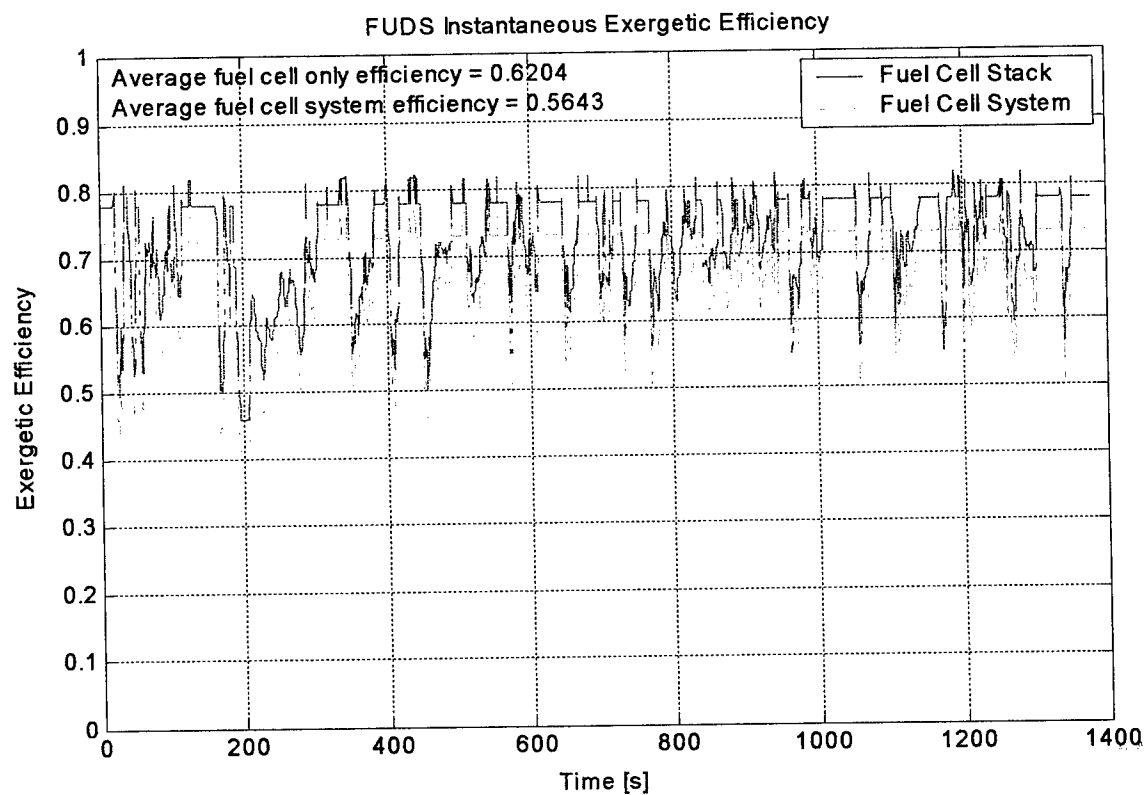
Figure 4.7: FUDS Instantaneous Exergetic Efficiency

Comparison of Fig. 4.6 with Fig. 4.7 shows that, in accordance with Figs. 3.7 through 3.9, high exergetic efficiency occurs at low current density while low exergetic efficiency occurs at high current density. In particular, the lowest instantaneous exergetic efficiency occurs at approximately 200 seconds, which corresponds to the time of highest actual current density during the cycle as shown in Fig. 4.6. The data of Figs. 4.6 and 4.7 also can be represented for each second during the driving cycle as in Fig. 4.8, which shows the instantaneous variation of exergetic efficiency with current density. For a given current density, exergetic efficiency values increase as the driving cycle evolves, reflecting the influence of rising fuel cell operating temperature during the cycle (Fig. 4.5). As the temperature approaches the target operating temperature, 353K, the trace of the exergetic efficiency approaches the shape of the exergetic efficiency-current density curve for constant fuel cell operating temperature as shown in Fig. 3.7.

The relative magnitude of power consumption and production associated with the auxiliary components in the fuel cell system is indicated in Fig. 4.9, which compares the power produced by the fuel cell stack and the fuel cell system. In agreement with the results of Sec. 4.2, the air compressor has the greatest power consumption (~99.5%) followed by the hydrogen recirculation pump (~0.5%) during the FUDS cycle. Note that the percent of power consumption by the compressor during the FUDS cycle is six percent higher than the percent of power consumption by the compressor in the stand-alone fuel cell system assessment in Sec. 4.2. This increase is due to no power consumption by the radiator fan and the cooling water pump since the fuel cell stack does
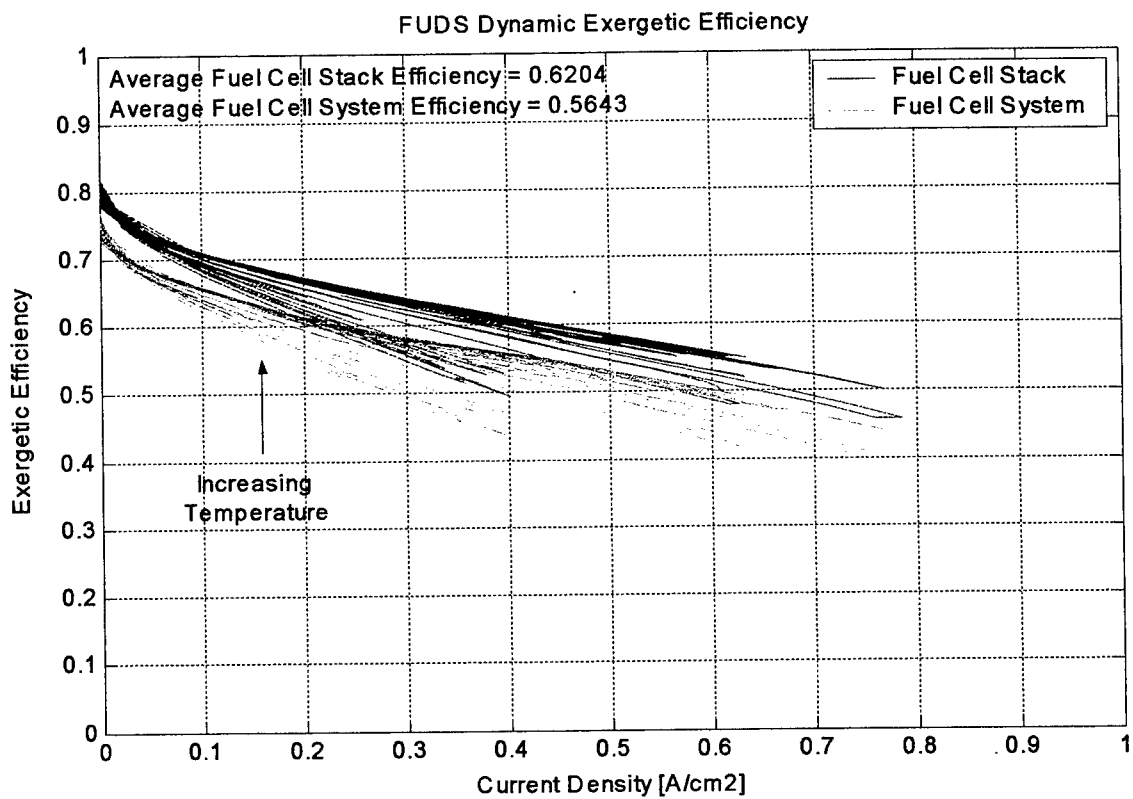
Figure 4.8: FUDS Fuel Cell and Fuel Cell System Time Varying Exergetic Efficiency vs. Current Density
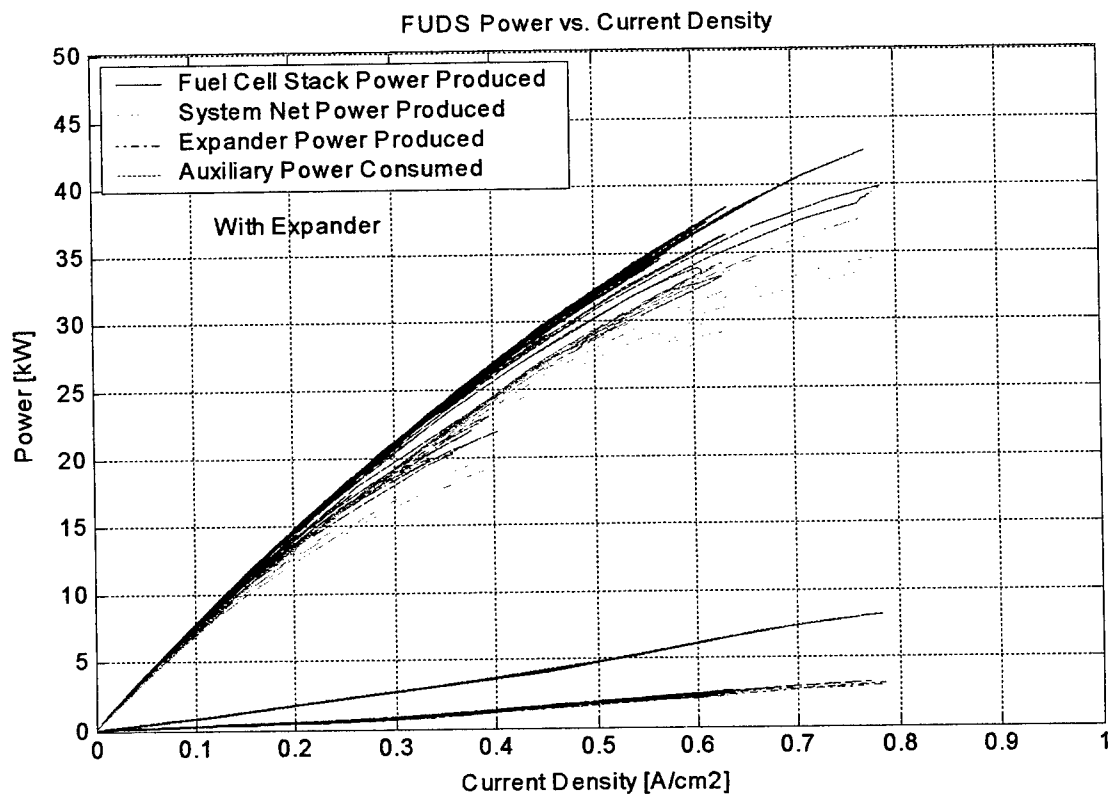
Figure 4.9: FUDS Fuel Cell, Fuel Cell System, and Auxiliary Components Dynamic Power vs. Current Density

110

not reach nominal operating temperature of 353K (Fig. 4.5) and the cooling system never turns on during the cold-start cycle. Power consumed by the air humidification pump and the hydrogen humidification pump is negligible.

4.3.2. FHDS Simulation Results

Warm-start of the vehicle is simulated during the FHDS cycle by assuming initial fuel cell stack operating temperature is nominal fuel cell operating temperature. Figure 4.10 shows the 765-second FHDS cycle used during simulation. The fuel cell system generally meets the load demand. During the simulation, hydrogen consumption is 0.1817 kg. Fuel economy during the FHDS simulation is 58.5 mpg.

Figure 4.11 shows the change in fuel cell operating temperature with time during the cycle. The fuel cell is initially at fuel cell operating temperature, 353K. As the fuel cell stack operates for longer periods, heat transfer due to the cell reactions causes the fuel cell stack temperature to rise. When the fuel cell temperature reaches 355K, the thermostatically controlled cooling system turns on. When the fuel cell temperature drops below 351K, the cooling system turns off.

Figure 4.12 displays instantaneous variation of fuel cell stack and fuel cell system exergetic efficiencies with current density during the FHDS cycle. The average exergetic efficiency over the cycle for the fuel cell stack is 64.12% while that for the fuel cell system is 58.13%. Since the fuel cell stack operating temperature remains close to the nominal operating temperature throughout the FHDS cycle, the trace of the exergetic efficiency reflects the shape of the exergetic efficiency-current density curve for constant fuel cell operating temperature as shown in Fig. 3.7. As mentioned in Sec. 4.3.1, if the efficiency associated with conversion of feedstock into compressed hydrogen stored
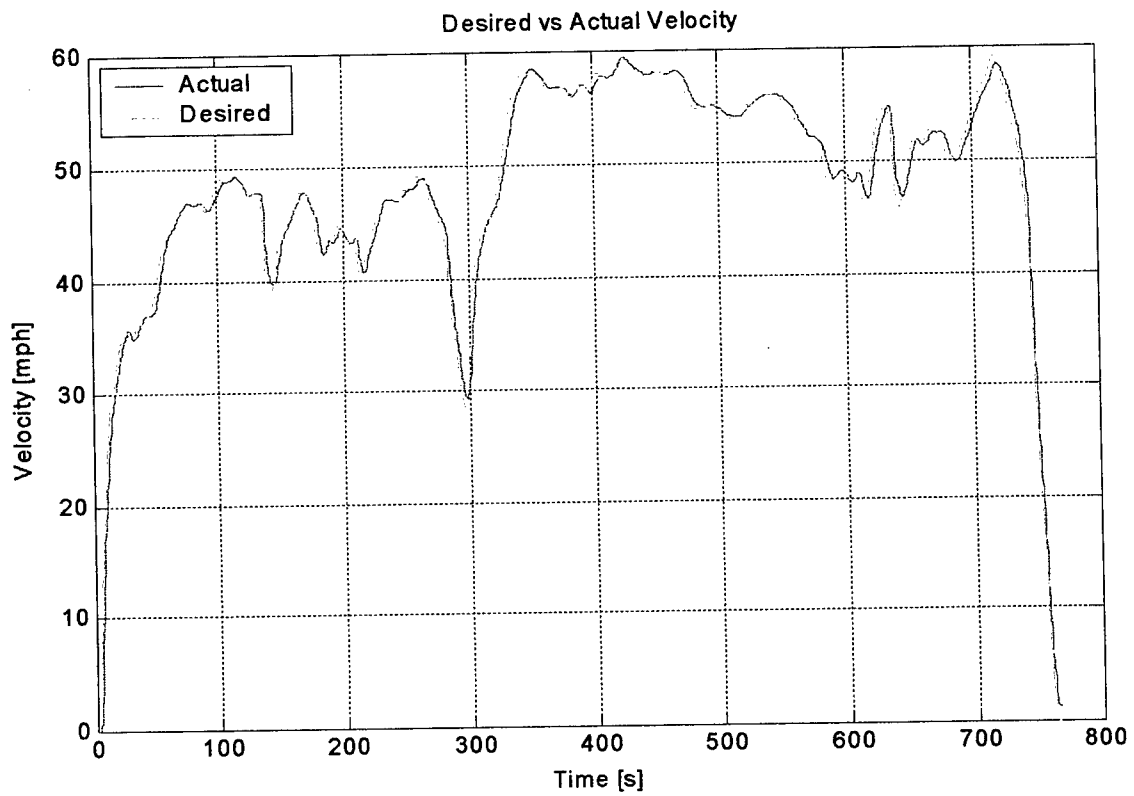
Figure 4.10: Vehicle Speed over FHDS Cycle
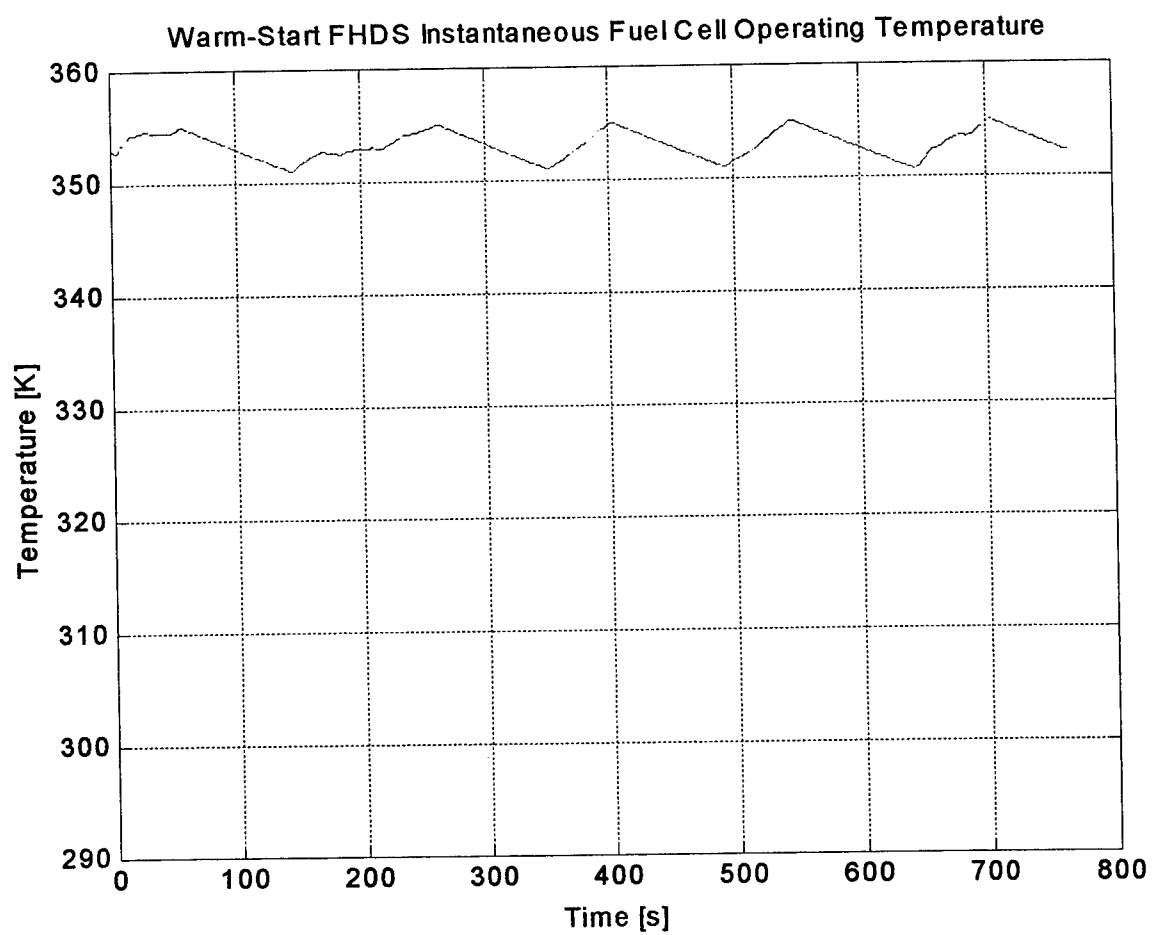
Figure 4.11: Warm-Start FHDS Instantaneous Fuel Cell Stack Temperature
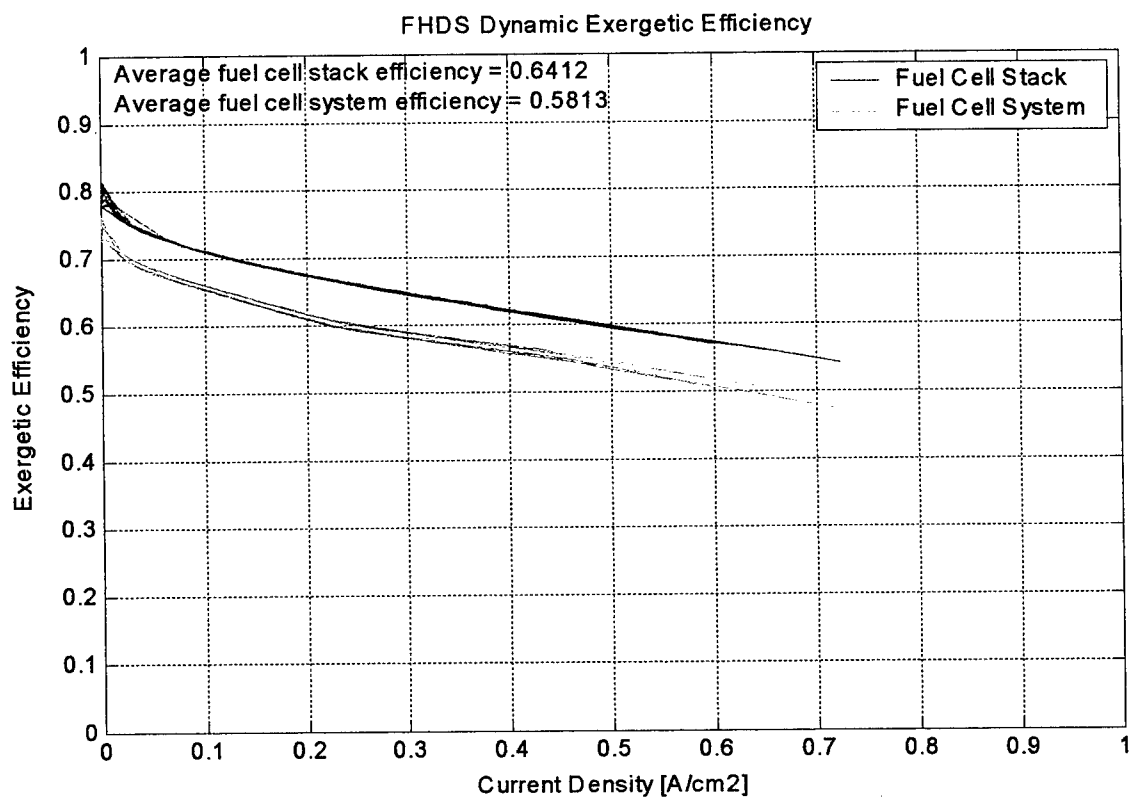
Figure 4.12: FHDS Fuel Cell and Fuel Cell System Time Varying Exergetic Efficiency vs. Current Density

114

on-board the vehicle is considered, fuel cell stack and fuel cell system total exergetic efficiency values will be substantially lower than those cited above that are based on the chemical exergy of the hydrogen stored on-board the vehicle.

Figure 4.13 compares the power produced by the fuel cell stack and the fuel cell system. The figure also indicates the magnitude of auxiliary power produced and consumed. Component power consumption percentages during the FHDS cycle are similar to the percentages associated with results in Sec. 4.2 since the fuel cell stack in both cases operates at or near nominal fuel cell operating temperature. The air compressor has the greatest power consumption (~94.2%) followed by the radiator fan (~4.6%), the hydrogen recirculation pump (~0.6%), and the cooling water pump (~0.6%). Power consumed by the air humidification pump and the hydrogen humidification pump is negligible.

4.3.3. Sensitivity Analysis

Sensitivity analysis uses a specified base case simulation to compare other simulations in which one selected design or operational parameter has been changed from the base case. For the base case simulations in the direct-hydrogen fuel cell vehicle study, the following operational and design parameters were used: nominal fuel cell stack operating temperature of 353K, anode pressure of 2 atm, fuel utilization of 0.8, molar air-fuel ratio of 2, compressor efficiency ranging between 49% and 71% dependent on air flow, reformate and air relative humidity of 100% at the fuel cell stack electrode inlets, expander efficiency ranging between 63% and 81% dependent on air flow, individual fuel cell active area of 400 cm^2 with 220 cells in the stack, ambient temperature of 293K, and vehicle mass of 1452 kg.

115

FHDS Power vs. Current Density

Legend:
- Fuel Cell Power Produced
- System Net Power Produced
- Expander Power Produced
- Auxiliary Power Consumed

With Expander

X-axis: Current Density [A/cm2]
Y-axis: Power [kW]
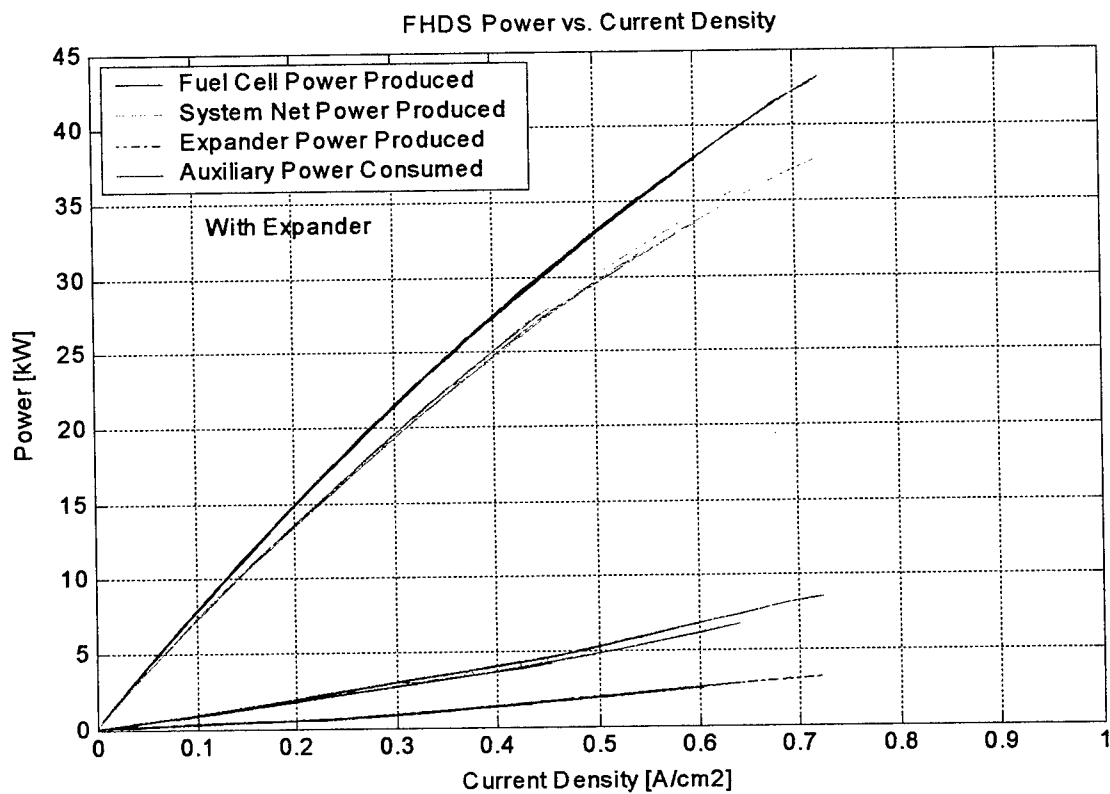
Figure 4.13: FHDS Fuel Cell, Fuel Cell System, and Auxiliary Components Dynamic Power vs. Current Density

116

In this study sensitivity analysis compares consequent percent change in fuel economy from the base case fuel economy to percent change in a selected system parameter from the base case parameter value. The quotient from dividing the percent change in fuel economy by the percent change in parameter value quantifies the sensitivity of fuel economy to the varied parameter and is referred to as *sensitivity*. Equation 4.1 is used to determine sensitivity:

$$Sensitivity = \frac{\left(\dfrac{\Delta Fuel\ Economy}{Base\ Case\ Fuel\ Economy}\right)}{\left(\dfrac{\Delta Parameter\ Value}{Base\ Case\ Parameter\ Value}\right)} \qquad (4.1)$$

Since it is non-dimensional, sensitivity provides a measure of the relative impact of changing various system parameters on fuel economy. A positive sensitivity value indicates fuel economy increases with increasing parameter value or fuel economy decreases with decreasing parameter value. A negative sensitivity value indicates fuel economy increases with decreasing parameter value or fuel economy decreases with increasing parameter value. Sensitivity analyses were conducted for the direct-hydrogen fuel cell vehicle operating on the FUDS and FHDS cycles and results for are provided in Tables 4.1 and 4.2 respectively.

For the cold-start FUDS simulations, fuel economy is most sensitive to vehicle mass. As shown in Table 4.1, a five percent increase in vehicle mass produces a 4.7% decrease in fuel economy. The sensitivity value of −0.94 for this case indicates that fuel economy decreases by 0.94% for each percent increase in vehicle mass from the base case. Fuel economy is next most sensitive to average compressor efficiency. A 9.9% decrease in average compressor efficiency resulted in a 2.1% decrease in fuel economy, a

117

Parameter	Base Case Value	% Change in Parameter [+/-]	% Change in Fuel Economy [+/-]	Fuel Economy Sensitivity
Fuel Economy [mpg]	52.9	- - -	- - -	- - -
Vehicle Mass [kg]	1452	+5.0	-4.7	-0.94
	1452	+10.0	-9.1	-0.91
Avg Compressor Efficiency [%]	53.7	-9.9	-2.1	0.21
	53.7	+5.0	+0.8	0.15
Molar Air Fuel Ratio	2	-25.0	+2.8	-0.11
	2	25.0	-2.8	-0.11
Avg Expander Efficiency [%]	73.6	-10.0	-0.8	0.08
	73.6	+4.9	+0.2	0.04
Hydrogen Utilization	0.8	-10.0	-0.1	0.01
	0.8	+10.0	+0.0	0.00
Nominal FC Temp [K]	353	-3.0	0.0	0.00
	353	+3.0	0.0	0.00

Table 4.1: Cold-Start FUDS Cycle Sensitivity Analysis for Direct-Hydrogen Fuel Cell Vehicle

Parameter	Base Case Value	% Change in Parameter [+/-]	% Change in Fuel Economy [+/-]	Fuel Economy Sensitivity
Fuel Economy [mpg]	58.5	- - -	- - -	- - -
Nominal FC Temp [K]	353	-3.0	-2.2	0.73
	353	+3.0	+2.1	0.70
Vehicle Mass [kg]	1452	+5.0	-2.7	-0.55
	1452	+10.0	-5.5	-0.55
Avg Compressor Efficiency [%]	54.4	-9.6	-1.9	0.20
	54.4	+4.8	+0.7	0.14
Molar Air Fuel Ratio	2	-25.0	+2.4	-0.10
	2	25.0	-2.6	-0.10
Avg Expander Efficiency [%]	70.2	-9.8	-0.7	0.07
	70.2	+5.0	+0.2	0.04
Hydrogen Utilization	0.8	-10.0	-0.1	0.01
	0.8	+10.0	+0.0	0.00

Table 4.2: Warm-Start FHDS Cycle Sensitivity Analysis for Direct-Hydrogen Fuel Cell Vehicle

sensitivity of 0.21. Similarly, increasing average compressor efficiency by 5% resulted in an average fuel economy increase of 0.8%, a sensitivity of 0.15. Fuel economy is next sensitive to molar air fuel ratio, which has a sensitivity of –0.11. Fuel economy did not show sensitivity to nominal fuel cell operating temperature during cold-start FUDS since the actual fuel cell operating temperature never reached the nominal fuel cell operating temperature during the cycle.

Sensitivity analysis results for the warm-start FHDS simulations reported in Table 4.2 indicate that fuel economy is most sensitive to nominal fuel cell operating temperature. Since the FHDS simulation is warm-start, actual fuel cell operating temperature remains near the nominal fuel cell temperature throughout the cycle and thus changes to this temperature impact fuel economy. A 3% decrease in operating temperature results in a 2.2% decrease in fuel economy, a sensitivity of 0.73. Similarly, a 3% increase in operating temperature results in a 2.1% increase in fuel economy, a sensitivity of 0.70. Fuel economy is next most sensitive to vehicle weight with a sensitivity of –0.55. Decreasing average compressor efficiency by 9.6% results in a 1.9% decrease in fuel economy, a sensitivity of 0.2. Increasing average compressor efficiency by 4.8% results in a 0.7% increase in fuel economy, a sensitivity of 0.14.

By examining results from sensitivity analyses, fuel cell system developers can identify component developmental and operational improvements that will afford greater fuel economy:

(1) For cold-start FUDS operation, limiting vehicle weight, choosing a compressor with high efficiency, and operating with low air fuel ratio result in improved fuel economy.

120

(2) For warm-start FHDS operation, sustaining high nominal fuel cell temperature, limiting vehicle weight, and choosing a compressor with high efficiency are three parameter improvements that are most promising for fuel economy improvement.

4.4. Summary

Assessment of a stand-alone fuel cell system indicates that the compressor is the auxiliary component with the largest power consumption. Reducing compressor power consumption through either component improvement or component control would contribute most to increased fuel cell system net power output. Performance of a direct-hydrogen fuel cell vehicle was assessed for cold-start FUDS and warm-start FHDS cycles. Fuel economy was 52.9 mpg for FUDS and 58.5 mpg for FHDS. FUDS fuel economy showed most sensitivity to vehicle mass, followed by compressor efficiency and molar air fuel ratio. FHDS fuel economy showed most sensitivity to nominal fuel cell operating temperature followed by vehicle mass and compressor efficiency. Performance of a methanol reforming fuel cell vehicle during FUDS and FHDS is considered next in Chapter 5.

CHAPTER 5

EFFECTS OF ON-BOARD REFORMING

5.1. Introduction

For automotive applications, PEM fuel cells require hydrogen provided directly from on-board storage tanks or produced via on-board reforming of a hydrogen-bearing fuel. The purpose of this chapter is to develop a reformer model for integration with the PEM fuel cell system model within the VP-SIM environment and to examine the effects of reforming on system efficiency and vehicle fuel economy.

Methanol is selected as a representative fuel for the purpose of this study. Owing to exergy destruction within the methanol reformer, the overall performance is expected to be less than in a direct-hydrogen fuel cell vehicle, and this is the case.

5.2. Literature Review

As discussed in Sec. 2.1.3.2, there are four primary types of reforming: steam reforming, partial oxidation, decomposition, and autothermal reforming. Several current studies have investigated reforming processes for use in automotive applications. Brown (2001) examines partial oxidation and steam reforming processes for production of hydrogen from methanol, natural gas, gasoline, diesel fuel, aviation jet fuel, and ethanol to assess relative advantages and disadvantages of fuel choice for fuel cell-driven vehicles. Ogden et al. (2000) consider direct-hydrogen, steam reforming of methanol,

122

and partial oxidation of gasoline and natural gas derived synthetic liquids to compare fuel economy of fuel cell vehicles using these alternative fuels. Wegeng et al. (2001) describe microchannel technology development and technical challenges for use in components supporting fuel reforming. Pettersson and Westerholm (2001) review technology required for development of reformers that can process more than one type of fuel into hydrogen (*multi-fuel reformers*). By examining partial oxidation, steam reforming, autothermal reforming, and catalytic decomposition processes, they conclude potential for development is more promising for fuel reformers designed for processing one specific fuel than multi-fuel reformers.

Ramaswamy et al. (2000) develop a methanol steam reformer model for integration with a fuel cell system in automotive applications. The fuel processor consists of a mixer/preheater chamber, a steam reformer, a catalytic burner, a water gas shift unit and a preferential oxidation unit. Effects of transient operation on fuel processor efficiency and strategies to optimize efficiency of the reformer are examined. The work of Kumar et al. (1996) is described in the next section and is the basis of the methanol reformer model developed in the current study.

5.3. Methanol Reformer Model

In this section a reformer model is developed and integrated with the VP-SIM fuel cell system model. Changes to the fuel cell system model due to addition of the reformer are discussed.

5.3.1. Introduction

Kumar et al. (1996) describe a low-temperature, catalytic methanol reformer that combines partial oxidation, steam reforming, decomposition, and water gas shift

123

reactions to produce hydrogen. Bench-scale tests using ambient-temperature methanol, water, and air at the inlet produced reformate at 200°C containing 50% hydrogen, 29% nitrogen, 20% carbon dioxide, and ~1% carbon monoxide. Important for the current study, hydrogen production was approximately 90.9% of theoretical hydrogen production, a result of incomplete reaction of methanol. Also relevant to current modeling considerations, Kumar reports that during reformer cold-start, catalytic reactions were initially slow until reformer operating temperature was achieved. Consequently, hydrogen production percentage increased with rising temperature. With no external heat input, time to achieve bench-scale temperature and reformate composition was approximately 175 seconds. For PEM fuel cell usage, Kumar indicates that the reformate must be conditioned to reduce the carbon monoxide concentration to less than 10 ppm (Sec. 2.2.1), cooled to near fuel cell operating temperature, and humidified prior to entering the fuel cell anode.

Ahmed and Krumpelt (2001) expand the autothermal reforming concept used by Kumar et al. (1996) to examine hydrogen production potential from any fuel in the family $C_nH_mO_p$ using idealized reaction stoichiometry.

5.3.2. Reformer Model Description

For methanol modeling purposes, the methanol reformer described by Kumar et al. (1996) is used for simplicity as the basis for this study. Simplicity of the methanol reformer results from the autothermal nature of the process and thus no requirement for external heat sources. Also, simply varying the rate at which reactants are provided to the reformer controls the amount of hydrogen produced. In addition, low-temperature reformer operation supports integration with the fuel cell system.

124

The reformer overall theoretical *complete reaction* to produce hydrogen is based on a combination of exothermic partial oxidation, endothermic steam reforming, endothermic decomposition, and endothermic water gas shift reactions and is given by Eq. 5.1:

$$CH_3OH(l) + x(O_2 + 3.76N_2) + (1-2x)H_2O(l) \rightarrow (3-2x)H_2 + CO_2 + 3.76xN_2 \qquad (5.1)$$
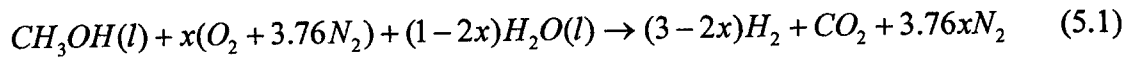
where x is the oxygen-to-methanol molar ratio. The value for x ranges between 0 and 0.5. The value of x determines whether the overall reaction is endothermic, exothermic, or involves no *net* energy transfer. When x is 0, Eq. 5.1 becomes the endothermic steam reforming reaction. When x is 0.5, Eq. 5.1 becomes the exothermic partial oxidation reaction. As values of x increase from 0 to 0.5, the energy absorbed during the reaction decreases from a maximum (corresponding to $x = 0$) until no net energy is required (corresponding to the *thermally neutral* value for x). As values of x increase from the thermally neutral value, the energy evolved during the reaction increases to a maximum (corresponding to $x = 0.5$). The value of x for the thermally neutral case can be obtained from an energy balance assuming Eq. 5.1 for the reformer. Whether energy is absorbed or evolved during the reaction primarily affects the reformer temperature. The only heat transfer between the reformer and its surroundings is a convective loss.

Since hydrogen mass flow is a principal element used by the fuel cell system model, the reformer model also must incorporate hydrogen mass flow to integrate the two systems. Accordingly, Eq. 5.1 is converted from a molar basis to a mass basis and normalized by the mass of hydrogen to determine quantities of reactants and products per kilogram of hydrogen produced. Equation 5.2 is the basis of the reformer model:

$$\frac{M_{CH_3OH}}{(3-2x)M_{H_2}}CH_3OH + \frac{xM_{O_2}}{(3-2x)M_{H_2}}O_2 + \frac{3.76xM_{N_2}}{(3-2x)M_{H_2}}N_2 + \frac{(1-2x)M_{H_2O}}{(3-2x)M_{H_2}}H_2O \rightarrow$$

$$H_2 + \frac{M_{CO_2}}{(3-2x)M_{H_2}}CO_2 + \frac{3.76xM_{N_2}}{(3-2x)M_{H_2}}N_2 \qquad (5.2)$$
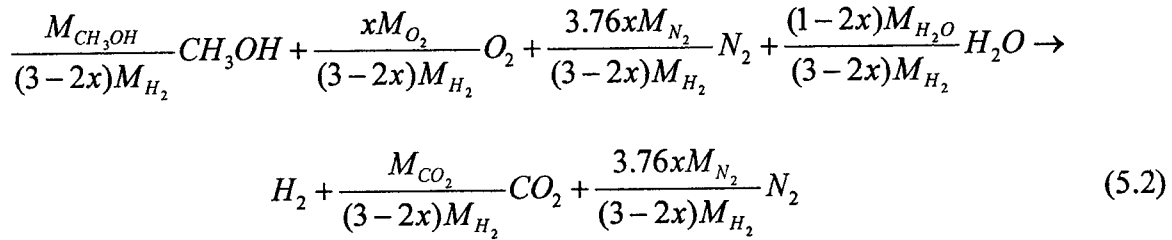
where M is the species molecular weight [kg/kmol].

At the reactor inlet, only the chemical exergy associated with the methanol is significant. Exergy is transferred from the reformer via mass flows of the reaction products and convective heat loss (if any). Exergy accompanying heat transfer from the reformer is considered a loss. At the exit, only the hydrogen component of the gas stream is important. Consequently, efficiency of the reformer is based on comparison of chemical exergy associated with hydrogen exiting the reformer to chemical exergy associated with methanol entering the reformer as indicated by Eq. 5.3.

$$\varepsilon_{reformer} = \frac{Mass\ Flow_{hydrogen\,out} \times Lower\ Heating\ Value_{hydrogen}}{Mass\ Flow_{methanol\,in} \times Lower\ Heating\ Value_{methanol}} \qquad (5.3)$$

To account for the impact of cold-start effects and incomplete reaction reported in Kumar's bench-scale tests, the reformer model includes an initial 175-second temperature rise from ambient temperature to fully warm reformer temperature. Associated with the rising reformer temperature is a rising hydrogen concentration (mole fraction of hydrogen in the products) to a maximum of 100% of the theoretical hydrogen concentration at a fully warm reformer temperature of 200°C. Additionally, associated with all reformer reactions is a typical hydrogen concentration of 90% of theoretical hydrogen production due to reaction kinetics. By combining these hydrogen concentration effects, reformer model results approximate the bench-scale test results.

126

Instead of reducing hydrogen production, the reformer model includes adjustments to the methanol flow from the fuel tank due to two causes: 1) presence of unreacted methanol in the reformer products due to incomplete reaction during cold-start and 2) actual hydrogen production approximately 90% of theoretical complete reaction hydrogen production. To account for effects of incomplete reaction on reformer efficiency, methanol required is multiplied by a factor equal to the reciprocal of the cold-start hydrogen concentration in the reaction products. Additionally, required quantities of reactants are multiplied by a factor equal to the reciprocal of 90%. For example, during cold-start when the temperature is such that hydrogen concentration is 50% of theoretical complete reaction hydrogen concentration, the reformer model should require an increased input of reactants compared to *theoretical* input of reactants rather than a decreased hydrogen concentration compared to the *theoretical* concentration. Instead of reducing the hydrogen production, however, the flow of methanol input to the reformer is increased: the methanol input based on Eq. 5.2 is multiplied by the factors 1/0.5 and 1/0.9 while the flows of air and water input to the reformer are multiplied by the factor, 1/0.9. The effects of cold-start and incomplete reaction are reflected as an increase in reformer input flows and result in a corresponding decrease in reformer efficiency expressed by Eq. 5.3.

As required by VP-SIM (Sec. 4.1), the reformer model is scalable. The approach used for scaling the reformer is different than for other VP-SIM components in that the scaling parameter used is based on fuel cell stack capability instead of physical dimensions associated with the reformer. Since reformer hydrogen production should not exceed *fuel cell maximum hydrogen flow rate*: the hydrogen flow rate associated with

127

fuel cell stack operation at maximum power, fuel cell maximum hydrogen flow rate is used to scale the reformer. Because fuel cell stack maximum power capability depends on the fuel cell stack size, reformer scaling is dependent on fuel cell stack size.

5.4. Reformer Model Integration within VP-SIM

Integration of the reformer with the fuel cell system requires changes in the direct-hydrogen fuel cell system model of Fig. 4.1. Figure 5.1 shows a schematic of the methanol reformer/fuel cell system model. Appendix C contains relevant equations associated with the reformer and its integration with the fuel cell system. Additional reformer auxiliary components including an air compressor, a fuel pump, and a water pump are required for pressurization of the reactants to specified anode pressure. Since the fuel cell stack provides power for these reformer auxiliary components, power requirements for these devices are included in the fuel cell system auxiliary requirements and affect net power produced by the fuel cell system, and thus the efficiency. The time needed to achieve reformer operating temperature can be decreased by burning unreacted methanol in the preheater also shown in Fig. 5.1.

In the direct-hydrogen fuel cell system model, only hydrogen is present in the anode inlet stream. Water required for humidification of the anode inlet stream is based on the mass flow of hydrogen. For the methanol reforming fuel cell system, species in addition to hydrogen are present in the reformate flowing to the anode inlet. Consequently, the water requirement for humidification of the anode inlet stream is based on the mass flow of reformate instead of the mass flow of hydrogen alone.

In the direct-hydrogen fuel cell system model, only hydrogen and water are present on the anode side. These two species are considered with the cathode species to
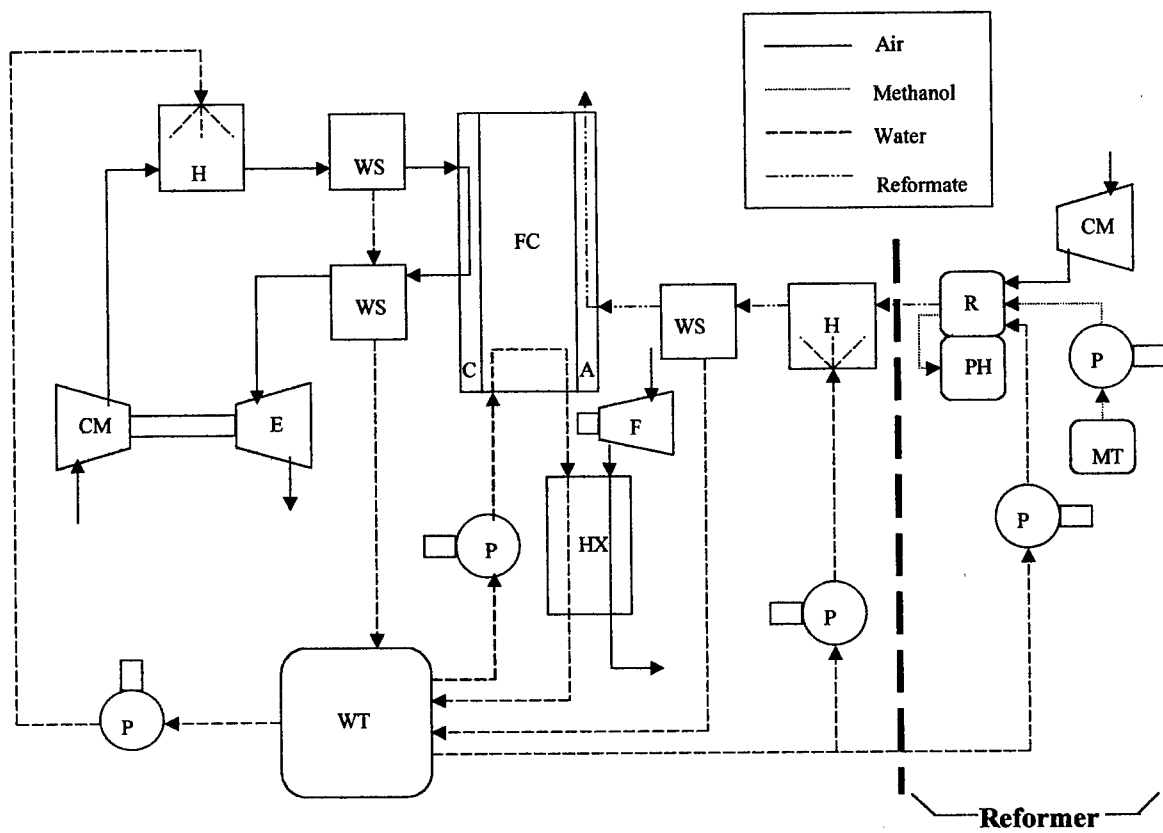
128

A = Anode   HX = Heat Exchanger
C = Cathode   MT = Methanol Tank
CM = Compressor   P = Pump
E = Expander   PH = Preheater
F = Fan   R = Reformer
FC = Fuel Cell Stack   WS = Water Separator
H = Humidifier   WT = Water Tank

Figure 5.1: Reformer/PEM Fuel Cell System Schematic

determine heat transfer associated with the fuel cell stack reaction. In the methanol reforming fuel cell system, carbon dioxide and nitrogen in addition to hydrogen and water are present on the anode side. Although their effects on heat transfer are slight, these additional species must be included in computing heat transfer associated with the fuel cell stack reaction.

Since reformate contains products in addition to hydrogen in the methanol reforming fuel cell system, the exhaust from the fuel cell stack anode is vented and not recirculated as in the direct-hydrogen fuel cell system. Because the anode exhaust is not used by the system, exergy associated with the anode exhaust is a loss. Thus when methanol reforming is used, fuel cell system efficiency is based on mass flow of hydrogen into the fuel cell stack:

$$\varepsilon_{sys} = \frac{Net\ System\ Power}{Mass\ Flow_{hydrogen\,in} \times Lower\ Heating\ Value_{hydrogen}} \tag{5.4}$$

For the direct-hydrogen case, fuel cell system efficiency is based on mass flow of hydrogen consumed by the fuel cell reaction (Eq. 3.14) instead of mass flow of hydrogen entering the fuel cell stack since any unused hydrogen in the stack reaction is recirculated.

In accordance with Eq. 1.2, total exergetic efficiency for the combined reformer/fuel cell system measures the extent of the conversion of the exergy input, chemical exergy associated with methanol, to the desired exergy product, fuel cell system net power. Since the hydrogen exiting the reformer equals the hydrogen entering the fuel cell system, total exergetic efficiency is the product of $\varepsilon_{reformer}$ and ε_{sys}; that is

$$\varepsilon_{total} = \frac{Net\ System\ Power}{Mass\ Flow_{methanol\ in} \times Lower\ Heating\ Value_{methanol}} \qquad (5.5)$$

Due to effects of irreversibilities and losses associated with the reformer, the total efficiency for the system consisting of the reformer and fuel cell system is lower than that of the direct-hydrogen fuel cell system.

5.5. Simulation Results

Using the same vehicle parameters, fuel cell sizing, and fuel cell operational parameters previously used for the direct-hydrogen fuel cell vehicle simulations in Sec. 4.3.1 and Sec. 4.3.2, vehicle simulations were conducted for the fuel cell vehicle with methanol reforming. With methanol reforming *cold-start* FUDS cycle uses ambient temperature for the reformate initial temperature as well as ambient temperature for the fuel cell stack initial temperature as was used in direct-hydrogen cold start in Sec. 4.3.1. *Warm-start* FUDS cycle uses an initial reformate temperature of 200°C while initial fuel cell stack temperature is nominal fuel cell stack temperature as was used in direct-hydrogen warm start in Sec. 4.3.2. Comparison between direct hydrogen and methanol reforming fuel cell vehicle performance measures for cold-start FUDS and warm-start FHDS cycles is shown in Table 5.1. Exergy destruction associated with the irreversible chemical reactions in the reformer significantly reduces overall performance of the fuel cell vehicle compared to the direct hydrogen fuel cell vehicle performance.

For the cold-start FUDS cycle as indicated in Table 5.1, direct-hydrogen fuel cell system efficiency is 56.4% while fuel cell system efficiency using methanol reforming is 38.6%, about two-thirds of the direct-hydrogen case. The substantial decrease in fuel cell system efficiency when using methanol reforming is primarily due to exergy losses

131

Performance Measure	Cold-Start FUDS		Warm-Start FHDS	
	Direct Hydrogen	Methanol Reforming	Direct Hydrogen	Methanol Reforming
Fuel Cell System Efficiency [%]	56.4	38.6	58.1	44.3
Reformer Efficiency [%]	- - -	75.8	- - -	81.1
Total Efficiency [%]	56.4	29.2	58.1	35.9
Fuel Economy [mpg]	52.9	24.8	58.5	35.5

Table 5.1: FUDS and FHDS Performance Measures for Direct-Hydrogen and Methanol Reforming Fuel Cell Vehicles

associated with venting of unused hydrogen from the fuel cell stack. For the direct-hydrogen fuel cell system, total system efficiency is the same as fuel cell system efficiency, 56.4%. Total efficiency for the methanol reformer/fuel cell system is 29.2%. The lower total system efficiency associated with methanol reforming reflects lower fuel cell system efficiency detailed above as well as exergy destruction due to chemical reaction in the reformer. Table 5.1 also shows the methanol reforming vehicle fuel economy is roughly half that of the direct-hydrogen fuel cell vehicle.

Warm-start FHDS cycle results shown in Table 1 indicate improved performance for both direct-hydrogen and methanol-reforming systems compared with their respective cold-start FUDS cycle results. Direct-hydrogen fuel cell system efficiency is 58.1% while fuel cell system efficiency using methanol reforming is 44.3%, again reflecting exergy losses due to venting of hydrogen. The total system efficiency using direct-hydrogen is 58.1%. As a result of lower fuel cell system efficiency and exergy destruction in the reformer the total system efficiency with methanol reforming is just 35.9%. These considerations also are reflected in the fuel economy values.

As mentioned in Secs. 4.3.1 and 4.3.2, considering the process associated with conversion of feedstock into compressed hydrogen results in total efficiencies that are about 61% of those shown for the direct hydrogen cases in Table 5.1. With like reasoning, using the methanol conversion efficiency of 65% in Table 1.1, total efficiencies for the methanol reforming cases are reduced significantly when considering the effects of producing methanol from feedstock. Thus, when the conversion from feedstock to fuel on-board is considered, direct-hydrogen maintains its advantage but by a smaller margin.

To assess the relative effect on performance due to fuel cell stack and reformer warm/cold start, FUDS and FHDS simulations were conducted varying the warm-start/cold-start combinations for the fuel cell stack and reformer. Reformer warm start corresponds to initial reformate temperature of $200^{\circ}C$ while reformer cold start corresponds to initial reformate temperature of ambient temperature. Fuel cell warm-start corresponds to initial fuel cell stack temperature of nominal fuel cell temperature while fuel cell cold-start corresponds to initial fuel cell stack temperature of ambient temperature. Results are presented in Table 5.2.

As expected for both FUDS and FHDS total efficiency and fuel economy are highest when both the fuel cell stack and reformer start warm. Conversely, total efficiency and fuel economy are lowest when both components start cold. Individually, fuel cell system efficiency and reformer efficiency are higher with warm-start compared to cold-start.

There is interdependence between the fuel cell system and the reformer. Operating conditions of one component may affect either adversely or favorably the individual performance of the other component as illustrated next.

Comparing Runs 2 and 3 in Table 5.2, total efficiency and fuel economy are better with warm-start fuel cell stack and cold-start reformer than with cold-start fuel cell stack and warm-start reformer. This indicates that the effect of fuel cell stack cold-start impacts overall performance more than reformer cold-start. However, the reformer model includes a preheater that uses unreacted methanol to increase the rate of temperature rise in the reformer compared to the rate of temperature rise without using a preheater. Reformer efficiency is significantly reduced when a preheater is not used.

134

	Run 1	Run 2	Run 3	Run 4
Fuel Cell Stack	Warm	Warm	Cold	Cold
Reformer	Warm	Cold	Warm	Cold
Fuel Cell System Efficiency [%]	40.7	40.7	38.6	38.6
Reformer Efficiency [%]	78.2	75.4	78.5	75.8
Total Efficiency [%]	31.8	30.7	30.3	29.2
Fuel Economy [mpg]	26.9	26.0	25.6	24.8

(a) FUDS

	Run 1	Run 2	Run 3	Run 4
Fuel Cell Stack	Warm	Warm	Cold	Cold
Reformer	Warm	Cold	Warm	Cold
Fuel Cell System Efficiency [%]	44.3	44.2	42.4	42.4
Reformer Efficiency [%]	81.1	78.2	81.2	78.4
Total Efficiency [%]	35.9	34.6	34.5	33.2
Fuel Economy [mpg]	35.5	34.3	34.0	32.9

(b) FHDS

**Table 5.2: Fuel Cell Stack and Reformer Warm-Start/Cold-Start Analysis:
(a) FUDS and (b) FHDS**

The small increase in reformer efficiency from Run 2 to Run 4 is due to increased hydrogen flow required by the cold-start fuel cell stack compared to the warm-start fuel cell stack to meet the electric motor current demand. Greater hydrogen demand by the fuel cell stack causes higher reformer reactant flows and reaction rates that produce faster temperature rise in the reformer with accompanying lower degree of incomplete reaction.

The small increase in reformer efficiency from Run 1 to Run 3 is also due to increased hydrogen flow required by the cold-start fuel cell stack compared to the warm-start fuel cell stack to meet the electric motor current demand. Greater hydrogen demand by the fuel cell stack causes higher reformer reactant flows. During warm-start reformer conditions, higher reactant flows produce greater heat transfer rates associated with the reformer reaction. As a consequence, the average value of x in Eq. 5.1 is slightly lower resulting in higher hydrogen production per amount of methanol used.

5.6. Sensitivity Analysis

Using Eq. 4.1 sensitivity analyses were conducted for the methanol reforming fuel cell vehicle operating on the FUDS and FHDS cycles. For the base case simulations in this study the following operational and design parameters were used: nominal fuel cell stack operating temperature of 353K, anode pressure of 2 atm, fuel utilization of 0.8, molar air-fuel ratio of 2, compressor efficiency ranging between 49% and 71% dependent on air flow, reformate and air relative humidity of 100% at the fuel cell stack electrode inlets, expander efficiency ranging between 63% and 81% dependent on air flow, individual fuel cell active area of 400 cm^2 with 220 cells in the stack, ambient temperature of 293K, and vehicle mass of 1452 kg. Results for FUDS and FHDS analyses are provided in Tables 5.3 and 5.4 respectively.

136

Parameter	Base Case Value	% Change in Parameter [+/-]	% Change in Fuel Economy [+/-]	Fuel Economy Sensitivity
Fuel Economy [mpg]	24.8	- - -	- - -	- - -
Hydrogen Utilization	0.8	-10.0	-10.3	1.03
	0.8	+10.0	+10.4	1.04
% Reformer Reaction	90	-11.1	-11.4	1.03
	90	+5.6	+5.7	1.02
Nominal FC Temp [K]	353	-3.0	-2.8	0.93
	353	+3.0	0.0	0.00
Vehicle Mass [kg]	1452	+5.0	-3.6	-0.72
	1452	+10.0	-7.1	-0.71
Avg Compressor Efficiency [%]	54.7	-10.9	-2.6	0.24
	54.7	+4.7	+1.1	0.23
Molar Air Fuel Ratio	2	-25.0	+3.4	-0.14
	2	25.0	-3.1	-0.12
Avg Expander Efficiency [%]	74.3	-10.0	-0.6	0.06
	74.3	+5.0	+0.4	0.08

Table 5.3: Cold-Start FUDS Cycle Sensitivity Analysis for Methanol Reforming Fuel Cell Vehicle

Parameter	Base Case Value	% Change in Parameter [+/-]	% Change in Fuel Economy [+/-]	Fuel Economy Sensitivity
Fuel Economy [mpg]	35.5	- - -	- - -	- - -
Hydrogen Utilization	0.8	-10.0	-10.2	1.02
	0.8	+10.0	+10.2	1.02
% Reformer Reaction	90	-11.1	-11.4	1.02
	90	+5.6	+5.7	1.02
Nominal FC Temp [K]	353	-3.0	-3.2	1.07
	353	+3.0	+2.8	0.93
Vehicle Mass [kg]	1452	+5.0	-3.0	-0.60
	1452	+10.0	-5.9	-0.59
Avg Compressor Efficiency [%]	55.6	-9.6	-2.4	0.25
	55.6	+4.8	+1.0	0.21
Molar Air Fuel Ratio	2	-25.0	+2.8	-0.11
	2	25.0	-2.9	-0.12
Avg Expander Efficiency [%]	71.6	-9.9	-0.7	0.07
	71.6	+5.0	+0.3	0.06

Table 5.4: Warm-Start FHDS Cycle Sensitivity Analysis for Methanol Reforming
Fuel Cell Vehicle

138

For the cold-start FUDS simulations, fuel economy is most sensitive to hydrogen utilization. As shown in Table 5.3, a ten percent decrease in hydrogen utilization results in a 10.3% decrease in fuel economy, sensitivity of 1.03. Similarly a ten percent increase in hydrogen utilization results in a 10.4% increase in fuel economy, sensitivity of 1.04. Fuel economy is next most sensitive to the extent of complete reaction within the reformer. Decreasing the extent of reaction by 11.1% results in a corresponding decrease in fuel economy by 11.4%, which is sensitivity of 1.03. Increasing the extent of complete reaction by 5.6% resulted in a 5.7% increase in fuel economy, sensitivity of 1.02. Fuel economy is next sensitive to nominal fuel cell temperature but only if this temperature is reached during the simulation. Fuel economy showed a sensitivity of 0.93 when the nominal temperature was reduced by 3%, however, fuel economy showed no sensitivity when the nominal temperature was increased by 3% because the fuel cell stack never reached the nominal fuel cell temperature. Fuel economy is next sensitive to vehicle mass showing sensitivity of –0.72 with a 5% increase in vehicle mass. Fuel economy also shows relative sensitivity to reduced and increased average compressor efficiency (0.24 and 0.23 respectively).

For the warm-start FHDS simulations, fuel economy shows significant sensitivity to hydrogen utilization, extent of complete reaction in the reformer, and nominal fuel cell temperature. As shown in Table 5.4, a ten percent decrease in hydrogen utilization results in a 10.2% decrease in fuel economy, sensitivity of 1.02. Similarly a ten percent increase in hydrogen utilization results in a 10.2% increase in fuel economy, sensitivity of 1.02. These results mirror the cold-start FUDS simulation results. Fuel economy also shows strong sensitivity to extent of reforming reaction with sensitivity of 1.02. Since

139

mass represents a 5.6% increase in vehicle mass from the direct-hydrogen vehicle. From the sensitivity analysis results, the methanol reforming fuel cell vehicle FUDS fuel economy would be 1.0 mpg less while the FHDS fuel economy would be 1.2 mpg less than the respective fuel economy results reported in Table 5.1.

5.6.2. Conclusions

The following conclusions are drawn from study of these sensitivity analyses:

(1) Since reformer use precludes recycling of unreacted hydrogen in the reformate exiting the fuel cell stack anode, there is a loss of hydrogen exergy and thus fuel economy is very sensitive to hydrogen utilization. One opportunity for increased fuel economy may exist by burning the discarded hydrogen to provide heat input for the methanol reformer, thus driving the average value of x in Eq. 5.1 down. By operating the reformer in this way, more hydrogen is produced per amount of methanol used.

(2) Compared with the direct-hydrogen fuel cell vehicle sensitivity results, sensitivity results for the methanol reforming fuel cell vehicle indicate parameters affected by reformer use (hydrogen utilization and extent of reformer reaction) have greater impact on fuel economy compared with those of the fuel cell system.

(3) Development of improved catalysts to support chemical reactions is important for maintaining a high extent of reaction in the reformer.

(4) Attaining high fuel cell operating temperature contributes to increased fuel economy.

(5) Maintaining maximal hydrogen utilization, extent of reformer reaction, and fuel cell operating temperature, as well as limiting vehicle weight contribute most to fuel economy for both cold-start FUDS and warm-start FHDS for the methanol reforming fuel cell vehicle.

CHAPTER 6

FUEL CELL SYSTEM/BATTERY HYBRID SIMULATION

6.1. Introduction

The purpose of this chapter is to apply the direct-hydrogen PEM fuel cell system model in a fuel cell system/battery hybrid configuration for automotive applications. The vehicle performance simulator determines fuel economy and allows consideration of control strategies. The simulator is used to explore relevant regions of the fuel cell powered hybrid electric vehicle design space by conducting simulations using two simple supervisory-control strategies: *thermostatic* control and *proportional* control. During the simulations power provided by the battery and fuel cell system and operational limits on battery state of charge and fuel cell system current density are varied while maintaining minimum component *sizing* to meet vehicle performance criteria. Analysis of results from these simulations provides component power sizing and limits of operation suitable for development of a more advanced supervisory vehicle control strategy for a fuel cell vehicle.

6.2. Control Strategies

A schematic of the hybrid configuration considered in this chapter is shown in Fig. 6.1. The fuel cell system is coupled to the DC high voltage battery bus through a power converter. The battery bus is coupled to the electric motor through another power

143
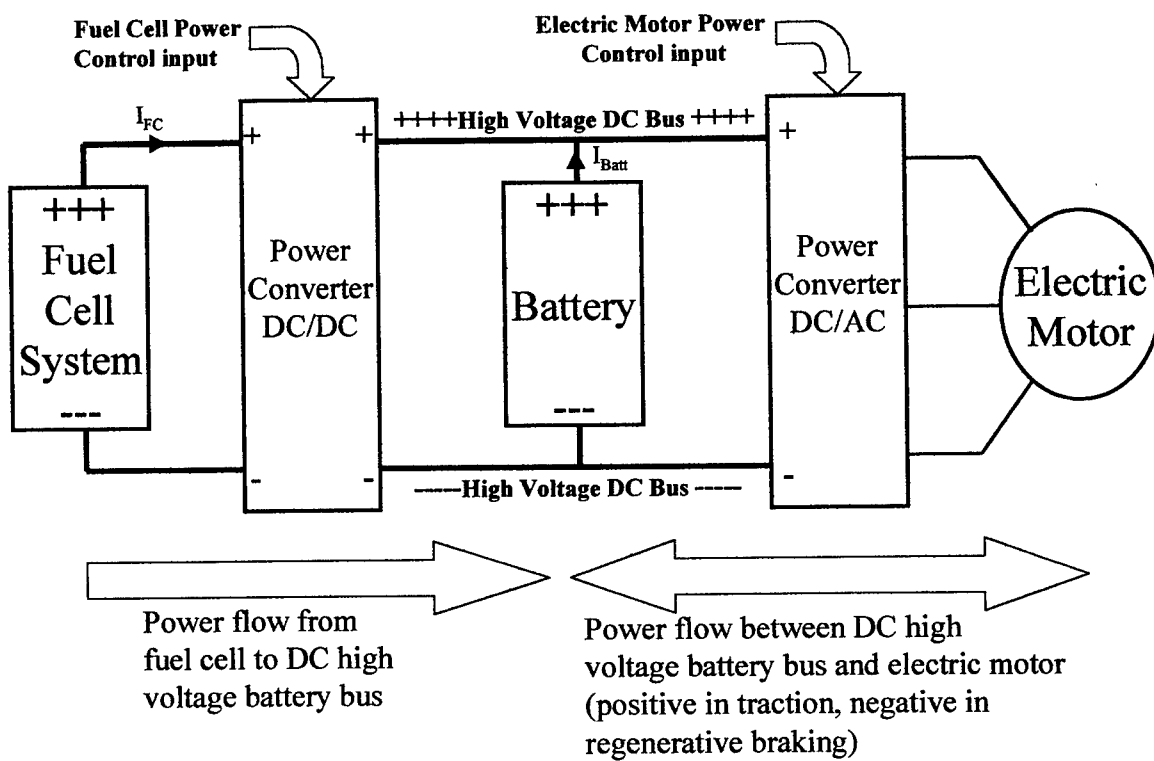
Figure 6.1: Battery/Fuel Cell System Hybrid Configuration Schematic

Thermostatic Control

Fuel Cell System
Current Density
[A/cm²]

Proportional Control

Fuel Cell System
Current Density
[A/cm²]
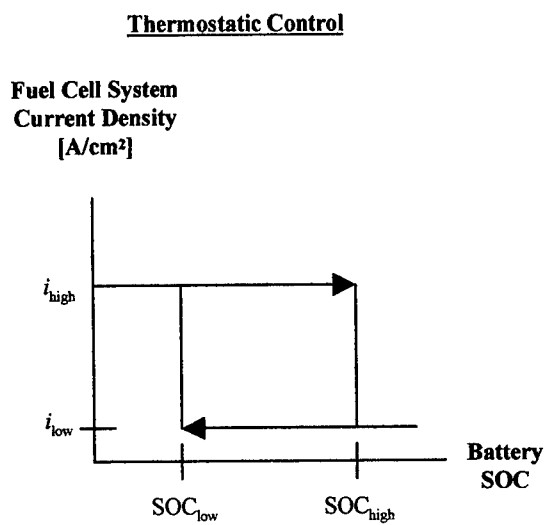
(a)
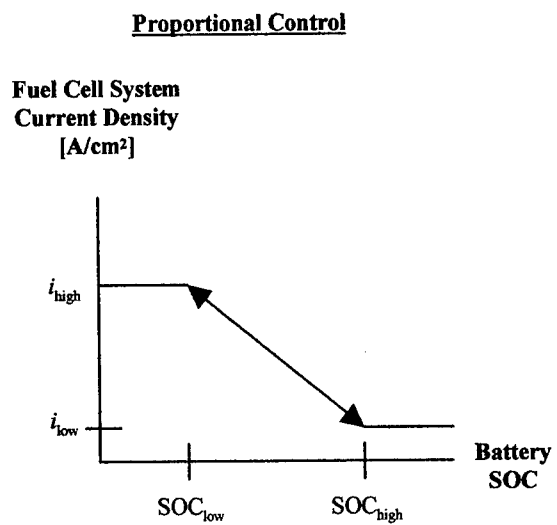
(b)

Figure 6.2: Thermostatic and Proportional Control Strategies:
(a) Thermostatic Control, (b) Proportional Control

146

system operates at its low current density setting when the battery is at or above its high state of charge threshold. When the battery state of charge is between its high and low state of charge limits, fuel cell system current density is related linearly to the state of charge as shown in Fig. 6.2(b). The methodology used for component sizing is described next.

6.3. Component Sizing and Specifications

For a minimum required power input to the electric motor, numerous simulations using both control strategies are conducted to examine the effects of varying five operational parameters: 1) fuel cell power, 2) battery power, 3) difference between battery high and low state of charge thresholds, 4) fuel cell system low current density setting, and 5) fuel cell system high current density setting. To conduct the simulations, stipulation of type of vehicle to be represented and electric motor, battery, and fuel cell system sizing is required.

For these simulations a 3200 lb, SUV-type vehicle is represented. Four minimum performance criteria are specified: 1) ability to *sustain* 85 mph cruise speed, 2) ability to *sustain* pulling a 2000 lb trailer on a 6% grade at 45 mph, 3) ability to accelerate from 0 to 60 mph in less than 9.5 seconds, and 4) ability to *attain* a top speed of at least 100 mph. Table 6.1 lists specifications used for the two cases considered: vehicle alone and vehicle with trailer.

6.3.1. Electric Motor Sizing

Sizing of the electric motor, battery, and fuel cell system is based on component power output capability. The first component sized is the electric motor. The electric motor is modeled as a simplified, traction application AC induction machine with the

147

Specification	Vehicle	Vehicle with Trailer
Mass [kg]	1452	2360
Frontal area [m^2]	2.7	4
Coefficient of drag	0.4	0.75
Coefficient of rolling resistance	0.015	0.015
Grade [%]	0	6

Table 6.1: Vehicle Specifications

following characteristics: 1) maximum speed of 8000 rpm, 2) a 2.5 *flexibility ratio* (ratio of maximum speed at which nominal power is available to minimum speed at which nominal power is available), 3) constant torque operation speed range from 0 to 3200 rpm, 4) constant nominal power operation speed range from 3200 to 8000 rpm, and 5) ability to produce twice the nominal power for short periods. Electric motor efficiency is estimated in the vehicle simulator by a simplified linearization approach described by Rizzoni et al. (2000). The sizing parameter for the electric motor is the nominal power. The electric motor must provide power necessary to meet all minimum performance criteria. Four tests are required for appropriate electric motor sizing: 1) cruise speed at 85 mph to determine continuous power requirement, 2) cruise speed at 45 mph while pulling trailer on 6% grade to determine continuous power requirement, 3) ten-second acceleration to determine time from 0 to 60 mph, and 4) 300-second acceleration to determine top speed.

At vehicle constant speed of 85 mph the required electric motor power output is 48.8 kW while power input is 59.0 kW. These values were determined by applying the following methodology to the vehicle simulator. Using the specifications for the vehicle in Table 6.1, impose a constant speed demand of 85 mph in the driver block by disconnecting the cycle velocity input and inserting a constant input of 38 m/s (85 mph). Tune the proportional, integral, and derivative (PID) control in the driver mask for these vehicle specifications. Values used were P=0.2*2, I=0.2*0.1, and D=0. Using a 0.5 time step and setting the drive cycle to Federal Highway Driving Schedule (FHDS), run the simulation for approximately 100 seconds. Plot speed versus time to ensure the vehicle maintains a constant 85 mph speed during the test. For a time at which the speed is 85

mph, determine the power output from the electric motor by multiplying the electric motor output torque (T) by the electric motor output rotational velocity (ω), which gave 48.8 kW. Determine the power input to the electric motor at 85 mph by multiplying the electric motor input voltage (V) by the electric motor input current (I) at the selected time, which gave 59.0 kW.

At vehicle constant speed of 45 mph while pulling a trailer on a 6% grade, the required electric motor power output is 53.3 kW while power input is 70.25 kW. These values were determined by applying the following methodology to the vehicle simulator. Using specifications for the vehicle with trailer in Table 6.1, impose a constant speed demand of 45 mph in the driver block by disconnecting the cycle velocity input and inserting a constant value of 20.1 m/s (45 mph). Tune the PID in the driver mask for the new vehicle specifications. Values used were P=0.2*1, I=0.2*0.1, and D=0. Using a 0.5 time step and setting the drive cycle to FHDS, run the simulation for approximately 100 seconds. Plot speed versus time to ensure the vehicle maintains a constant 45 mph speed during the test. Selecting a time at which the speed is 45 mph, determine the power output from the electric motor by multiplying the electric motor output torque (T) by the electric motor output rotational velocity (ω), which gave 53.3 kW. Determine the power input to the electric motor at 45 mph by multiplying the electric motor input voltage (V) by the electric motor input current (I), which gave 70.25 kW. On completion of the first two tests, reconnect the cycle velocity input in the driver block.

Based on the results of the first two tests, the electric motor is sized to meet the more stringent continuous output power requirement: 53.3 kW while pulling trailer on 6% grade at 45 mph. Electric motor continuous power rating is set at 54 kW with a

150

corresponding continuous torque rating of 162 N-m based on the 2.5 flexibility ratio. For this electric motor size the vehicle reaches 60 mph in 8.7 seconds and attains top speed of 112.2 mph indicating the electric motor is adequately sized to meet all four minimum performance criteria. These values were determined by applying the following methodology to the vehicle simulator. Using the specifications for the vehicle in Table 6.1 and resetting the control PID values to the values used in Test 1, select the acceleration test in the driver mask. Using a 0.05 time step and setting the acceleration test time to 10 seconds, run the simulation. Plot speed versus time to determine the time required for the vehicle to reach 60 mph, which was 8.7 seconds. Using a 0.5 time step and setting the acceleration test time to 300 seconds, rerun the simulation. Plot speed versus time to determine the top speed reached by the vehicle, which was 112.2 mph.

6.3.2. Battery and Fuel Cell System Sizing

The battery and the fuel cell stack are then sized. Due to battery energy storage limitation, the fuel cell system must be able to provide all power for sustained cruise speed. The fuel cell system and battery together provide power required for acceleration.

The battery is modeled as a nickel metal hydride battery with nominal voltage of 300 V and specific power of 500 W/kg and specific energy of 50 Wh/kg, representative of nickel metal hydride battery pack short-term target upper bound values. The sizing parameter is the maximum power available from the battery. In VP-SIM changing the battery maximum current setting varies battery power.

Maximum power required by the electric motor during acceleration from 0 to 60 mph in less than 9.5 seconds is 126.5 kW. This value was determined by applying the following methodology to the vehicle simulator. For convenience use battery power

151

alone to determine required power input to the electric motor to achieve acceleration from 0 to 60 mph in less than 9.5 seconds. Reduce the fuel cell stack size to a single cell (N=1). Vary the battery size and repeat the ten-second acceleration test until the time to accelerate from 0 to 60 mph approaches 9.5 seconds. When the battery maximum current was 472 amperes, the time to reach 60 mph was 9.49 seconds. The corresponding maximum power required by the electric motor was 126.5 kW while the maximum current required was 472 A. Run the 300-second acceleration test to check the top speed achieved. Top speed reached was 111 mph, well above the 100 mph top speed requirement. Consequently, the battery and fuel cell system together must provide a minimum of 126.5 kW of power.

Since the fuel cell system must provide the power for sustained cruising, the minimum power required from the fuel cell system is 70.25 kW (the more stringent electric motor continuous input power requirement from tests 1 and 2). The fuel cell design and operating parameters used for this study are representative of those used in automotive applications and are shown in Table 6.2. The fuel cell sizing parameter is the number of cells. For the specified fuel cell design and operating parameters fuel cell stack sizing of 366 cells provides a maximum fuel cell system power of 70.3 kW at nominal fuel cell operating temperature of 353K. Consequently, the minimum fuel cell stack size must be 366 cells. Fuel cell system power sizing relative to battery power sizing is considered as part of the analysis. This study looks at three other battery/fuel cell system size combinations, which produce total power of at least 126.5 kW. The four specified battery/fuel cell system combinations used are listed in Table 6.3. Figures 6.3 and 6.4 illustrate representative fuel cell system model power and exergetic efficiency

152

Input Parameter	Value
Active Area [cm^2]	400
Nominal operating temperature [K]	353
Air and hydrogen inlet temperature [K]	333
Air and hydrogen inlet relative humidity [%]	100
Anode pressure [atm]	2
Fuel utilization	0.8
Ambient temperature [K]	293
Stack Current Density for Maximum Power at Nominal Operating Temperature [A/cm^2]	0.98
System Current Density for Maximum Power at Nominal Operating Temperature [A/cm^2]	0.84

Table 6.2: Fuel Cell Stack Input Parameters

Case No.	Battery		Fuel Cell System		Maximum Total Power [kW]	0 to 60 mph Acceleration Time [s]
	Maximum Current [A]	Maximum Battery Power [kW]	Number of Cells	Maximum FC System Power [kW]		
1	190	56.5	366	70.3	127.3	9.49
2	173	51.9	390	74.9	126.8	9.48
3	156	46.8	415	79.7	126.5	9.46
4	140	42.0	440	84.5	126.5	9.42

Table 6.3: Battery Size/Fuel Cell System Size Combinations

440 Cells, 400 cm2 Active Area
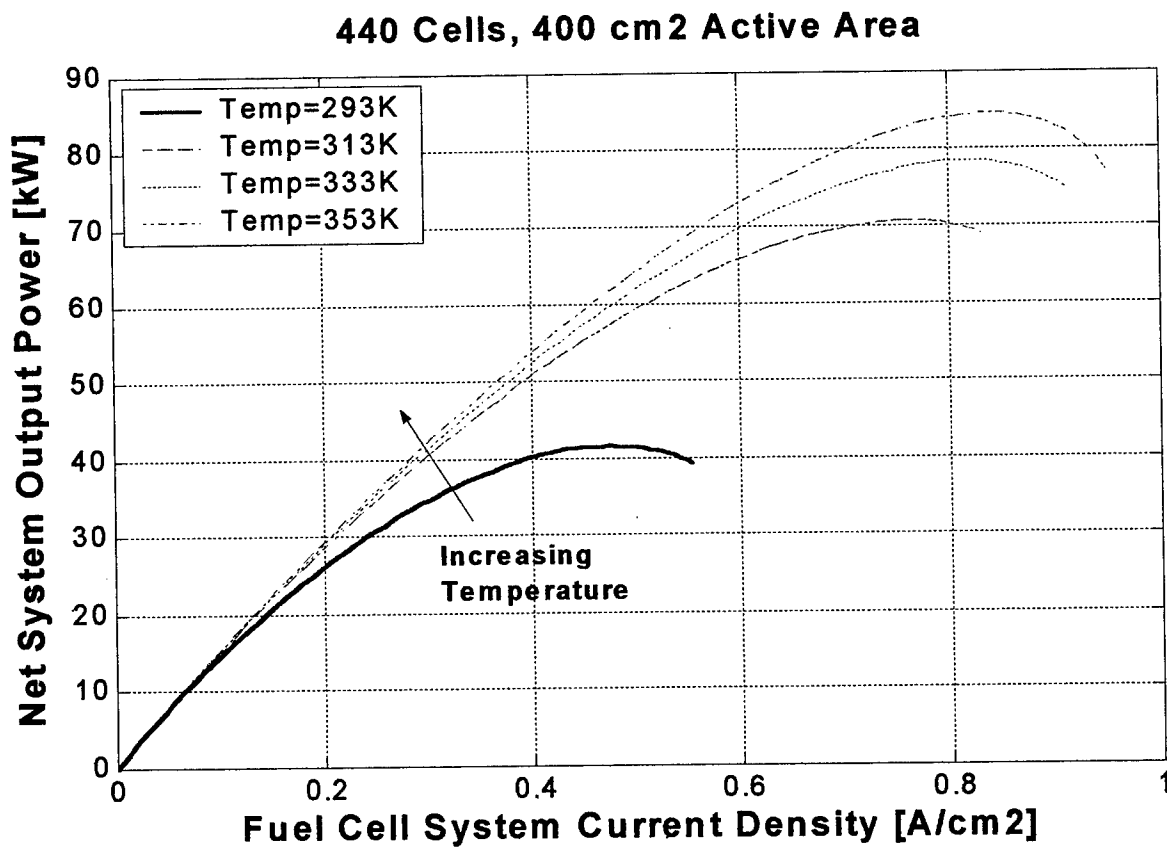
Figure 6.3: Effects of Fuel Cell Operating Temperature and System Current
Density on Fuel Cell System Power

440 Cells, 400 cm2 Active Area
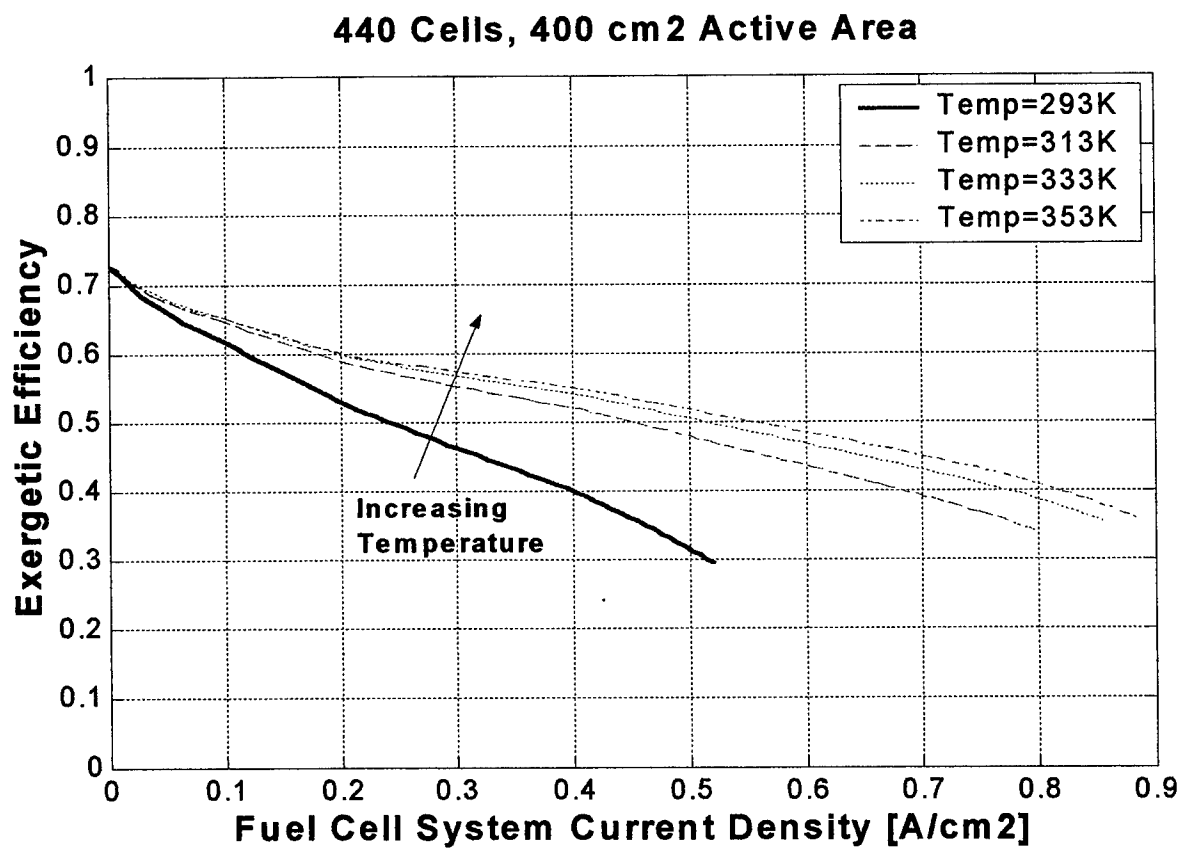
Figure 6.4: Effects of Fuel Cell Operating Temperature and System Current
Density on Fuel Cell System Exergetic Efficiency

characteristics respectively for a fuel cell stack containing 440 cells with individual active areas of 400 cm^2 corresponding to Case 4 in Table 6.3. Both of these figures clearly show the strong effect of operating temperature on power and efficiency as mentioned previously in Sec. 3.1.2.

6.4. Simulation Thresholds and Settings

Preliminary Federal Urban Driving Schedule (FUDS) and Federal Highway Driving Schedule (FHDS) simulations were conducted using the four battery/fuel cell system combinations (Table 6.3) to determine appropriate values for battery state of charge high and low thresholds and the fuel cell system high and low current density settings. Note that the power required during FUDS and FHDS is not nearly as high as the power required to meet the minimum performance criteria. Consequently, during these cycles maximum power available from the battery/fuel cell system is not required.

For the FUDS simulations, the fuel cell starts at ambient temperature to represent cold start. For the FHDS simulations, the fuel cell starts at nominal fuel cell operating temperature to represent a fully warmed vehicle. Initial battery state of charge is the average of the high and low battery state of charge thresholds. Based on preliminary simulation runs using various battery state-of-charge thresholds and fuel cell system current density settings, the relevant range of values used for the study was established.

Table 6.4(a) provides a summary of the battery state of charge limits used for the control analyses. Minimum battery low state of charge threshold is selected as 50% to ensure reserve power is available. Battery high state of charge is set at 80% to allow capacity for regenerative braking. Low battery state of charge limit is considered between 50% and 70% equating to a state of charge difference ranging from 30%

157

Battery Low State of Charge Threshold [%]	Battery High State of Charge Threshold [%]	Battery Initial State of Charge [%] $\left(\dfrac{\text{SOC High} + \text{SOC Low}}{2}\right)$
50	80	65
60	80	70
70	80	75

(a)

Fuel Cell System Low Current Density Settings Considered [A/cm^2]	Fuel Cell System High Current Density Settings Considered [A/cm^2]
	0.1
0.00	0.2
0.01	0.3
0.02	0.4
0.03	0.5
	0.6

(b)

Table 6.4: Battery State of Charge Thresholds and Fuel Cell System Current Density Settings:
(a) Battery State of Charge Thresholds and
(b) Fuel Cell System Current Density Settings

to 10%. Preliminary runs showed that battery charge and discharge occur more often as the difference between the limits of battery high and low states of charge is reduced.

Table 6.4(b) summarizes the fuel cell system settings considered for the study. The preliminary runs indicated fuel cell system low current density setting should not exceed 0.03 A/cm² (5.3% of maximum power at nominal temperature) to prevent overcharge of the battery. Since maximum power available from the battery/fuel cell system is not required during FUDS and FHDS, fuel cell system high current density setting is limited to 0.6 A/cm², which equates to 86.5% of maximum power at nominal temperature. Since fuel cell system efficiency increases as current density decreases, lowering the high current density setting results in improved efficiency over the cycles (see Fig. 6.4).

For each control strategy, a total of 288 possible design candidates with FUDS and FHDS performance data are generated. For each design candidate, fuel usage is state of charge-corrected based on the electricity used (reflected by the difference between battery final state of charge and initial state of charge), using the corresponding average fuel cell system efficiency from that simulation to convert net electricity usage to equivalent fuel consumption. Furthermore, the corrected fuel (hydrogen) usage is then converted to equivalent gasoline usage based on the relative lower heating value of hydrogen and gasoline. All fuel economy figures listed in this chapter are converted in the same fashion. The formula to determine fuel economy (mpg) is shown in Eq. 6.1:

$$mpg = \frac{\left(LHV_{gas}\left[\frac{MJ}{kg}\right]\right)\left(\rho_{gas}\left[\frac{kg}{m^3}\right]\right)(x[m])\left(1000\frac{kJ}{MJ}\right)}{\left[\left(\frac{elec\_used[kJ]}{(\varepsilon_{sys})(\eta_{batt\_chg})}\right) + \left(m_{H_2}[kg] \times LHV_{H2}\left[\frac{kJ}{kg}\right]\right)\right]\left(264.2\frac{gal}{m^3}\right)\left(1609.3\frac{m}{mile}\right)} \qquad (6.1)$$

where:

LHV_{gas} = gasoline lower heating value [MJ/kg]; (LHV_{gas} = 43.5 MJ/kg)

ρ_{gas} = gasoline density [kg/m³] (ρ_{gas} = 755 kg/m³)

x = cycle distance [m]; (x_{FUDS} = 11,989 m and x_{FHDS} = 16,495 m)

$elec\_used$ = battery electricity used during cycle [kJ]; (positive or negative value)

ε_{sys} = average fuel cell system efficiency for cycle

η_{batt_chg} = battery charging efficiency (0.85)

m_{H2} = mass of hydrogen used during cycle [kg]

LHV_{H2} = hydrogen lower heating value [kJ/kg]; (LHV_{H2} = 119,950 kJ/kg)

6.5. Evaluation Criteria

Analysis of simulation results is based on four criteria of evaluation: 1) FUDS fuel economy, 2) FHDS fuel economy, 3) FUDS fuel cell system efficiency, and 4) FHDS fuel cell system efficiency. Two techniques are used to analyze the simulation results: *dominance filtering* and *principal component analysis*.

Josephson et al. (1998) describe dominance filtering. A design candidate dominates another candidate if it is superior or equal to the other candidate in every criterion of evaluation and absolutely superior for at least one criterion. Dominated candidates are eliminated. Surviving candidates are *Pareto optimal*: improvement on any criterion will reduce value on another. This approach is ideally suited for multi-criteria optimization, as it does not require the *a priori* weighting of the various criteria. Trade-off analysis can be performed *a posteriori* on the remaining survivor candidates.

Principal component analysis is a multivariate statistics technique that considers a group of variables together rather than each variable individually. Principal component

analysis transforms the four criteria of evaluation into a new set of four variables or principal components. The principal components are linear combinations of the original criteria of evaluation and form a new orthogonal basis for the data space. Projection of the original criteria of evaluation onto each principal component defines data in the new coordinate system. The first principal component is chosen such that the variance of the newly defined data is maximum among all possible choices for the first axis. Subsequent principal components are chosen in a similar manner. Total variance of the original data can be described by the variability associated with each principal component. In other words, principal component analysis optimally projects the available data on a new coordinate system.

6.6. Thermostatic Control Simulation Results and Analysis

Based on results from the simulation runs, a graphical overview of the 288 design candidates is shown in Fig. 6.5 using fuel economy and fuel cell system efficiency for FUDS and FHDS as axes. Figure 6.5(a) indicates a high correlation between FUDS and FHDS fuel economy. Figures 6.5(b) and 6.5(c) indicate that the correlations between FHDS fuel cell system efficiency and FHDS fuel economy and between FUDS fuel cell system efficiency and FUDS fuel economy are strongly positive. Figures 6.5(d) indicates a high correlation between FUDS and FHDS fuel cell system efficiency.

Two cases of non-charge sustaining design candidates are eliminated from further consideration: 1) candidates that have a final battery state of charge less than the battery low state of charge threshold and 2) candidates that do not begin thermostatic cycling during either FUDS or FHDS. Figure 6.6 illustrates why candidates that do not initiate

161
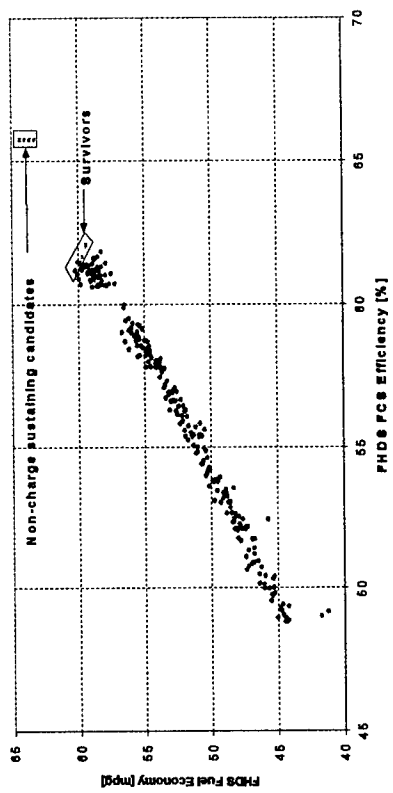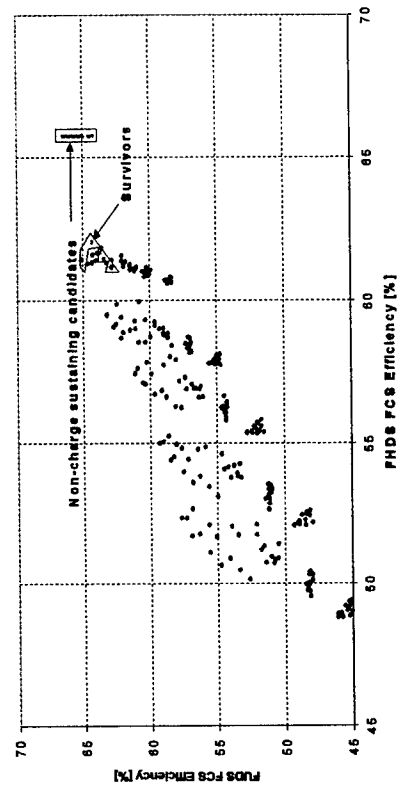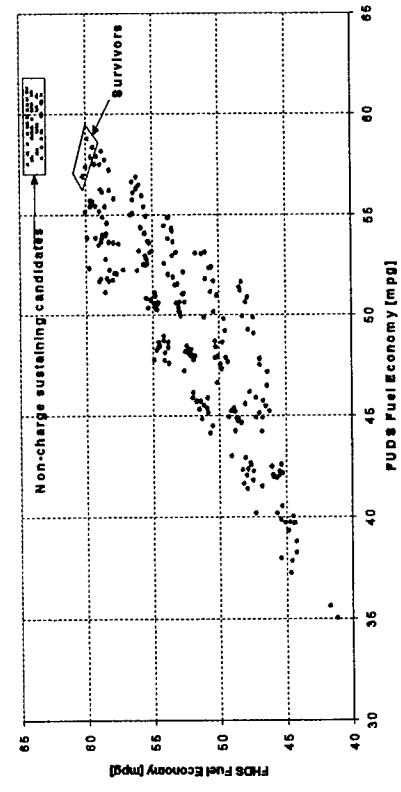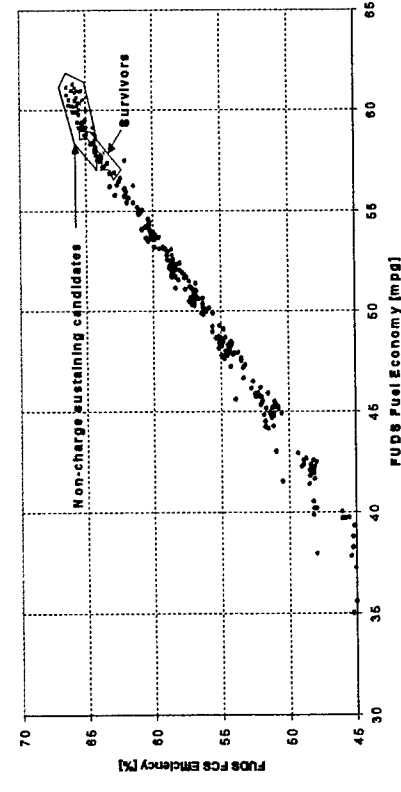
Figure 6.5: Thermostatic Control Design Candidates:
(a) FHDS Fuel Economy versus FUDS Fuel Economy, (b) FHDS Fuel Economy versus FHDS FCS Efficiency,
(c) FUDS FCS Efficiency versus FUDS Fuel Economy, (d) FUDS FCS Efficiency versus FHDS FCS Efficiency

162
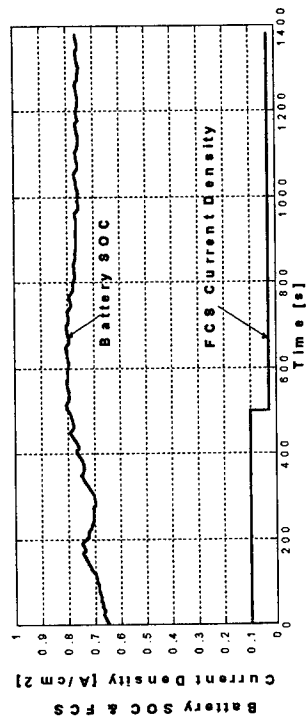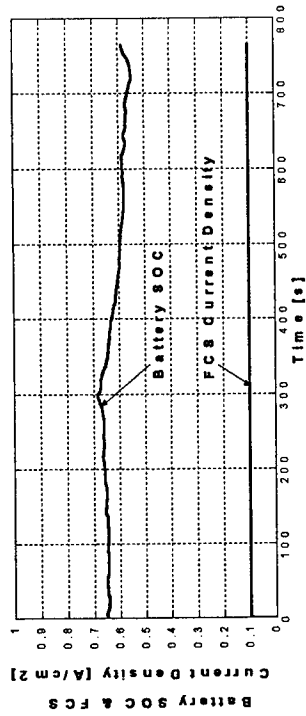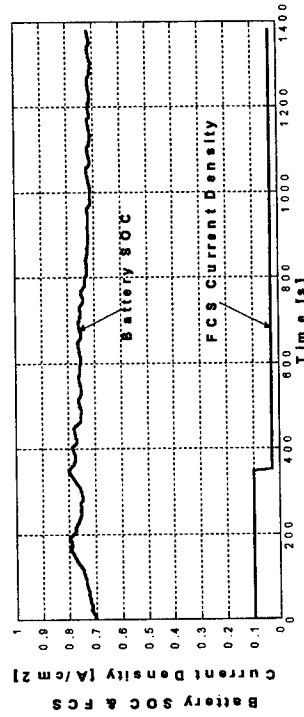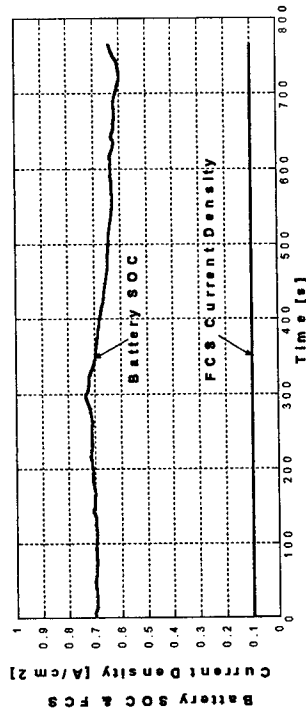
Figure 6.6: Case 2 Non-charge Sustaining Thermostatic Control Run Examples: (a) Run 220 FUDS, (b) Run 220 FHDS, (c) Run 244 FUDS, (d) Run 244 FHDS

thermostatic cycling are not charge sustaining. For thermostatic control Runs 220 and 244, thermostatic cycling begins during FUDS but does not begin during FHDS. Examination of Figs. 6.6(b) and 6.6(d) indicates these candidates are not charge sustaining during FHDS. The battery never fully charges from its initial state of charge to the high state of charge limit, 0.8. The battery state of charge slowly decreases during the cycle while the fuel cell system operates at its high current density setting, 0.1 A/cm^2. Results from this analysis suggest that candidates that do not begin thermostatic cycling during either FUDS or FHDS cannot meet the average vehicle power requirement and should be eliminated as non-charge sustaining.

From the original 288 candidates, 48 design candidates are eliminated as non-charge sustaining (24 for the first case and 24 for the second case) leaving 240 candidates. The 48 design candidates eliminated as non-charge sustaining comprise all of the candidates using a fuel cell system high current density of 0.1 A/cm^2. These 48 candidates are identified in Fig. 6.5.

Dominance filtering is applied to the 240 charge-sustaining design candidates using fuel economy and fuel cell system efficiency as criteria of evaluation. Two separate analyses are conducted using the following sets of criteria for dominance filtering: 1) highest FUDS and FHDS fuel economy and 2) highest FUDS and FHDS fuel economy and fuel cell system efficiency.

Dominance filtering using the first set of criteria produces three surviving design candidates while using the second set of criteria produces five survivors. The three survivors using the first set of criteria are among the five survivors using the second set

of criteria. The surviving candidates are identified in Fig. 6.5. Performance data for all five survivors are given in Table 6.5. For the FUDS cycle shown in Fig. 6.7(a), battery state of charge, fuel cell system current density, and fuel cell operating temperature levels during the cycle are indicated for survivor Run 56 in Figs. 6.7(b) and 6.7(c) and for survivor Run 248 in Figs 6.7(d) and 6.7(e). The corresponding FHDS information for these two runs is shown in Fig. 6.8.

Since all candidates using a fuel cell system high current density setting of 0.1 A/cm^2 have been eliminated as non-charge sustaining, the minimum value for fuel cell system high current density, which is charge sustaining, is 0.2 A/cm^2. All surviving candidates have a fuel cell system high current density setting of 0.2 A/cm^2. These results indicate that consistently operating the fuel cell at lower current density where fuel cell system power output is close to the average power demand is more efficient than operating the fuel cell with bursts of high current density. Figure 6.4 illustrates why fuel cell systems operating with a small high current density limit are more efficient. A fuel cell system functioning with a high current density limit of 0.2 A/cm^2 at a relatively cool 313K operating temperature has an efficiency of 58% while a fuel cell functioning with a high current density limit of 0.6 A/cm^2 at a fully warm 353K operating temperature has an efficiency of 48%.

Principal component analysis applied to the 240 charge-sustaining candidates reveals the percentage of total variance of the original criteria of evaluation explained by each principal component: first principal component explains 93.5%, second principal component explains 6.1%, and third and fourth principal components each explain less than 0.5%. This result indicates that the first principal component alone provides most of

Run No.	Battery High SOC [%]	Battery Low SOC [%]	Fuel Cell Sys High Current Density [A/cm2]	Fuel Cell Sys Low Current Density [A/cm2]	Battery Maximum Current [A]	No. of Cells in Fuel Cell Stack	Battery Initial State of Charge [%]	FUDS Battery Final State of Charge [%]	FUDS Fuel Economy [mpg]	FUDS Fuel Cell Sys Efficiency [%]	FHDS Battery Final State of Charge [%]	FHDS Fuel Economy [mpg]	FHDS Fuel Cell Sys Efficiency [%]
56*	80	70	0.2	0.03	190	366	75	74.0	56.9	62.9	80.7	60.3	61.2
128*	80	70	0.2	0.03	173	390	75	72.5	57.4	63.4	76.8	60.0	61.5
200	80	70	0.2	0.03	156	415	75	73.9	57.9	63.7	78.4	59.7	61.7
248*	80	60	0.2	0.03	140	440	70	62.0	58.8	65.1	81.9	59.9	61.5
272	80	70	0.2	0.03	140	440	75	72.3	58.4	64.3	72.9	59.4	62.1

* Denotes dominance filter survivors using criteria of highest FUDS and FHDS fuel economy.

Table 6.5: Thermostatic Control Dominance Filter Survivors Using Criteria of Highest FUDS and FHDS Fuel Economy and Fuel Cell System Efficiency
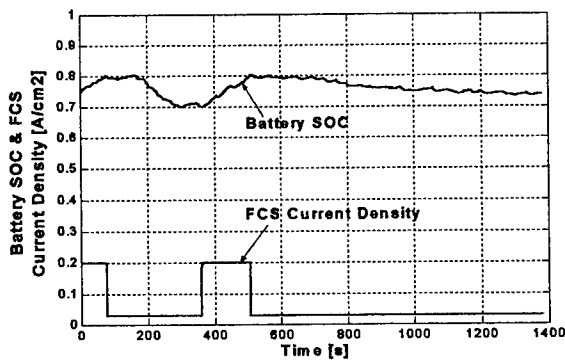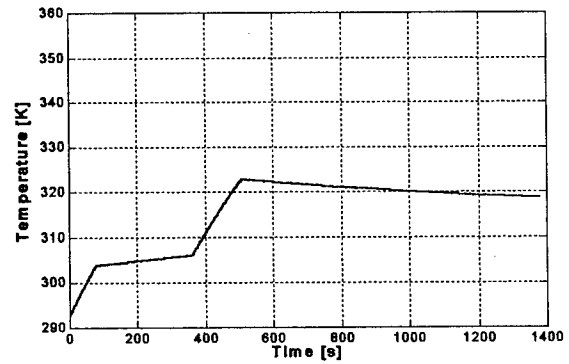
Figure 6.7: **Thermostatic Control Survivor Performance for FUDS: (a) FUDS cycle, (b) Run 56 Battery SOC & FCS Current Density, (c) Run 56 Temperature, (d) Run 248 Battery SOC & FCS Current Density, (e) Run 248 Temperature**

167

(a)
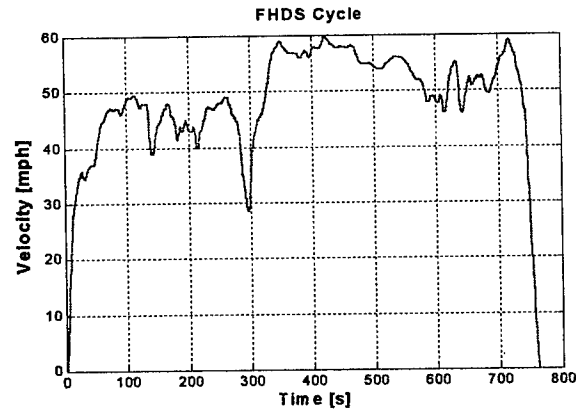
Thermostatic Control Run 56 FHDS
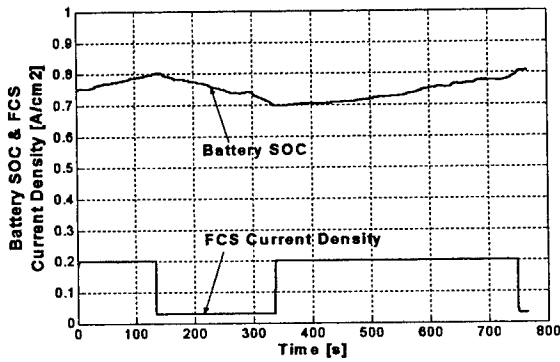
(b)

(c)
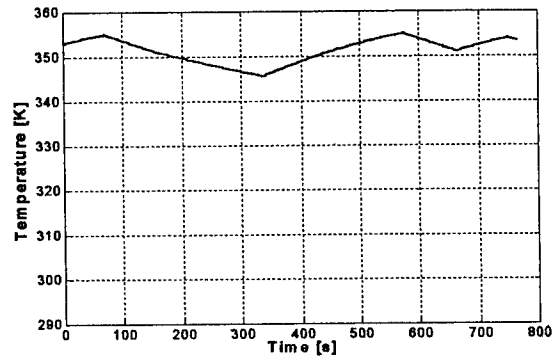
Thermostatic Control Run 248 FHDS
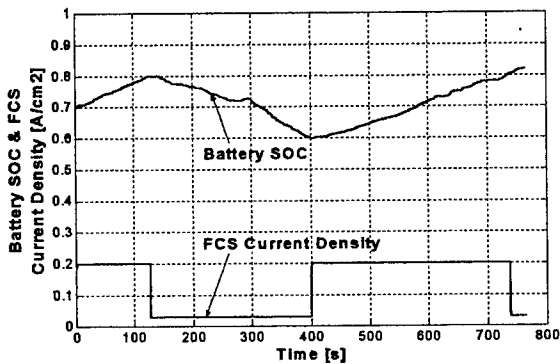
(d)
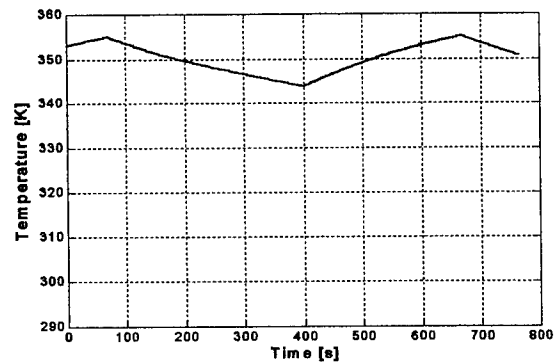
(e)

Figure 6.8: Thermostatic Control Survivor Performance for FHDS: (a) FHDS cycle, (b) Run 56 Battery SOC & FCS Current Density, (c) Run 56 Temperature, (d) Run 248 Battery SOC & FCS Current Density, (e) Run 248 Temperature

168

the information given by the four original criteria of evaluation. Principal component analysis reinforces the conclusion of strong correlation among the criteria of evaluation as noted in the analysis of Fig. 6.5.

To assess regenerative braking effects, the 288 simulations were rerun without regenerative braking. Forty-eight non-charge sustaining candidates were eliminated. Dominance filtering produced five survivors based on the first set of criteria and eight survivors based on the second set of criteria. Considering the first set of criteria survivors, the average fuel economies were 51.6 mpg for FUDS and 58.2 mpg for FHDS compared with 57.7 mpg for FUDS and 60.1 mpg for FHDS for the comparable three survivors using regenerative braking. Results indicate that regenerative braking is advantageous over no regenerative braking especially for the FUDS cycle, which shows an 11.8% increase in fuel economy.

6.7. Proportional Control Simulation Results and Analysis

A graphical overview of the 288 proportional control design candidates is shown in Fig. 6.9 using fuel economy and fuel cell system efficiency for FUDS and FHDS as axes. As observed for the thermostatic control candidates, the proportional control candidates also show strong, positive correlation between FUDS and FHDS fuel economy, between FHDS fuel cell system efficiency and FHDS fuel economy, between FUDS fuel cell system efficiency and FUDS fuel economy, and between FUDS and FHDS fuel cell system efficiency.
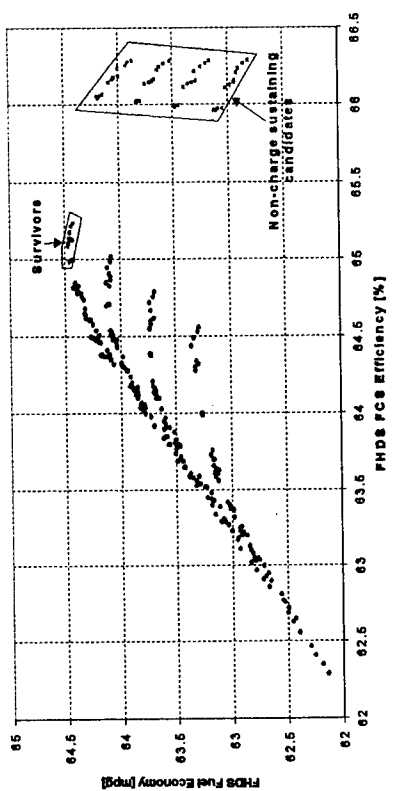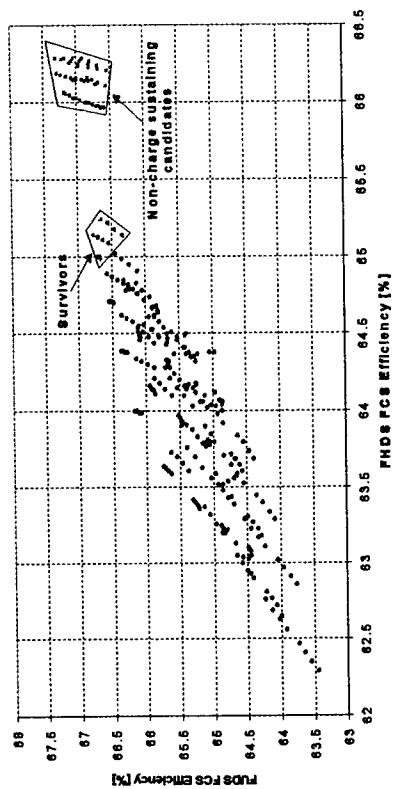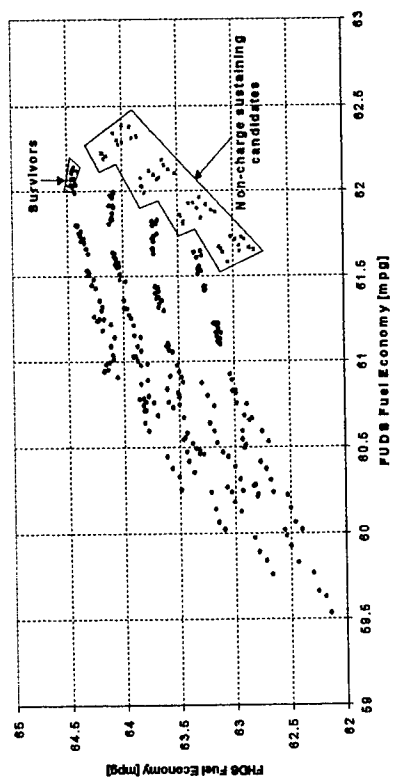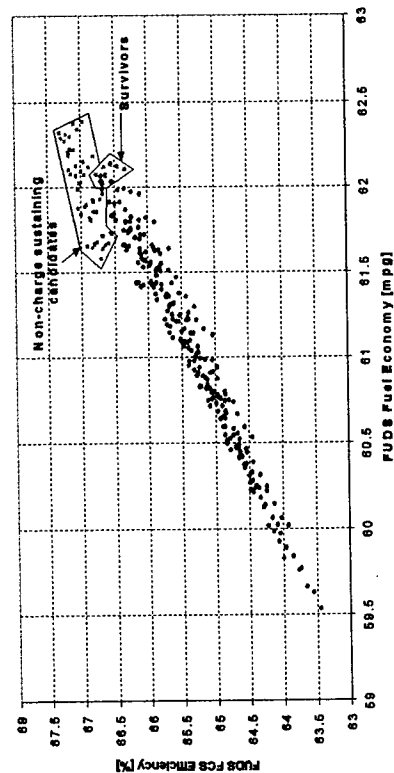
Figure 6.9: Proportional Control Design Candidates:
(a) FHDS Fuel Economy versus FUDS Fuel Economy, (b) FHDS Fuel Economy versus FHDS FCS Efficiency,
(c) FUDS FCS Efficiency versus FUDS Fuel Economy, (d) FUDS FCS Efficiency versus FHDS FCS Efficiency

Forty-eight design candidates are eliminated as non-charge sustaining leaving 240 design candidates. The non-charge sustaining candidates eliminated are indicated in Fig. 6.9. These eliminated candidates comprise all candidates with a high current density limit of 0.1 A/cm^2.

Dominance filtering is applied to the 240 design candidates using the same sets of criteria previously used for thermostatic control analysis: 1) highest FUDS and FHDS fuel economy and 2) highest FUDS and FHDS fuel economy and fuel cell system efficiency. Dominance filtering using the first set of criteria produces five surviving design candidates while using the second set of criteria produces eight survivors. The five survivors using the first set of criteria are among the eight survivors using the second set of criteria. All eight surviving candidates use the largest size fuel cell stack considered. To produce a given power, larger fuel cell stacks require less power per cell resulting in operation at a lower current density where the efficiency is higher. The surviving candidates are identified in Fig. 6.9. Performance data for all eight survivors are given in Table 6.6. All candidates are nominally equal based on fuel economy. For two of the survivors (Runs 222 and 248), battery state of charge, fuel cell system current density, and fuel cell operating temperature levels during FUDS and FHDS are shown in Figs. 6.10 and 6.11 respectively.

Principal component analysis applied to the 240 charge-sustaining candidates produces results similar to those of thermostatic control. Percentage of total variance of the original criteria of evaluation explained by each principal component is as follows: first principal component explains 91.6%, second principal component explains 7.5%, third principal component explains 0.6%, and fourth principal components explains 0.3%.

171

Run No.	Battery High SOC [%]	Battery Low SOC [%]	Fuel Cell Sys High Current Density [A/cm2]	Fuel Cell Sys Low Current Density [A/cm2]	Battery Maximum Current [A]	No. of Cells in Fuel Cell Stack	Battery Initial State of Charge [%]	FUDS Battery Final State of Charge [%]	FUDS Fuel Economy [mpg]	FUDS Fuel Cell Sys Efficiency [%]	FHDS Battery Final State of Charge [%]	FHDS Fuel Economy [mpg]	FHDS Fuel Cell Sys Efficiency [%]
221	80	50	0.2	0.00	140	440	65	75.8	62.1	66.7	65.4	64.4	65.2
222*	80	50	0.2	0.01	140	440	65	77.1	62.1	66.6	66.0	64.4	65.2
223*	80	50	0.2	0.02	140	440	65	78.6	62.1	66.5	66.7	64.5	65.2
224*	80	50	0.2	0.03	140	440	65	80.2	62.1	66.3	67.5	64.5	65.1
245	80	60	0.2	0.00	140	440	70	77.4	62.1	66.8	71.3	64.4	65.1
247*	80	60	0.2	0.02	140	440	70	79.3	62.1	66.6	72.2	64.5	65.1
248*	80	60	0.2	0.03	140	440	70	80.5	62.0	66.6	72.7	64.5	65.1
272	80	70	0.2	0.03	140	440	75	80.8	62.0	66.7	77.8	64.5	65.0

* Denotes dominance filter survivors using criteria of highest FUDS and FHDS fuel economy.

Table 6.6: Proportional Control Dominance Filter Survivors Using Criteria of Highest FUDS and FHDS Fuel Economy and Fuel Cell System Efficiency
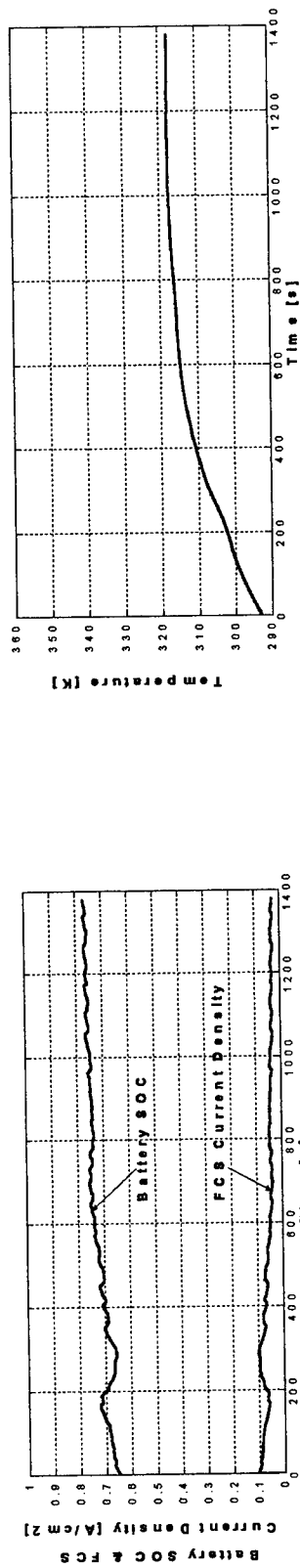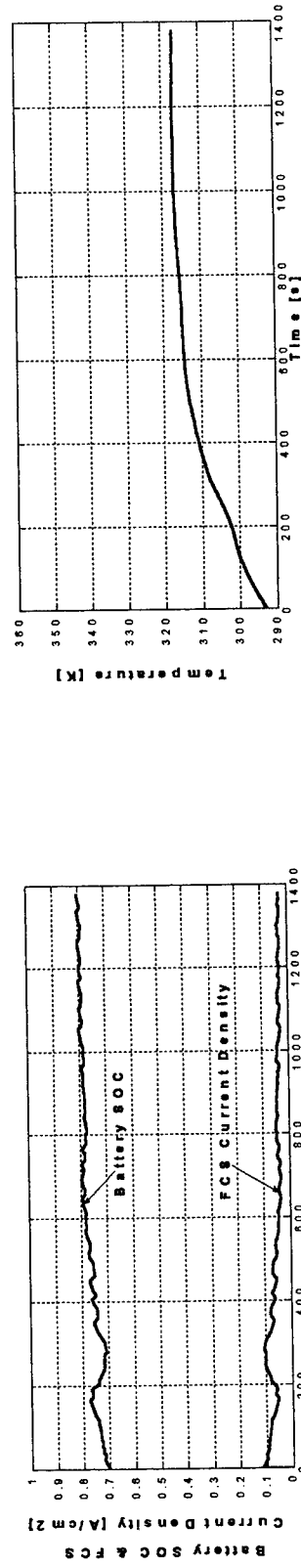
Figure 6.10: Proportional Control Survivor Performance for FUDS:
(a) Run 222 FUDS Battery SOC and FCS Current Density, (b) Run 222 FUDS Temperature,
(b) Run 248 FUDS Battery SOC and FCS Current Density, (d) Run 248 FUDS Temperature

173

Proportional Control Run 222 FHDS
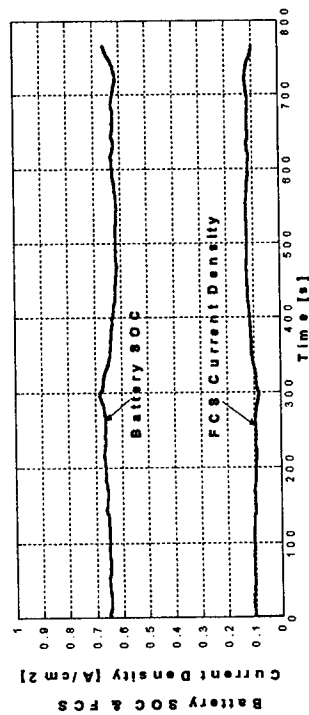
(a)

(b)
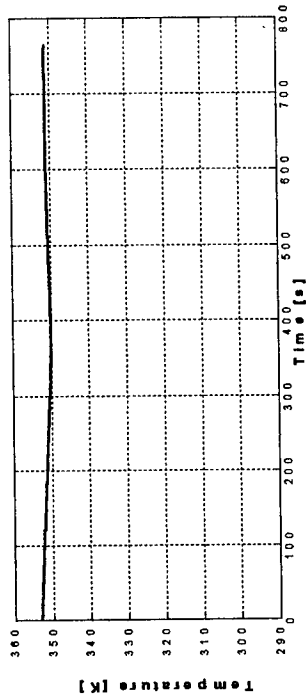
Proportional Control Run 248 FHDS
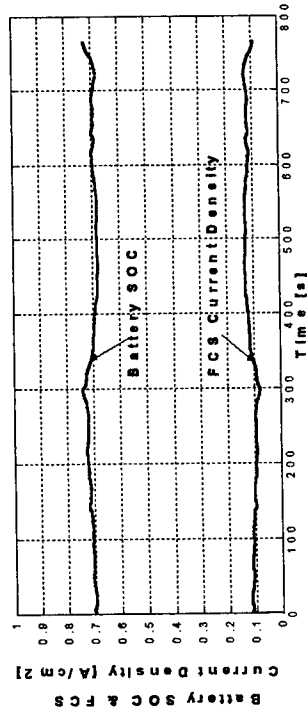
(c)
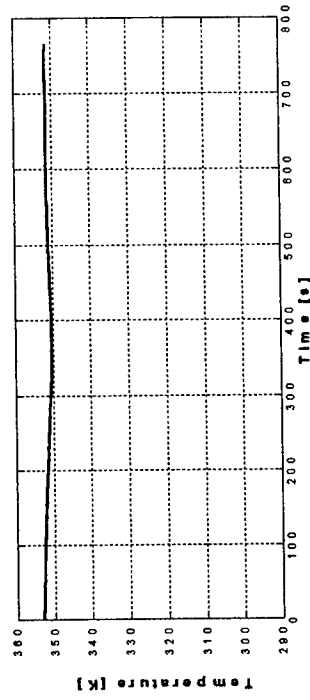
(d)

Figure 6.11: Proportional Control Survivor Performance for FHDS:
(a) Run 222 FHDS Battery SOC and FCS Current Density, (b) Run 222 FHDS Temperature,
(c) Run 248 FHDS Battery SOC and FCS Current Density, (d) Run 248 FHDS Temperature

174

The first principal component alone provides most of the information given by the four original criteria of evaluation. Principal component analysis results reinforce the conclusion of strong correlation among the criteria of evaluation observed in Fig. 6.9.

To assess regenerative braking effects, the 288 simulations were rerun without regenerative braking. Forty-eight non-charge sustaining candidates were eliminated. Dominance filtering produced three survivors based on the first set of criteria and nine survivors based on the second set of criteria. Considering the first set of criteria survivors, the average fuel economies were 56.2 mpg for FUDS and 62.7 mpg for FHDS compared with 62.1 mpg for FUDS and 64.5 mpg for FHDS for the comparable five survivors using regenerative braking. Results again indicate that regenerative braking is advantageous over no regenerative braking especially for the FUDS cycle, which shows a 10.5% increase in fuel economy.

Sensitivity analyses using Eq. 4.1 were conducted for the direct-hydrogen fuel cell system/battery hybrid vehicle proportional control survivor run #248 operating on the FUDS and FHDS cycles. Results are provided in Tables 6.7 and 6.8 respectively. For the cold-start FUDS simulations, fuel economy shows most sensitivity to vehicle mass followed by fuel cell system air compressor isentropic efficiency and molar air-fuel ratio. For the warm-start FHDS simulations, fuel economy shows most sensitivity to vehicle mass followed by decreased nominal fuel cell stack operating temperature and fuel cell system air compressor isentropic efficiency.

During proportional control simulations, fuel cell system operation is similar to that of the survivors from thermostatic control strategy: operation at minimal fuel cell system current density to maintain high battery state of charge. The proportional control

175

Parameter	Base Case Value	% Change in Parameter [+/-]	% Change in Fuel Economy [+/-]	Fuel Economy Sensitivity
Fuel Economy [mpg]	62.0	- - -	- - -	- - -
Vehicle Mass [kg]	1452	+5.0	-3.9	-0.77
	1452	+10.0	-7.7	-0.77
Avg Compressor Efficiency [%]	53.0	-10.0	-1.4	0.14
	53.0	+5.0	+0.4	0.10
Molar Air Fuel Ratio	2	-25.0	+1.9	-0.08
	2	25.0	-1.9	-0.08
Avg Expander Efficiency [%]	75.0	-10.0	-0.5	0.05
	75.0	+4.9	+0.2	0.04
Hydrogen Utilization	0.8	-10.0	-0.0	0.00
	0.8	+10.0	+0.0	0.00
Nominal FC Temp [K]	353	-3.0	0.0	0.00
	353	+3.0	0.0	0.00

Table 6.7: Cold-Start FUDS Cycle Sensitivity Analysis for Direct-Hydrogen Fuel Cell System/Battery Vehicle (Proportional Control Run #248)

Parameter	Base Case Value	% Change in Parameter [+/-]	% Change in Fuel Economy [+/-]	Fuel Economy Sensitivity
Fuel Economy [mpg]	64.5	- - -	- - -	- - -
Vehicle Mass [kg]	1452	+5.0	-2.5	-0.50
	1452	+10.0	-4.8	-0.48
Nominal FC Temp [K]	353	-3.0	-0.9	0.31
	353	+3.0	+0.2	0.05
Avg Compressor Efficiency [%]	52.6	-10.8	-1.4	0.13
	52.6	+4.2	+0.5	0.12
Molar Air Fuel Ratio	2	-25.0	+1.9	-0.07
	2	25.0	-2.0	-0.08
Avg Expander Efficiency [%]	73.9	-11.9	-0.6	0.05
	73.9	+2.8	+0.2	0.07
Hydrogen Utilization	0.8	-10.0	-0.2	0.02
	0.8	+10.0	+0.0	0.00

Table 6.8: Warm-Start FHDS Cycle Sensitivity Analysis for Direct-Hydrogen Fuel Cell System/Battery Vehicle (Proportional Control Run #248)

177

results reinforce the conclusion drawn from thermostatic control analysis: operating the fuel cell system at low current density results in higher fuel cell system efficiency and fuel economy. With regard to FUDS and FHDS fuel economy and fuel cell system efficiency, the proportional control survivors outperform all surviving candidates from the thermostatic control analysis.

6.8. Implications of Control Strategy Results

For consistency the same control parameters have been used for both thermostatic control and proportional control. For practical applications the fuel cell system must be able to operate over the full range of current density between 0 and *current density maximum limit*: current density corresponding to maximum power. As indicated by the simulation results, using these current density limits with thermostatic control would be inefficient. However, as shown in Fig. 6.12, a practicable proportional control strategy can be developed from the proportional control survivors by extrapolating the line of proportionality up to the fuel cell system current density maximum limit and down to 0 current density. A proportional control strategy is then defined by a slope (gain) and the battery state of charge that corresponds to the point at which the fuel cell system current density maximum limit is reached. Results from the proportional control analysis can be used to define a proportional control strategy that serves as a basis of comparison for more advanced supervisory-level control strategies. Only control strategies that produce higher state of charge-corrected fuel economy should be implemented.

178

Fuel Cell System Current Density [A/cm²]
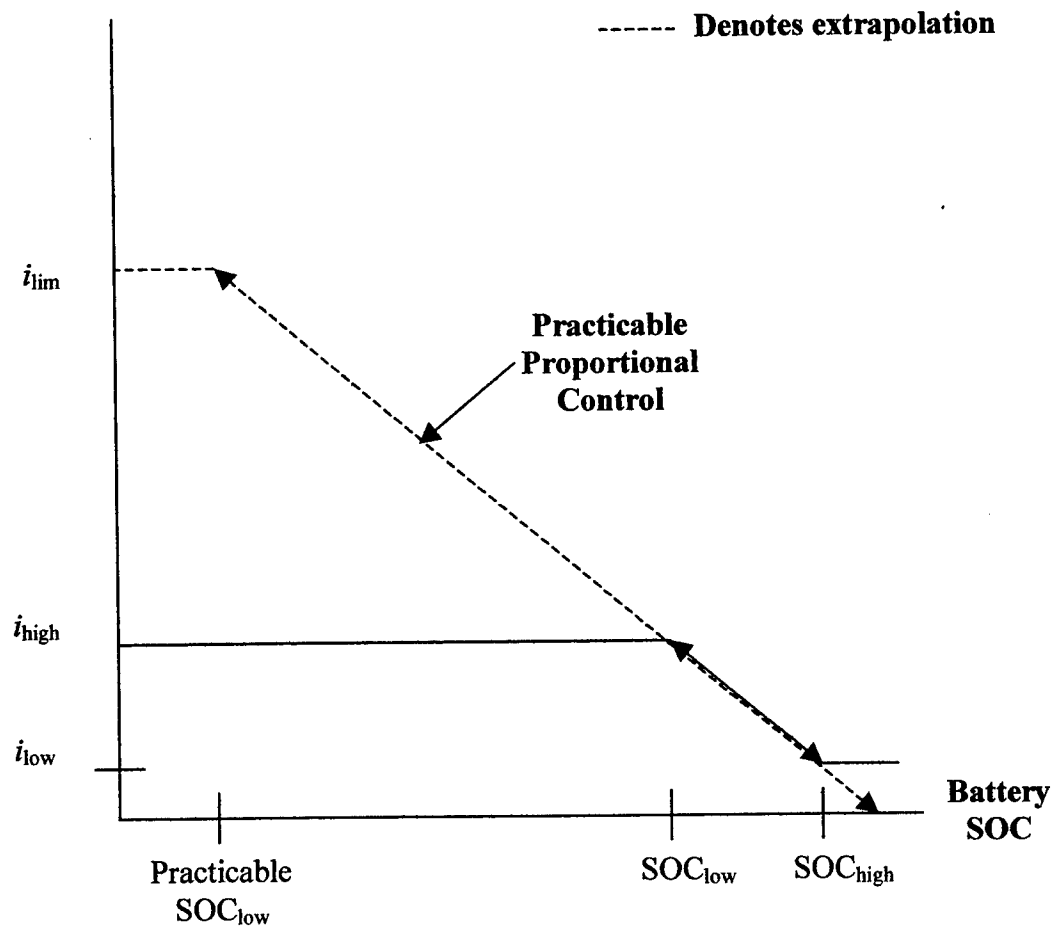
Figure 6.12: Practicable Proportional Control Strategy

179

6.9. Additional Considerations

The methodology used to explore the hybrid vehicle design space identifies component power sizing and limits of operation that offer potential for high system efficiency and fuel economy. The conclusions drawn here are strictly valid only for the criteria employed.

Results from this analysis consider the exergetic efficiency of the fuel cell system based on the chemical exergy of the hydrogen stored on-board the vehicle. If the efficiency associated with conversion of feedstock into compressed hydrogen stored on-board the vehicle is considered, total efficiency values will be substantially lower than those determined during the simulations, as discussed in Secs. 4.3.1 and 4.3.2.

Vehicle mass is assumed constant for all four fuel cell system/battery configurations considered in this analysis. Consideration of variance in total vehicle mass with changes in component sizes is possible using sensitivity analysis results in Tables 6.7 and 6.8. The fuel cell system specific power target of 300 W/kg (or mass per power capability of 1/0.3 kg/kW) quoted by Chalk et al. (2000) is used to determine fuel cell system mass based on power capability. Additional assumptions for the nickel metal hydride battery pack include power density of 500 W/kg (or mass per power capability of 2 kg/kW) and specific energy of 50 W-hr/kg specified in Sec. 6.3.2. Using the 1452 kg fuel cell vehicle with a 42 kW-capacity fuel cell system basis from Chapter 4, added mass for the four configurations (cases) in Table 6.3 can be determined. Considering Case 1 with maximum battery power of 56.5 kW and maximum fuel cell system power of 70.3 kW, added mass is computed as follows:

Added Mass due to battery: *56.5 kW× (2 kg/kW) = 113.0 kg*

Added Mass due to fuel cell system: *(70.3 kW − 42 kW)× [(1/0.3) kg/kW] = 94.3 kg*

Total added mass: *207.3 kg*

Similar computations for the other three cases result in additional masses of 213.5 kg, 219.3 kg, and 225.7 kg respectively. Expected fuel economy for the four cases would show corresponding decline of 6.8 mpg, 7.0 mpg, 7.2 mpg, and 8.0 mpg for FUDS and decline of 4.6 mpg, 4.7 mpg, 4.9 mpg, and 5.0 mpg for FHDS.

Considering impacts of fuel conversion efficiency and vehicle mass fuel economy adjustments, dominance filtering results would provide alternative candidates with high fuel cell system efficiency and fuel economy potential. Conclusions may differ depending upon choice of chemical exergy input to the system and total vehicle mass considered.

CHAPTER 7

PERFORMANCE COMPARISON BY VEHICLE CONFIGURATION,
SOURCE FUEL, AND POWER CAPACITY

7.1. Introduction

Simulation results for a direct-hydrogen fuel cell vehicle with maximum fuel cell

stack power capacity of 50 kW and maximum fuel cell system net power capacity of 42

kW at nominal temperature are described in Chapter 4. For the *same size* fuel cell system

simulation results for a methanol reforming fuel cell vehicle are described in Chapter 5.

In Chapter 6 four combinations of fuel cell stack and battery component sizes are

considered for a direct-hydrogen hybrid (fuel cell system/battery) vehicle. Two control

strategies were applied to the hybrid vehicle to determine the component sizing and

operational parameters that offer the greatest potential for high fuel economy. The aim of

this chapter is twofold: (1) to compare performance of the fuel cell vehicle with that of

the hybrid vehicle using the *same size* fuel cell stack (power capacity) for both vehicles

and (2) to examine performance of the fuel cell vehicle using two *different size* fuel cell

stacks. For these analyses, both direct-hydrogen and methanol reforming are considered

as a source fuel.

7.2. Results for Vehicle Configurations with Constant Size Fuel Cell Stack

Vehicle performance for four cases is considered: direct-hydrogen and methanol

reforming fuel cell vehicle and direct-hydrogen and methanol reforming hybrid vehicle.

To compare relative fuel economy and fuel cell system efficiency among the four cases considered, constant total vehicle mass is maintained and the same size fuel cell stack is employed in each case for consistency. The fuel cell stack size selected is based on one of the proportional control survivors, Run #248. All simulations use proportional control run #248 fuel cell system power capacity: 84.5 kW (fuel cell stack size of 440 cells each with active area of 400 cm^2). For the hybrid vehicle simulations, electric motor size, battery size, and operational parameters also correspond to those of proportional control run #248. Additionally, proportional control strategy is used during the hybrid vehicle simulations.

Results for the four cases are shown in Table 7.1. For both pure fuel cell vehicle and hybrid vehicle cold-start FUDS and warm-start FHDS simulations, fuel cell system efficiency, total efficiency, and vehicle fuel economy using methanol reforming are lower than those associated with the corresponding direct-hydrogen vehicle. Fuel cell system efficiency is higher for the direct-hydrogen fuel cell vehicle since hydrogen in the fuel cell stack anode exhaust can be recirculated and reused in the stack. When methanol reforming is used, the anode exhaust cannot be recirculated due to the presence of species other than hydrogen and water. Consequently, hydrogen is lost through venting of anode exhaust. For the direct-hydrogen vehicles, total efficiency corresponds to fuel cell system efficiency. For the methanol reforming vehicles, reformer inefficiencies primarily due to incomplete chemical reaction and heat rejection from the reformer result in total efficiencies significantly lower than those associated with the direct-hydrogen vehicles. Lower total efficiency is reflected by lower fuel economy for methanol reforming vehicles.

183

Cold-Start FUDS	Fuel Cell Vehicle		Hybrid Vehicle	
	Direct-Hydrogen	Methanol Reforming	Direct-Hydrogen	Methanol Reforming
Fuel Cell System Efficiency [%]	61.3	44.5	66.5	51.7
Reformer Efficiency [%]	- - -	68.0	- - -	67.2
Total Efficiency [%]	61.3	30.3	66.5	34.7
Fuel Economy [mpg]	56.6	25.7	62.1	30.6

(a) Cold-Start FUDS

Warm-Start FHDS	Fuel Cell Vehicle		Hybrid Vehicle	
	Direct-Hydrogen	Methanol Reforming	Direct-Hydrogen	Methanol Reforming
Fuel Cell System Efficiency [%]	63.9	49.7	65.1	51.0
Reformer Efficiency [%]	- - -	77.8	- - -	77.8
Total Efficiency [%]	63.9	38.7	65.1	39.6
Fuel Economy [mpg]	63.8	38.3	64.5	38.9

(b) Warm-Start FHDS

Table 7.1: Fuel Cell System Efficiency, Reformer Efficiency, Total Efficiency, and Fuel Economy Comparison among Direct-Hydrogen Fuel Cell Vehicle, Methanol Reforming Fuel Cell Vehicle, Direct-Hydrogen Fuel Cell System/Battery Hybrid Vehicle, and Methanol Reforming Fuel Cell System/Battery Hybrid Vehicle Using 84.5 kW Fuel Cell System and Constant Total Vehicle Mass of 1452 kg: (a) Cold-Start FUDS and (b) Warm-Start FHDS

For each fuel source considered (direct-hydrogen and methanol reforming), the hybrid configuration produces higher fuel cell system efficiency and higher fuel economy compared with the pure fuel cell vehicle using the same fuel source. These results indicate that a hybrid vehicle operating on direct hydrogen has the potential for highest fuel economy.

7.3. Results for Fuel Cell Vehicles with Different Size Fuel Cell Stacks

Table 5.1 consolidates results from the direct-hydrogen fuel cell vehicle simulations in Chapter 4 with results from the methanol reforming fuel cell vehicle simulations in Chapter 5. In both of these simulations the fuel cell stack size (220 cells) was such that fuel cell system power capacity was 42 kW. Table 7.1 also includes results for simulations involving the direct-hydrogen fuel cell vehicle and the methanol reforming fuel cell vehicle. In these simulations the fuel cell stack size (440 cells) was such that fuel cell system power capacity was 84.5 kW. In order to compare performance of fuel cell vehicles with the same total vehicle mass but with different fuel cell system sizes, fuel cell vehicle simulation results from Table 5.1 and Table 7.1 are consolidated in Table 7.2.

As expected fuel cell system efficiency is lower when the small fuel cell stack is used. The small fuel cell stack must operate at higher average current density than the large fuel cell stack to produce the same power. As explained in Sec. 3.1.2, operating at high current density results in lower fuel cell stack efficiency.

It is interesting to note that reformer efficiency is significantly higher when the small fuel cell stack is used during cold-start FUDS cycle. This occurs because the small fuel cell stack requires a high mass flow of hydrogen to produce a high average current

185

Cold-Start FUDS	Direct-Hydrogen		Methanol Reforming	
	42 kW Fuel Cell System (220 Cells)	84.5 kW Fuel Cell System (440 Cells)	42 kW Fuel Cell System (220 Cells)	84.5 kW Fuel Cell System (440 Cells)
Fuel Cell System Efficiency [%]	56.4	61.3	39.5	45.3
Reformer Efficiency [%]	- - -	- - -	81.1	73.6
Total Efficiency [%]	56.4	61.3	32.0	33.3
Fuel Economy [mpg]	52.9	56.6	27.3	28.4

(a) Cold-Start FUDS

Warm-Start FHDS	Direct-Hydrogen		Methanol Reforming	
	42 kW Fuel Cell System (220 Cells)	84.5 kW Fuel Cell System (440 Cells)	42 kW Fuel Cell System (220 Cells)	84.5 kW Fuel Cell System (440 Cells)
Fuel Cell System Efficiency [%]	58.1	63.9	44.4	50.1
Reformer Efficiency [%]	- - -	- - -	83.8	83.6
Total Efficiency [%]	58.1	63.9	37.3	41.9
Fuel Economy [mpg]	58.5	63.8	36.9	41.4

(b) Warm-Start FHDS

Table 7.2: Fuel Cell System Efficiency, Reformer Efficiency, Total Efficiency, and Fuel Economy Comparison using 84.5 kW Fuel Cell System and 42 kW Fuel Cell System for Direct-Hydrogen Fuel Cell Vehicle and Methanol Reforming Fuel Cell Vehicle (Constant Total Vehicle Mass of 1452 kg): (a) Cold-Start FUDS and (b) Warm-Start FHDS

186

density. Consequently, during cold-start conditions the reformer reactant flows and reaction rates are higher resulting in faster temperature rise and lower degree of incomplete reaction. When the large fuel cell stack is used, the average current density is lower resulting in lower demand for hydrogen from the reformer. As a consequence, there is slower temperature rise in the reformer and a higher degree of incomplete reaction.

Total efficiency and fuel economy are higher with the large fuel cell stack for both direct-hydrogen and methanol reforming. Considering the cold-start FUDS methanol reforming case, high methanol reforming efficiency is associated with lower fuel cell system efficiency for the small size fuel cell stack while low methanol reforming efficiency is associated with higher fuel cell system efficiency for the large size fuel cell stack. The large size fuel cell stack has the greater total efficiency and fuel economy indicating that fuel cell system efficiency has a stronger influence on overall efficiency and fuel economy than reformer efficiency.

7.4. Total Efficiency Considerations

The total efficiency values shown in Tables 7.1 and 7.2 are based on the chemical exergy of the source fuel stored *on-board* the vehicle. Indeed, values for total efficiency will differ depending on whether feedstock or fuel stored on-board the vehicle is considered as the chemical exergy input to the system. If the efficiency associated with conversion of feedstock into the source fuel stored on-board the vehicle is considered, total efficiency values will be substantially lower than those shown in these tables, as discussed in Secs. 4.3.1, 4.3.2, and 5.5.

187

7.5. Closing Comment

The analyses considered in this chapter illustrate the utility of the vehicle simulator embedded with the fuel cell system model and the methanol reformer model. Other cases that might be considered include performance of vehicles that have parameters different from those considered in this study, vehicle performance during driving cycles that require higher average power than the FUDS and FHDS cycles, and consideration of alternative control strategies for hybrid vehicle operation. There are many possibilities for use of this analysis tool.

CHAPTER 8

CONCLUSIONS AND RECOMMENDATIONS FOR FURTHER STUDY

8.1. Introduction

Contemporary interest in developing power systems that achieve increased system exergetic efficiency and/or decreased environmental impacts is strong. Fuel cells do not require an intermediate combustion process to accomplish exergy conversion. Elimination of the combustion process reduces inherent combustion exergy destruction and may lower/eliminate undesirable emissions. Consequently, fuel cells have the potential to provide more power from a given supply of fuel and be less polluting than conventional engines.

This study has focused on fuel cells in automotive applications. Issues associated with fuel cells, modeling of fuel cells, and simulation of fuel cell systems in automotive applications have been considered:

- This study has developed models for a PEM fuel cell stack, direct-hydrogen fuel cell system, and methanol reforming fuel cell system. The exergetic efficiency associated with each model has been examined and in-vehicle sources of inefficiency have been identified.

- The models developed in this study were embedded in a vehicle simulator. Using the FUDS and FHDS driving cycles, fuel economy was determined in four

cases: direct-hydrogen fuel cell vehicle, methanol reforming fuel cell vehicle, direct-hydrogen hybrid (fuel cell system/battery) vehicle, and methanol reforming hybrid vehicle.

- Additionally, for the direct-hydrogen hybrid vehicle, thermostatic control and proportional control strategies for the fuel cell system and battery were used to examine component sizing and operational limits. Dominance filtering was employed to identify component sizing and operational limits that provide the potential for highest fuel economy. Results of this analysis can be used as a point of departure to develop more advanced control strategies.

8.2. Summary of Primary Findings

Several tasks were completed in the current study. A summary of the primary findings associated with these tasks is provided below:

(1) During development of a PEM fuel cell stack model for incorporation into the vehicle simulator, GCtool was used to determine PEM fuel cell performance trends while several parameters were varied. Findings for PEM fuel cell performance include:

(a) Increasing cathode pressure results in higher voltage for a given current density with the onset of concentration polarization occurring at higher current densities as cathode pressure increases (Figs 3.1 through 3.3). Generally as temperature increases, the voltage for a given current density increases. This trend changes at high current density in the region of concentration polarization dominance. The onset of concentration polarization occurs at lower current densities as fuel cell operating temperature increases (Figs 3.10 through 3.12).

190

(b) For a given fuel cell operating temperature and cathode pressure, as current density increases, power density reaches a maximum value and then sharply declines. Increasing cathode pressure results in greater power density for a given current density (Figs 3.4 through 3.6). Increasing fuel cell operating temperature results in increased power density for a given current density. As fuel cell operating temperature increases, the maximum power density occurs at higher current density (Figs 3.13 through 3.15).

(c) Fuel cell exergetic efficiency is directly proportional to fuel cell power, which is directly proportional to voltage for a given current density. Consequently, fuel cell exergetic efficiency exhibits trends with respect to pressure and temperature similar to those for voltage: increasing cathode pressure and increasing temperature result in higher efficiency for a given current density (Figs. 3.7 through 3.9).

(2) For a fuel cell stack to be functional, auxiliary components are required for air flow, fuel flow, cooling, and humidification. These auxiliary components were incorporated with the fuel cell stack model to develop a fuel cell system model (Fig. 3.19). Findings associated with the fuel cell system are:

(a) As most auxiliary components in the fuel cell system consume power (compressor, pumps, fan), net power production by the fuel cell system is less than that by the fuel cell stack (Sec. 4.2).

(b) Similarly, since some auxiliary components in the fuel cell system consume power and all have associated exergy destruction, the exergetic efficiency of the fuel cell system is characteristically less than for the fuel cell stack (Sec. 3.2.3).

(c) The air compressor has by far the greatest average power consumption of the auxiliary components in the fuel cell system. Consequently, reduction in compressor power consumption would contribute most to increased fuel cell system net power output (Sec. 4.2).

(d) Opportunities exist for performance improvement via fuel cell system component control efforts. Low-level control efforts targeting the compressor have the greatest potential for improved system performance (Sec. 4.2). However, to develop compressors able to maintain high isentropic efficiency over a large range of mass flows, advances in technology and innovations in component control are required.

(3) The fuel cell system model described in Sec. 3.2.3 was embedded into a vehicle simulator (Sec. 4.1), which was used to perform direct-hydrogen fuel cell vehicle simulations operating under cold-start FUDS and warm-start FHDS driving cycles. Findings from these simulations are:

(a) FUDS fuel economy showed most sensitivity to vehicle mass, followed by compressor efficiency and molar air fuel ratio (Sec. 4.3.3).

(b) FHDS fuel economy showed most sensitivity to nominal fuel cell operating temperature followed by vehicle mass and compressor efficiency (Sec. 4.3.3).

192

(4) A methanol reformer model (Sec. 5.3) was developed and integrated with the fuel cell system model (Fig. 5.1) in the vehicle simulator. Simulations of a methanol reforming fuel cell vehicle operating under cold-start FUDS and warm-start FHDS driving cycles were conducted to determine the effects of fuel reforming on fuel cell system performance and overall vehicle fuel economy. Findings from these simulations are:

(a) Exergy destruction associated with the irreversible chemical reactions in the reformer significantly reduces overall performance of the fuel cell vehicle compared to the direct-hydrogen fuel cell vehicle performance (Sec. 5.5). Table 5.1 compares results for direct-hydrogen and methanol reforming fuel cell vehicle simulations.

(b) For both FUDS and FHDS the fuel cell stack and reformer perform best when these components start warm resulting in highest total efficiency and fuel economy. Conversely, the fuel cell stack and reformer perform worst when these components start cold resulting in lowest total efficiency and fuel economy (Table 5.2). The effect of fuel cell stack cold-start impacts overall performance more than reformer cold-start since the reformer model uses unreacted methanol in a preheater to rapidly raise reformer temperature during simulations.

(c) There is interdependence between the fuel cell system and the reformer. Operating conditions of one component may affect either adversely or favorably the individual performance of the other component (Sec. 5.5).

(d) Since reformer use precludes recycling of unreacted hydrogen in the reformate exiting the fuel cell stack anode, there is a loss of hydrogen exergy and thus fuel economy is very sensitive to hydrogen utilization (Sec. 5.6).

(e) Compared with the direct-hydrogen fuel cell vehicle sensitivity results (Sec. 4.3.3), sensitivity results for the methanol reforming fuel cell vehicle (Sec. 5.6) indicate parameters affected by reformer use (hydrogen utilization and extent of reformer reaction) have greater impact on fuel economy compared with those of the fuel cell system.

(f) Development of improved catalysts to support chemical reactions is important for maintaining a high extent of reaction in the reformer.

(g) Maintaining maximal hydrogen utilization and extent of reformer reaction, as well as limiting vehicle weight contribute most to fuel economy for both cold-start FUDS and warm-start FHDS for the methanol reforming fuel cell vehicle. Additionally, maintaining fuel cell operating temperature at an appropriate level contributes to fuel economy in warm-start FHDS (Sec. 5.6).

(5) Thermostatic control and proportional control strategies were employed in direct-hydrogen hybrid simulations to assess system performance in vehicles operating under FUDS and FHDS driving cycles. Findings from these simulations are:

(a) Both thermostatic control and proportional control results support the conclusion that operating the fuel cell system at low current density results in higher fuel cell system efficiency and fuel economy (Secs. 6.6 and 6.7).

(b) With regard to FUDS and FHDS fuel economy and fuel cell system efficiency, proportional control survivors outperform all surviving candidates from the thermostatic control analysis (Sec. 6.7).

(c) To produce a given power, larger fuel cell stacks require less power per cell resulting in operation at a lower current density where efficiency is higher (Sec. 6.7).

(d) Regenerative braking is advantageous over conventional braking especially for the FUDS cycle, which shows a 10.5% increase in fuel economy (Sec. 6.7).

(e) Results from the proportional control analysis can be used to define a proportional control strategy that serves as a basis of comparison for more advanced supervisory-level control strategies (Sec. 6.8).

(6) Simulations were conducted to compare performance of the fuel cell vehicle with that of the hybrid vehicle using the same size fuel cell stack for both vehicles. Additionally, performance of the fuel cell vehicle using two different size fuel cell stacks was examined. Both analyses considered direct-hydrogen and methanol reforming. Findings from these simulations are:

(a) For both pure fuel cell vehicle and hybrid vehicle cold-start FUDS and warm-start FHDS simulations with same size fuel cell stacks and total vehicle mass, fuel cell system efficiency, total efficiency, and vehicle fuel economy using methanol reforming are lower than those associated with the corresponding direct-hydrogen vehicle (Table 7.1).

(b) Hybrid vehicles operating on direct hydrogen have the potential for highest vehicle fuel economy (Sec 7.1).

(c) Using larger fuel cell stacks in fuel cell vehicles with the same total vehicle mass results in higher total efficiency and fuel economy (Table 7.2).

(d) For methanol reforming fuel cell vehicles fuel cell system efficiency has a stronger influence on overall efficiency and fuel economy than reformer efficiency (Sec. 7.3).

(e) Values for total efficiency vary depending on whether feedstock or fuel stored on-board the vehicle is considered as the chemical exergy input to the system. (Sec. 7.4). Exergetic efficiency based on chemical exergy of fuel stored on-board the vehicle neglects the inherent exergy destruction and losses associated with conversion of feedstock. Consequently, total efficiency based on chemical exergy of fuel stored on-board the vehicle is higher than that based on chemical exergy of feedstock.

(f) When comparing efficiencies of fuel cell systems, with or without reforming, to efficiencies of conventional internal combustion engines, consideration should be given to conversion of feedstock to fuel stored on-board the vehicle.

8.3. Future Work

Opportunities for future work using the results of the current study exist in three areas: (1) reformer, fuel cell system, and battery model improvements, (2) model applications and analyses, and (3) operational laboratory support. Each of these areas is discussed further in the following sections.

8.3.1. Model Improvement

The current reformer model is based on theoretical complete chemical reactions that do not include carbon monoxide as a product. In actual methanol reforming PEM fuel cell systems, carbon monoxide management is an important issue due to its detrimental effect on platinum catalysts used in PEM fuel cell stacks. Incorporation of incomplete reaction kinetics for the reformer and auxiliary processes for carbon monoxide removal would significantly improve the current reformer model. These improvements could provide insight into exergy requirements associated with carbon monoxide reduction and their effects on overall system performance. Additionally, the relative magnitude of harmful emissions such as the greenhouse gases carbon monoxide and carbon dioxide could be assessed.

The current reformer model also applies only for methanol as the fuel. Development of models to accommodate other hydrogen-bearing fuels would provide greater flexibility in the choice of fuel considered for analysis. Overall fuel economy using various fuels could be compared to identify fuels having significant fuel economy advantage.

Results from sensitivity analyses in Sec. 4.3.3, Sec. 5.6, and Sec. 6.7 indicate that fuel economy is particularly sensitive to vehicle mass. By explicitly incorporating into the vehicle simulator mass associated with fuel cell stack, reformer, and battery sizing, total vehicle mass could be adjusted based on size of component selected. Response to load demand and resulting fuel economy could be examined for various size components.

Incorporation of dynamics associated with components such as compressors, fans, and pumps would allow consideration of response time to changes in flow demands.

197

Response time associated with these components would influence component-level control strategy in order to meet the overall load demand by the vehicle and the resulting fuel economy. Since there is strong interaction between low-level component control and supervisory control strategy, inclusion of component dynamics would also influence choice of supervisory control strategy. For example, ability of fuel cell system individual components to respond rapidly to load demand changes may influence whether the fuel cell system is used in a load following or a load leveling capacity for hybrid configurations. Trade-off analyses using various strategies for component-level control and supervisory control could identify control strategies to achieve best overall performance.

Incorporation of volume and costs associated with fuel cell stack and auxiliary components, reformer, and battery sizing also would improve overall analysis capability. Component volume information could help identify total space requirements for the engine compartment. Configurations greatly exceeding appropriate space and/or total cost thresholds might be eliminated from consideration.

In the direct-hydrogen fuel cell system model, cathode inlet temperature was specified as an average temperature of 333K, which was within 3% of the temperature associated with the average compressor pressure ratio during simulations (Sec.4.3). Since actual cathode inlet temperature varies with ambient temperature, compressor pressure ratio, compressor isentropic efficiency, and humidification, the fuel cell system model would be nominally more accurate by computing actual electrode inlet temperature rather than assuming an average value.

8.3.2. Model Applications and Analyses

The current study considered performance of a fuel cell system in an SUV-type of vehicle. The model also could be applied to other types of vehicles such as heavy trucks and military vehicles to examine fuel economy and perform trade-off analysis on component sizing and operational limits for hybrid configurations.

As mentioned in Sec. 4.2, consideration of alternative air flow strategies at the fuel cell stack cathode inlet would indicate which strategy most favorably affects system efficiency while maintaining required system performance level. The model could be used to examine such alternative air flow strategies and to conduct trade-off analyses for load demand response capability, overall fuel economy, and system complexity with associated costs.

Continuing the work of Sec. 6.8, the model could be used to assess performance of alternative supervisory-level control strategies for the fuel cell system and battery in a hybrid configuration. Using results of the current study as a basis, fuel economy resulting from such control strategies could be compared to the fuel economy from the current study to identify potentially effective strategies worthy of further development.

Based on assessment of relative effect on performance due to fuel cell stack and reformer warm/cold start (Sec. 5.5), direct-hydrogen and methanol-reforming vehicle simulations might incorporate use of a fuel cell stack preheater. Results of these simulations could quantify any relative advantage/disadvantage of a fuel cell stack preheater on overall system efficiency and fuel economy.

In the current methanol reforming fuel cell system, fuel cell stack anode exhaust is vented resulting in hydrogen loss and lower system efficiency. Alternative uses of this

199

exhaust gas such as fuel cell stack preheat or power production via expansion might be considered to determine whether potential for significant efficiency improvement exists.

Since the models developed and used in the current study do not include the effects of dynamics but operate with immediate response to load demand changes, results of this study represent best-level performance of realizable systems. Results from this study can serve as a benchmark for comparison with results from future model incorporation of effects of dynamics.

8.3.3. Operational Laboratory Support

The fuel cell system and reformer models resulting from the current study could be used in tandem with an actual fuel cell system and/or reformer laboratory. Operational parameters associated with actual system components such as isentropic efficiencies, temperature, pressure, etc., could be adjusted in the model to determine limits of operation. Laboratory test results can provide information for improvements in the model. Effects of varying species mass flows on fuel cell stack and reformer operations, time response associated with auxiliary components such as compressors, fans, pumps, and expanders, component-level control strategy implementation and resulting performance, and emissions associated with reforming could be incorporated into the model to expand its capability. Understanding the effects of dynamics associated with individual components and using appropriate control strategies to improve total system performance is key to realizing the benefits of fuel cell system integration for automotive applications.

8.4. Closing Comments

Stimulated by the need for more fuel-efficient vehicles that produce fewer harmful emissions, fuel cell vehicle research and development will continue. Since a fuel cell system contains many interrelated components, consideration of the effects of change in one component on overall system performance is critical. Use of vehicle simulators and fuel cell system models such as developed in this study will allow engineers to identify component design parameters, operational parameters, and control strategies that offer the highest potential for overall fuel cell system improvement.

Before fuel cell vehicles become widely accepted by the general public, these vehicles will have to match existing commercially available vehicles in the areas of performance, refueling simplicity, and cost. Results from this study indicate that direct-hydrogen fuel cell vehicles have the potential for significantly higher fuel economy while methanol reforming fuel cell vehicles only show potential comparable to current conventional vehicles. On the other hand, on-board storage and refueling of hydrogen pose greater challenges than on-board storage and refueling of methanol. These findings suggest that significant hurdles remain to be overcome before fuel cell vehicles are in widespread use.

BIBLIOGRAPHY

Ahmed, S. and Krumpelt, M., 2001, "Hydrogen from Hydrocarbon Fuels for Fuel Cells," *International Journal of Hydrogen Energy*, Vol. 26, Issue 4, pp. 291-301.

Amphlett, J. C., Baumert, R. M., Mann, R. F., Peppley, B. A., and Roberge, P. R., 1995, "Performance Modeling of the Ballard Mark IV Solid Polymer Electrolyte Fuel Cell, I. Mechanistic Model Development," *Journal of Electrochemistry Society*, Vol 142, No. 1, pp. 1-8, January 1995.

Amphlett, J. C., Baumert, R. M., Mann, R. F., Peppley, B. A., and Roberge, P. R., 1995a, "Performance Modeling of the Ballard Mark IV Solid Polymer Electrolyte Fuel Cell, II. Empirical Model Development," *Journal of Electrochemistry Society*, Vol 142, No. 1, pp. 9-15, January 1995.

Appleby, A. J. and Foulkes, F. R., 1993, *Fuel Cell Handbook*, Krieger Publishing Company, Malabar, Florida.

Bagger, C., Christiansen, N., Hendriksen, P. V., Jensen, E. J., Larsen, S. S., and Mogensen, M., 1996, "Technical Problems to be Solved Before the Solid Oxide Fuel Cell Will Be Commercialized," *Fuel Cell Seminar Program and Abstracts*, November 17-20, Orlando, Florida, pp. 44-47.

Barbir, F., Balasubramanian, B., and Neutzler, J., 1999, "Trade-off Design Analysis of Operating Pressure and Temperature in PEM Fuel Cell Systems," *Proceedings, ASME Advanced Energy Systems Division, ASME International Mechanical Engineering Congress and Exposition*, Nashville, Tennessee, November 14-19, Vol 39, pp. 305-315.

Bejan, A., Tsatsaronis, G., and Moran, M., 1996, *Thermal Design and Optimization*, John Wiley and Sons, Inc., New York.

Berlowitz, P. J. and Darnell, C.P., 2000, "Fuel Choices for Fuel Cell Powered Vehicles," SAE Publication *Fuel Cell Power for Transportation 2000* (SP-1505), Paper 2000-01-0003, pp.15-25.

Bonville, L. J., Scheffler, G. W., and Smith, M. J., 1996, "Progress and Prospects for Phosphoric Acid Fuel Cell Power Plants," *Fuel Cell Seminar Program and Abstracts*, November 17-20, Orlando, Florida, pp. 24-27.

202

Braun, R. J., Gaggioli, R. A., Moody, S. D., and Dunbar, W. R., 1995, "An Analysis of a Phosphoric Acid Fuel Cell Cogeneration System, Part I. Improvements via System Integration," *Proceeding of the International Symposium ECOS 1995*, Istanbul, Turkey, Vol 1, pp. 139-148.

Braun, R. J., Gaggioli, R. A., and Dunbar, W. R., 1995a, "Analysis of a Demonstration Molten Carbonate Fuel Cell Power Plant," *Second Law Analysis of Energy Systems: Towards the 21st Century*, E. Sciubba and M. J. Moran, ed., CIRCUS, Rome, Italy, pp. 135-144.

Braun, R. J., Gaggioli, R. A., and Dunbar, W. R., 1996, "Improvements of a Molten Carbonate Fuel Cell Power Plant via Exergy Analysis," *Proceedings, ASME Advanced Energy Systems Division, ASME International Mechanical Engineering Congress and Exposition*, Atlanta, Georgia, November 17-22, Vol 36, pp. 321-331.

Brown, L. F., 2001, "A Comparative Study of Fuels for On-Board Hydrogen Production for Fuel-Cell-Powered Automobiles," *International Journal of Hydrogen Energy*, Vol. 26, pp. 381-397.

Burke, A.F. and Miller, M., 2000, "Fuel Efficiency Comparisons of Advanced Transit Buses Using Fuel Cell and Engine Hybrid Electric Drivelines," *Proceedings of the Intersociety Energy Conversion Engineering Conference*, Las Vegas, Nevada, July 24-28, Vol 2, pp. 1333-1340.

Call, F.W., 1996, "Thermodynamic Analysis of High Temperature Fuel Cells: Methane Reforming," *Proceedings, ASME Advanced Energy Systems Division, ASME International Mechanical Engineering Congress and Exposition*, Atlanta, Georgia, November 17-22, Vol 36, pp. 305-311.

Casten, S., Teagan, P., and Stobart, R., 2000, "Fuels for Fuel Cell-Powered Vehicles," SAE Publication *Fuel Cell Power for Transportation 2000* (SP-1505), Paper 2000-01-0001, pp. 1-7.

Chalk, S. G., Miller, J. F., and Wagner, F. W., 2000, "Challenges for Fuel Cells in Transport Applications," *Journal of Power Sources*, Vol 86, pp. 40-51.

Cui, S. Q., Gaggioli, R. A., and Dunbar, W. R., 1995, "An Analysis of a Phosphoric Acid Fuel Cell Cogeneration System, Part II. Improvements via System Reconfiguration," *Proceeding of the International Symposium ECOS 1995*, Istanbul, Turkey, Vol 1, pp. 149-156.

Dobbs, H., 2000, "Solid Oxide Fuel Cells and Department of Defense Applications," *Proceedings, Solid State Energy Conversion Alliance Workshop*, June 1-2, Baltimore, Maryland, pp.37-42.

Dunbar, W. R. and Gaggioli, R.A., 1988, "Computer Simulation of Solid Electrolyte Fuel Cell," *Proceedings Intersociety Energy Conversion Engineering Conference*, ASME, Vol. 2, pp. 257-264.

Dunbar, W. R. and Gaggioli, R.A., 1990, "Modeling of Solid Electrolyte Fuel Cells," Proceedings, Florence World Energy Research Symposium, Firenze, Italy, May 28-Jun 1, *A Future for Energy*, S. Stecco and M. J. Moran, ed., Pergamon Press, Oxford, pp.49-60.

Dyer, C. K., 1999, "Replacing the Battery in Portable Electronics," *Scientific American*, July 1999, pp. 88-93.

Eggert, A., Friedman, D., Ramaswamy, S., Hauer, K., Cunningham, J., and Moore, R., 2001, "Simulated Performance of an Indirect Methanol Fuel Cell System," *SAE 2001 World Congress*, Detroit, Michigan, March 5-8, Paper 2001-01-0544.

Friedman, D. J., 1999, "Maximizing Direct-Hydrogen PEM Fuel Cell Vehicle Efficiency – Is Hybridization Necessary?" SAE Publication *Fuel Cell Power for Transportation* (SP-1425), Paper 1999-01-0530, pp. 9-17.

Gavalas, G. R., Voecks, F. E., Moore, N. R., Ferrall, J. F., and Prokopius, P. R., 1994, "Fuel Cell Locomotive Development and Demonstration Program, Phase One: Systems Definition," Draft Report JPL D-12087 prepared for South Coast Air Quality Management District.

Georgetown University and Booz-Allen & Hamilton, Inc., 1999, "Vehicle Identification and Concept Definition Study," Draft report prepared for SunLine Services Group and U.S. Army Automotive and Armaments Command, November 4.

Geyer, H. K. and Ahluwalia, R. K., 1998, *GCtool for Fuel Cell Systems Design and Analysis: User Documentation*, ANL-98/8, Argonne National Laboratory, Argonne, Illinois, for U. S. Department of Energy under Contract W-31-109-Eng-38.

Geyer, H. K., 2000, Private Communication, Argonne National Laboratory, Argonne, Illinois, telephone number: (630) 252-5995, e-mail address: geyer@td.anl.gov.

Gurau, V., Liu, H., and Kakac, S., 1998, "Mathematical Model for Proton Exchange Membrane Fuel Cells," *Proceedings, ASME Advanced Energy Systems Division, ASME International Mechanical Engineering Information Congress and Exposition*, Anaheim, California, November 15-20, Vol 38, pp. 205-214.

Hauer, K. H., Moore, R. M., and Ramaswamy, S., 2001, "A Simulation Model for an Indirect Methanol Fuel Cell Vehicle," *SAE 2000 Future Transportation Technology Conference*, Costa Mesa, California, August 21-23, Paper 2000-01-3083.

Hauer, K. H., Moore, R. M., and Ramaswamy, S., 2001, "The Hybridized Fuel Cell Vehicle Model of the University of California, Davis," *SAE 2001 World Congress*, Detroit, Michigan, March 5-8, Paper 2001-01-0543.

Hirschenhofer, J. H., Stauffer, D. B., Engleman, R. R., and Klett, M. G., 1998, *Fuel Cell Handbook*, Fourth Edition, DOE/FETC-99/1076.

Johansson, K. and Alvfors, P., 2000, "Steady-state Model of a Proton Exchange Membrane Fuel Cell System for Automotive Applications," *Proceeding of the International Symposium ECOS 2000, From Thermo-economics to Sustainability, Part 1*, G. G. Hirs, ed., Universiteit Twente, Nederland, pp. 725-736.

Jones, P. B., Lakeman, J. B., Mepsted, G. O., and Moore, J. M., 1999, "A Hybrid Power Source for Pulse Power Applications," *Journal of Power Sources*, Vol 80, pp. 242-247.

Joon, K., 1998, "Fuel Cells – A 21st Century Power System," *Journal of Power Sources*, Vol 71, pp. 12-18.

Josephson, J., Chandrasekaran, B., Carroll, M., Iyer, N., Wasacz, B., Rizzoni, G., Qingyuan, L., and Erb, D., 1998, "An Architecture for Exploring Large Design Spaces," *Proceedings of the 15th National Conference on Artificial Intelligence, American Association for Artificial Intelligence*, Madison, Wisconsin, Jul 26-30, pp. 143-150.

Kalhammer, F., Prokopius, P., Roan, V., and Voecks, G., 1998, "Status and Prospect of Fuel Cells as Automobile Engines: A Report of the Fuel Cell Technical Advisor Panel," prepared for the State of California Air Resources Board.

King, D. L., Faz, C., and Flynn, T., 2000, "Desulfurization of Gasoline Feedstocks for Application in Fuel Reforming," SAE Publication *Fuel Cell Power for Transportation 2000* (SP-1505), Paper 2000-01-0002, pp. 9-13.

Kordesch, K. and Simader, G., 1996, *Fuel Cells and Their Applications*, VCH Publishers, Inc., New York.

Kumar, R., Ahmed, S., and Krumpelt, M., 1996, "The Low-Temperature Partial-Oxidation Reforming of Fuels for Transportation Fuel Cell Systems," *Fuel Cell Seminar Program and Abstracts*, November 17-20, Orlando, Florida, pp. 750-753.

Lee, J. H., Lalk, T. R., and Appleby, A. J., 1998, "Modeling Electrochemical Performance in Large Scale Proton Exchange Membrane Fuel Cell Stacks," *Journal of Power Sources*, Vol 70, pp. 258-268.

Lloyd, A. C., 1999, "The Power Plant in Your Basement," *Scientific American*, July 1999, pp. 80-86.

Maggio, G., Freni, S., and Cavallaro, S., 1998, "Light Alcohols/Methane Fuelled Molten Carbonate Fuel Cells: A Comparative Study," *Journal of Power Sources*, Vol. 74, pp. 17-23.

Mann, R. F., Amphlett, J. C., Hooper, M. A. I., Jensen, H. M., Peppley, B. A., and Roberge, P. R., 2000, "Development and Application of a Generalised Steady-State Electrochemical Model for a PEM Fuel Cell," *Journal of Power Sources*, Vol. 86, pp. 173-180.

McConnell, D. P., 2000, "SECA: Transportation Applications," *Proceedings, Solid State Energy Conversion Alliance Workshop*, June 1-2, Baltimore, Maryland, pp.29-36.

Miller, C., 2000, "Delphi Automotive Systems," *Proceedings, Solid State Energy Conversion Alliance Workshop*, June 1-2, Baltimore, Maryland, pp. 53-60.

Mok, P. P. and Martin, A., 1999, "Automotive Fuel Cells – Clean Power for Tomorrow's Vehicles," *SAE International Congress and Exposition*, Detroit, Michigan, March 1-4, Paper 1999-01-0320, pp.1-6.

Moody, S. D., Gaggioli, R. A., and Dunbar, W. R., 1995, "Analysis and Improvement of a Proposed Solid Oxide Fuel Cell Cogeneration System," *Second Law Analysis of Energy Systems: Towards the 21st Century*, E. Sciubba and M. J. Moran, ed., CIRCUS, Rome, Italy, pp. 155-163.

Moore, J. M., Adcock, P. L., Lakeman, J. B., and Mepsted, G. O., 2000, "The Effects of Battlefield Contaminants on PEMFC Performance," *Journal of Power Sources*, Vol. 85, pp. 254-260.

Ogden, J. M., Steinbugler, M. M., and Kreutz, T. G., 1999, "A Comparison of Hydrogen, Methanol and Gasoline as Fuels for Fuel Cell Vehicles: Implications for Vehicle Design and Infrastructure Development," *Journal of Power Sources*, Vol. 79, pp. 143-168.

Ogden, J.M., Kreutz, T. G., and Steinbugler, M. M., 2000, "Fuels for Fuel Cell Vehicles," *Fuel Cells Bulletin*, Vol. 3, Issue 16, pp. 5-12.

Pettersson, L. J. and Westerholm, R., 2001, "State of the Art of Multi-fuel Reformers for Fuel Cell Vehicles: Problem Identification and Research Needs," *International Journal of Hydrogen Energy*, Vol. 26, Issue 3, pp. 243-264.

Ramaswamy, S., Sundaresan, M., Hauer, K. H., Eggert, A., and Moore, R. M., 2000, "Fuel Processor for an Indirect Methanol Fuel Cell Vehicle," *SAE 2000 Future Transportation Technology Conference*, Costa Mesa, California, August 21-23, Paper 2000-01-3111.

Ratkje, S. K. and Moller-Holst, S., 1993, "Exergy Efficiency and Local Heat Production in Solid Oxide Fuel Cells," *Electrochimica Acta*, Vol. 38, No.2/3, pp. 447-453.

Rizzoni, G., Guezennec, Y., Brahma, A., Wei, X., and Miller, T., 2000, "VP-SIM: A Unified Approach to Energy and Power Flow Modeling Simulation and Analysis of Hybrid Vehicles," *SAE Future Car Congress*, Crystal City, Virginia, April, Paper 2000-01-1565.

Rodatz, P., Guzzella, L., and Pellizzari, L., 2000, "System Design and Supervisory Controller Development for a Fuel-Cell Vehicle," *Proceedings, 1ˢᵗ International Federation of Automatic Control Conference on Mechatronic Systems*, Vol. 1, Darmstadt, Germany, Sept 18-20, pp. 173-178.

Springer, T. E., Zawodzinski, T. A., and Gottesfeld, S., 1991, "Polymer Electrolyte Fuel Cell Model," *Journal of Electrochemistry Society*, Vol 138, No. 8, pp. 2334-2342.

Srinivasan, S., Velev, O. A., Parthasarathy, A., Mando, D. J., and Appleby, A. J., 1991, "High Energy Efficiency and High Power Density Proton Exchange Membrane Fuel Cells – Electrode Kinetics and Mass Transport," *Journal of Power Sources*, Vol. 36, pp. 299-320.

Srinivasan, S., Dave, B. B., Murugesamoorthi, K. A., Parthasarathy, A. and Appleby, A. J., 1993, "Overview of Fuel Cell Technology," *Fuel Cell Systems*, L. J. M. J. Blomen and M. N. Mugerwa, ed., Plenum Press, New York, pp. 37-72.

Stephens, J., 1999, "The US Army Portable Fuel Cell Program," *Fuel Cells Bulletin*, Issue 13, pp. 6-9.

Take, T., Kuwata, Y., Adachi, M., and Ogata, T., 1996, "Progress and Prospects for Phosphoric Acid Fuel Cell Power Plants," *Fuel Cell Seminar Program and Abstracts*, November 17-20, Orlando, Florida, pp. 63-66.

Thomas, S. and Zalbowitz, M., 1999, *Fuel Cells Green Power*, LA-UR-99-3231, Los Alamos National Laboratory, Los Alamos, New Mexico.

Wang, M. Q., 1999, *GREET 1.5 — Transportation Fuel-Cycle Model: Volume 1, Methodology, Use, and Results*, ANL/ESD-39, Vol.1, Center for Transportation Research, Argonne National Laboratory, Argonne, Illinois, Aug.

Wang, M. Q., 1999a, *GREET 1.5 — Transportation Fuel-Cycle Model: Volume 2, Detailed Results*, ANL/ESD-39, Vol.2, Center for Transportation Research, Argonne National Laboratory, Argonne, Illinois, Aug.

Wang, M. Q., 2000, Private Communication, Argonne National Laboratory, Argonne, Illinois, telephone number: (630) 252-2819.

Wegeng, R. S., Pederson, L. R., TeGrotenhuis, W. E., and Whyatt, G. A., 2001, "Compact Fuel Processors for Fuel Cell Powered Automobiles Based on Microchannel Technology," *Fuel Cells Bulletin*, Vol. 3, Issue 28, pp. 8-13.

APPENDIX A

MATLAB PROGRAM

The following MATLAB program determines fuel cell stack efficiency and fuel cell system efficiency.

```
%Fuel Cell Program
%filename=fcmodel.m

clear; %Clears all previous inputs

%Define Constants
LHV_h2=119950; %Lower heating value of hydrogen [kJ/kg]
T_amb=293; %Ambient air temperature [K]
T_ref=298; %Reference temperature for liquid water heat of formation [K]
MW_h2=2.016; %Molecular weight of H2 [kg H2/kmol H2]
MW_o2=32; %Molecular weight of O2 [kg O2/kmol O2]
MW_n2=28.01; %Molecular weight of N2 [kg N2/kmol N2]
MW_h2o=18.02; %Molecular weight of H2O [kg H2O/kmol H2O]
MW_air=28.97; %Molecular weight of air [kg air/kmol air]
R_u = 8.314;  %Universal gas constant [kJ/(kmol-K)]
k_air=1.4; %Specific heat ratio of air
Cp_air=1.004; %Specific heat of air [kJ/(kg-K)]
k_h2=1.4; %Specific heat ratio of hydrogen
Cp_h2=14.36; %Specific heat of H2 [kJ/(kg-K)]
Cp_o2=0.923; %Specific heat of O2 [kJ/(kg-K)]
Cp_n2=1.04; %Specific heat of N2 [kJ/(kg-K)]
Cp_h2ov=1.874; %Specific heat of H2O(v) [kJ/(kg-K)]
Cp_h2ol=4.19; %Specific heat of H2O(l) [kJ/(kg-K)]
rho_h2o=998; %Liquid water density [kg/m^3]
hf_h2ol=-285830; %Enthalpy of formation of liquid water [kJ/kmol]
F=96487000; %Faraday's constant [Coulombs/kmol equiv e-]

%Define operating parameters
P_cath=2; %Cathode Pressure [atm]
P_an=2; %Anode Pressure [atm]
```

Area_fc=400; %Fuel Cell Active Area [cm^2]
T_fc=353; %Fuel Cell Stack Temperature [K]
T_air=333; %Air temperature at cathode inlet [K]
T_h2=333; %H$_2$ temperature at anode inlet [K]
mu_h2=0.8014; %fuel utilization
AF=2; %Molar air-fuel ratio [kmol air/kmol H$_2$]
rh_airin=1; %Relative Humidity of air at cathode inlet
rh_h2in=1; %Relative Humidity of H$_2$ at anode inlet
curden=0.5; %Current density [A/cm^2]

%Computation of Saturation Pressures (Pg) (Equation 3.12)
Pg_Th2=exp(11.7384-(3875.52/T_h2)-(159296/(T_h2^2))-(10651805/(T_h2^3)))...
   %Saturation pressure at T_h2 [atm]

Pg_Tair=exp(11.7384-(3875.52/T_air)-(159296/(T_air^2))-(10651805/(T_air^3)))...
   %Saturation pressure at T_air [atm]

Pg_Tfc=exp(11.7384-(3875.52/T_fc)-(159296/(T_fc^2))-(10651805/(T_fc^3)))...
   %Saturation pressure at T_fc [atm]

%Computation of hydrogen enthalpy values (h_h2)
R_h2 = R_u/MW_h2; %Gas constant for H$_2$ [kJ/kmol-K]

A_h2 = [0.30574e1 0.26765e-2 -0.58099e-5 0.55210e-8 -0.18123e-11 -0.98890e3];
   %Vector of coefficients to calculate enthalpy values

h_h2_T_fc = R_h2.*T_fc.*((A_h2(1)+A_h2(2)/2.*T_fc+A_h2(3)/3.*T_fc.^2+...
   A_h2(4)/4.*T_fc.^3+A_h2(5)/5.*T_fc.^4+A_h2(6)./T_fc)); %Hydrogen enthalpy at
   fuel cell operating temperature [kJ/kg]

h_h2_T_h2 = R_h2.*T_h2.*((A_h2(1)+A_h2(2)/2.*T_h2+A_h2(3)/3.*T_h2.^2+...
   A_h2(4)/4.*T_h2.^3+A_h2(5)/5.*T_h2.^4+A_h2(6)./T_h2)); %Hydrogen enthalpy at
   H$_2$ temperature at anode inlet [kJ/kg]

%Computation of oxygen enthalpy values (h_o2)
R_o2 = R_u/MW_o2; % Gas constant for O$_2$ [kJ/kmol-K]

A_o2 = [0.36256e1 -0.18782e-2 0.70555e-5 -0.67635e-8 0.21556e-11 -0.10475e4];
   %Vector of coefficients to calculate enthalpy values

h_o2_T_fc = R_o2.*T_fc.*((A_o2(1)+A_o2(2)/2.*T_fc+A_o2(3)/3.*T_fc.^2+...
   A_o2(4)/4.*T_fc.^3+A_o2(5)/5.*T_fc.^4+A_o2(6)./T_fc)); %Oxygen enthalpy at
   fuel cell operating temperature [kJ/kg]

h_o2_T_air = R_o2.*T_air.*((A_o2(1)+A_o2(2)/2.*T_air+A_o2(3)/3.*T_air.^2+...
  A_o2(4)/4.*T_air.^3+A_o2(5)/5.*T_air.^4+A_o2(6)./T_air)); %Oxygen enthalpy at
air temperature at cathode inlet [kJ/kg]

%Computation of nitrogen enthalpy values (h_n2)
R_n2 = R_u/MW_n2; % Gas constant for N_2 [kJ/kmol-K]

A_n2 = [0.36748e1 -0.12082e-2 0.23240e-5 -0.63218e-9 -0.22577e-12 -0.10612e4];
  %Vector of coefficients to calculate enthalpy values

h_n2_T_fc = R_n2.*T_fc.*((A_n2(1)+A_n2(2)/2.*T_fc+A_n2(3)/3.*T_fc.^2+...
  A_n2(4)/4.*T_fc.^3+A_n2(5)/5.*T_fc.^4+A_n2(6)./T_fc)); %Nitrogen enthalpy at
fuel cell operating temperature [kJ/kg]

h_n2_T_air = R_n2.*T_air.*((A_n2(1)+A_n2(2)/2.*T_air+A_n2(3)/3.*T_air.^2+...
  A_n2(4)/4.*T_air.^3+A_n2(5)/5.*T_air.^4+A_n2(6)./T_air)); %Nitrogen enthalpy at
air temperature at cathode inlet [kJ/kg]

%Computation of water vapor enthalpy values (h_h2ov)
R_h2ov = R_u/MW_h2o; % Gas constant for water vapor [kJ/kmol-K]

A_h2ov = [0.40701e1 -0.11084e-2 0.41521e-5 -0.29637e-8 0.80702e-12 -0.30280e5];
  %Vector of coefficients to calculate enthalpy values

h_h2ov_T_fc =
  R_h2ov.*T_fc.*((A_h2ov(1)+A_h2ov(2)/2.*T_fc +A_h2ov(3)/3.*T_fc.^2+...
  A_h2ov(4)/4.*T_fc.^3+A_h2ov(5)/5.*T_fc.^4+A_h2ov(6)./T_fc)); %Water vapor
enthalpy at fuel cell operating temperature [kJ/kg]

h_h2ov_T_air =
  R_h2ov.*T_air.*((A_h2ov(1)+A_h2ov(2)/2.*T_air+A_h2ov(3)/3.*T_air.^2+...
  A_h2ov(4)/4.*T_air.^3+A_h2ov(5)/5.*T_air.^4+A_h2ov(6)./T_air)); %Water vapor
enthalpy at air temperature at cathode inlet [kJ/kg]

h_h2ov_T_h2 =
  R_h2ov.*T_h2.*((A_h2ov(1)+A_h2ov(2)/2.*T_h2+A_h2ov(3)/3.*T_h2.^2+...
  A_h2ov(4)/4.*T_h2.^3+A_h2ov(5)/5.*T_h2.^4+A_h2ov(6)./T_h2)); %Water vapor
enthalpy at H_2 temperature at anode inlet [kJ/kg]

%Computation of carbon dioxide enthalpy values (h_co2) (Used with reforming)
R_co2 = R_u/MW_co2; % Gas constant for N_2 [kJ/kmol-K]

A = [0.24008e1 0.87351e-2 -0.66071e-5 0.20022e-8 0.63274e-15 -0.48378e5];
  %Vector of coefficients to calculate enthalpy values

211

h_co2_T_fc = R_co2.*T_fc.*((A_co2(1)+A_co2(2)/2.*T_fc+A_co2(3)/3.*T_fc.^2+...
    A_co2(4)/4.*T_fc.^3+A_co2(5)/5.*T_fc.^4+A_co2(6)./T_fc); %Carbon dioxide
enthalpy at fuel cell operating temperature [kJ/kg]

h_co2_T_h2 = R_co2.*T_h2.*((A_co2(1)+A_co2(2)/2.*T_h2+A_co2(3)/3.*T_h2.^2+...
    A_co2(4)/4.*T_h2.^3+A_co2(5)/5.*T_h2.^4+A_co2(6)./T_h2); %Carbon dioxide
enthalpy at H2 temperature at anode inlet [kJ/kg]

%Define air compressor constants
rp_comp=2; %Pressure ratio
eff_comp=0.85; %Compressor isentropic efficiency

%Define hydrogen pump constants
rp_pumph2=1.11; %Pressure ratio
eff_pumph2=0.8; %Pump isentropic efficiency

%Define air humidification water pump constants
delP_pumpairhumid=2.4; %Pressure change through pump [atm]
eff_pumpairhumid=0.8; %Pump isentropic efficiency

%Define hydrogen humidification water pump constants
delP_pumph2humid=2.4; %Pressure change through pump [atm]
eff_pumph2humid=0.8; %Pump isentropic efficiency

%Define cooling water loop constants
delP_pumpcool=0.7; %Pressure change through pump [atm]
eff_pumpcool=0.8; %Pump isentropic efficiency
delTcw_fc=10; %Increase in cooling water temperature through the fuel cell [K]
delTcw_hx=10; %Decrease in cooling water temperature through the heat exchanger [K]

%Define radiator air flow constants
rp_fan=1.003; %Pressure ratio
eff_fan=0.85; %Fan isentropic efficiency
delTair_hx=30; %Increase in air temp through the heat exchanger [K]

%Define expander constants
eff_exp=0.85; %Expander isentropic efficiency

%Compute partial pressure of oxygen (Po2) entering cathode (Equation 3.11)

Po2=(8*P_cath)/(38.0955+(37.9751*(rh_airin*Pg_Tair)/(P_cath-(rh_airin*Pg_Tair))));
    %[atm]

%Compute maximum current density (curden_max).
%Maximum current density is based on maximum power density.

```
%Table contains pressures in first row, temperatures in first column
%(Row 1, Column 1 position (0) is not used). Table entries for each row-column
%combination correspond to maximum current density for that combination.

imax_max_pwr=[0 1.0 1.5 2.0 2.5 3.0 3.5;
    243 0.2 0.2 0.21 0.21 0.21 0.21;
    253 0.23 0.24 0.24 0.24 0.24 0.24;
    263 0.27 0.27 0.28 0.28 0.29 0.29;
    273 0.33 0.33 0.34 0.34 0.35 0.35;
    283 0.41 0.42 0.43 0.44 0.45 0.45;
    293 0.54 0.56 0.58 0.60 0.61 0.62;
    303 0.70 0.77 0.82 0.87 0.91 0.95;
    313 0.70 0.78 0.84 0.89 0.94 0.98;
    323 0.69 0.78 0.85 0.92 0.96 1.01;
    333 0.66 0.76 0.85 0.92 0.98 1.04;
    343 0.60 0.74 0.83 0.92 0.99 1.05;
    353 0.51 0.68 0.80 0.90 0.98 1.06;
    363 0.36 0.59 0.75 0.86 0.96 1.05];


curden_max=table2(imax_max_pwr,T_fc,P_cath); %Maximum current density
    corresponding to specified fuel cell operating temperature and cathode pressure
    determined by double interpolation in Table above [A/cm^2]


%Verify input current density does not exceed maximum current density
if curden > curden_max
    'Current density exceeds maximum'
    curden=curden_max; % [A/cm^2]
else
    curden=curden; % [A/cm^2]
end


%Calculate voltage (V) based on current density
if curden>0.001 % [A/cm^2]
    if T_fc>303.15 % [K]
        Vact=1.05-(0.055*log10(1000*curden))-((1.0604-(0.002493*T_fc))*curden)+...
            (0.055*log10(Po2)) % (Equation 3.6)
    else
        Vact=1.05-(0.055*log10(1000*curden))-((8.966-(0.02857*T_fc))*curden)+...
            (0.055*log10(Po2)) % (Equation 3.7)
    end
else
    Vact=1.0+(0.055*log10(Po2)); % (Equation 3.8)
end


i_lim=1.4+(3.924*((Po2/P_cath)-0.21))+(0.2*(P_cath-3.0)); % (Equation 3.9)
```

```
if curden<i_lim % [A/cm²]
  V=Vact+(0.1*log(1-(curden/i_lim))) % (Equation 3.10) [V]
else
  V=0;
end
```

```
%Compute power density (PA_fc)
PA_fc=(V*curden)/1000 %Power density [kW/cm²]
```

```
%Compute inlet fuel mass flow per area (mfuelA_in) (Equation 3.1)
mfuelA_in=(curden*MW_h2)/(2*F*mu_h2) %[kg H2/(cm²-s)]
```

```
%Compute consumed fuel mass flow per area (mfuelA_cons)
mfuelA_cons=mfuelA_in*mu_h2 %[kg H2/(cm²-s)]
```

```
%Compute exit fuel mass flow per area (mfuelA_out)
mfuelA_out=(1-mu_h2)*mfuelA_in; %[kg H2/(cm²-s)]
```

```
%Compute water requirement per area to humidify incoming fuel (mv_h2)
mvA_h2=8.94*rh_h2in*Pg_Th2*mfuelA_in/(P_an-(rh_h2in*Pg_Th2))
  %[kg H2O/(cm²-s)]
```

```
%Compute inlet air mass flow per area (mairA_in)
mairA_in=34.343*AF*mfuelA_cons %[kg air/(cm²-s)]
```

```
%Compute exit air mass flow per area (mairA_out)
mairA_out=(8*(AF-1)+26.343*AF)*mfuelA_cons %[kg air/(cm²-s)]
```

```
%Compute water requirement per area to humidify incoming air (mvA_air)
mvA_air=0.622*rh_airin*Pg_Tair*mairA_in/(P_cath-(rh_airin*Pg_Tair))
  %[kg H2O/(cm²-s)]
```

```
%Compute water mass flow per area exiting at anode (mh2oAaout_vap)
%(assuming anode is saturated)
mh2oAaout_vap=8.94*(1-mu_h2)*mfuelA_in*Pg_Tfc/(P_an-Pg_Tfc);
  %[kg H2O/(cm²-s)]
```

```
%Compute total water mass flow per area exiting at cathode (mh2ocout_tot)
%(assuming anode is saturated)
mh2oAcout_tot=mvA_h2 + mvA_air + 9*mfuelA_cons - mh2oAaout_vap;
  %[kg H2O/(cm²-s)]
```

```
%Compute water vapor mass flow per area needed for saturation at exit of cathode
%(mh2ocout_sat)
mh2oAcout_sat=9.01*((2.38095*AF)-0.5)*mfuelA_cons*Pg_Tfc/(P_cath-Pg_Tfc);
   %[kg H2O/(cm²-s)]


%Determine whether liquid water exits the cathode
if mh2oAcout_sat <= mh2oAcout_tot
   rh_airout=1;
   mh2oAcout_liq = mh2oAcout_tot - mh2oAcout_sat; %[kg H2O/(cm²-s)]
   mh2oAcout_vap = mh2oAcout_sat; %[kg H2O/(cm²-s)]
else
   mh2oAcout_liq = 0;
   mh2oAcout_vap = mh2oAcout_tot; %[kg H2O/(cm²-s)]
   rh_airout=(mh2oAcout_vap*P_cath)/(Pg_Tfc*(9.01*((2.38095*AF)- 0.5)*...
      mfuelA_cons + mh2oAcout_vap));
end


%Compute change in enthalpy per area for fuel cell reaction (delhA)
delhA=(-mfuelA_cons*h_h2_T_fc)+(-8*mfuelA_cons*h_o2_T_fc)...
   +((mh2oAaout_vap+mh2oAcout_vap-mvA_h2-mvA_air)*h_h2ov_T_fc)...
   +(mh2oAcout_liq*((hf_h2ol/MW_h2o)+(Cp_h2ol*(T_fc-T_ref))))...
   + mfuelA_in*(h_h2_T_fc - h_h2_T_h2)...
   + 8*AF*mfuelA_cons*(h_o2_T_fc - h_o2_T_air)...
   + 26.343*AF*mfuelA_cons*(h_n2_T_fc - h_n2_T_air)...
   + mvA_h2*(h_h2ov_T_fc - h_h2ov_T_h2)...
   + mvA_air*(h_h2ov_T_fc - h_h2ov_T_air); %[kW/cm²]


%Compute Heat Transfer per Area (QA_fc)
QA_fc = delhA + PA_fc %[kW/cm²]


%Compute air compressor power per area requirement (PA_comp)
PA_comp=(mairA_in*Cp_air*T_amb/eff_comp)*(rp_comp^((k_air-1)/k_air)-1)...
   %[kW/cm²]


%Compute expander power per area requirement (PA_exp)
PA_exp=(mairA_out*Cp_air*T_amb*eff_comp)*(1-((1/P_cath)^((k_air-1)/k_air)))...
   %[kW/cm²]


%Compute hydrogen pump power per area requirement (PA_pumph2)
PA_pumph2=(((mfuelA_out*Cp_h2)+(mh2oAaout_vap*Cp_h2ov))* ...
   T_fc/eff_pumph2)*(rp_pumph2^((k_h2-1)/k_h2)-1) %[kW/cm²]
```

215

%Compute water pump power per area requirement to humidify air
%(PA_pumpairhumid)
PA_pumpairhumid=(101.325*mvA_air*delP_pumpairhumid)/...
   (rho_h2o*eff_pumpairhumid) %[kW/cm^2]

%Compute water pump power per area requirement to humidify H$_2$
%(PA_pumph2humid)
PA_pumph2humid=(101.325*mvA_h2*delP_pumph2humid)/...
   (rho_h2o*eff_pumph2humid) %[kW/cm^2]

%Compute cooling water mass flow per area requirement (mcoolA_h2o)
mcoolA_h2o=-QA_fc/(Cp_h2ol*delTcw_fc) %[kg H$_2$O/(cm^2-s)]

%Compute water pump power per area requirement for cooling water
%(PA_pumpcool)
PA_pumpcool=(101.325*mcoolA_h2o*delP_pumpcool)/(rho_h2o*eff_pumpcool)
   %[kW/cm^2]

%Compute heat exchanger air flow per area requirement (mairA_hx)
mairA_hx=(mcoolA_h2o*Cp_h2ol*delTcw_hx)/(Cp_air*delTair_hx)...
   %[kg air/(cm^2-s)]

%Compute cooling fan power per area requirement (PA_fan)
PA_fan=(mairA_hx*Cp_air*T_amb/eff_fan)*(rp_fan^((k_air-1)/k_air)-1) %[kW/cm^2]

%Compute overall system exergetic efficiency (eff_sys) (Equation 3.14)
eff_sys=(PA_fc+ PA_exp -PA_comp-PA_pumph2-PA_pumpairhumid-...
   PA_pumph2humid-PA_pumpcool-PA_fan)/(mfuelA_cons*LHV_h2)

%Compute fuel cell stack exergetic efficiency (eff_fc) (Equation 3.13)
eff_fc=PA_fc/(mfuelA_cons*LHV_h2)

APPENDIX B

DIRECT-HYDROGEN FUEL CELL SYSTEM RELEVANT EQUATIONS

B.1. Specified Parameters:

The following parameters are user-specified. During vehicle simulations, current density request is automatically generated based on load demand.

Parameter	Symbol	Units
Current Density	i	Amp/cm^2
Anode Pressure	P_{an}	atm
Air Inlet Temperature	T_{air}	K
Hydrogen Inlet Temperature	T_{h2}	K
Air Inlet Relative Humidity	$\phi_{air,in}$	
Hydrogen Inlet Relative Humidity	$\phi_{h2,in}$	
Air-Fuel Ratio	AF	kmol air/kmol H$_2$ consumed
Fuel Cell Operating Temperature	T_{cell}	K
Fuel Utilization	μ	kmol H$_2$ consumed/ kmol H$_2$ in
Active Fuel Cell Area	A	cm^2
Pressure Drop through Cathode	ΔP_{cath}	atm
Ambient Temperature	T_{amb}	K
Hydrogen Pump Isentropic Efficiency	eff_pumph2	
Hydrogen Pump Pressure Ratio	rp_pumph2	
Compressor Isentropic Efficiency	eff_comp	
Compressor Pressure Ratio	rp_comp	
Expander Isentropic Efficiency	eff_exp	
Air Humidification Pump Isentropic Efficiency	$eff\_pumpairhumid$	
Pressure Change through Air Humidification Pump	$delP\_pumpairhumid$	atm
Hydrogen Humidification Pump Isentropic Efficiency	$eff\_pumph2humid$	
Pressure Change through Hydrogen Humidification Pump	$delP\_pumph2humid$	atm
Temperature Change of Cooling Water through Fuel Cell Stack	$delTcw\_fc$	K
Cooling Pump Isentropic Efficiency	$eff\_pumpcool$	
Pressure Change through Cooling Water Pump	$delP\_pumpcool$	atm

217

Parameter	Symbol	Units
Temperature Change of Cooling Water through Radiator (Heat Exchanger)	delTcw_hx	K
Temperature Change of Air through Radiator (Heat Exchanger)	delTair_hx	K
Fan Isentropic Efficiency	eff_fan	
Fan Pressure Ratio	rp_fan	

B.2. Balanced Cell Reaction for hydrogen and oxygen:

$$H_2 + \frac{1}{2}O_2 \rightarrow H_2O$$
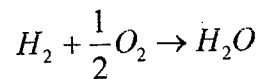
is converted from molar basis to mass basis using species molecular weights:

$$1\left(kmol_{h2}\right) \times 2\left(\frac{kg_{h2}}{kmol_{h2}}\right) + \frac{1}{2}\left(kmol_{o2}\right) \times 32\left(\frac{kg_{o2}}{kmol_{o2}}\right) \rightarrow 1\left(kmol_{h2o}\right) \times 18\left(\frac{kg_{h2o}}{kmol_{h2o}}\right)$$

(2 kg) H_2 + (16 kg) $O_2 \rightarrow$ (18 kg) H_2O

(1 kg) H_2 + (8 kg) $O_2 \rightarrow$ (9 kg) H_2O
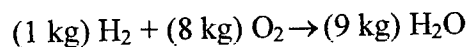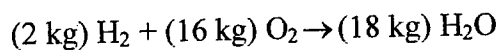
to produce the following result:

For every kg H_2 consumed,   8 kg O_2 are consumed,
9 kg H_2O are produced.

B.3. Balanced Cell Reaction for stoichiometric hydrogen and air:
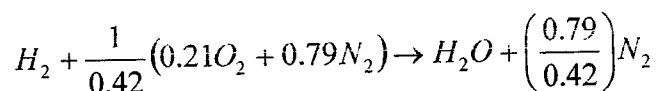
$$H_2 + \frac{1}{0.42}\left(0.21O_2 + 0.79N_2\right) \rightarrow H_2O + \left(\frac{0.79}{0.42}\right)N_2$$

is converted from molar basis to mass basis using species molecular weights (assuming molecular weight of air is based on 21% oxygen and 79% nitrogen):

$$1\left(kmol_{h2}\right) \times 2\left(\frac{kg_{h2}}{kmol_{h2}}\right) + \frac{1}{0.42}\left(kmol_{air}\right) \times 28.8479\left(\frac{kg_{air}}{kmol_{air}}\right)$$

$$\rightarrow 1\left(kmol_{h2o}\right) \times 18\left(\frac{kg_{h2o}}{kmol_{h2o}}\right) + \frac{0.79}{0.42}\left(kmol_{n2}\right) \times 28.01\left(\frac{kg_{n2}}{kmol_{n2}}\right)$$

(2 kg) H_2 + (68.6855 kg) air $\rightarrow$ (18 kg) H_2O + (52.6855 kg) N_2

(1 kg) H_2 + (34.343 kg) air $\rightarrow$ (9 kg) H_2O + (26.343 kg) N_2
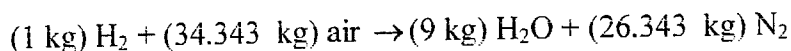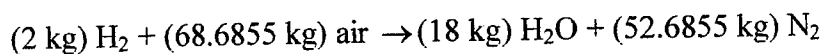
to produce the following result:

For every kg H₂ consumed,   34.343 kg air are consumed
(8 kg O₂ are consumed,
26.343 kg N₂ are consumed),
9 kg H₂O are produced,
26.343 kg N₂ are produced.

B.4. <u>Balanced Cell Reaction for hydrogen and air with air fuel ratio:</u>

$$H_2 + \left(\overline{AF}\right)\frac{1}{0.42}\left(0.21O_2 + 0.79N_2\right) \rightarrow H_2O + \left(\frac{\overline{AF}-1}{2}\right)O_2 + \overline{AF}\left(\frac{0.79}{0.42}\right)N_2$$

is converted from molar basis to mass basis using species molecular weights (assuming molecular weight of air is based on 21% oxygen and 79% nitrogen):

$$1\left(kmol_{h2}\right) \times 2\left(\frac{kg_{h2}}{kmol_{h2}}\right) + \frac{\overline{AF}}{0.42}\left(kmol_{air}\right) \times 28.8479\left(\frac{kg_{air}}{kmol_{air}}\right)$$

$$\rightarrow 1\left(kmol_{h2o}\right) \times 18\left(\frac{kg_{h2o}}{kmol_{h2o}}\right) + \frac{0.79 \times \overline{AF}}{0.42}\left(kmol_{n2}\right) \times 28.01\left(\frac{kg_{n2}}{kmol_{n2}}\right)$$

(2 kg) H₂ + (68.6855 $\overline{AF}$ kg) air → (18 kg) H₂O + (16 ($\overline{AF}$ -1) kg) O₂ + (52.6855 $\overline{AF}$ kg) N₂

(1 kg) H₂ + (34.343 $\overline{AF}$ kg) air → (9 kg) H₂O + (8 ($\overline{AF}$ -1) kg) O₂ + (26.343 $\overline{AF}$ kg) N₂

to produce the following result:

For every kg H₂ consumed,   34.343 $\overline{AF}$ kg air are consumed
(8 $\overline{AF}$ kg O₂ are consumed,
26.343 $\overline{AF}$ kg N₂ are consumed)
9 kg H₂O are produced,
8 ($\overline{AF}$ - 1) kg O₂ are produced,
26.343 $\overline{AF}$ kg N₂ are produced.

B.5. <u>Water Requirements for Humidification.</u>

(a) Water requirement for humidification of air at cathode inlet:

Determine mass flow of water required to humidify air. (Assumption: air and water vapor are ideal gases.) Specific ratio of water in air is defined as the ratio of water vapor mass to the ratio of dry air mass:

$$\frac{\dot{m}_v}{\dot{m}_{air}} = \frac{m_v}{m_{air}} = \frac{\dfrac{P_v V (M_{h_2o})}{\overline{R}T}}{\dfrac{P_{air} V (M_{air})}{\overline{R}T}} = \frac{P_v (M_{h_2o})}{P_{air} (M_{air})} = 0.622 \frac{P_v}{P_{air}} = 0.622 \frac{P_v}{P_{cathode,in} - P_v}$$

Relative Humidity (ϕ) is defined as the ratio of the partial pressure of water vapor (P_v) to the saturation pressure (P_g) at the specified temperature and pressure:

$$\phi = \left(\frac{P_v}{P_g} \right)_{T,P}$$

Substituting $P_v = \phi P_g$, mass flow rate of water required to humidify air to relative humidity (ϕ_{air}) is:

$$\dot{m}_v = 0.622 \dot{m}_{air} \left(\frac{\phi_{air} P_g}{P_{cathode,in} - \phi_{air} P_g} \right)_{Tcathode,Pcathode,in}$$

For humidification of air when fuel and air with air fuel ratio are used, water mass flow required is:

$$\dot{m}_v = 0.622 \times 34.343 \, \overline{AF} \left(\frac{\phi_{air} P_g}{P_{cathode,in} - \phi_{air} P_g} \right)_{Tcathode,Pcathode,in}$$

$$\dot{m}_v = 21.361 \, \overline{AF} \left(\frac{\phi_{air} P_g}{P_{cathode,in} - \phi_{air} P_g} \right)_{Tcathode,Pcathode,in}$$

(b) Water requirement for humidification of hydrogen at anode inlet:

Determine mass flow of water required to humidify hydrogen. (Assumption: hydrogen and water vapor are ideal gases.) Specific ratio of water in hydrogen is defined as the ratio of water vapor mass to the ratio of hydrogen mass:

$$\frac{\dot{m}_v}{\dot{m}_{h2}} = \frac{m_v}{m_{h_2}} = \frac{\dfrac{P_v V \left(M_{h_2 o} \right)}{RT}}{\dfrac{P_{h_2} V \left(M_{h_2} \right)}{RT}} = \frac{P_v \left(M_{h_2 o} \right)}{P_{h_2} \left(M_{h_2} \right)} = 8.94 \frac{P_v}{P_{h_2}} = 8.94 \frac{P_v}{P_{anode} - P_v}$$

Mass flow rate of water required to humidify hydrogen at anode inlet to relative humidity (ϕ_{h2}) is:

$$\dot{m}_v = 8.94 \dot{m}_{h_2} \left(\frac{\phi_{h_2} P_g}{P_{anode} - \phi_{h_2} P_g} \right)_{Tanode, Panode}$$

B.6. <u>Compressor Performance Parameters:</u>

If constant compressor pressure ratio and isentropic efficiency are not used, compressor performance is based on air mass flow as summarized in the following table:

Percent Flow [%]	$\dot{m}_{air}$ [kg/s]	Isentropic Efficiency [%] (includes 85% motor/controller efficiency)	Pressure Ratio
100	0.076	68	3.2
80	0.0608	71	3.2
60	0.0456	69	2.7
40	0.0304	64	2.1
20	0.0152	49	1.6
10	0.0076	53	1.3

For the required air mass flow based on the fuel consumption mass flow, the cathode pressure results from compressor performance.

B.6. <u>Pressure Drop through Cathode:</u>

Pressure drop through cathode is proportional to the square of air flow through the compressor:

$$\Delta P = \alpha \, (\dot{m}_{air})^2$$

For nominal flow of 0.076 kg/s through compressor, a pressure drop of 0.4 atm is experienced by the flow through the fuel cell cathode. Using this criterion, solve for the constant, α.

$$\alpha = \frac{0.4}{(0.076)^2} = 69.25$$

221

Relationship for pressure drop through cathode is:

$$\Delta P[\text{atm}] = 69.25 \, (\dot{m}_{air} \, [\text{kg/s}])^2$$

Exit pressure from cathode is the inlet cathode pressure minus the pressure drop:

$$P_{cathode,out} = P_{cathode,in} - \Delta P$$

B.8. Expander Performance Parameters:

If constant expander isentropic efficiency is not used, expander performance is based on air mass flow as summarized in the following table:

Percent Flow [%]	$\dot{m}_{air}$ [kg/s]	Isentropic Efficiency [%] (includes 85% motor/controller efficiency)
100	0.082	81
80	0.0656	81
60	0.0492	80
40	0.0328	78
20	0.0164	63
10	0.0082	75

B.9. Saturation Pressure of Water at Cathode Inlet Temperature:

Equation to determine saturation pressure of water, P_{sat} [atm], at a specified temperature was developed using regression analysis of temperature-saturation pressure data.

$$ln(P_{sat})[atm] = 11.7384 - 3875.52\left(\frac{1}{T[K]}\right) - 159{,}296\left(\frac{1}{T[K]}\right)^2 - 10{,}651{,}805\left(\frac{1}{T[K]}\right)^3$$

Solving for P_{sat}:

$$P_{sat}[atm] = exp\left(11.7384 - 3875.52\left(\frac{1}{T[K]}\right) - 159{,}296\left(\frac{1}{T[K]}\right)^2 - 10{,}651{,}805\left(\frac{1}{T[K]}\right)^3\right) \qquad (3.12)$$

B.10. Calculate partial pressure of oxygen entering cathode.

(a) Molar flow rate of oxygen into cathode ($\dot{n}_{o2,in}$) [kmol/s] based on balanced cell reaction for hydrogen and air with air fuel ratio is:

$$\dot{n}_{o2,in} = \frac{8 \times \overline{AF}}{M_{o2}}\left(\dot{m}_{h2,cons}\right)$$

(b) Total molar flow rate of all species entering cathode ($\dot{n}_{cath,in}$) [kmol/s] based on balanced cell reaction for hydrogen and air with air fuel ratio and mass flow of water required to achieve desired relative humidity is:

$$\dot{n}_{cath,in} = \left[\frac{8 \times \overline{AF}}{M_{o2}} + \frac{26.343 \times \overline{AF}}{M_{n2}} + \frac{21.361 \times \overline{AF}}{M_{h2o}} \left(\frac{\phi_{air,in} P_g}{P_{cathode,in} - \phi_{air,in} P_g} \right)_{Tair,in} \right] \left(\dot{m}_{h2,cons} \right)$$

(c) Derive the expression for the mole fraction of oxygen entering the cathode (x_{o2}):

$$x_{o2} = \frac{\dot{n}_{o2,in}}{\dot{n}_{cath,in}}$$

$$x_{o2} = \frac{\dfrac{8 \times \overline{AF}}{M_{o2}} \left(\dot{m}_{h2,cons} \right)}{\left[\dfrac{8 \times \overline{AF}}{M_{o2}} + \dfrac{26.343 \times \overline{AF}}{M_{n2}} + \dfrac{21.361 \times \overline{AF}}{M_{h2o}} \left(\dfrac{\phi_{air,in} P_g}{P_{cathode,in} - \phi_{air,in} P_g} \right)_{Tair,in} \right] \left(\dot{m}_{h2,cons} \right)}$$

$$x_{o2} = \frac{\dfrac{8}{M_{o2}}}{\left[\dfrac{8}{M_{o2}} + \dfrac{26.343}{M_{n2}} + \dfrac{21.361}{M_{h2o}} \left(\dfrac{\phi_{air,in} P_g}{P_{cathode,in} - \phi_{air,in} P_g} \right)_{Tair,in} \right]}$$

$$x_{o2} = \frac{\dfrac{8}{32}}{\left[\dfrac{8}{32} + \dfrac{26.343}{28.01} + \dfrac{21.361}{18} \left(\dfrac{\phi_{air,in} P_g}{P_{cathode,in} - \phi_{air,in} P_g} \right)_{Tair,in} \right]}$$

$$x_{o2} = \frac{8}{\left[38.0955 + 37.9751 \left(\dfrac{\phi_{air,in} P_g}{P_{cathode,in} - \phi_{air,in} P_g} \right)_{Tair,in} \right]}$$

(d) Partial pressure of oxygen entering cathode is:

$$P_{o2} = x_{o2} P_{cathode,in}$$

223

$$P_{o2} = \cfrac{8 \times P_{cathode,in}}{\left[38.0955 + 37.9751 \left(\cfrac{\phi_{air,in} P_g}{P_{cathode,in} - \phi_{air,in} P_g} \right)_{Tair,in} \right]}$$

B.11. Compute output voltage (V) using appropriate equation for specified current density and fuel cell temperature.

For $i > 0.001 \dfrac{Amp}{cm^2}$ and $T_{cell} > 303.15K$:

$$V_{act} = 1.05 - 0.055 \log(1000i) - (1.0604 - 0.002493 T_{cell})i + 0.055 \log(P_{o2,in}) \qquad (3.6)$$

For $T_{cell} < 303.15K$:

$$V_{act} = 1.05 - 0.055 \log(1000i) - (8.966 - 0.02857 T_{cell})i + 0.055 \log(P_{o2,in}) \qquad (3.7)$$

For $i < 0.001$ Amp/cm^2:

$$V_{act} = 1.0 + 0.055 \log(P_{o2,in}) \qquad (3.8)$$

The actual cell voltage is adjusted based on a limit current (i_{lim}):

$$i_{lim} = 1.4 + 3.924 \left(\frac{P_{o2,in}}{P_{cathode,in}} - 0.21 \right) + 0.2(P_{cathode,in} - 3.0) \qquad (3.9)$$

If $i < i_{lim}$, then V_{act} is adjusted as:

$$V = V_{act} + 0.1 \ln \left(1 - \frac{i}{i_{lim}} \right) \qquad (3.10)$$

If $i > i_{lim}$, then $V = 0$.

B.12. Compute power density (P/A) [kW/cm^2] produced by fuel cell.

$$\frac{P}{A} = \frac{V \times i}{1000}$$

$$\text{(Units: } \frac{P}{A}\left[\frac{kW}{cm^2} \right] = V[V] \times i \left[\frac{Amp}{cm^2} \right] \times \left[\frac{W}{VAmp} \right] \times \left[\frac{kW}{1000W} \right] \text{)}$$

224

B.13. Compute fuel cell anode inlet fuel mass flow per area, (mfuelA_in) [kg_{h2,in}/(cm²-s)] based on specified fuel utilization.

$$\mu = \frac{n_{h2,cons} \times M_{h2}}{n_{h2,in} \times M_{h2}} = \left(\frac{i \times A \times M_{h2}}{2F} \right) \left(\frac{1}{mfuel\_in} \right) = \frac{i \times M_{h2}}{2F \times mfuelA\_in}$$

$$mfuelA\_in = \frac{i \times M_{h2}}{2F\mu}$$

$$\text{(Units: } mfuelA\_in \left[\frac{kg_{h2,in}}{cm^2 \times s} \right] = \frac{i \left[\frac{Amp}{cm^2} \right] \times M_{h2} \left[\frac{kg_{h2,cons}}{kmol_{h2,cons}} \right]}{2 \left[\frac{kmol_{e^-}}{kmol_{h2,cons}} \right] \times 96,487,000 \left[\frac{Coulomb}{kmol_{e^-}} \right] \times \mu \left[\frac{kg_{h2,cons}}{kg_{h2,in}} \right] \times \left[\frac{Amp \times s}{Coulomb} \right]} \text{)}$$

B.14. Compute consumed mass flow of fuel per area (mfuelA_cons) [kg_{h2,cons}/(cm²-s)]:

$$mfuelA\_cons = \mu \times mfuelA\_in$$

$$\text{(Units: } mfuelA\_cons \left[\frac{kg_{h2,cons}}{cm^2 \times s} \right] = \mu \left[\frac{kg_{hw,cons}}{kg_{h2,in}} \right] \times mfuelA\_in \left[\frac{kg_{h2,in}}{cm^2 \times s} \right] \text{)}$$

B.15. Compute exit fuel mass flow per area (mfuelA_out) [kg_{h2out}/(cm²-s)] from anode:

$$mfuelA\_out = mfuelA\_in - mfuelA\_cons$$

$$\text{(Units: } mfuelA\_out \left[\frac{kg_{h2,out}}{cm^2 \times s} \right] = mfuelA\_in \left[\frac{kg_{h2,in}}{cm^2 \times s} \right] - mfuelA\_cons \left[\frac{kg_{h2,cons}}{cm^2 \times s} \right] \text{)}$$

B.16. Compute water requirement per area to humidify incoming fuel (mvA_h2) at anode. (Assumption: hydrogen from tank has zero relative humidity.)

$$\frac{m_v}{m_{h_2}} = \frac{\dfrac{P_v V M_{h_2o}}{RT}}{\dfrac{P_{h_2} V M_{h_2}}{RT}} = \frac{P_v M_{h_2o}}{P_{h_2} M_{h_2}} = 8.94 \frac{P_v}{P_{h_2}} = 8.94 \frac{P_v}{P_{anode} - P_v}$$

225

$$m_v = 8.94 m_{h_2} \left(\frac{\phi_{h_2} P_g}{P_{anode} - \phi_{h_2} P_g} \right)_{Tanode, Panode}$$

On a per area basis, water requirement to humidify hydrogen [kg H_2O/(cm^2-s)] is:

$$mvA\_h2 = 8.94 mfuelA \left(\frac{\phi_{h_2} P_g}{P_{anode} - \phi_{h_2} P_g} \right)_{Tanode, Panode}$$

B.17. Determine cathode inlet air mass flow per area (mairA_in) [kg air/(cm^2-s)]:

$$mairA\_in = 34.343 \times \overline{AF} \times mfuelA\_cons$$

B.18. Determine water requirement per area to humidify the cathode incoming air (mvA_air): (Assumption: ambient air has zero relative humidity.)

$$\frac{m_v}{m_{air}} = \frac{\frac{P_v V M_{h_2o}}{RT}}{\frac{P_{air} V M_{air}}{RT}} = \frac{P_v M_{h_2o}}{P_{air} M_{air}} = 0.622 \frac{P_v}{P_{air}} = 0.622 \frac{P_v}{P_{cathode,in} - P_v}$$

$$m_v = 0.622 m_{air} \left(\frac{\phi_{air} P_g}{P_{cathode,in} - \phi_{air} P_g} \right)_{Tcathode, Pcathode,in}$$

On a per area basis, water requirement to humidify air (mvA_air) [kg H_2O/(cm^2-s)] is:

$$mvA\_air = 0.622 mairA\_in \left(\frac{\phi_{air} P_g}{P_{cathode,in} - \phi_{air} P_g} \right)_{Tcathode, Pcathode,in}$$

B.19. Compute water mass flow per area exiting at anode (mh2oAaout_vap) [kg H_2O/(cm^2-s)]. (Assumptions: hydrogen exiting anode is fully saturated (ϕ=1) and hydrogen has no pressure drop from anode inlet to exit.)

$$mh2oAaout\_vap = 8.94 \left(mfuelA\_in - mfuelA\_cons \right) \left(\frac{P_g}{P_{anode} - P_g} \right)_{Tcell, Panode}$$

226

B.20. Compute total water mass flow per area exiting at cathode (mh2oAcout_tot) [kg H₂O/(cm²-s)]. Total water mass flow exiting at cathode is the amount of water entering at the anode and cathode and the water produced during the cell reaction minus the water exiting at the anode.

$$mh2oAcout\_tot = mvA\_h2 + mvA\_air + 9(mfuelA\_cons) - mh2oAaout\_vap$$

B.21. Determine cathode exit pressure $P_{cathode,out}$ [atm]. (Assumption: depleted air exiting cathode has a pressure drop from cathode inlet to exit.)

$$P_{cathode,out} = P_{cathode,in} - \Delta P_{cathode}$$

B.22. Determine the water vapor mass flow per area needed for saturation of depleted air at the exit of the cathode (mh2oAcout_sat) [kg H₂O/(cm²-s)].

$$mh2oAcout\_sat = 9.01\left(2.38095\overline{AF} - 0.5\right)mfuelA\_cons\left(\frac{P_g}{P_{cathode,out} - P_g}\right)_{Tcell,Pcathode,out}$$

B.23. Determine whether liquid water exits the cathode.

(a) If the amount of water vapor mass flow per area for saturation of depleted air at the exit of the cathode (mh2oAcout_sat) is less than or equal to the total water mass flow per area exiting the cathode (mh2oAcout_tot), then the depleted air exits the cathode saturated ($\phi=1$). The mass flow per area of water vapor exiting the cathode is the water vapor mass flow per area needed for saturation of depleted air at the cathode exit:

$$mh2oAcout\_vap = mh2oAcout\_sat.$$

The mass flow per area of liquid water exiting the cathode (mh2oAcout_liq) [kg H₂O/(cm²-s)] is the difference between the total and the saturated water mass flows per area for the cathode exit: (Assumption: water vapor and liquid water are in thermodynamic equilibrium at the cell temperature.)

$$mh2oAcout\_liq = mh2oAcout\_tot - Mh2oAcout\_sat$$

(b) If the amount of water vapor mass flow per area for saturation of depleted air at the exit of the cathode (mh2oAcout_sat) is greater than the total water mass flow per area exiting the cathode (mh2oAcout_tot), then the depleted air exiting the cathode is not saturated and no liquid water exits the cathode. The mass flow per area of water vapor exiting the cathode is the total water mass flow per area exiting the cathode:

$$mh2oAcout\_vap = mh2oAcout\_tot.$$

227

B.24. Compute the change in enthalpy per area (delhA) [kW/cm²] (the right hand side of the energy balance below) for the fuel cell reaction.

$$\dot{Q} - \dot{W} = \sum_{\text{Pr}od} \dot{m}_P h_P \left(T_{cell}\right) - \left(\sum_{\text{Re}act,anode} \dot{m}_{R,anode} h_{R,anode} \left(T_{anode}\right) + \sum_{\text{Re}act,cathode} \dot{m}_{R,cathode} h_{R,cathode} \left(T_{cathode}\right) \right)$$

(a) Anode reactants are H_2 and $H_2O(vap)$. Cathode reactants are O_2, N_2, and $H_2O(vap)$. Products at the anode are H_2 and $H_2O(vap)$. Products at the cathode are O_2, N_2, $H_2O(vap)$, and $H_2O(liq)$.

(b) By adding to and subtracting from the energy equation above the following terms:

$$\sum_{\text{Re}act,anode} \dot{m}_{R,anode} h_{R,anode} \left(T_{cell}\right) + \sum_{\text{Re}act,cathode} \dot{m}_{R,cathode} h_{R,cathode} \left(T_{cell}\right)$$

the change in enthalpy can be expressed in two parts: a change in enthalpy due to a change in mass flow of species at T_{cell} and a change in enthalpy due to a change in temperature. The resulting equation is:

$$\dot{Q} - \dot{W} = \left(\dot{m}_{h_2,a,out} - \dot{m}_{h_2,a,in}\right) h\left(T_{cell}\right)_{h_2} + \left(\dot{m}_{o_2,c,out} - \dot{m}_{o_2,c,in}\right) h\left(T_{cell}\right)_{o_2}$$

$$+ \left(\dot{m}_{n_2,a,out} - \dot{m}_{n_2,a,in}\right) h\left(T_{cell}\right)_{n_2} + \left(\dot{m}_{h_2o(liq),c,out}\right) h\left(T_{cell}\right)_{h_2o(liq)}$$

$$+ \left(\dot{m}_{h_2o(vap),a,out} + \dot{m}_{h_2o(vap),c,out} - \dot{m}_{h_2o(vap),a,in} - \dot{m}_{h_2o(vap),c,in}\right) h\left(T_{cell}\right)_{h_2o(vap)}$$

$$+ \dot{m}_{h_2,a,in} \left(h\left(T_{cell}\right) - h\left(T_{h2,in}\right)\right) + \dot{m}_{o_2,c,in} \left(h\left(T_{cell}\right) - h\left(T_{air,in}\right)\right) + \dot{m}_{n_2,a,in} \left(h\left(T_{cell}\right) - h\left(T_{air,in}\right)\right)$$

$$+ \dot{m}_{h_2o(vap),a,in} \left(h\left(T_{cell}\right) - h\left(T_{h2,in}\right)\right) + \dot{m}_{h_2o(vap),c,in} \left(h\left(T_{cell}\right) - h\left(T_{air,in}\right)\right)$$

(c) Since nitrogen does not participate in the chemical reaction, the mass flow of nitrogen into the cathode equals the mass flow of nitrogen exiting the cathode. Consequently, the term

$$\left(\dot{m}_{n_2,a,out} - \dot{m}_{n_2,a,in}\right) h\left(T_{cell}\right)_{n_2}$$

is zero and is dropped from the energy balance equation.

(d) Liquid water enthalpy value is computed using assumption that

$$h\left(T_{cell}\right)_{h_2o(vap)} = \left(\frac{\overline{h}_f^o}{M_{h2o}}\right) + C_{h2o(liq)}\left(T_{cell} - T_{ref}\right)$$

228

(e) Energy balance equation becomes:

$$\dot{Q} - \dot{W} = \left(\dot{m}_{h_2,a,out} - \dot{m}_{h_2,a,in}\right) h\left(T_{cell}\right)_{h_2} + \left(\dot{m}_{o_2,c,out} - \dot{m}_{o_2,c,in}\right) h\left(T_{cell}\right)_{o_2}$$

$$+ \left(\dot{m}_{h_2o(liq),c,out}\right) \left[\left(\frac{\bar{h}_f^o}{M_{h2o}} \right) + C_{h2o(liq)} \left(T_{cell} - T_{ref}\right) \right]$$

$$+ \left(\dot{m}_{h_2o(vap),a,out} + \dot{m}_{h_2o(vap),c,out} - \dot{m}_{h_2o(vap),a,in} - \dot{m}_{h_2o(vap),c,in}\right) h\left(T_{cell}\right)_{h_2o(vap)}$$

$$+ \dot{m}_{h_2,a,in} \left(h\left(T_{cell}\right) - h\left(T_{h2,in}\right)\right) + \dot{m}_{o_2,c,in} \left(h\left(T_{cell}\right) - h\left(T_{air,in}\right)\right) + \dot{m}_{n_2,a,in} \left(h\left(T_{cell}\right) - h\left(T_{air,in}\right)\right)$$

$$+ \dot{m}_{h_2o(vap),a,in} \left(h\left(T_{cell}\right) - h\left(T_{h2,in}\right)\right) + \dot{m}_{h_2o(vap),c,in} \left(h\left(T_{cell}\right) - h\left(T_{air,in}\right)\right)$$

Enthalpy values for all ideal gas species are computed from MATLAB routine included in Appendix A.

(f) Change in enthalpy per fuel cell active area (delhA) [kW/cm^2] is computed from right hand side of energy balance equation, substituting mass flows per area for mass flows.

$$delhA = \left(mfuelA\_out - mfuelA\_in\right) h\left(T_{cell}\right)_{h_2} + \left(\frac{\dot{m}_{o_2,c,out}}{A} - \frac{\dot{m}_{o_2,c,in}}{A} \right) h\left(T_{cell}\right)_{o_2}$$

$$+ \left(mh2oAcout\_liq\right) \left[\left(\frac{\bar{h}_f^o}{M_{h2o}} \right) + C_{h2o(liq)} \left(T_{cell} - T_{ref}\right) \right]$$

$$+ \left(mh2oAaout\_vap + mh2oAcout\_vap - mvA\_h2 - mvA\_air\right) h\left(T_{cell}\right)_{h_2o(vap)}$$

$$+ mfuelA\_in\left(h\left(T_{cell}\right) - h\left(T_{h2,in}\right)\right) + \frac{\dot{m}_{o_2,c,in}}{A} \left(h\left(T_{cell}\right) - h\left(T_{air,in}\right)\right) + \frac{\dot{m}_{n_2,a,in}}{A} \left(h\left(T_{cell}\right) - h\left(T_{air,in}\right)\right)$$

$$+ mvA\_h2\left(h\left(T_{cell}\right) - h\left(T_{h2,in}\right)\right) + mvA\_air\left(h\left(T_{cell}\right) - h\left(T_{air,in}\right)\right)$$

B.25. Compute the heat transfer per area (QA_fc) [kW/cm2] from the energy balance equation

$$QA\_fc = delhA + PA\_fc$$

B.26. Compute power per area associated with auxiliary components.

(a) Compute air compressor power per area requirement (PA_comp) [kW/cm^2]:

$$PA\_comp = \left(\frac{mairA\_in \times Cp\_air \times T_{amb}}{eff\_comp} \right) \left(rp\_comp^{\left(\frac{k\_air-1}{k\_air} \right)} - 1 \right)$$

(b) Compute expander power per area produced (*PA_exp*) [kW/cm^2]:

$$PA\_exp = eff\_exp \times \left((mo2A\_out \times Cp\_o2) + (mn2A\_out \times Cp\_n2) \right) \times Tcell \left(1 - \left(\frac{1}{P_{cathode,out}} \right)^{\left(\frac{k\_air-1}{k\_air} \right)} \right)$$

(c) Compute hydrogen pump power per area requirement (*PA_pumph2*) [kW/cm^2]:

$$PA\_pumph2 =$$
$$\frac{\left((mfuelA\_out \times Cp\_h2) + (mh2oAaout\_vap \times Cp\_h2ov) \right) \times Tcell}{eff\_pumph2} \left(rp\_pumph2^{\left(\frac{k\_h2-1}{k\_h2} \right)} - 1 \right)$$

(d) Compute water pump power per area requirement to humidify air (*PA_pumpairhumid*) [kW/cm^2]:

$$PA\_pumpairhumid = \frac{101.325 \times mvA\_air \times delP\_pumpairhumid}{rho\_h2o \times eff\_pumpairhumid}$$

(e) Compute water pump power per area requirement to humidify H$_2$ (*PA_pumph2humid*) [kW/cm^2]:

$$PA\_pumph2humid = \frac{101.325 \times mvA\_h2 \times delP\_pumph2humid}{rho\_h2o \times eff\_pumph2humid}$$

(f) Compute cooling water mass flow per area requirement (*mcoolA_h2o*) [kg H$_2$O/(cm^2-s)]:

$$mcoolA\_h2o = \frac{-QA\_fc}{Cp\_h2ol \times delTcw\_fc}$$

(g) Compute water pump power per area requirement for cooling water (*PA_pumpcool*) [kW/cm^2]:

$$PA\_pumpcool = \frac{101.325 \times mcoolA\_h2o \times delP\_pumpcool}{rho\_h2o \times eff\_pumpcool}$$

(h) Compute heat exchanger air flow per area requirement (*mairA_hx*) [kg air/(cm^2-s)]:

$$mairA\_hx = \frac{mcoolA\_h2o \times Cp\_h2ol \times delTcw\_hx}{Cp\_air \times delTair\_hx}$$

(i) Compute cooling fan power per area requirement (PA_fan) [kW/cm^2]:

$$PA\_fan = \frac{mairA\_hx \times Cp\_air \times T_{amb}}{eff\_fan}\left(rp\_fan^{\left(\frac{k\_air-1}{k\_air}\right)} - 1\right)$$

B.27. <u>Compute fuel cell stack exergetic efficiency (<i>eff fc</i>).</u>

$$eff\_fc = \frac{PA\_fc}{mfuelA\_cons \times LHV\_h2} \qquad (3.13)$$

B.28. <u>Compute power density associated with auxiliary components (<i>PA aux</i>) [kW/cm^2].</u>

$$PA\_aux = PA\_exp - PA\_comp - PA\_pumph2 - PA\_pumpairhumid$$

$$-PA\_pumph2humid - PA\_pumpcool - PA\_fan$$

B.29. <u>Compute overall system exergetic efficiency (<i>eff sys</i>).</u>

$$eff\_sys = \frac{PA\_fc + PA\_aux}{mfuelA\_cons \times LHV\_h2} \qquad (3.14)$$

APPENDIX C

METHANOL REFORMING FUEL CELL SYSTEM RELEVANT EQUATIONS

C.1. General Comment

Equations in Appendix C are similar to those in Appendix B. Sections in Appendix C that contain equations that are new or reflect changes to those in Appendix B are marked with an asterisk (*).

C.2. Specified Parameters

The following parameters are user-specified. During vehicle simulations, current density request is automatically generated based on load demand.

Parameter	Symbol	Units
Current Density	i	Amp/cm^2
Anode Pressure	P_{an}	atm
Air Inlet Relative Humidity	$\phi_{air,in}$	
Hydrogen Inlet Relative Humidity	$\phi_{h2,in}$	
Air-Fuel Ratio	AF	kmol air/kmol H$_2$ consumed
Fuel Cell Operating Temperature	T_{cell}	K
Fuel Utilization	μ	kmol H$_2$ consumed/kmol H$_2$ in
Active Fuel Cell Area	A	cm^2
Pressure Drop through Cathode	ΔP_{cath}	atm
Ambient Temperature	T_{amb}	K
Methanol Pump Isentropic Efficiency	$eff\_pumpmeth$	
Pressure Change through Methanol Pump	$delP\_pumpmeth$	atm
Reformer Water Pump Isentropic Efficiency	$eff\_pumph2oref$	
Pressure Change through Reformer Water Pump	$delP\_pumph2oref$	atm
Reformer Air Compressor Isentropic Efficiency	$eff\_compref$	
Reformer Air Compressor Pressure Ratio	$rp\_compref$	
FC Air Compressor Isentropic Efficiency	eff_comp	
FC Air Compressor Pressure Ratio	rp_comp	
Expander Isentropic Efficiency	eff_exp	

232

Parameter	Symbol	Units
Air Humidification Pump Isentropic Efficiency	*eff_pumpairhumid*	
Pressure Change through Air Humidification Pump	*delP_pumpairhumid*	atm
Reformate Humidification Pump Isentropic Efficiency	*eff_pumprefhumid*	
Pressure Change through Reformate Humidification Pump	*delP_pumprefhumid*	atm
Temperature Change of Cooling Water through Fuel Cell Stack	*delTcw_fc*	K
Cooling Pump Isentropic Efficiency	*eff_pumpcool*	
Pressure Change through Cooling Water Pump	*delP_pumpcool*	atm
Temperature Change of Cooling Water through Radiator (Heat Exchanger)	*delTcw_hx*	K
Temperature Change of Air through Radiator (Heat Exchanger)	*delTair_hx*	K
Fan Isentropic Efficiency	*eff_fan*	
Fan Pressure Ratio	*rp_fan*	

*C.3. Theoretical Reformer Equation:

$$CH_3OH(l) + x(O_2 + 3.76N_2) + (1-2x)H_2O(l) \rightarrow (3-2x)H_2 + CO_2 + 3.76xN_2 \quad (5.1)$$
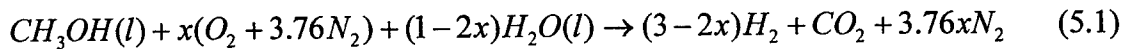
is converted from molar basis to mass basis using species molecular weights and normalized by the mass of hydrogen to determine quantities of reactants and products per kilogram of hydrogen produced:

$$\frac{M_{CH_3OH}}{(3-2x)M_{H_2}}CH_3OH + \frac{xM_{O_2}}{(3-2x)M_{H_2}}O_2 + \frac{3.76xM_{N_2}}{(3-2x)M_{H_2}}N_2 + \frac{(1-2x)M_{H_2O}}{(3-2x)M_{H_2}}H_2O \rightarrow$$

$$H_2 + \frac{M_{CO_2}}{(3-2x)M_{H_2}}CO_2 + \frac{3.76xM_{N_2}}{(3-2x)M_{H_2}}N_2 \quad (5.2)$$
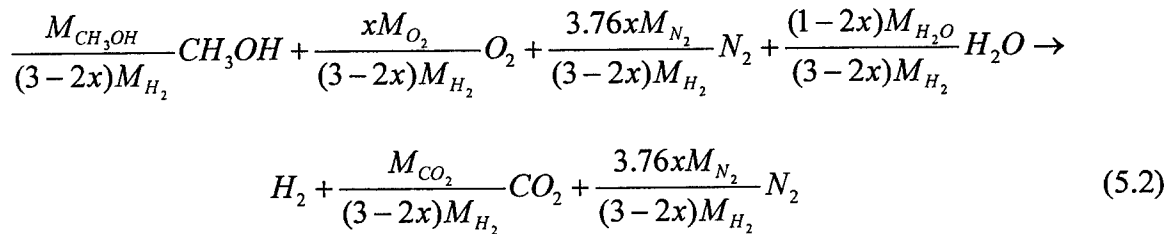
to produce the following result:

For every kg H2 produced, $\dfrac{M_{CH_3OH}}{(3-2x)M_{H_2}}$ **kg CH₃OH are consumed,**

$\dfrac{xM_{O_2}}{(3-2x)M_{H_2}}$ **kg O₂ are consumed.**

$$\frac{3.76xM_{N_2}}{(3-2x)M_{H_2}} \text{ kg } N_2 \text{ are consumed.}$$

$$\frac{(1-2x)M_{H_2O}}{(3-2x)M_{H_2}} \text{ kg } H_2O(l) \text{ are consumed.}$$

$$\frac{M_{CO_2}}{(3-2x)M_{H_2}} \text{ kg } CO_2 \text{ are produced.}$$

$$\frac{3.76xM_{N_2}}{(3-2x)M_{H_2}} \text{ kg } N_2 \text{ are produced.}$$

*C.4. <u>Fuel Cell Balanced Reaction for hydrogen and air with air fuel ratio:</u>

$$H_2 + \left(\overline{AF}\right)\frac{1}{0.42}\left(0.21O_2 + 0.79N_2\right) \rightarrow H_2O + \left(\frac{\overline{AF}-1}{2}\right)O_2 + \overline{AF}\left(\frac{0.79}{0.42}\right)N_2$$

is converted from molar basis to mass basis using species molecular weights (assuming molecular weight of air is based on 21% oxygen and 79% nitrogen):

$$1\left(kmol_{h2}\right) \times 2\left(\frac{kg_{h2}}{kmol_{h2}}\right) + \frac{\overline{AF}}{0.42}\left(kmol_{air}\right) \times 28.8479\left(\frac{kg_{air}}{kmol_{air}}\right)$$

$$\rightarrow 1\left(kmol_{h2o}\right) \times 18\left(\frac{kg_{h2o}}{kmol_{h2o}}\right) + \frac{0.79 \times \overline{AF}}{0.42}\left(kmol_{n2}\right) \times 28.01\left(\frac{kg_{n2}}{kmol_{n2}}\right)$$

(2 kg) H_2 + (68.6855 $\overline{AF}$ kg) air $\rightarrow$ (18 kg) H_2O + (16 ($\overline{AF}$ -1) kg) O_2 + (52.6855 $\overline{AF}$ kg) N_2

(1 kg) H_2 + (34.343 $\overline{AF}$ kg) air $\rightarrow$ (9 kg) H_2O + (8 ($\overline{AF}$ -1) kg) O_2 + (26.343 $\overline{AF}$ kg) N_2

to produce the following result:

For every kg H_2 consumed, **34.343 $\overline{AF}$ kg air are consumed**
(8 $\overline{AF}$ kg O_2 are consumed,
26.343 $\overline{AF}$ kg N_2 are consumed)
9 kg H_2O are produced,
8 ($\overline{AF}$ - 1) kg O_2 are produced,
26.343 $\overline{AF}$ kg N_2 are produced.

C.5. Water Requirements for Humidification.

(a) Water requirement for humidification of air at cathode inlet:

Determine mass flow of water required to humidify air. (Assumption: air and water vapor are ideal gases.) Specific ratio of water in air is defined as the ratio of water vapor mass to the ratio of dry air mass:

$$\frac{\dot{m}_v}{\dot{m}_{air}} = \frac{m_v}{m_{air}} = \frac{\dfrac{P_v V (M_{h_2o})}{\overline{R}T}}{\dfrac{P_{air} V (M_{air})}{\overline{R}T}} = \frac{P_v (M_{h_2o})}{P_{air}(M_{air})} = 0.622\frac{P_v}{P_{air}} = 0.622\frac{P_v}{P_{cathode,in} - P_v}$$

Relative Humidity (ϕ) is defined as the ratio of the partial pressure of water vapor (P_v) to the saturation pressure (P_g) at the specified temperature and pressure:

$$\phi = \left(\frac{P_v}{P_g}\right)_{T,P}$$

Substituting $P_v = \phi P_g$, mass flow rate of water required to humidify air to relative humidity (ϕ_{air}) is:

$$\dot{m}_v = 0.622\dot{m}_{air}\left(\frac{\phi_{air}P_g}{P_{cathode,in} - \phi_{air}P_g}\right)_{Tcathode,Pcathode,in}$$

For humidification of air when fuel and air with air fuel ratio are used, water mass flow required is:

$$\dot{m}_v = 0.622 \times 34.343\,\overline{AF}\left(\frac{\phi_{air}P_g}{P_{cathode,in} - \phi_{air}P_g}\right)_{Tcathode,Pcathode,in}$$

$$\dot{m}_v = 21.361\,\overline{AF}\left(\frac{\phi_{air}P_g}{P_{cathode,in} - \phi_{air}P_g}\right)_{Tcathode,Pcathode,in}$$

*(b) Water requirement for humidification of reformate at anode inlet:

Determine mass flow of water required to humidify reformate. (Assumption: reformate and water vapor are ideal gases.) Specific ratio of water in reformate is defined as the ratio of water vapor mass to the ratio of reformate mass:

235

$$\frac{\dot{m}_v}{\dot{m}_{ref}} = \frac{m_v}{m_{ref}} = \frac{\dfrac{P_v V \left(M_{h_2o}\right)}{\overline{R}T}}{\dfrac{P_{ref} V \left(M_{ref}\right)}{\overline{R}T}} = \frac{P_v \left(M_{h_2o}\right)}{P_{ref} \left(M_{ref}\right)} = \frac{M_{h_2o}}{M_{ref}} \left(\frac{P_v}{P_{anode} - P_v}\right)$$

Mass flow rate of water required to humidify reformate to relative humidity (ϕ_{ref}) is:

$$\dot{m}_v = \dot{m}_{ref} \left(\frac{M_{h_2o}}{M_{ref}}\right) \left(\frac{\phi_{ref} P_g}{P_{anode} - \phi_{reform} P_g}\right)_{Tanode, Panode}$$

C.6. Compressor Performance Parameters:

If constant compressor pressure ratio and isentropic efficiency are not used, compressor performance is based on air mass flow as summarized in the following table:

Percent Flow [%]	$\dot{m}_{air}$ [kg/s]	Isentropic Efficiency [%] (includes 85% motor/controller efficiency)	Pressure Ratio
100	0.076	68	3.2
80	0.0608	71	3.2
60	0.0456	69	2.7
40	0.0304	64	2.1
20	0.0152	49	1.6
10	0.0076	53	1.3

For the required air mass flow based on the fuel consumption mass flow, the cathode pressure results from compressor performance.

C.7. Pressure Drop through Cathode:

Pressure drop through cathode is proportional to the square of air flow through the compressor:

$$\Delta P = \alpha \left(\dot{m}_{air}\right)^2$$

For nominal flow of 0.076 kg/s through compressor, a pressure drop of 0.4 atm is experienced by the flow through the fuel cell cathode. Using this criterion, solve for the constant, α.

$$\alpha = \frac{0.4}{(0.076)^2} = 69.25$$

236

Relationship for pressure drop through cathode is:

$$\Delta P[\text{atm}] = 69.25 \ (\dot{m}_{air} \ [\text{kg/s}])^2$$

Exit pressure from cathode is the inlet cathode pressure minus the pressure drop:

$$P_{cathode,out} = P_{cathode,in} - \Delta P$$

C.8. Expander Performance Parameters:

If constant expander isentropic efficiency is not used, expander performance is based on air mass flow as summarized in the following table:

Percent Flow [%]	$\dot{m}_{air}$ [kg/s]	Isentropic Efficiency [%] (includes 85% motor/controller efficiency)
100	0.082	81
80	0.0656	81
60	0.0492	80
40	0.0328	78
20	0.0164	63
10	0.0082	75

C.9. Saturation Pressure of Water at Cathode Inlet Temperature:

Equation to determine saturation pressure of water, P_{sat} [atm], at a specified temperature was developed using regression analysis of temperature-saturation pressure data.

$$ln(P_{sat})[atm] = 11.7384 - 3875.52\left(\frac{1}{T[K]}\right) - 159,296\left(\frac{1}{T[K]}\right)^2 - 10,651,805\left(\frac{1}{T[K]}\right)^3$$

Solving for P_{sat}:

$$P_{sat}[atm] = exp\left(11.7384 - 3875.52\left(\frac{1}{T[K]}\right) - 159,296\left(\frac{1}{T[K]}\right)^2 - 10,651,805\left(\frac{1}{T[K]}\right)^3\right) \quad (3.12)$$

C.10. Calculate partial pressure of oxygen entering cathode.

(a) Molar flow rate of oxygen into cathode ($\dot{n}_{o2,in}$) [kmol/s] based on balanced cell reaction for hydrogen and air with air fuel ratio is:

237

$$\dot{n}_{o2,in} = \frac{8 \times \overline{AF}}{M_{o2}} \left(\dot{m}_{h2,cons} \right)$$

(b) Total molar flow rate of all species entering cathode ($\dot{n}_{cath,in}$) [kmol/s] based on balanced cell reaction for hydrogen and air with air fuel ratio and mass flow of water required to achieve desired relative humidity is:

$$\dot{n}_{cath,in} = \left[\frac{8 \times \overline{AF}}{M_{o2}} + \frac{26.343 \times \overline{AF}}{M_{n2}} + \frac{21.361 \times \overline{AF}}{M_{h2o}} \left(\frac{\phi_{air,in} P_g}{P_{cathode,in} - \phi_{air,in} P_g} \right)_{Tair,in} \right] \left(\dot{m}_{h2,cons} \right)$$

(c) Derive the expression for the mole fraction of oxygen entering the cathode (x_{o2}):

$$x_{o2} = \frac{\dot{n}_{o2,in}}{\dot{n}_{cath,in}}$$

$$x_{o2} = \frac{\dfrac{8 \times \overline{AF}}{M_{o2}} \left(\dot{m}_{h2,cons} \right)}{\left[\dfrac{8 \times \overline{AF}}{M_{o2}} + \dfrac{26.343 \times \overline{AF}}{M_{n2}} + \dfrac{21.361 \times \overline{AF}}{M_{h2o}} \left(\dfrac{\phi_{air,in} P_g}{P_{cathode,in} - \phi_{air,in} P_g} \right)_{Tair,in} \right] \left(\dot{m}_{h2,cons} \right)}$$

$$x_{o2} = \frac{\dfrac{8}{M_{o2}}}{\left[\dfrac{8}{M_{o2}} + \dfrac{26.343}{M_{n2}} + \dfrac{21.361}{M_{h2o}} \left(\dfrac{\phi_{air,in} P_g}{P_{cathode,in} - \phi_{air,in} P_g} \right)_{Tair,in} \right]}$$

$$x_{o2} = \frac{\dfrac{8}{32}}{\left[\dfrac{8}{32} + \dfrac{26.343}{28.01} + \dfrac{21.361}{18} \left(\dfrac{\phi_{air,in} P_g}{P_{cathode,in} - \phi_{air,in} P_g} \right)_{Tair,in} \right]}$$

$$x_{o2} = \frac{8}{\left[38.0955 + 37.9751 \left(\dfrac{\phi_{air,in} P_g}{P_{cathode,in} - \phi_{air,in} P_g} \right)_{Tair,in} \right]}$$

238

(d) Partial pressure of oxygen entering cathode is:

$$P_{o2} = x_{o2} P_{cathode,in}$$

$$P_{o2} = \frac{8 \times P_{cathode,in}}{\left[38.0955 + 37.9751 \left(\dfrac{\phi_{air,in} P_g}{P_{cathode,in} - \phi_{air,in} P_g} \right)_{Tair,in} \right]}$$

C.11. Compute output voltage (V) using appropriate equation for specified current density and fuel cell temperature.

For $i > 0.001 \; \dfrac{Amp}{cm^2}$ and $T_{cell} > 303.15K$:

$$V_{act} = 1.05 - 0.055 \log(1000i) - (1.0604 - 0.002493 T_{cell})i + 0.055 \log(P_{o2,in}) \qquad (3.6)$$

For $T_{cell} < 303.15K$:

$$V_{act} = 1.05 - 0.055 \log(1000i) - (8.966 - 0.02857 T_{cell})i + 0.055 \log(P_{o2,in}) \qquad (3.7)$$

For $i < 0.001 \; Amp/cm^2$:

$$V_{act} = 1.0 + 0.055 \log(P_{o2,in}) \qquad (3.8)$$

The actual cell voltage is adjusted based on a limit current (i_{lim}):

$$i_{lim} = 1.4 + 3.924 \left(\frac{P_{o2,in}}{P_{cathode,in}} - 0.21 \right) + 0.2(P_{cathode,in} - 3.0) \qquad (3.9)$$

If $i < i_{lim}$, then V_{act} is adjusted as:

$$V = V_{act} + 0.1 \ln \left(1 - \frac{i}{i_{lim}} \right) \qquad (3.10)$$

If $i > i_{lim}$, then $V = 0$.

C.12. Compute power density (P/A) [kW/cm²] produced by fuel cell.

$$\frac{P}{A} = \frac{V \times i}{1000}$$

(Units: $\frac{P}{A}\left[\frac{kW}{cm^2}\right] = V[V] \times i\left[\frac{Amp}{cm^2}\right] \times \left[\frac{W}{VAmp}\right] \times \left[\frac{kW}{1000W}\right]$)

C.13. Compute fuel cell anode inlet hydrogen mass flow per area, (mfuelA_in) [kg_{h2,in}/(cm²-s)] based on specified fuel utilization.

$$\mu = \frac{n_{h2,cons} \times M_{h2}}{n_{h2,in} \times M_{h2}} = \left(\frac{i \times A \times M_{h2}}{2F}\right)\left(\frac{1}{mfuel\_in}\right) = \frac{i \times M_{h2}}{2F \times mfuelA\_in}$$

$$mfuelA\_in = \frac{i \times M_{h2}}{2F\mu}$$

(Units: $mfuelA\_in\left[\frac{kg_{h2,in}}{cm^2 \times s}\right] = \dfrac{i\left[\frac{Amp}{cm^2}\right] \times M_{h2}\left[\frac{kg_{h2,cons}}{kmol_{h2,cons}}\right]}{2\left[\frac{kmol_{e^-}}{kmol_{h2,cons}}\right] \times 96,487,000\left[\frac{Coulomb}{kmol_{e^-}}\right] \times \mu\left[\frac{kg_{h2,cons}}{kg_{h2,in}}\right] \times \left[\frac{Amp \times s}{Coulomb}\right]}$)

*C.14. Compute fuel cell anode inlet reformate mass flow per area, (mreformA_in) [kg_{reform,in}/(cm²-s)] based on inlet hydrogen mass flow.

$$mco2A\_in = \frac{M_{CO_2}}{(3-2x)M_{H_2}} \times mfuelA\_in$$

$$mn2Aa\_in = \frac{3.76xM_{N_2}}{(3-2x)M_{H_2}} \times mfuelA\_in$$

mreformA_in = mfuelA_in + mco2A_in + mn2Aa_in

C.15. Compute consumed mass flow of fuel per area (mfuelA_cons) [kg_{h2,cons}/(cm²-s)]:

$$mfuelA\_cons = \mu \times mfuelA\_in$$

(Units: $mfuelA\_cons\left[\frac{kg_{h2,cons}}{cm^2 \times s}\right] = \mu\left[\frac{kg_{hw,cons}}{kg_{h2,in}}\right] \times mfuelA\_in\left[\frac{kg_{h2,in}}{cm^2 \times s}\right]$)

C.16. Compute anode exit fuel mass flow per area (mfuelA_out) [kg_{h2out}/(cm²-s)] from anode:

$$mfuelA\_out = mfuelA\_in - mfuelA\_cons$$

(Units: $mfuelA\_out\left[\dfrac{kg_{h2,out}}{cm^2 \times s}\right] = mfuelA\_in\left[\dfrac{kg_{h2,in}}{cm^2 \times s}\right] - mfuelA\_cons\left[\dfrac{kg_{h2,cons}}{cm^2 \times s}\right]$)

*C.17. Compute water requirement per area to humidify incoming reformate at anode (mvA_ref). (Assumption: incoming reformate has zero relative humidity.)

$$\frac{\dot{m}_v}{\dot{m}_{ref}} = \frac{m_v}{m_{ref}} = \frac{\dfrac{P_v V\left(M_{h_2o}\right)}{RT}}{\dfrac{P_{ref}V\left(M_{ref}\right)}{RT}} = \frac{P_v\left(M_{h_2o}\right)}{P_{ref}\left(M_{ref}\right)} = \frac{M_{h_2o}}{M_{ref}}\left(\frac{P_v}{P_{anode}-P_v}\right)$$

$$m_v = m_{ref}\left(\frac{M_{h_2o}}{M_{ref}}\right)\left(\frac{\phi_{ref}P_g}{P_{anode}-\phi_{ref}P_g}\right)_{Tanode,Panode}$$

On a per area basis, water requirement to humidify reformate [kg H₂O/(cm²-s)] is:

$$mvA\_ref = mfuelA\left(\frac{M_{h_2o}}{M_{ref}}\right)\left(\frac{\phi_{ref}P_g}{P_{anode}-\phi_{ref}P_g}\right)_{Tanode,Panode}$$

C.18. Determine cathode inlet air mass flow per area (mairA_in) [kg air/(cm²-s)]:

$$mairA\_in = 34.343 \times \overline{AF} \times mfuelA\_cons$$

C.19. Determine water requirement per area to humidify the incoming air (mvA_air) at the cathode: (Assumption: ambient air has zero relative humidity.)

$$\frac{m_v}{m_{air}} = \frac{\dfrac{P_v VM_{h_2o}}{RT}}{\dfrac{P_{air}VM_{air}}{RT}} = \frac{P_v M_{h_2o}}{P_{air}M_{air}} = 0.622\frac{P_v}{P_{air}} = 0.622\frac{P_v}{P_{cathode,in}-P_v}$$

$$m_v = 0.622 m_{air}\left(\frac{\phi_{air}P_g}{P_{cathode,in}-\phi_{air}P_g}\right)_{Tcathode,Pcathode,in}$$

241

On a per area basis, water requirement to humidify air (mvA_air) [kg $H_2O/(cm^2\text{-}s)$] is:

$$mvA\_air = 0.622mairA\_in\left(\frac{\phi_{air}P_g}{P_{cathode,in} - \phi_{air}P_g}\right)_{Tcathode,Pcathode,in}$$

*C.20. **Compute mass flow per area of depleted reformate exiting anode (mrefA_out) [kg reform/cm^2].**

$mco2A\_out = mco2A\_in$
$mn2Aa\_out = mn2Aa\_in$
$mrefA\_out = mfuelA\_out + mco2A\_out + mn2Aa\_out$

*C.21. **Compute Molecular Weight of depleted reformate exiting anode (M_{DR}) [kg ref/kmol ref].**

$$total\_kmol\_DR = \frac{mfuelA\_out}{M_{h2}} + \frac{mco2A\_out}{M_{co2}} + \frac{mn2Aa\_out}{M_{n2}}$$

$$M_{DR} = \frac{mfuelA\_out + mco2A\_out + mn2Aa\_out}{total\_kmol\_DR}$$

*C.22. **Compute water mass flow per area exiting at anode (mh2oAaout_vap) [kg H$_2$O/(cm^2-s)].** (Assumptions: depleted reformate exiting anode is fully saturated (ϕ=1) and reformate has no pressure drop from anode inlet to exit.)

$$mh2oAaout\_vap = \frac{M_{h2o}}{M_{DR}}(mrefA\_out)\left(\frac{P_g}{P_{anode} - P_g}\right)_{Tcell,Panode}$$

*C.23. **Compute total water mass flow per area exiting at cathode (mh2oAcout_tot) [kg H$_2$O/(cm^2-s)].** Total water mass flow exiting at cathode is the amount of water entering at the anode and cathode and the water produced during the cell reaction minus the water exiting at the anode.

$$mh2oAcout\_tot = mvA\_ref + mvA\_air + 9(mfuelA\_cons) - mh2oAaout\_vap$$

C.24. **Determine cathode exit pressure $P_{cathode,out}$ [atm].** (Assumption: depleted air exiting cathode has a pressure drop from cathode inlet to exit.)

$$P_{cathode,out} = P_{cathode,in} - \Delta P_{cathode}$$

C.25. Determine the water vapor mass flow per area needed for saturation of depleted air at the exit of the cathode (mh2oAcout_sat) [kg H₂O/(cm²-s)].

$$mh2oAcout\_sat = 9.01 \left(2.38095 \overline{AF} - 0.5 \right) mfuelA\_cons \left(\frac{P_g}{P_{cathode,out} - P_g} \right)_{Tcell, Pcathode, out}$$

C.26. Determine whether liquid water exits the cathode.

(a) If the amount of water vapor mass flow per area for saturation of depleted air at the exit of the cathode (mh2oAcout_sat) is less than or equal to the total water mass flow per area exiting the cathode (mh2oAcout_tot), then the depleted air exits the cathode saturated (ϕ=1). The mass flow per area of water vapor exiting the cathode is the water vapor mass flow per area needed for saturation of depleted air at the cathode exit:

$$mh2oAcout\_vap = mh2oAcout\_sat.$$

The mass flow per area of liquid water exiting the cathode (mh2oAcout_liq) [kg H₂O/(cm²-s)] is the difference between the total and the saturated water mass flows per area for the cathode exit: (Assumption: water vapor and liquid water are in thermodynamic equilibrium at the cell temperature.)

$$mh2oAcout\_liq = mh2oAcout\_tot - mh2oAcout\_sat$$

(b) If the amount of water vapor mass flow per area for saturation of depleted air at the exit of the cathode (mh2oAcout_sat) is greater than the total water mass flow per area exiting the cathode (mh2oAcout_tot), then the depleted air exiting the cathode is not saturated and no liquid water exits the cathode. The mass flow per area of water vapor exiting the cathode is the total water mass flow per area exiting the cathode:

$$mh2oAcout\_vap = mh2oAcout\_tot.$$

C.27. Compute the change in enthalpy per area (delhA) [kW/cm²] (the right hand side of the energy balance below) for the fuel cell reaction.

$$\dot{Q} - \dot{W} = \sum_{Prod} \dot{m}_P h_P \left(T_{cell} \right) - \left(\sum_{React,anode} \dot{m}_{R,anode} h_{R,anode} \left(T_{anode} \right) + \sum_{React,cathode} \dot{m}_{R,cathode} h_{R,cathode} \left(T_{cathode} \right) \right)$$

*(a) Anode reactants are H_2, CO_2, N_2, and $H_2O(vap)$. Cathode reactants are O_2, N_2, and $H_2O(vap)$. Products at the anode are H_2, CO_2, N_2, and $H_2O(vap)$. Products at the cathode are O_2, N_2, $H_2O(vap)$, and $H_2O(liq)$.

243

*(b) By adding to and subtracting from the energy equation above the following terms:

$$\sum_{\mathrm{Re}\,act,anode} \dot{m}_{R,anode} h_{R,anode} \left(T_{cell}\right) + \sum_{\mathrm{Re}\,act,cathode} \dot{m}_{R,cathode} h_{R,cathode} \left(T_{cell}\right)$$

the change in enthalpy can be expressed in two parts: a change in enthalpy due to a change in mass flow of species at T_{cell} and a change in enthalpy due to a change in temperature. The resulting equation is:

$$
\begin{aligned}
\dot{Q} - \dot{W} &= \left(\dot{m}_{h_2,a,out} - \dot{m}_{h_2,a,in}\right) h\!\left(T_{cell}\right)_{h_2} + \left(\dot{m}_{co_2,a,out} - \dot{m}_{co_2,a,in}\right) h\!\left(T_{cell}\right)_{co_2} \\
&+ \left(\dot{m}_{n_2,a,out} - \dot{m}_{n_2,a,in}\right) h\!\left(T_{cell}\right)_{n_2} + \left(\dot{m}_{o_2,c,out} - \dot{m}_{o_2,c,in}\right) h\!\left(T_{cell}\right)_{o_2} \\
&+ \left(\dot{m}_{n_2,c,out} - \dot{m}_{n_2,c,in}\right) h\!\left(T_{cell}\right)_{n_2} + \left(\dot{m}_{h_2o(liq),c,out}\right) h\!\left(T_{cell}\right)_{h_2o(liq)} \\
&+ \left(\dot{m}_{h_2o(vap),a,out} + \dot{m}_{h_2o(vap),c,out} - \dot{m}_{h_2o(vap),a,in} - \dot{m}_{h_2o(vap),c,in}\right) h\!\left(T_{cell}\right)_{h_2o(vap)} \\
&+ \dot{m}_{h_2,a,in}\left(h(T_{cell}) - h(T_{h2,in})\right) + \dot{m}_{co2,a,in}\left(h(T_{cell}) - h(T_{h2,in})\right) + \dot{m}_{n_2,a,in}\left(h(T_{cell}) - h(T_{h2,in})\right) \\
&+ \dot{m}_{o_2,c,in}\left(h(T_{cell}) - h(T_{air,in})\right) + \dot{m}_{n_2,c,in}\left(h(T_{cell}) - h(T_{air,in})\right) \\
&+ \dot{m}_{h_2o(vap),a,in}\left(h(T_{cell}) - h(T_{h2,in})\right) + \dot{m}_{h_2o(vap),c,in}\left(h(T_{cell}) - h(T_{air,in})\right)
\end{aligned}
$$

*(c) Since nitrogen does not participate in the chemical reaction, the mass flow of nitrogen into the cathode equals the mass flow of nitrogen exiting the cathode. Consequently, the term

$$\left(\dot{m}_{n_2,a,out} - \dot{m}_{n_2,a,in}\right) h\!\left(T_{cell}\right)_{n_2}$$

is zero and is dropped from the energy balance equation. Similarly, since carbon dioxide and nitrogen do not participate in the reaction in the anode, these mass flows do not change and appropriate terms are dropped from the energy balance equation.

(d) Liquid water enthalpy value is computed using assumption that

$$h\!\left(T_{cell}\right)_{h_2o(liq)} = \left(\frac{\overline{h}_f^{\,o}}{M_{h2o}}\right) + C_{h2o(liq)}\left(T_{cell} - T_{ref}\right)$$

244

*(e) Energy balance equation becomes:

$$\dot{Q} - \dot{W} = \left(\dot{m}_{h_2,a,out} - \dot{m}_{h_2,a,in} \right) h(T_{cell})_{h_2} + \left(\dot{m}_{o_2,c,out} - \dot{m}_{o_2,c,in} \right) h(T_{cell})_{o_2}$$

$$+ \left(\dot{m}_{h_2o(liq),c,out} \right) \left[\left(\frac{\overline{h}_f^o}{M_{h2o}} \right) + C_{h2o(liq)} \left(T_{cell} - T_{ref} \right) \right]$$

$$+ \left(\dot{m}_{h_2o(vap),a,out} + \dot{m}_{h_2o(vap),c,out} - \dot{m}_{h_2o(vap),a,in} - \dot{m}_{h_2o(vap),c,in} \right) h(T_{cell})_{h_2o(vap)}$$

$$+ \dot{m}_{h_2,a,in} \left(h(T_{cell}) - h(T_{h2,in}) \right) + \dot{m}_{co_2,a,in} \left(h(T_{cell}) - h(T_{h2,in}) \right) + \dot{m}_{n_2,a,in} \left(h(T_{cell}) - h(T_{h2,in}) \right)$$

$$+ \dot{m}_{o_2,c,in} \left(h(T_{cell}) - h(T_{air,in}) \right) + \dot{m}_{n_2,c,in} \left(h(T_{cell}) - h(T_{air,in}) \right)$$

$$+ \dot{m}_{h_2o(vap),a,in} \left(h(T_{cell}) - h(T_{h2,in}) \right) + \dot{m}_{h_2o(vap),c,in} \left(h(T_{cell}) - h(T_{air,in}) \right)$$

Enthalpy values for all ideal gas species are computed from MATLAB routine included in Appendix A.

*(f) Change in enthalpy per fuel cell active area ($delhA$) [kW/cm^2] is computed from right hand side of energy balance equation, substituting mass flows per area for mass flows.

$$delhA = \left(mfuelA\_out - mfuelA\_in \right) h(T_{cell})_{h_2} + \left(\frac{\dot{m}_{o_2,c,out}}{A} - \frac{\dot{m}_{o_2,c,in}}{A} \right) h(T_{cell})_{o_2}$$

$$+ \left(mh2oAcout\_liq \right) \left[\left(\frac{\overline{h}_f^o}{M_{h2o}} \right) + C_{h2o(liq)} \left(T_{cell} - T_{ref} \right) \right]$$

$$+ \left(mh2oAaout\_vap + mh2oAcout\_vap - mvA\_ref - mvA\_air \right) h(T_{cell})_{h_2o(vap)}$$

$$+ mfuelA\_in \left(h(T_{cell}) - h(T_{h2,in}) \right) + mco2A - out \left(h(T_{cell}) - h(T_{h2,in}) \right)$$

$$+ mn2Aa\_out \left(h(T_{cell}) - h(T_{h2,in}) \right)$$

$$+ \frac{\dot{m}_{o_2,c,in}}{A} \left(h(T_{cell}) - h(T_{air,in}) \right) + \frac{\dot{m}_{n_2,c,in}}{A} \left(h(T_{cell}) - h(T_{air,in}) \right)$$

$$+ mvA\_ref \left(h(T_{cell}) - h(T_{h2,in}) \right) + mvA\_air \left(h(T_{cell}) - h(T_{air,in}) \right)$$

C.28. Compute the heat transfer per area (QA_fc) [kW/cm2] from the energy balance equation

$$QA\_fc = delhA + PA\_fc$$

*C.29. <u>Compute power per area associated with reformer auxiliary components.</u>

(a) Compute air compressor power per area requirement ($PA\_compref$) [kW/cm^2]:

$$PA\_compref = \left(\frac{\left(\frac{mairref\_in}{A} \right) \times Cp\_air \times T_{amb}}{eff\_compref} \right) \left(rp\_compref^{\left(\frac{k\_air-1}{k\_air} \right)} - 1 \right)$$

(b) Compute reformer water pump power per area requirement ($PA\_pumph2oref$) [kW/cm^2]:

$$PA\_pumph2oref = \frac{101.325 \times \left(\frac{mh2oref\_in}{A} \right) \times delP\_pumph2oref}{rho\_h2o \times eff\_pumph2oref}$$

(c) Compute reformer methanol pump power per area requirement ($PA\_pumpmeth$) [kW/cm^2]:

$$PA\_pumpmeth = \frac{101.325 \times \left(\frac{mmeth\_in}{A} \right) \times delP\_pumpmeth}{rho\_h2o \times eff\_pumpmeth}$$

C.30. <u>Compute power per area associated with fuel cell system auxiliary components.</u>

(a) Compute air compressor power per area requirement (PA_comp) [kW/cm^2]:

$$PA\_comp = \left(\frac{mairA\_in \times Cp\_air \times T_{amb}}{eff\_comp} \right) \left(rp\_comp^{\left(\frac{k\_air-1}{k\_air} \right)} - 1 \right)$$

(b) Compute expander power per area produced (PA_exp) [kW/cm^2]:

$$PA\_exp = eff\_exp \times \left((mo2A\_out \times Cp\_o2) + (mn2A\_out \times Cp\_n2) \right) \times Tcell \left(1 - \left(\frac{1}{P_{cathode,out}} \right)^{\left(\frac{k\_air-1}{k\_air} \right)} \right)$$

246

(c) Compute water pump power per area requirement to humidify air (*PA_pumpairhumid*) [kW/cm^2]:

$$PA\_pumpairhumid = \frac{101.325 \times mvA\_air \times delP\_pumpairhumid}{rho\_h2o \times eff\_pumpairhumid}$$

*(d) Compute water pump power per area requirement to humidify reformate (*PA_pumprefhumid*) [kW/cm^2]:

$$PA\_pumprefhumid = \frac{101.325 \times mvA\_ref \times delP\_pumprefhumid}{rho\_h2o \times eff\_pumprefhumid}$$

(f) Compute cooling water mass flow per area requirement (*mcoolA_h2o*) [kg H$_2$O/(cm^2-s)]:

$$mcoolA\_h2o = \frac{-QA\_fc}{Cp\_h2ol \times delTcw\_fc}$$

(g) Compute water pump power per area requirement for cooling water (*PA_pumpcool*) [kW/cm^2]:

$$PA\_pumpcool = \frac{101.325 \times mcoolA\_h2o \times delP\_pumpcool}{rho\_h2o \times eff\_pumpcool}$$

(h) Compute heat exchanger air flow per area requirement (*mairA_hx*) [kg air/(cm^2-s)]:

$$mairA\_hx = \frac{mcoolA\_h2o \times Cp\_h2ol \times delTcw\_hx}{Cp\_air \times delTair\_hx}$$

(i) Compute cooling fan power per area requirement (*PA_fan*) [kW/cm^2]:

$$PA\_fan = \frac{mairA\_hx \times Cp\_air \times T_{amb}}{eff\_fan}\left(rp\_fan^{\left(\frac{k\_air-1}{k\_air}\right)} - 1\right)$$

C.31. Compute fuel cell stack exergetic efficiency (*eff_fc*).

$$eff\_fc = \frac{PA\_fc}{mfuelA\_cons \times LHV\_h2}$$

(3.13)

247

*C.32. Compute power density associated with auxiliary components (*PA_aux*) [kW/cm²].

$$PA\_aux = PA\_exp - PA\_comp - PA\_pumpairhumid - PA\_pumprefhumid$$
$$- PApumpcool - PA\_fan - PA\_compref - PA\_pumprefh2o - PA\_pumpmeth$$

C.33. Compute overall system exergetic efficiency (*eff_sys*).

$$eff\_sys = \frac{PA\_fc + PA\_aux}{mfuelA\_cons \times LHV\_h2} \qquad (3.14)$$

248